Fall 12-16-2016

INPUT PARAMETERS IN DISCRETE ELEMENT MODELING

Seyedali Yousefi

SeyedAli Yousefi

Candidate

Department of Civil Engineering

Department

This dissertation is approved, and it is acceptable in quality and form for publication:

Approved by the Dissertation Committee:

Prof. Tang-Tat Ng

Chairperson

Prof. Arup Kanti Maji

Prof. Walter Gerstle

Prof. Yu-Lin Shen

INPUT PARAMETERS IN DISCRETE ELEMENT MODELING

by

ALI YOUSEFI

B.S., Civil Engineering, Tabriz University, Tabriz, Iran, 2001

M.S., Earthquake Engineering, University of Tehran, Tehran, Iran, 2004

DISSERTATION

Submitted in Partial Fulfillment of the

Requirements for the Degree of

Doctor of Philosophy

Engineering

The University of New Mexico

Albuquerque, New Mexico

May, 2017

DEDICATION

To Humanity, for Prosperity

In Macroscale

To my Dearest Wife, Tania, for her Love and Patience

And my Beloved Daughter, Nora, for her Sweet Smiles

In Microscale

ACKNOWLEDGHMENTS

I wish to express my sincere appreciation to my doctoral advisor, Prof. Tang-Tat Ng (Percy) for his constructive guidance and great patience in spite of my curiosity and eccentricity, and the difficulties in the past six years. I am particularly thankful for his trust and for providing me with the liberty to accomplish this research as I imagined. This freedom was important to perform this research. I am looking forward to further collaborations with him in future.

Special thanks goes to my doctoral committee members, Prof. Yu-Lin Shen, Prof. Walter Gerstle, and Prof. Arup Kanti Maji who accepted to serve on the committee and reviewed my dissertation despite their busy schedules. I will not forget Prof. Arup Kanti Maji's effort in my admission. I am grateful to Prof. Timothy J. Ross for the opportunity to work with him in the past. I learned a great deal from him. I would like to extend my gratitude to Prof. Mahmoud Reda Taha for his encouragement and invaluable advises, and to the Department of Civil Engineering for providing the facilities, especially the computer lab.

I thank my friends and colleagues for their keen assistance and faithful friendship, Ms. Sadia Faiza in particular for whom I wish good luck in their life and career. My deepest thanks goes to my parents for their unconditional and endless love and support, to my dear wife for continuous care and encouragement, and to our little girl for keeping me hopeful and happy all the time.

INPUT PARAMETERS IN DISCRETE ELEMENT MODELING

by

Ali Yousefi

B.S., Civil Engineering, Tabriz University, Tabriz, Iran, 2001

M.S., Earthquake Engineering, University of Tehran, Tehran, Iran, 2004

Ph.D., Engineering, The University of New Mexico, Albuquerque, 2017

ABSTRACT

The discrete element method (DEM) is employed to study complex behaviors of particulate media. Input parameters may greatly affect the response of DEM models and should therefore be selected carefully. Scaling techniques are employed to enlarge prohibitively small time-steps. To study these techniques, dimensionless input parameters were defined. Responses of models in the dimensionless scale were invariant with choice of density, elastic modulus, and characteristic length if the dimensionless parameters were kept constant. Hence, density scaling is equivalent to use of a higher strain-rate, and stiffness scaling results in a higher strain-rate and an elevated stress state in the dimensionless scale.

In quasi-static simulations, the equilibrium state should be monitored by the proposed moment index. The conventional mass-damping model causes different damping ratios for particles. A new damping model was introduced to address this issue. Comparisons showed superiority of the presented model. The optimum damping ratio was defined as the damping ratio using which the imbalance is minimized in terms of the

moment index. For the conventional and proposed damping models the optimum damping ratio were determined approximately equal to 0.3% and 0.5%, respectively.

In quasi-static simulations, very small strain-rates are applied that should not exceed a specific value beyond which the quasi-static conditions cannot be preserved. The quasi-static strain-rate was defined based on the moment index equal to 0.1%. An approximate quasi-static strain-rate can be determined from a few simulations at high strain-rates. Predictive equations were developed based on initial void ratio, confining pressure, and particle-size distribution of samples. The equations showed adequate accuracy in estimating quasi-static strain-rate, better than that of the inertial number, and suited for the peak state.

Three relationships were developed. The imbalance, in terms of the moment index, depends on the product of strain-rate and damping ratio. Peak friction coefficient shows a linear relationship with the moment index. Using this relationship, the quasi-static peak friction coefficient can be estimated by conducting a few simulations at higher strain-rates (saving of computation effort). The relationship between peak friction coefficient and product of damping ratio and dimensionless strain-rate was derived, which can, also, be utilized to estimate the quasi-static peak friction coefficient.

TABLE OF CONTENTS

LIST OF FIGURES

LIST OF TABLES

PREFACE

The following publications have been coauthored by the Ph.D. student during the course of study.

Journal Articles

[1] **Yousefi, A.** & Ng, T.-T., (2016). Dimensionless Input Parameters in Discrete Element Modeling and Assessment of Scaling Techniques. Computers and Geotechnics, In Review.

Book Chapters

[1] **Yousefi, A.** & Rodriguez, A., (2011). Solutions Manual for Instructors: Fuzzy Logic with Engineering Applications, Timothy J. Ross, 3rd Edition.

Conference Articles

[1] **Yousefi, A.** & Ng, T.-T., (2017). Dimensionless Input Parameters in Discrete Element Modeling and Assessment of Scaling Techniques. EMI 2017, June 4-7, San Diego, CA, Mini-Symposium 72.

[2] Ng, T.-T. & **Yousefi, A.**, (2011). Mechanics of Bi-disperse Granular Materials. 22th EMI 2011, June 2-4, Boston, MA.

In Preparation

[1] **Yousefi, A.** & Ng, T.-T., Size-Dependent Mass-Damping for Discrete Element Modeling.

[2] **Yousefi, A.** & Ng, T.-T., Constitutive Relations for Particulate Media and Applications for Approximation of Peak Friction Angle Using DEM.

[3] **Yousefi, A.** & Ng, T.-T., Quasi-Static Strain Rate for Modeling Particulate Media Using DEM.

CHAPTER 1

Introduction and Scope of Work

1.1. Overview

Particulate media have abundant applications in various technological fields. Due to the amorphous structure of particulate media, these materials exhibit complex behaviors that are not easily predictable. The discrete element method (DEM), which nowadays is utilized more frequently by emerging high-speed computers, is a popular modeling technique used for the study of these complex behaviors. It has unique features, such as the possibility of performing multiple tests on one sample and investigation into microstructure, which are hard to achieve in physical experiments. To accomplish realistic predictions using DEM, it is important to select appropriate input parameters. However, firm guidelines for the selection of input parameters are still scarce, which is addressed in the present research.

1.2. Motivations

Following are the main topics that promoted this research:

Inter-Particle Friction Coefficient and Sample preparation

Every DEM simulation needs a sample with predetermined properties. Sample preparation is a challenging task that sometimes requires as much effort as the main simulation itself. The dynamic sample preparation methods yield realistic samples.

Where dynamic methods are used, building granular samples for DEM simulations requires special considerations and long runtimes. In these methods, samples with different void ratios are created by applying appropriate values for the inter-particle friction coefficient. However, users need to select suitable values for this parameter to obtain samples with desired void ratios.

An automatic algorithm that enables the building of realistic samples with predefined specifications in a consistent manner can be useful to simplify this cumbersome task by eliminating the need to manually prepare samples. Therefore, sample preparation using a dynamic method is addressed in this study, as well as study of the correlation between the inter-particle friction coefficient and void ratio of created samples, which can be used to adjust the inter-particle friction coefficient to yield samples with desired void ratios.

Time-Step and Scaling Techniques

The most prohibitive aspect of DEM is the requirement of long runtimes resulting from the use of small time increments and low strain rates, as the simulation runtime is proportional to the time step and strain rate. Both of these parameters have upper limits. An explicit finite-difference scheme, which requires a time-marching approach, is employed to solve the equilibrium equations of particles in every time step. If a time step greater than the critical time increment is applied in the explicit methods, solutions diverge and become unstable; moreover, major events in DEM simulations, such as the formation and breakage of contacts, are missed.

To cope with this problem, scaling methods have been widely used to increase the critical time step artificially, by increasing the density or size of particles or reducing

contact stiffness using a lower elastic modulus where a Hertzian contact model is adopted. It is not clear how these techniques influence the material response. Clarification of this matter is one of the subjects covered in the present study.

Quasi-**S**tatic Strain Rate

DEM is often intended to simulate static loading conditions, which have more applications in practice. In a static state, particles are in equilibrium at any given moment. DEM is a method that is based on movement and Newton's second law of motion. In order to perform a DEM simulation close to a static state, i.e., a quasi-static simulation, it is necessary to limit unbalanced forces that cause movements relative to inter-particle contact forces, which tend to stabilize particles; that is, the inertial forces should be insignificant compared to the static forces. For this purpose, the loading rate has to be small enough to prevent developing excessive inertial forces. Hence, in quasi-static simulations, very small strain rates are applied that should not exceed a specific value beyond which the quasi-static conditions cannot be preserved. However, determining the strain rate at which quasi-static conditions are fulfilled has not gained much attention. Hence, a quantitative definition for quasi-static strain rate is covered in this work, in addition to the determination of this value.

Evaluation of Equilibrium State

In a quasi-static simulation, it is necessary to evaluate how close the simulation to a quasi-static state is. For assessment of the equilibrium state of samples, quantitative and qualitative methods exist. The use of a quantitative method is simpler and prone to less

error. To quantify the equilibrium state, an indicator is proposed in this study.

Damping

If the equilibrium state of samples can be maintained at higher strain rates, the upper limit of the allowable strain rate in quasi-static conditions increases. For this purpose, damping mechanisms are applied. Selecting an appropriate damping model and damping value are important. The global mass-damping model is one of the most widely used damping models. In this model, the damping coefficient (which is multiplied by particle mass to produce a damping constant) is equally applied to all particles in an assembly. This causes different damping ratios for the particles. That is, it results in a damping ratio proportional to the particle size; meaning that the rate at which velocity and acceleration of each particle are reduced differs depending on the particle size. This leads to less efficiency of the conventional mass-damping model. In this study, a new damping model is introduced to address this issue. To improve the equilibrium state, determining an optimum damping ratio is required as well, which is carried out in the present study.

1.3. Dissertation Layout and Scope of Work

In Chapter 2, the technical literature is reviewed for the discrete element method, damping models, input parameters, scaling methods, and sample preparation techniques.

In Chapter 3, dimensionless input parameters are defined using a characteristic time and length. The dimensionless equations of motion are derived for a single particle. The effects of selected values for dimensionless input parameters on the mechanical behavior

of samples are studied. Then, the effects of density, elastic modulus, and characteristic size of particles on the mechanical response are studied, while keeping the dimensionless parameters constant. Finally, using the dimensionless scheme, scaling techniques are evaluated.

Many samples are required in this study. In Chapter 4, an algorithm is proposed that automatically creates samples with user-defined parameters in a consistent manner. Using the samples that are prepared with this approach, the relationship between inter-particle friction coefficients used in the sample preparation stage and void ratios of the final samples is studied.

In Chapter 5, an index is presented for the assessment of equilibrium state of samples quantitatively, namely moment index. A new mass-damping model is proposed that does not suffer from the drawback of the conventional mass-damping model. The new damping model is compared with the conventional one using the moment index. Then, the relationship between the moment index and damping ratio is studied.

Most DEM simulations are aimed to determine the quasi-static peak friction coefficient of samples. The relationship between the peak friction coefficient and moment index is studied, and using this relationship, an approximation method is presented to estimate the peak friction coefficient in quasi-static conditions. This method requires a few simulations at a high strain rate, which takes much less runtime than a simulation at quasi-static strain rate.

In Chapter 6, the main goal is to determine the quasi-static strain rate. After study of the relationship between the moment index and strain rate, the quasi-static strain rate is defined based on the moment index. Then, using this relationship, an approximate method is presented for determining the quasi-static strain rate. This method requires a few simulations at high strain rates, which can be accomplished within short runtimes.

Another method is proposed that enables the estimation of the quasi-static strain rate based on the specs of a sample without the need for preliminary simulations. For this purpose, several samples with different specs are subjected to different strain rates, and the quasi-static strain rates of the samples are determined. Then, individual correlations between the specs and the quasi-static strain rates are studied. In this study, to reduce the number of the influential parameters, the density, elastic modulus, and characteristic size of the samples are ruled out employing the dimensionless scheme; thereby, the effects of the initial void ratio, confining pressure, and particle-size distribution are merely considered. A characteristic parameter, namely dispersity index, is proposed to represent the particle-size distribution of samples. Combining the identified correlations, predictive equations to estimate the quasi-static strain rate are proposed in dimensionless forms and generalized to dimensional forms for practical uses.

In addition, the relationship between the peak friction coefficient and strain rate is studied. Finally, two more methods are presented to estimate the quasi-static peak friction coefficient of samples. These methods require a few simulations at high strain rates to avoid time-consuming simulations at small quasi-static strain rates.

Eventually, in Chapter 7, the findings are summarized and a few works are suggested for future studies.

CHAPTER 2

Literature Review

2.1. Overview

In this chapter, the technical literature is reviewed for the discrete elements method and the input parameters (e.g., damping, time-step, and strain-rate). The speed-up techniques such as mass-scaling and stiffness-scaling methods are then reviewed. After that, the sample preparation procedure in discrete element modeling is explained.

2.2. Discrete Elements Method

Nowadays, the discrete element method (DEM) is becoming widely accepted as an effective way of addressing engineering problems in granular and discontinuous materials. Macroscopic constitutive laws that can predict the various complicated aspects of granular material are scarce. Attempts to do so often result in macroscopic equations with a huge number of parameters that of those some have obscure physical meanings.

DEM is a numerical scheme to model the mechanical behavior of an assembly of a large number of particles. Every particle is considered a rigid body with translational and rotational degrees of freedom assigned to its center of mass. Each particle moves and interacts with its immediate neighbors through particle-to-particle contacts that can be formed and broken at any time. These interactions result in the overall behavior of a particulate assembly. The simulation is triggered by an external force/displacement imposed by the boundary conditions acting on the assembly or by an applied strain field.

DEM is employed to simulate the interactions and movements of particles.

The “soft contact” method (Cundall, 1971) is widely used discrete element method. The algorithm involves two stages: In the first stage, interaction forces are computed when particles slightly interpenetrate each other that actually represent the small deformations at the contact areas. The contact forces are calculated using contact mechanics. In the second stage, by tracking the contact forces acting on each particle, Newton’s second law is used for each particle to determine the resulting acceleration, which is then integrated to find the new position and velocity of each particle at the next time increment using an explicit finite difference scheme. This process is repeated until the simulation is completed by reaching a specific strain level.

Particle shape is one of the important issues in DEM. Most of the present three-dimensional DEM codes use spherical particles due to the minimum computational effort for contact detection and contact force evaluation. The present work is more focused on the geotechnical application of DEM. The geometries of general sand particles cannot be well described by spheres. The main problem with spherical particles is their small resistance against rolling, which does not allow the model to capture the real behavior of a soil sample. To overcome this problem, several particle shapes have been proposed, such as ellipsoids, polyhedral particles, and particles built of clusters of spheres.

Ng and Dobry (1994) reported 3D simulation results and investigated the effects of particle rotation and inter-particle friction. When particle rotation was inhibited, they found higher strength, greater stiffness, and stronger dilation compared to a case in which rotation was allowed. Ellipsoids represent soil grains better than spherical particles due to their higher resistance to rolling (Wang et al., 1999). Lin and Ng (1997) developed a 3D

DEM code at the University of New Mexico called ELLIPSE3D. In this program, spheroidal particles (ellipsoids with two equal semi-diameters) are used. Ellipsoidal particles are relatively easy to handle mathematically, since, there is no singularity encountered as in using any polygonal element. Also, despite angular elements, there are authentic contact solutions for spheroids. The use of spheroids provides a better opportunity to investigate the mechanical behavior of granular materials while keeping the computational cost reasonable.

A numerical study on the mechanical behavior of mono-sized particle arrays using the ELLIPSE3D program was performed. Higher shear strength, larger initial modulus, more dilation, and less particle rotation were observed with the ellipsoid assembly during the triaxial tests, which indicates greater resemblance to actual sand specimens. The results demonstrated that use of non-spherical particles in discrete element modeling is essential to improving the simulations of the granular materials that intended to represent sand particles.

2.3. Input Parameters

Since its creation in 1971, the discrete elements method has demonstrated its usefulness by capturing certain behaviors of discontinuous media that cannot be simulated easily by continuum methods. Running a DEM simulation requires some numerical parameters as well as actual data, such as the geometry of the problem, material properties, and loading/boundary conditions. The numerical parameters have no link or weak links to actual media and conditions in reality. Using input parameters without any justification may introduce questions about the validity of the results while

different input values may affect simulation results, hence the conclusions. Therefore, investigating the effect of input parameters can be beneficial. With this knowledge, we can present our results with greater confidence. Besides the existence of various DEM programs that nowadays have been developed, it is difficult to compare different researchers' results on similar materials when input parameters are not the same. Among such parameters, the most important ones are damping, and strain rate.

2.3.1. Damping

Damping occurs naturally in any granular assembly subjected to movement. As mentioned by Cavarretta et al. (2010), in real inter-particle contacts there is damage to surface asperities and plastic yielding from the initial contact formation. Also, plastic strains develop in solid particles as the stress continues to increase (Thornton & Ning, 1998). These damages and yielding dissipate energy, so the completely elastic contact models frequently used to describe the contact normal response in DEM codes are unrealistic. Munjiza (2004) describes this as a lack of "material damping" in rigid particulate DEM codes. The consequence for a DEM simulation is that if there is no yielding by contact separation or frictional sliding, particles will vibrate constantly like a highly complex system of connected elastic springs. To avoid this non-physical phenomenon, DEM analysts often introduce numerical or artificial damping in their simulations to reach static equilibrium faster, particularly in quasi-static simulations where velocities of particles do not matter.

The most common approaches to apply the damping effect are mass-proportional damping, viscous damping, and non-viscous damping. Cundall and Starck (1979)

proposed a system of global damping in the form of mass-proportional damping, which can be envisioned as the effect of dashpots connecting each particle to the ground. The amount of damping that each particle receives is proportional to its mass; this is so-called mass-proportional damping. The way in which this type of damping is implemented in a DEM analysis is summarized hereafter. The equation of motion for a particle is:

$$Ma(t) + Cv(t) = F(t) \tag{1}$$

where *M* is the mass matrix, *v(t)* and *a(t)* are the velocity and acceleration vectors at time *t*, *C* is the damping matrix, and *F(t)* is force vector. Assuming $C = \alpha M$ and by using the Verlet time integration approach with a time increment of Δt, the velocity at time $t + \frac{\Delta t}{2}$ can be written in the following form:

$$v\left(t + \frac{\Delta t}{2}\right) = v\left(t - \frac{\Delta t}{2}\right)\left(\frac{1 - \alpha\frac{\Delta t}{2}}{1 + \alpha\frac{\Delta t}{2}}\right) + \left(\frac{\Delta t}{1 + \alpha\frac{\Delta t}{2}}\right)M^{-1}F(t) \tag{2}$$

In fact, Eq. (2) is equivalent to the equation for dynamic relaxation. Cundall (1987) discusses some of the limitations of this type of mass-proportional damping:

1. This form of damping introduces body forces, which may be erroneous in flowing regions and may influence the mode of failure.
2. The optimum proportionality constant (α) depends on the eigenvalues of the stiffness matrix.
3. The damping is applied equally to all nodes. In reality, different amounts of damping may be appropriate for different regions.

Munjiza et al. (1998) introduced a new class of mass-proportional damping in the form $\alpha = \xi(\frac{k}{m})^n$ where *k* and *n* are stiffness and mass of a single (or a multi) degree-of-

freedom system, respectively, α is the mass-damping coefficient, and ξ is a damping ratio that can take a value from zero to one where $\xi = 1$ leads to critical damping. According to the author, the superiority of this method over the mass-proportional damping model of Cundall and Strack (1979) is that in this method *n* can be tuned so that the damping can target a specific frequency range of vibrations. Depending on the value of *n*, this type of damping has the following effects:

n > 1/2: damping ratio for higher frequencies is larger.

n < 1/2: damping ratio for lower frequencies is larger.

n = 1/2: damping ratio is constant over whole range of frequencies.

According to Cleary (2000), viscous (dashpot) damping is another method that works in the contact scale; that is, a viscous damping force is added to the contact force. The expression of this contribution is $-CV$, where *C* is the viscous damping constant and *V* is the relative velocity at the contact. The viscous damping constant is defined by $C = 2\beta\sqrt{m^* k}$, where β is the critical damping ratio, and m^* is effective mass at the contact ($m^* = \frac{m_1 m_2}{m_1 + m_2}$ where m_1 and m_2 are the colliding masses). Where a specific restitution value, *e*, is required, the critical damping ratio can be selected as follows:

$$\beta = \frac{-\ln(e)}{\sqrt{\pi^2 + \ln(e)^2}} \tag{3}$$

By using Eq. (3), viscous contact damping can be linked to the physical properties of the material. However, to prevent erroneous results, it is recommended to use the minimum damping that yields stable results. For this purpose, Frangin et al. (2007) stated that the damping constant must be over half a percent of critical damping and less than a

few percent.

Cundall (1987) proposed an alternative non-viscous damping system, namely local damping, in which the damping at each node is proportional to the magnitude of the out-of-balance force, with a sign that ensures that only the vibrational modes are damped, rather than the steady motion. The out-of-balance force is the non-zero resultant force that acts on a particle to cause acceleration. Referring to Itasca (2004), the damping force is given by

$$F_d{}^p = -\alpha^* |F^p| sign(v^p) \tag{4}$$

where $F_d{}^p$ is the damping force for particle p, α^* is the damping constant (with default value of 0.7), F^p is the resultant or out-of-balance force acting on particle p, and v^p is the velocity vector for particle p. $F_d{}^p$acts in the opposite direction to v^p, and $sign(v^p)$ indicates the sign of the velocity vector. As discussed by Itasca (2004), this form of damping has the advantage that only accelerating motion is damped; therefore, no erroneous damping forces arise from steady-state motion. The damping constant is non-dimensional and the damping is frequency independent. Also, it is similar to hysteretic damping, as the energy loss per cycle is independent of the rate at which the cycle is executed.

Ng (2006) included a discussion on the sensitivity of the output results to the damping parameter adopted, indicating that this parameter can influence both the macro-scale and particle-scale responses. For example, he concluded that with increasing damping, the volume change and peak shear strength of the material increases where velocities of particles decrease.

While damping is one means to overcome the non-physical nature of the contact

constitutive models used in DEM simulations, it is difficult to select a physically meaningful value for damping or to relate the damping algorithms used to physical phenomena.

As discussed by O'Sullivan and Bray (2002), if mass-proportional damping is used in a quasi-static simulation, it is best to use a small amount of damping during the specimen generation stage of analysis and then to reduce this value to zero or close to zero during subsequent deformation of the material. This will minimize the potential for this parameter to unduly influence the overall material response.

2.3.2. Time Step

In their description of the distinct element method, Cundall and Strack (1979) proposed the use of a computationally efficient, explicit, central-difference type time integration scheme. A limitation of this scheme is that it is only conditionally stable, so small time steps must be used. To successfully capture the inherent non-linearity of the problem (changing contact conditions and non-linear contact response), the incremental changes in the practical positions and contact forces in a given time step must be small. This translates into a size constraint on the time increment to capture the non-linearity of the system. Ideally the selected time increment in a DEM simulation should be small enough that the motion of the particle over a given time step influences only its immediate neighboring particles. Cundall and Strack (1978) stated that a fundamental idea of DEM is that the time step should be sufficiently small that in a single time step, disturbances cannot propagate from a particle further than its nearest neighbors.

The stability of the central-difference time integration approach is outlined in many

basic numerical analysis texts. Typically, in numerical analysis/dynamics courses the concept is introduced by considering the free vibration of a particle of mass, *m*, suspended on a simple elastic spring with stiffness *k*. In this simple system, if the central-difference approach is used, the maximum time increment that can be used is $\Delta t_{crit} = \frac{T}{\pi}$, where T is the fundamental period for free oscillation of the system. This period is calculated as $T = 2\pi\sqrt{\frac{m}{k}}$, and therefore, $\Delta t_{crit} = 2\sqrt{\frac{m}{k}}$. If predictions are made using a time increment that exceeds this critical value, the results quickly become physically unreasonable and the analysis is said to be unstable. These restrictions on the choice of the time increment encountered when using the central-difference approach for a single degree-of-freedom system also apply in multi degree-of-freedom simulations in DEM.

In DEM simulations, the critical time increment for stable analysis is proportional to $\sqrt{m/k_{eq}}$ where *m* is the particle mass and k_{eq} is the effective contact stiffness—that is, $\Delta t_{crit} = \beta\sqrt{\frac{m}{k_{eq}}}$. O'Sullivan and Bray (2004) demonstrated that β should not exceed 0.221 for stable three-dimensional analyses with multiple particle contacts.

$$\Delta t_{crit} = 0.221\sqrt{\frac{m}{k_{eq}}} \tag{5}$$

An additional challenge is posed where a non-linear contact model is used (i.e., where stiffness varies). As the Hertzian contact model is non-linear, the following expression is recommended by O'Sullivan et al. (2008) to estimate the equivalent linear spring stiffness:

$$k_{eq} = \frac{\sqrt{8\alpha}}{3} G r_{max} \tag{6}$$

where r_{max} is the maximum radius of spherical particles, αr_{min} is the maximum allowable overlap of the spherical particles in the system, and *G* is the shear modulus of material.

Thornton (2000) and Thornton and Antony (2000) stated that they selected the simulation time increment by considering the minimum particle size and Rayleigh wave speed. According to Sheng et al. (2004), the Rayleigh wave velocity (v_r) for an elastic material with shear modulus of *G* and density of ρ is:

$$v_r = \alpha \sqrt{\frac{G}{\rho}} \tag{7}$$

and α is given by the roots of:

$$(2-\alpha)^4 = 16(1-\alpha^2)\left[1 - \frac{1-2\upsilon}{2(1-\upsilon)}\alpha^2\right] \tag{8}$$

An approximate value of α is given by $\alpha = 0.1631\upsilon + 0.876605$, where υ is the Poisson's ratio for the material. The critical time increment for DEM simulations with spheres and a Hertzian contact model is then given by:

$$\Delta t_{\text{crit}} = \frac{\pi r_{\text{min}}}{\alpha} \sqrt{\frac{\rho}{G}} \tag{9}$$

where r_{min} is the minimum particle radius (Sheng et al., 2004).

In general, Eq. (9) can be simplified in the following form:

$$\Delta t_{\text{crit}} = \alpha' r_{\text{min}} \sqrt{\frac{\rho}{E}} \tag{10}$$

where α' is given in Table 1 for different Poisson's ratios.

Table 1 Coefficients of Rayleigh wave speed and time step using wave propagation

ν	0.10	0.15	0.20	0.25	0.30	0.35	0.40
α	0.893	0.902	0.911	0.919	0.927	0.935	0.942
α'	5.217	5.281	5.342	5.403	5.462	5.521	5.579

Li et al. (2005) suggested a slightly different version of Eq. (9) using average particle radius rather than the minimum particle radius.

Similar to Eq. (9), Šmilauer and Chareyre (2010) estimated the critical time increment based on sonic (P-wave) speed as follows.

$$\Delta t_{\text{crit}} = \text{l}_{\text{min}}\sqrt{\frac{\rho}{E}} \tag{11}$$

where E and ρ are elastic modulus and density of particles, respectively. In this equation, l_{min} can be replaced by the minimum radius of particles, r_{min}. Technically, $\text{l}_{\text{min}} = 2\text{r}_{\text{min}}$ can be used, but because of possible interactions of spheres and facets (which have zero thickness), they consider $\text{l}_{\text{min}} = \text{r}_{\text{min}}$ where rigid boundaries are implemented.

Using Eq. (11), P-wave gives an estimate to the actual $\Delta\text{t}_{\text{crit}}$, so the value of about $\Delta\text{t} = 0.3\Delta\text{t}_{\text{crit}}$ should be used to guarantee a stable simulation.

The mass of a particle with radius r is proportional to r^3. Therefore, a relatively large number of small particles may exist within a very small mass. From a DEM perspective, these particles will add significantly to the computational cost of the simulations, since the simulation runtime increases as the number of particles increases. Furthermore, considering that the critical time increment is proportional to $\sqrt{m/k_{eq}}$, where m is the mass of smallest particle, a very small particle size leads to a small time step. These restrictions have led analysts to neglect the smallest fraction of the particle

size distribution curve. For example, in her simulations of Castlegate Sandstone, Cheung (2000) did not include the smallest 5% fraction by mass of the particles. This can be justified at the particle scale by assuming that these particles do not contribute to the strong force chains that transmit stress across the sample. Potyondy and Cundall (2004), in their simulations of rock mass, describe a procedure for removing the particles with no contacts (termed “floaters”, “rattlers”, or “idle particles” in different sources).

2.3.3. Strain Rate

A DEM model resembles a large assembly of individual masses connected by means of elastic springs. Care needs to be taken in selecting the speed at which a sample is compressed or sheared. For example, Hanley et al. (2013) observed a clear sensitivity of stress-strain response to the strain rate in undrained loading conditions.

For many geomechanical applications, the objective is to simulate a quasi-static response. This means that the system is not flowing and is in, or is close to, a state of static equilibrium. If the deformation rate is too fast, a dynamic response will be recorded (i.e., propagating stress waves through the system) rather than a static response, as might be intended.

The strain rate refers to magnitude of load or displacement prescribed on the boundaries per unit time step. A large strain rate tends to make the computed response dynamic rather than quasi-static. As an extreme case, a large strain would result in unreasonably large contact forces if applied to a particulate assembly in just one step.

According to Tu and Andrade (2008), quasi-static conditions may be monitored by comparing the average stresses acting on opposite rigid walls or by comparing the

boundary stress with the average stress within the sample. Both these two stress conditions (symmetry of stress tensor and equivalence of external stresses and internal stresses) should be met within a small tolerance of 1% or less.

A parametric study can be useful to determine the maximum strain rate that does not violate the quasi-static conditions. For example, as illustrated in Fig. 1 (Plassiard et al., 2009), a dependence for the value of peak shear stress, q_{peak}, is observed in the simulations against the applied strain rate. As strain rate decreases, shear stress decreases, too. But there is a strain rate below which the shear stress does not decease; hence, a quasi-static value for q_{peak} can be deduced. The strain rate for quasi-static simulations can then be chosen as high as the generated inertial effects do not cause more than a specific error level on the shear strength.

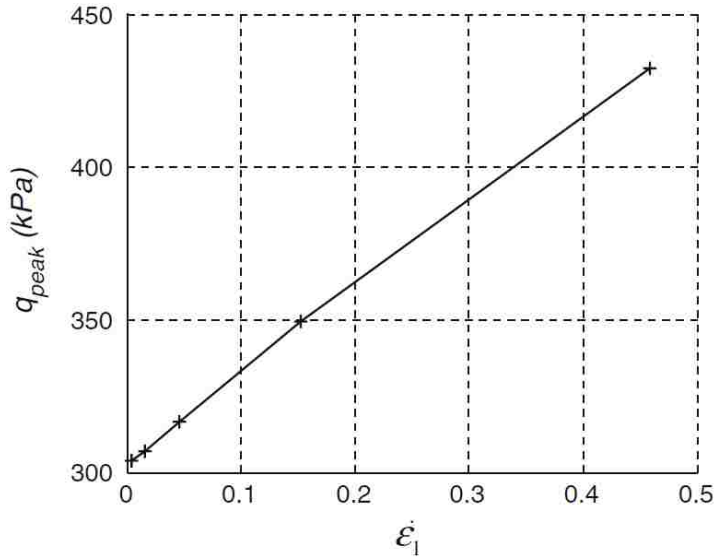

Fig. 1 Influence of strain rate on peak shear stress (Plassiard et al., 2009)

Also, quantitative measures exist to assess whether a system is in equilibrium. da Cruz et al. (2005) proposed a definition for an "inertial number" that can be used to identify whether a flow is quasi-static. The inertial number for 3D simulations, *I*, is given

by

$$I = \dot{\varepsilon}_q \sqrt{\frac{m}{pd}} \tag{12}$$

where $\dot{\varepsilon}_q$ is the shear strain rate, m is the particle mass, d is the particle diameter, and p is the confining pressure. For a simulation to be quasi-static, the condition $I \ll 1$ should be met, giving an indication that the inertial forces are significantly lower than the contact forces. Agnolin and Roux (2008) consider $I < 10^{-4}$ small enough to maintain quasi-static conditions. Where it is intended to determine the critical state strength under drained conditions, $I < 2.5 \times 10^{-3}$ is recommended by Perez et al. (2016), and I is described as insensitive to the initial void ratio.

Ng (2006) and Kuhn (2006) invented a ratio that is the magnitude of the resultant forces (i.e., the out-of-balance forces) acting on the particles to the magnitude of the average contact force. Kuhn (2006) considers the average moment acting on the particles as a further indication of the pseudo-static during simulations. Ng (2006) defines an index to be monitored during simulations:

$$I_{uf} = \sqrt{\frac{\sum_{p=1}^{N_p} \left(f_{res}^{p}\right)^2 / N_p}{\sum_{c=1}^{N_c} (f^c)^2 / N_c}} \tag{13}$$

where f_{res}^{p} is the resultant force acting on particle p, f^c is the contact force for contact c, N_p is the number of particles, and N_c is the number of contacts in the system, respectively.

2.4. Scaling Techniques in DEM

As discussed in Section 2.3.2, the nature of DEM requires the choice of small time increments that lead to "unreasonably" long runtimes for simulations. This encourages DEM users to artificially increase the time step to reduce the computational cost (O'Sullivan et al., 2008). There are three approaches for this purpose throughout the literature: Density Scaling, Stiffness Scaling, and Size Scaling. The most common one is Density Scaling.

The critical time step is proportional to the particle mass. In static analysis, DEM users often scale-up the particle density to artificially increase the particle masses, hence the critical time increment, to achieve results in reasonable runtimes by reducing dynamic effects (Thornton, 2000). This approach is called "density scaling" or "mass scaling". The higher mass value is assigned with the sole purpose of achieving a quasi-static state, i.e. dissipating kinetic energy while balancing external forces throughout the particulate system. The idea behind mass scaling is simple; under the same loading conditions, it is believed that a heavier mass results in less significant dynamic effects (Tu & Andrade, 2008).

Considering this option from a general computational mechanics prospective, Belytschko et al. (2000) suggest that mass scaling should be used in problems where high-frequency effects are not important. When mass scaling is used, it is assumed that the response of the system is not sensitive to inertia effects. Mass or density scaling is frequently used in discrete element analyses, such as in the simulations presented in Thornton (2000). In a DEM simulation, when a force or displacement is applied to a boundary, the response propagates through the system. The speed of propagation of this

"disturbance" is a function of the properties of the system, most notably the stiffness of contacts, the particle mass, and the contact density (i.e., coordination number). A higher mass lowers the wave speed that results in a better quasi-static state.

In order to ensure a quasi-static deformation state with "reasonable" simulation times, Thornton (2000) and Thornton and Antony (2000) scaled the particle density up to 10^{12} times while avoiding global mass-proportional damping. They argue that where this scaling of density is used, the velocities and accelerations are affected; that is, there will be order-of-magnitude changes in particle velocities and accelerations. Since the simulations are quasi-static and body forces are not applied, the contact forces and displacements will remain insensitive to the density value used. However, the contact forces and displacement of particles will be affected if the density scale is not properly selected. Sheng et al. (2004) defined a dimensionless variable, R_e, to consider the effect of the density scales for various strain rates applied to the particle assembly, as follows:

$$R_e = \left[\frac{\dot{\varepsilon}^2 \rho \, r_{min}^2}{p_y}\right]^{\frac{1}{2}} \tag{14}$$

where $\dot{\varepsilon}$ is the strain rate applied to the particle assembly, ρ is the density of the particles, r_{min} is the diameter of the smallest particle, and p_y is the elastic limit of contact pressure between the particles. The result of this assessment on the effect of density scaling with different combinations of strain rates and notional densities is shown in Fig. 2.

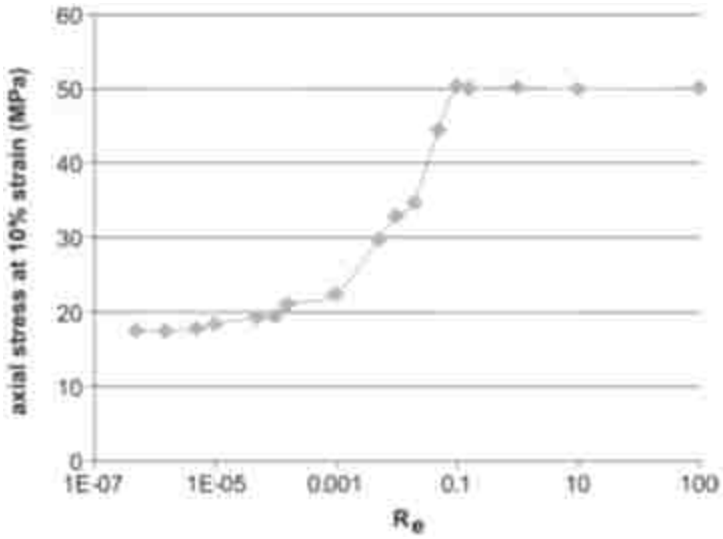

Fig. 2 Effect of density scaling in quasi-static problems

As mentioned by Sheng et al. (2003), a transition zone is seen in this figure, where the axial stress at 10% strain changes dramatically with the strain rate and density. The upper-level line indicates the dynamic response of the assembly caused by the rising magnitude of the strain rate or density beyond a certain level. The results on the lower-level line reflect the stable quasi-static response of the assembly. Between these two horizontal lines, the results for the stress depend on the density-scaling value. Therefore, the notional density should be carefully selected to guarantee that the results are within the quasi-static region. In their study, for the strain rate of $10^{-5}s^{-1}$, the notional density could be scaled up by a factor of 10^{12}.

O'Sullivan (2009) pointed out that the use of density scaling should be approached with caution, and it is questionable whether its use can ever be recommended. To reduce the runtime of the simulations, it seems preferable to maximize the rate of deformation in the simulations while ensuring that the simulations remain quasi-static by carefully monitoring the required conditions. A parametric study by Tu and Andrade (2008)

implies that the mass-scaling method is not ideally effective in helping an explicit DEM computation obtain quasi-static solutions. Furthermore, setting the mass scale to an arbitrarily large number tends to yield unrealistic results distant from the quasi-static state.

According to Malone and Xu (2008), reducing the contact stiffness, the so-called stiffness scaling, is another approach to increase the time step in DEM to reduce the runtime. A case in which the stiffness has been manipulated within "reasonable" limits can be found in a paper by Milburn et al. (2005), who used a stiffness of 1000 N/m in their simulations of beds of bronze spheres. These authors noted that this value resulted in a mean inter-particle overlap in the order of 0.1% of the particle diameter and that system dynamics did not change appreciably by increasing the stiffness.

Also, numerous authors have used DEM to simulate granular materials at a higher scale (e.g., Plassiard et al., 2009; Donzé & Bernasconi, 2004; Sibelle et al., 2007; Shiu et al., 2006); in other words, the size of an element is higher than the real grain size. In these cases, the discrete approach also gives interesting insights into the local behavior.

2.5. Sample Preparation in DEM

A DEM simulation is a transient analysis where the response of the system at discrete points in time is predicted based upon the system state at slightly earlier times. Therefore, specifying the initial condition is as important as specifying the boundary conditions. From an applied perspective of geomechanics, the response of a granular material is known to be highly dependent on the initial state (packing density and stress level). The initial state can be described by the fabric anisotropy (determined from the

particle and the contact orientations), the stress anisotropy, and the orientation of principal stresses relative to the fabric. Just as experimentalists expend significant effort in preparing their samples for physical tests, DEM analysts need to consider carefully how they construct their specimen. Preparation of "virtual" samples for use in subsequent simulations can sometimes be as challenging and costly as the main simulation itself.

Currently, the available algorithms to generate DEM samples are classified in four different types: geometric methods (also called constructive methods), dynamic methods, combined methods, and experimental methods. As used in the present study, the dynamic methods are described next.

2.5.1. Dynamic Methods

The dynamic methods generate samples with random particles through DEM dynamic simulations. Newton's second law of motion is used to determine the trajectory and the final positions of the particles inside a container. A large variety of dynamic algorithms exist that differ by which technique they use: for example, gravitational (Ng, 2005; Siiria & Yliruus, 2007; Marketus & Bolton, 2010), uniaxial compaction (Jiang et al., 2003; Dutt et al., 2005), and isotropic compaction (Stroeven & Stroeven, 1999; Kong & Lannutti, 2000; Barreto et al., 2008).

In nature, sand is typically deposited as particles fall downward under gravitation. Gravitational methods mimic this procedure. For example, Abbireddy and Clayton (2010) developed an algorithm that first creates a cloud of particles (non-overlapping, randomly generated particles) with predefined sizes. Then, the particles are moved downward by a gravitational body force until reaching equilibrium. When generating the cloud of non-

overlapping particles, it is best to start by generating larger particles, and then move successively through the smaller sizes. By doing this, a denser cloud is created, and thus less computation time is necessary for densification.

Jiang et al. (2003) developed a uniaxial compaction method that is effective in making loose samples. In this method, rather than filling the entire volume at the beginning, the sample is built up layer by layer. At each stage of development, the sample is compressed in the vertical direction to achieve a target void ratio ($e_1, e_2, \dots$) that is higher than the final required void ratio, e_{target}. The void ratio should monotically converge toward the target value: $e_1 > e_2 > \cdots > e_{target}$. After each layer is compacted, the boundary is extended vertically to have enough space for creating a new cloud of particles for the next layer over the compacted part.

In most isotropic compaction methods, such as the SPACE algorithm developed by Stroeven and Stroeven (1999), the generation technique consists of two major steps: First, the non-overlapping spheres are randomly positioned inside a container with an initial sphere size distribution. Then, the container undergoes isotropic compression until a specific packing density is reached or a confinement threshold value is obtained. The isotropic compression induces an isotropic dense sphere packing with a reduced amount of contactless spheres. As in most dynamic methods, in the SPACE algorithm, the sphere size distribution is controlled and the packing properties are close to those of a granular medium.

2.5.2. Special Considerations in Sample Preparation

The target stress state should be achieved monotonically (i.e., the stress should be increased gradually from a lower value to the target value); otherwise, the sample produced may become over-consolidated, and that might not be desired. Setting the friction coefficient in the sample preparation stage to a value greater than its final value may produce a similar effect.

In order to reach a static equilibrium state at the final stage, it is important to perform some computation cycles in the absence of boundary movements or body forces prior to the main simulation (O'Sullivan, 2011).

As mentioned by Ng (2006), changes in material properties of constituting particles (e.g., density and elastic modulus) and the artificial input parameters (e.g., damping value) should have only a negligible effect on the resulting samples. This can be considered as a factor in the success of a sample generation algorithm.

In a DEM sample preparation, the target void ratio cannot simply be specified as an input parameter. Rather, a sample must be explicitly created. The range of packing densities that can be achieved in physical lab tests is similarly limited. Therefore, achieving a predefined void ratio is a plus for the success of a method.

Also, some methods are capable of making either loose or dense samples. For example, the uniaxial compaction method of Jiang et al. (2003) makes loose samples and the ballistic deposition method makes loose and medium samples, whereas the tessellation method of Jerier et al. (2009), which is based on tetrahedral meshes, builds only dense packing. Therefore, it is a privilege for an algorithm to be capable of preparing both loose and dense samples.

Isotropic compaction methods have this advantage. Samples with different densities can be achieved by varying the friction coefficient in the early stage of compaction. For example, Cundall (1988) described the use of friction to control the final porosity of specimens constructed for periodic cell simulations. If the friction coefficient is set to zero, a dense specimen is achieved, whereas a large friction coefficient (not more than its final value) generates a loose packing. A further reduction in packing density can be achieved by prohibiting the rotation of particles in the early stage of sample preparation, according to Gong et al. (2011). Medium samples can be prepared by applying a friction coefficient in the intermediate range. Ng (2005) adopted a similar approach to vary the sample density in the gravitational method.

In addition, boundary conditions and sample size (i.e., the number of particles) may affect the simulation results. Desmond and Weeks (2009) investigated random close-packing of spheres in 2D and 3D and concluded that a confining boundary (e.g., rigid walls) alters the structure of the samples in the vicinity of the boundaries, leading to non-homogeneity of samples. However, Cundall (1988) confirmed that periodic boundaries have little effect on the behavior of the samples.

Plassiard et al. (2009) studied sample-size effect by creating four samples with different numbers of particles (10,000, 20,000, 50,000, and 90,000 particles). A triaxial test was carried out for each sample. The stress-strain curves resulting from the triaxial tests showed a global constant response. It was verified that a proportional transformation of the sample does not affect the behavior. The mechanical response was independent of the mean size of the particles and the characteristic size of the sample. Thus, using 10,000 particles in a model seems reasonable to avoid size effect on the numerical response.

CHAPTER 3

Dimensionless DEM and Material Properties

3.1. Overview

The Discrete Elements Method (DEM) has proven its superiority at simulating the behavior of granular matter. However, the input parameters have to be selected carefully so that it can replicate the mechanical behavior of materials. When different sets of input parameters are used for a specific sample, they may result in different mechanical behaviors. Thus, a set of standard parameters is needed. To this end, first, suitable bases need to be defined for the parameters, then, the appropriate value of each parameter should be determined on those bases.

In this chapter, a set of dimensionless parameters (i.e. expressed in terms of natural units) is defined for Discrete Elements Modeling to fulfill the first goal. Then, the dimensionless formulation of discrete elements modeling is derived to explore the scale-invariant capability of DEM. The analytical derivation is validated by DEM simulations. Finally, the effectiveness of the scaling methods is evaluated with the help of this formulation.

3.2. Nondimensionalization of Variables

In a mechanical model, all of the variables can be expressed by means of three fundamental dimensions, namely, **M**, mass, **L**, length, and **T**, time. Therefore, based on the Buckingham π theorem, three independent variables can be used to express all of the

variables involved in this problem. We select ρ, the density of the material of the particles, E, the elastic modulus of the material of the particles, and L_0, an arbitrary characteristic length.

3.2.1. Dimensionless Time and Geometrical Variables

In the present study, the diameter of the smallest particle is taken as the characteristic length, i.e.

$$L_0 = 2R_{min} \tag{15}$$

For non-spherical particles, the diameter of the largest sphere that can be inscribed in the smallest particle can be used for this purpose. Alternatively, the diameter of the sphere whose volume equals the volume of the smallest particle in the assembly can be taken as the characteristic length.

The dimensionless characteristic time is defined as:

$$T_0 = L_0\sqrt{\frac{\rho}{E}} \tag{16}$$

In Appendix 1, it is shown that T_0 is proportionate to the critical time step of the assembly of particles. In an explicit finite difference formulation of differential equations the time step is limited to the critical time step in order to avoid numerical instability.

The dimensionless time variable is defined by the normalization of time, t, by the characteristic time, i.e.

$$\tau = \frac{t}{T_0} \tag{17}$$

The volume of particle i, V_i, can be normalized by the third power of the characteristic length as

$$\bar{V}_i = \frac{V_i}{L_0^3} \tag{18}$$

Then, the mass of the particle is:

$$m_i = \rho L_0^3 \bar{V}_i \tag{19}$$

The inertia tensor of the particle with an arbitrary shape is given by:

$$I_i = \rho \int_{V_i} \left[(r \cdot r)\hat{I} - r \otimes r \right] dV \tag{20}$$

where $r = (x, y, z)$ is the radius vector to a point in the particle's body originating from the particle centroid, $\hat{I}$ is the identity tensor of rank three, and "·" and "⊗" denote dot and dyadic products, respectively.

The corresponding dimensionless inertia tensor is introduced as:

$$\bar{I}_i = \int_{\bar{V}_i} \left[(\bar{r} \cdot \bar{r})\hat{I} - \bar{r} \otimes \bar{r} \right] d\bar{V} \tag{21}$$

The relationship between Eqs. (20) and (21) can be established by:

$$I_i = \rho L_0^5 \bar{I}_i \tag{22}$$

3.2.2. Mass Damping

The damping force of particle *i* is defined as:

$$F_i^d = c_i \dot{X}_i \tag{23}$$

where $\dot{X}_i$ is the velocity of particle i, c_i is the damping constant proportional to the particle mass, m_i, and is defined as

$$c_i = \alpha_0 m_i \tag{24}$$

and α_0 is the coefficient of mass proportional Rayleigh damping. With regard to dimensions of α_0, it can be defined as follows:

$$\alpha_0 = \frac{4\xi}{T_0} \tag{25}$$

where ξ_0 is the damping ratio. See Appendix 2 for the derivation.

Using Eqs. (23) to (25), the damping force is obtained as follows:

$$F_i^d = \frac{4\xi}{T_0} m_i \dot{X}_i \tag{26}$$

The damping moment of the particle, M_i^d, for the rotational degrees of freedom can be defined in the same manner:

$$M_i^d = C_i \dot{\theta}_i \tag{27}$$

$$C_i = \alpha_0 I_i \tag{28}$$

where C_i is the rotational damping constant and $\dot{\theta}_i$ is the angular velocity of particle *i*.

Using Eqs. (25), (27) and (28), the damping moment is obtained as follows:

$$M_i^d = \frac{4\xi}{T_0} I_i \dot{\theta}_i \tag{29}$$

3.2.3. Dimensionless Strain Rate

Recalling Eq. (17), by using the chain rule one gets:

$$\frac{d}{dt} = \frac{1}{T_0} \times \frac{d}{d\tau} \tag{30}$$

ε indicates the strain tensor of the Representative Volume Element (RVE) and $\dot{\varepsilon}$ represents the constant strain rate tensor of the RVE where "$\cdot$" denotes the derivative with respect to time, t. Then, $\varepsilon' = \frac{d\varepsilon}{d\tau}$ is called the dimensionless strain rate, where " $'$ " denotes the derivative with respect to τ. Using Eq. (30) one gets:

$$\dot{\varepsilon} = \frac{\varepsilon'}{T_0} \tag{31}$$

3.2.4. Dimensionless Degrees of Freedom

Using the characteristic length, the dimensionless displacement is defined as:

$$\bar{X}_i = \frac{X_i}{L_0} \tag{32}$$

where X_i is displacement vector of particle i; and $\dot{X}_i$ and $\ddot{X}_i$ are its velocity and acceleration, respectively. According to Eq. (30), the dimensionless velocity and dimensionless acceleration of the particle are, respectively,

$$\bar{X}_i' = \frac{T_0}{L_0}\dot{X}_i \tag{33}$$

$$\bar{X}_i'' = \frac{{T_0}^2}{L_0}\ddot{X}_i \tag{34}$$

If the rotation vector of particle i is indicated by θ_i, the following relationships for the dimensionless vectors of velocity and acceleration of the particle, respectively, can be derived using Eq. (30):

$$\theta_i' = T_0\dot{\theta}_i \tag{35}$$

$$\theta_i'' = T_0^2\ddot{\theta}_i \tag{36}$$

3.2.5. Dimensionless Forces, Moments and Stresses

The out-of-balance force and moment of particle i are the sum of the contact forces and sum of the contact moments, respectively, applied by the adjacent contacting particles, i.e.

$$F_i^p = \sum_{j=1}^{n_i} F_{ij}^c \tag{37}$$

$$M_i^p = \sum_{j=1}^{n_i} M_{ij}^c \tag{38}$$

F_{ij}^c and M_{ij}^c are, respectively, the force and the moment applied by the contacting particle j on the particle i. Contact forces can be modeled by linear or nonlinear contact mechanics. In either case, the out-of-balance force and moment of the particle are related to their dimensionless counterparts in the following ways, respectively:

$$F_i^p = EL_0^2 \bar{F}_i^p \tag{39}$$

$$M_i^p = EL_0^3 \bar{M}_i^p \tag{40}$$

A variable marked with an overbar refers to the dimensionless equivalent of the corresponding non-barred variable. In Appendix 3, it is shown that dimensionless forces and moments are invariant with respect to ρ, E, and L_0.

Dimensionless stress is defined through the normalization of stress by the elastic modulus. For the *ij* component of the stress tensor, we can write:

$$\sigma_{ij} = \bar{\sigma}_{ij} E \tag{41}$$

In Appendix 4, it is shown that dimensionless stress is also invariant with respect to ρ, E, and L_0.

3.3. DEM Formulations

In a discrete element model, the equation of translational motion of particle *i* (i.e. the force equilibrium equation) is generally expressed in the following form:

$$m_i \ddot{X}_i + F_i^d = F_i^p \tag{42}$$

For an arbitrarily shaped (symmetric or asymmetric) particle *i*, the Euler's equation

below (i.e. the moment equilibrium equation) expresses the rotational motion in the local coordinate system centered on the particle's center of mass with its axes fixed to the particle and aligned with the particle's principal axes of inertia:

$$I_i\,\ddot{\theta}_i + \dot{\theta}_i \times \left(I_i\dot{\theta}_i\right) + M_i^d = M_i^p \tag{43}$$

"×" denotes the vector cross product.

3.3.1. Dimensionless DEM Formulations

By substituting Eqs. (19), (26), (33), (34) and (39) in Eq. (42), and recalling Eq. (16), the following dimensionless equation is obtained for the translational motion of the particle.

$$\bar{X}_i'' + 4\xi\bar{X}_i' = \frac{\bar{F}_i^p}{\bar{V}_i} \tag{44}$$

Similarly, by substituting Eqs. (22), (29), (35), (36) and (40) in Eq. (43) and recalling Eq.(16), the following dimensionless equation is derived for the rotational motion of the particle.

$$\bar{I}_i\theta_i'' + \theta_i' \times (\bar{I}_i\theta_i') + 4\xi\bar{I}_i\theta_i' = \bar{M}_i^p \tag{45}$$

Implementations of the periodic and rigid boundary conditions are explained in Appendix 5.

3.3.2. Dimensionless Discrete Element Modeling

In Appendix 6, it is demonstrated that:

> "Every DEM model with a constant dimensionless strain rate and a constant mass proportional damping ratio is independent of the density and elastic modulus of the particles and the size scale (characteristic length) of the problem when expressed in terms of the natural units."

The above statement is true if no dimensional artifacts are used in the numerical implementation. Also, the initial state, i.e. the geometry and forces at the beginning of a simulation have to be constant in the natural units. Thus, the initial dimensionless conditions require a constant dimensionless initial stress state.

In our choice of the natural system of units, i.e. the dimensionless units, all of the parameters are expressed in terms of an arbitrary characteristic length, L_0, and the corresponding characteristic time, $T_0 = L_0\sqrt{\frac{\rho}{E}}$, where ρ and E are the density and elastic modulus of the particles, respectively.

Since the dimensionless strain rate and the mass-proportional damping ratio are constant, the ordinary strain rate and the mass proportional damping coefficient are inversely proportionate to the characteristic time.

When expressed in the dimensionless forms, the output parameters are independent of the choice of the density and elastic modulus of the particles and the size scale at any specific dimensionless time, i.e. time normalized by T_0. For example, some of the major parameters are the displacement, velocity, acceleration, rotation, angular velocity and

angular acceleration of the particle and the stress tensor of the assembly.

Our discrete element modeling involves Hertz-Mindlin contact laws and the use of the mass-proportional global damping model. In order to simulate a granular model with this DEM, the following major parameters are required: the density and elastic modulus of the particles, ρ and E, respectively, the characteristic length, L_0 , the initial stress tensor, σ, the constant strain rate, $\dot{\varepsilon}$, the mass-proportional damping coefficient, α, and the inter-particle friction coefficient, μ. The critical time step of the model is used to calculate the dimensionless strain rate, ε', and the mass damping ratio, ξ, and all of the stress measures are normalized by E and denoted by $\bar{\sigma}$. With this method, the response of the model in the dimensionless scale is independent of ρ, E, and L_0. As a result, only four parameters ($\bar{\sigma}$, ε', ξ and μ) affect the response of the model independently in the dimensionless scale.

3.4. Numerical Validation of Dimensionless DEM and Evaluation of Scaling Methods

In this part, the aim is to demonstrate the applicability of the dimensionless DEM through some numerical simulations.

3.4.1. DEM Program and Implementation

ELLIPSE3D is a FORTRAN-based DEM code developed at the University of New Mexico by Lin and Ng (1997). It is used throughout the present study. The code was selected because it is capable of modeling ellipsoidal particles. Particles of this type have a simple geometry that can be defined with a fewer parameters. They are easier and less

costly to handle numerically without encountering singularity. They represent soil grains better than spherical particles due to the higher resistance to rolling (Wang et al., 1999).

In this program, Hertzian contact mechanics is used for the normal contact forces. This model is preferred as it needs no calibration. For tangential force calculation, the simplified Mindlin-Deresiewicz model is used. The model in question depends on the inter-particle friction coefficient. Although this parameter has a physical meaning, it should be calibrated such that the computational results match the experimental ones due to the difference between the smooth surface of the idealized particles and the rough surface of the real soil grains. However, it is not studied herein, and a constant value of 0.5 (equivalent to the friction angle of 26.6°) is considered. This seems a reasonable match for the behavior of actual soil grains. Important features of this program and some of the properties that all of the models used in this chapter share are listed in Table 2.

Three series of numerical tests were conducted. Some of the common properties and parameters of the series are presented in Table 3. Note that the consistent system of units used in the present study includes mg for mass, mN for force, mm for length and msec for time. Other units can be derived based on these ones. For instance, the stress unit is mN/mm^2, which is equivalent to kPa.

Table 2 Features of ELLIPSE3D and common properties of all models in Chapter 3

Computation Code	ELLIPSE3D
Particle Shape	Spheroid
Contact Laws	Simplified Hertz-Mindlin
Boundary Conditions	Periodic
Aspect Ratios of Sample (Cuboid)	1, 1, $4/3$*
Sample Preparation Method	Automatic Three-Phase Method
Initial Stress State of Samples	$\sigma_{11} = \sigma_{22} = \sigma_{33}$
Poisson's Ratio (ν)	0.3
Inter-Particle Friction Coefficient in Loading Stage (μ)	0.5
Time Step Ratio (c_t)	0.3
Aspect Ratio of Particles (R_1/R_2)	1.20

* Major loading direction

Table 3 Common properties and parameters shared within each series

Series Number, (Name)	1, (U1)	2, (U2)	3, (D)
Particle Size Distribution (PSD)	Mono	Binary ($R_{Large}/R_{Small} = 8$) (60% Large + 40% Small)	Mono
Number of Particles (n_p)	12288	12324	12288
Friction Coefficient in Sample Preparation Stage (μ_0), Sample Compaction	0.5 (Loose sample)	0.5 (Loose sample)	0.15 (Medium sample)
Loading Path	Undrained	Undrained	Drained
Final Strain (ε)	2%	3%	50%
Particle Major Radius (R_1)	varies	0.24, 0.03	0.24
Particle Minor Radii (R_2)	varies	0.2, 0.025	0.2
Characteristic Length ($L = 2R_2$)	varies	0.05	0.4
Initial Void Ratio (e_{ini})	0.7409	0.380	varies
Initial Dimensionless Mean Stress ($\bar{\sigma}_{m,ini}$)	2×10^{-5}	1.28×10^{-6}	varies
Dimensionless Strain Rate (ε')	-10^{-8}	-2×10^{-8} for Groups A, B, C and D -1×10^{-7} for Group A1, -2×10^{-7} for Group A2, -5×10^{-7} for Group A3, -2×10^{-6} for Group A4,	varies
Mass Damping Ratio (ξ)	1.0%	0.3% for Groups A, A1, A2, A3 and A4, 1.5% for Group B, 3.0% for Group C, 7.5% for Group D	0.3%

3.4.2. Series (1): An undrained test with two sets of different but equivalent parameters

Two samples, U1-0 and U1-1, were modeled under constant volume axisymmetric triaxial loading condition. The common properties of Models U1-0 and U1-1 are presented in Table 3. The other parameters of the models are listed in Table 4. The density and elastic modulus of U1-1 were 60,000 times and 1/150 times those of U1-0,

respectively. The particle sizes of U1-1 were 40 times those of U1-0. Therefore, the critical time step of U1-1 was 1.2×10^5 times that of U1-0. The two samples were initially generated from the same random seeds, i.e. identical normalized positions and orientations for the corresponding particles in the particle generation stage. The same procedure was employed to prepare both samples. However, the confining pressure of U1-1 was 150 times less than that of U1-0 resulting in the same dimensionless initial mean stress for the models. Although different strain rates and mass damping coefficients were applied to the two models in the loading stage, they had the same dimensionless strain rate and mass damping ratio.

According to Section 3.3, the two models were expected to exhibit the same mechanical behavior in the dimensionless measures. This is verified by Fig. 3 that shows the stress paths for the models in terms of the dimensionless mean and deviator stresses, p/E and q/E, respectively, where p and q denote the mean stress and the deviator stress, respectively. The deviator stress is defined by $= \sigma_1 - \sigma_3$, where σ_1 is the major principle stress which is in the direction of the applied axial strain, ε_a, and σ_3 is the minor principle stress, which is equal to the minimal stress measured in the lateral directions. Note that the applied strains in the lateral directions were equal to $-\varepsilon_a/2$ for the undrained (constant volume) tests. However, for the drained tests, the lateral strains were determined by a servo-control procedure to maintain the lateral stresses at the initial confining stress.

Both models indicated complete liquefaction and an identical dimensionless strength with $\phi = 7°$ which corresponded to $q_{peak} = 88$ kPa and $p = 390$ kPa for Model U1-0.

Table 4 Parameters of two models in Series (1)

Model Name	U1-0	U1-1
Particle Major Radius, R_1 (mm)	0.24	9.6
Particle Minor Radii, R_2 (mm)	0.2	8.0
Characteristic Length, $L = 2R_2$ (mm)	0.4	16.0
Density, ρ (mg/mm^3)	2.65	1.59×10^5
Elastic Modulus, E, (mN/mm^2)	7.8×10^7	5.2×10^5
Critical Time Step, Δt_c (msec)	7.373×10^{-5}	8.847
Initial Mean Stress, $\sigma_{m,ini}$ (mN/mm^2)	390	2.6
Strain Rate in Major Direction, $\dot{\varepsilon}$ (msec^{-1})	-1.356×10^{-4}	-1.130×10^{-9}
Mass Damping Coefficient, α (msec^{-1})	542.5	4.52×10^{-3}
Density Scale, $S_\rho = \rho/\rho_0$ †	1	6×10^4
Stiffness Scale, $S_E = E/E_0$ †	1	$1/150$
Size Scale, $S_L = L/L_0$ †	1	40
$\Delta t^c/\Delta t_0^c$ †	1	1.2×10^5
$\sigma_{m,ini}/\sigma_{m,ini,0}$ †	1	$1/150$
$\dot{\varepsilon}/\dot{\varepsilon}_0$ †	1	8.333×10^{-6}
α/α_0 †	1	8.333×10^{-6}

† Subscript 0 denotes the value associated with the model that ends in 0

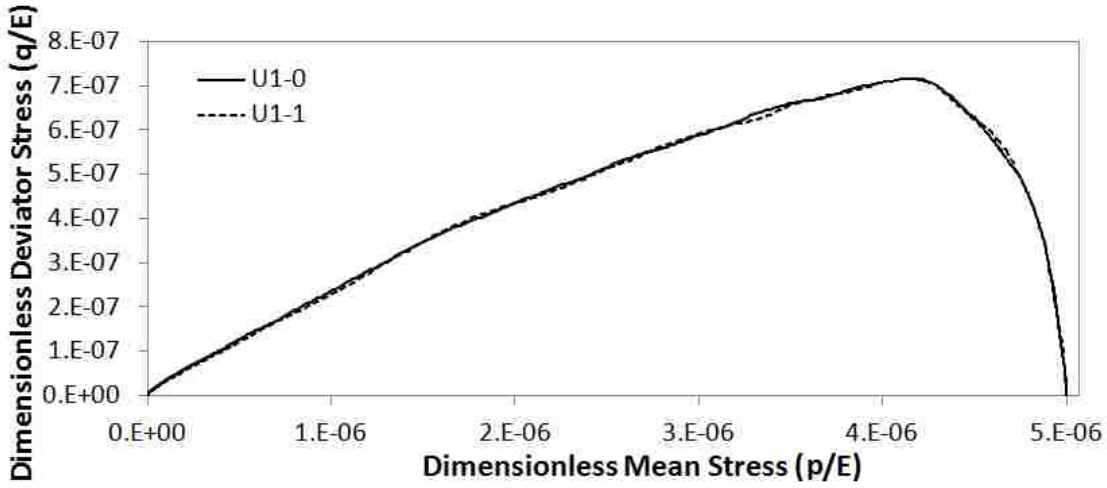

Fig. 3 Stress paths of the two models in Series (1) with different dimensional input parameters yet the same dimensionless values

Discussion for Series (1)

Series (1) demonstrated that any two models with different settings for the input parameters but the same initial dimensionless configuration (and, thereby, the same dimensionless initial stress state) yielded identical results in the dimensionless units as they were subjected to the same dimensionless strain rate with the same damping ratio regardless of the actual density, the elastic modulus and the characteristic length.

3.4.3. Series (2): Undrained tests to evaluate the damping ratio and the dimensionless strain rate

In Series (2), 36 models whose properties and input parameters are listed in Table 3 and Table 5 were used to evaluate the efficiency of the damping ratio and dimensionless strain rate. These models included the tests conducted on the six samples, U2-0, U2-1,…, U2-5.

To prepare the samples, U2-0 was created using an algorithm. We invented this algorithm (explained in Chapter 4) to create consistent samples automatically. Then, in order to derive the five remaining samples, the density of the baseline model, U2-0, was increased for U2-1, U2-2 and U2-3 while the contact stiffness was reduced for U2-4 and U2-5 by reducing the elastic modulus. However, for the two latter samples the initial confining pressure was reduced accordingly so that all of the six samples would initially have the same dimensionless mean stress. Then, the samples were allowed to reach equilibrium again.

All of the six samples had the same initial geometry (i.e. particle sizes, positions, orientations and overlaps), which were inherited from the baseline sample. Each model

consisted of one of the samples subjected to the undrained loading condition with specific damping and specific strain rate. According to Section 3.3, the models with the same damping ratios and the same dimensionless strain ratios were expected to have identical dimensionless measures (i.e. displacement, velocity, stress, etc.). Hence, two sets of tests were planned for the purpose of verification.

Table 5 Input parameters of the six samples in Series (2)

Model Name	U2-0	U2-1	U2-2	U2-3	U2-4	U2-5
Density, ρ (mg/mm^3)	2.65	2.65×10^2	2.65×10^4	2.65×10^6	2.65	2.65
Elastic Modulus, E, (mN/mm^2)	7.8×10^7	7.8×10^7	7.8×10^7	7.8×10^7	7.8×10^5	7.8×10^3
Critical Time Step, Δt_c (msec)	9.22×10^{-6}	9.22×10^{-5}	9.22×10^{-4}	9.22×10^{-3}	9.22×10^{-5}	9.22×10^{-4}
Initial Mean Stress, $\sigma_{m,ini}$ (mN/mm^2)	100	100	100	100	1	0.01
Density Scale, $S_\rho = \rho/\rho_0$ †	1	10^2	10^4	10^6	1	1
Stiffness Scale, $S_E = E/E_0$ †	1	1	1	1	10^{-2}	10^{-4}
$\Delta t^c/\Delta t_0^c$ †	1	10	10^2	10^3	10	10^2
$\sigma_{m,ini}/\sigma_{m,ini,0}$ †	1	1	1	1	10^{-2}	10^{-4}
$\dot{\varepsilon}/\dot{\varepsilon}_0$ †	1	10^{-1}	10^{-2}	10^{-3}	10^{-1}	10^{-2}
α/α_0 †	1	10^{-1}	10^{-2}	10^{-3}	10^{-1}	10^{-2}
α for groups A, A1, A2, A3 and A4 (msec^{-1})	1302	130.2	13.02	1.302	130.2	13.02
α for group B (msec^{-1})	6510	651	65.1	6.51	651	65.1
α for group C (msec^{-1})	13021	1302	130.2	13.02	1302	130.2
α for group D (msec^{-1})	32552	3255	325.5	32.55	3255	325.5
Strain Rate in Major Direction for groups A, B, C and D, $\dot{\varepsilon}$ (msec^{-1})	-2.17×10^{-3}	-2.17×10^{-4}	-2.17×10^{-5}	-2.17×10^{-6}	-2.17×10^{-4}	-2.17×10^{-5}
Strain Rate in Major Direction for group A1,$\dot{\varepsilon}$ (msec^{-1})	-1.09×10^{-2}	-1.09×10^{-3}	No Test	No Test	No Test	-1.09×10^{-4}
Strain Rate in Major Direction for group A2,$\dot{\varepsilon}$ (msec^{-1})	-2.17×10^{-2}	-2.17×10^{-3}	No Test	No Test	No Test	-2.17×10^{-4}
Strain Rate in Major Direction for group A3,$\dot{\varepsilon}$ (msec^{-1})	-5.43×10^{-2}	-5.43×10^{-3}	No Test	No Test	No Test	-5.43×10^{-4}
Strain Rate in Major Direction for group A4,$\dot{\varepsilon}$ (msec^{-1})	-2.17×10^{-1}	-2.17×10^{-2}	No Test	No Test	No Test	-2.17×10^{-3}

† Subscript 0 denotes the value associated with the model that ends in 0

In the first set, the dimensionless strain rate was kept constant at $\varepsilon' = -2 \times 10^{-8}$ for all of the models, while a specific damping ratio was assigned to each group. Groups A, B, C and D had damping ratios equal to 0.3%, 1.5%, 3.0% and 7.5%, respectively. Fig. 4 shows the stress paths of the models in terms of the stresses normalized by the elastic modulus.

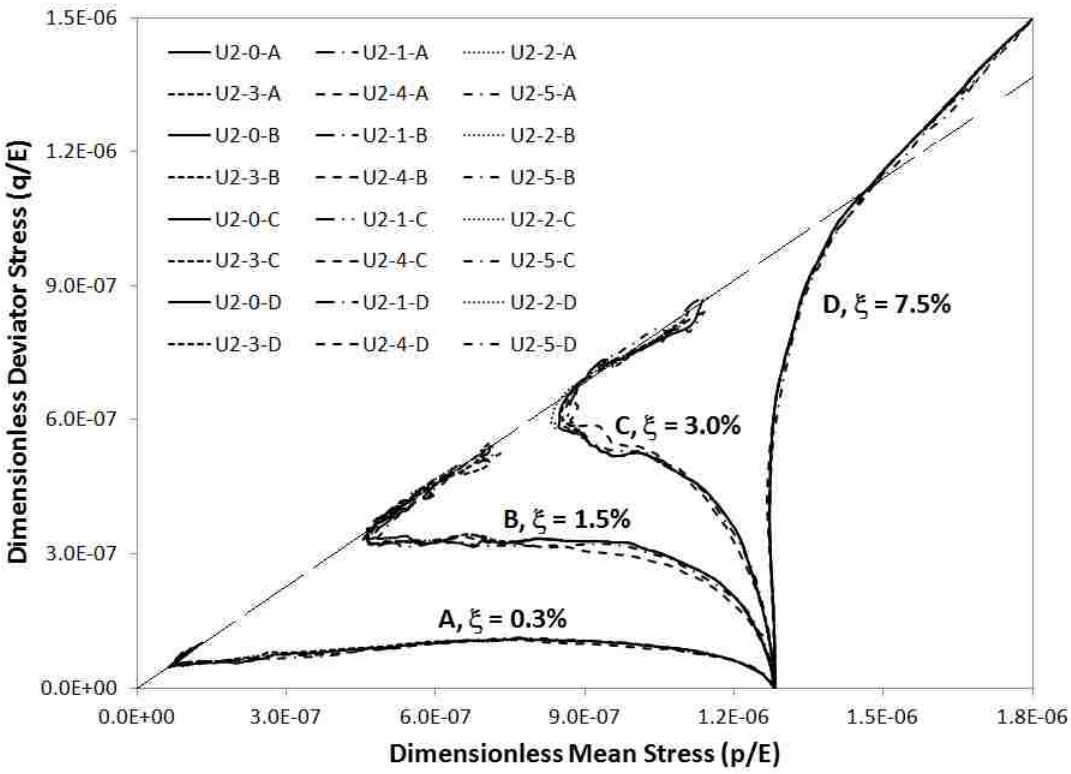

Fig. 4 Stress paths of models in Series (2) for different mass damping ratios at a constant dimensionless strain rate of $\varepsilon' = -2 \times 10^{-8}$

In the second set, the damping ratio was kept the same as that of Group A for all of the models (i.e. $\xi = 0.3\%$), and each group was sheared with a specific dimensionless strain rate in the constant volume conditions. The dimensionless strain rate of Groups A, A1, A2, A3 and A4 can be found in Table 3. The stress paths of the model in terms of dimensionless mean and deviator stresses are demonstrated in Fig. 5.

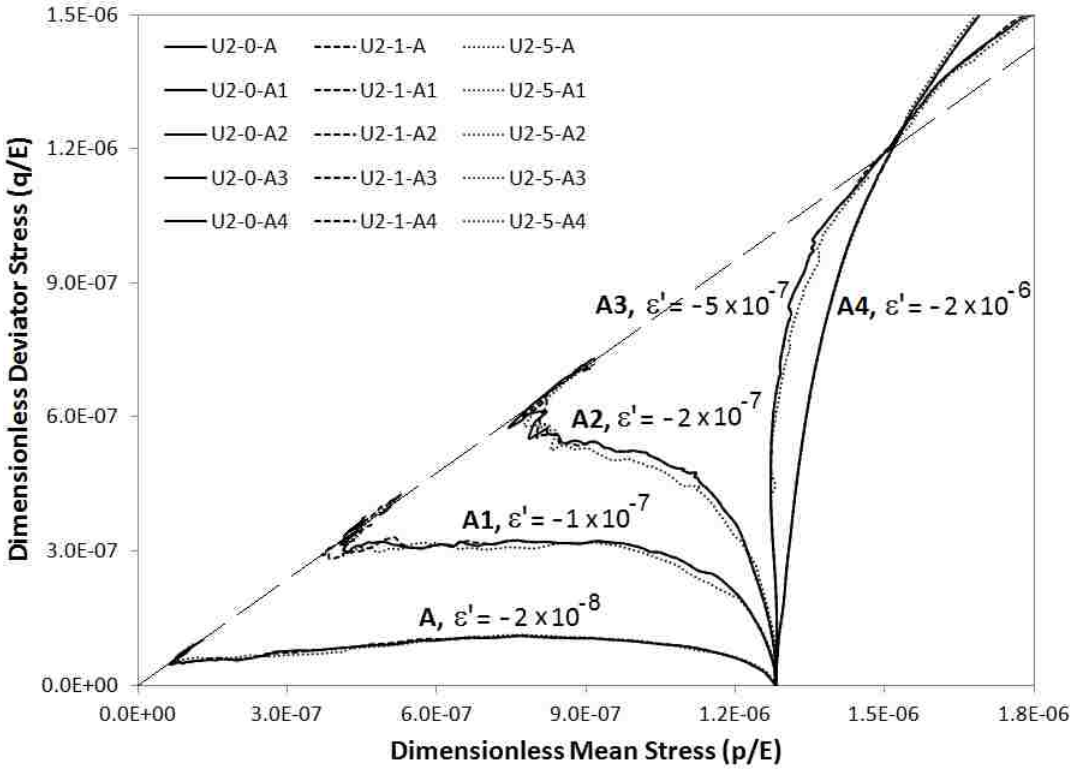

Fig. 5 Stress paths of models in Series (2) for different dimensionless strain rates with a constant mass damping ratio of $\xi = 0.3\%$

Discussion for Series (2)

In the first set of Series (2), the samples with different densities, ρ, and elastic moduli, E, and different mass damping ratios, ξ, i.e. Groups A, B, C and D, were tested at a constant dimensionless strain rate, ε'. The models in each group shared a specific damping ratio. According to Fig. 4, which shows the stress paths for each model in terms of dimensionless mean and deviator stresses, all of the models in each group, i.e. the models with the same ξ, exhibited identical behavior in the dimensionless scale. For instance, the response curves of the models of Group A lie on top of each other with good approximation. Similarly, models of the Groups B and C separately lie on top of each other in virtual terms.

This is not necessarily the case for the models with the same mass damping coefficient, α. For example, referring to Table 5, Models U2-1-C and U2-0-A have the same α, but they behave differently. Models U2-2-C and U2-5-C have the same α, and they show the same response because they have the same damping ratio.

It is also observable that when ξ is changed at a constant ε′, the mechanical behavior is influenced qualitatively and quantitatively. As ξ was increased, the shear strength, i.e. the peak q/E in Fig. 4, increased. The models with $\xi = 0.3\%$ indicated temporary liquefaction (referring to Verdugo and Ishihara ,1996, Yoshimine et al. ,1998, Alarcon-Guzman et al. ,1988, and Ishihara et al. ,1975). Moreover, the models with $\xi = 1.5\%$ and $\xi = 3.0\%$ showed a transformation phase only, while the models with $\xi = 7.5\%$ did not show instability which is not the expected behavior of the material as the sample was considered loose. All of the models ultimately formed a clear steady-state with a friction angle of about $\phi_{cv} = 20°$. The models with $0.3\% \leq \xi \leq 3.0\%$ demonstrated contractive behavior while the models with $\xi = 7.5\%$ showed dilative behavior without instability. Hence, the use of a high damping ratio is not recommended due to the artificial nature of this type of damping and the related influence on the mechanical behavior.

In the second set of Series (2), the samples with different ρs and Es and with a constant ξ, i.e. Groups A1, A2, A3 and A4, were subjected to various dimensionless strain rates. It was observed that for each group where the dimensionless strain-rate was constant the behavioral curves of the models in the dimensionless scale lay on top of each other. For example, according to Fig. 5, Models U2-0-A1, U2-1-A1 and U2-5-A1 exhibited identical behavior although they had different values for ρ and E. This was also

evident for the models in Groups A2, A3, and A4.

However, the models did not necessarily had identical responses when they were exposed to the same dimensional strain rate. For instance, three models, U2-0-A, U2-1-A2 and U2-5-A4 had equal dimensional strain rates. But, they did not go through the same stress path. Nevertheless, U2-1-A and U2-4-A, which shared equal dimensional strain rates, had identical stress paths. This was due to the fact that the two models had equal dimensionless strain rate as well.

Similar to the damping ratio, the dimensionless strain rate had a significant effect on the mechanical behavior. As this value was increased, the peak dimensionless shear strength increased (as observed in Fig. 5). The models in Groups A and A1 which had relatively low strain rates demonstrated temporary liquefaction. Group A2 was characterized by a transformation phase while Groups A3 and A4 showed no instability. A steady state was observed for all of the models with a $\phi_{cv} = 20°$. The stress paths of Groups A, A1 and A2 revealed contractive responses, whereas A3 and A4 had dilative responses.

Altogether, it was perceived from the analyses of Series (2) that the models with the same initial dimensionless conditions produced an identical dimensionless mechanical behavior when subjected to equal dimensionless strain rates and the same damping ratio. Thus, the actual values of ρ, E, α, and Δt_c had no effect on the dimensionless responses of the models.

By comparing Fig. 4 and Fig. 5, one can see that, where $\xi\varepsilon'$ was constant in the tested range for ξ and ε' in the present study, the behavior in the dimensionless scale was very similar qualitatively and quantitatively. Table 6 lists pairs of the groups that were

similar in this way despite their different values for ξ and ε' and for ρ and E. For instance, The responses of Groups A1 and B are very similar. This means that increasing ξ by a specific factor had the same effect as increasing ε' by the same factor. Furthermore, when the absolute value of $\xi\varepsilon'$ increased, a higher shear strength was observed. More research is required to arrive at the analytical reason behind this phenomenon if one exists. It should be emphasized that this is only based on a few observations for narrow ranges of ξ and ε'.

Table 6 Value of $\xi\varepsilon'$ for the models in Series (2)

Models	$\boldsymbol{\xi\varepsilon'}$
Groups A1 and B	-3×10^{-10}
Groups A2 and C	-6×10^{-10}
Groups A3 and D	-15×10^{-10}

Since ξ and ε' proved to have significant impacts on the outcome of the DEM simulations, the precise determination of suitable values for every specific application appears to be necessary to reproduce experimental test results.

3.5. Scaling Methods

Scaling methods are the techniques by which the allowable time increment of a dynamic system is artificially increased through the manipulation of the parameters involved in determination of the allowable time increment. The allowable (or critical) time step is a limiting factor for explicit finite difference solutions. DEM simulations can be performed in less runtime by relaxing this limiting measure. Recalling Eq. (92) in Appendix 1, the effective parameters are ρ, E, and R_{min}. According to the equation, Δt_c can be increased by upscaling ρ (which is known as density scaling or mass scaling), by

downscaling E (which is called stiffness scaling as the contact stiffness decreases), by upscaling the characteristic length of the problem (which is called size scaling as the particle sizes increase), or by engaging in a combination of these approaches.

3.5.1. Series (3): The application of the scaling methods in drained conditions

As indicated in Table 7, the models in this series were subjected to drained triaxial loading conditions of up to 50% strain in the vertical direction. Other parameters of these models can be found in Table 3. The baseline model was D-0 whose material properties were very similar to Ottawa sand #20/30. Model D-0 was created using $\mu_0 = 0.15$ in the early stage of sample preparation that ended with $e_0 = 0.6447$, which was considered a medium sample. The density was increased 160,000 times for D-1, while the elastic modulus was reduced 100 times for D-2. It should be mentioned that an excessive reduction of the elastic modulus, above the limits applied in this study, results in large particle overlaps. At such large overlaps, the assumptions of the Hertz contact model are not valid and, thus, cannot be applied. A damping ratio of 0.3% was applied to the models before shearing.

All of the models had the same initial geometry, which they inherited from the baseline model. The overall instructions regarding the creation of the scaled samples were that after the creation of Model D-0, the upscaled density in the case of Model D-1 and the downscaled elastic modulus in the case of Model D-2 were applied. Then, the samples were allowed to reach the equilibrium state again.

Table 7 Input Parameters of models in Series (3)

Model Name	D-0	D-1	D-2	D-1e	D-2e
Initial Void Ratio (e_{ini})	0.6447	0.6447	0.6449	0.6447	0.6461
Density, ρ (mg/mm^3)	2.65	4.24×10^5	2.65	2.65	2.65
Elastic Modulus, E, (mN/mm^2)	7.8×10^7	7.8×10^7	7.8×10^5	7.8×10^7	7.8×10^7
Critical Time Step, Δt_c (msec)	7.373×10^{-5}	2.949×10^{-2}	7.373×10^{-4}	7.373×10^{-5}	7.373×10^{-5}
Initial Mean Stress, $\sigma_{m,ini}$ (mN/mm^2)	390	390	390	390	39000
Initial Dimensionless Mean Stress, $\bar{\sigma}_{m,ini}$	2×10^{-5}	2×10^{-5}	2×10^{-3}	2×10^{-5}	2×10^{-3}
Strain Rate in Major Direction, $\dot{\varepsilon}$ (msec^{-1})	-1.356×10^{-3}	-1.356×10^{-3}	-1.356×10^{-3}	-5.425×10^{-1}	-1.356×10^{-2}
Dimensionless Strain Rate in Major Direction, ε'	-10^{-7}	-4×10^{-5}	-10^{-6}	-4×10^{-5}	-10^{-6}
Density Scale, $S_\rho = \rho/\rho_0$ †	1	1.6×10^5	1	1	1
Stiffness Scale, $S_E = E/E_0$ †	1	1	10^{-2}	1	1
$\Delta t^c/\Delta t_0^c$ †	1	400	10	1	1
$\sigma_{m,ini}/\sigma_{m,ini,0}$ †	1	1	1	1	10^2
$\dot{\varepsilon}/\dot{\varepsilon}_0$ †	1	1	1	400	10
Mass Damping Coefficient, α	1.628×10^3	4.069	1.628×10^2	1.628×10^3	1.628×10^3
α/α_0	1	2.5×10^{-3}	0.1	1	1

† Subscript 0 denotes the value associated with the model that ends in 0

However, in the process of making Model D-2, the confining pressure dropped to 3.9 kPa after one cycle that the contact forces were recalculated. It was due to the fact that the contact stiffnesses decreased by using the 100 times smaller elastic modulus. When the model underwent compaction again so that it could produce the same confining pressure as the baseline model, the void ratio decreased significantly to $e_0 = 0.539$. This model was not comparable to the baseline model as the lower void ratio would lead to different behavior. To overcome this issue, and enable Model D-2 to have the same void ratio as

D-0, several samples were created from scratch with different initial inter-particle friction coefficients. It was revealed that using $\mu_0 = 0.276$ resulted in a sample with $e_0 = 0.6449$ and an elastic modulus 100 times lower at the same confining pressure. The latter model was called D-2.

Due to the manipulation of the density and elastic modulus, D-1 and D-2 had greater critical time steps, which were 400 times and 10 times that of the baseline model, respectively. D-0, D-1, and D-2 were sheared in the major direction by the same strain rate, while the confining pressure was maintained at 390 kPa in the lateral directions by the employment of a servo-controlled mechanism.

The simulation runtimes that allowed D-1 and D-2 to complete loading up to the 50% strain level were 400 times and 10 times less than that of D-0, respectively. Fig. 6 shows the friction angle of the models evolved by the applied strain. Model D-1 exhibited a higher peak friction angle than the baseline model, while D-2 produced a peak friction angle marginally higher than Model D-0. However, all of the three models converged towards the critical state at large deformations. ϕ_{cs} of Model D-1 was higher than that of D-2 whereas ϕ_{cs} was the same for D-0 and D-2.

As shown in Fig. 7, D-0 and D-1 indicate dilative behaviors. However, the dilation is higher for D-1. Model D-2 exhibit completely different volumetric behavior. In the beginning, a contractive response is observed for D-2. This switches to dilation after a strain of about 3% is applied. The critical state formation (i.e. zero dilation or the horizontal segment of e vs. ε_a curve) for each model is also evident in Fig. 7.

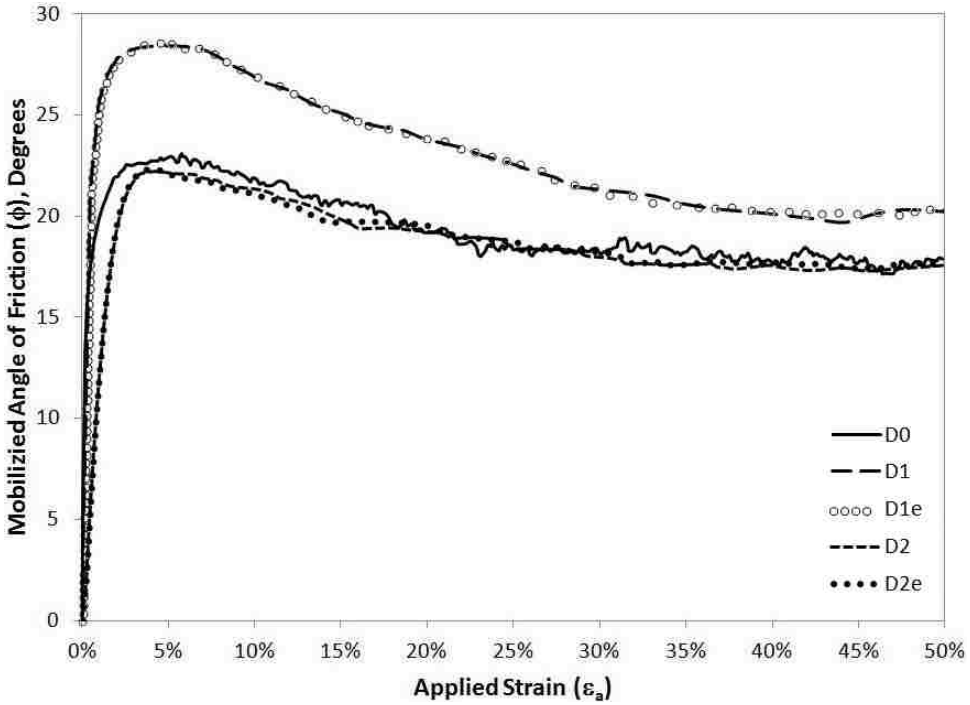

Fig. 6 Evolution of the friction angle with the applied strain for the models in Series (3)

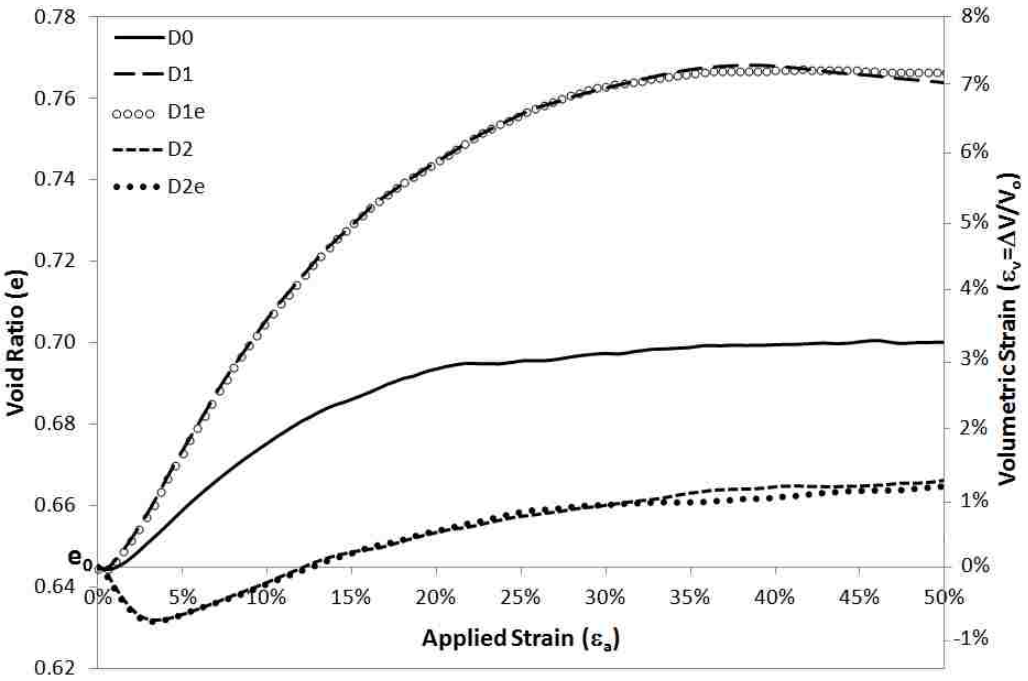

Fig. 7 Evolution of the volumetric strain with the applied strain for the models in Series (3)

Using the dimensionless scheme we aimed to determine the equivalent models of D-1 and D-2 with the same density and elastic modulus as those of Model D-0. The equivalent models were named D-1e and D-2e, respectively. Their input parameters, including strain rate, initial confining stress, etc. are shown in Table 7. It is evident that the strain rates for D-1e and D-2e were 400 times and 10 times that of D-0, respectively. Moreover, the confining pressure of D-1e remained the same as that of D-0, whereas the confining pressure of D-2e was 100 times higher than that of D-0.

In order to create the sample for D-1e, the density was reduced 1.6×10^5 times to match that of the baseline model and the sample was allowed to reach equilibrium. To create the sample for D-2e, the elastic modulus of D-2 was increased 100 times to match that of Model D-0. Then, the force and the moment vectors of all of the particles were increased 100 times and the sample was allowed to reach the equilibrium state at a confining stress 100 times higher than that of D-0, i.e. 39,000 kPa. In this case the void ratio varied marginally and got to $e_0 = 0.6461$. In Fig. 6 and Fig. 7, it is observed that D-1e and D-2e reproduced the response curves of Models D-1 and D-2, respectively.

Discussion for Series (3)

From the comparison of the behaviors of Models D-1 and D-1e, it is evident that the 1.6×10^5-fold increase in the density was equivalent to the $\sqrt{1.6 \times 10^5} = 400$-fold increase in the strain rate. Also, from the comparison of Models D-2 and D-2e, it is evident that the 100-fold reduction in the elastic modulus is equivalent to the $\sqrt{100} =$ 10-fold increase in the strain rate as well as the 100-fold increase in the confining

pressure. These results agree with the proposed dimensionless scheme.

The analyses of Series (3) showed that, without the modification of the strain rate, the scaling methods did not lead to the same mechanical behavior as the original parameters. Instead, they were equivalent to applying heightened strains rate and a higher confining stress in the case of stiffness scaling.

Regarding the sample in which the elastic modulus was reduced 100 times, it was observed that the stress measures decreased 100 times after the contact forces were recalculated. Stress in the regular scale is proportional to the dimensionless stress and elastic modulus in reference to Eq. (41). According to Appendix 4, the dimensionless stress is independent of the elastic modulus. When the dimensionless geometry remains unchanged, the dimensionless stress remains constant; thus the stress is only proportional to the elastic modulus. When the elastic modulus is reduced, the confining stress decreases by the same factor without compressing the sample to develop the original confining stress. Therefore, a sample with a reduced elastic modulus cannot have the same fabric as a sample for which the elastic modulus is not reduced even if they have the same confining stress and void ratio. As a result, stiffness scaling leads to a model with an increased strain rate and a different fabric. This model has substantially larger inter-particle overlaps at the contact points than the model with the original elastic modulus.

We need to determine which model is able to maintain the quasi-static conditions and is capable of reproducing similar behavior to that in the actual experimental tests.

Static loading is of great interest in the field of geotechnical engineering. DEM is not capable of simulating static loading conditions due to its dynamic modeling nature, which

is based on Newton's second law of motion. For a DEM model to approximate a response sufficiently close to static conditions, the deformation has to be applied very slowly using a small strain rate to prevent large dynamic effects from building up. This type of loading is called quasi-static loading. It is assumed that, in quasi-static conditions, the strain rate is so small that the velocities of particles are very small and the inertia-induced forces and moments are also very small compared to the inter-particle contact forces within the assembly. The inertial force is represented by the out-of-balance force of each particle, which is the resultant of the contact forces of the particle and is also in charge of moving the particles around within the assembly. By monitoring the equilibrium state of the particles, one can ensure that the unbalanced forces are relatively small and, thus, that the quasi-static conditions are fulfilled.

Various dimensionless indices have been defined in DEM to evaluate and monitor the equilibrium state of the granular assemblies. Ng (2006) proposed the Unbalanced Force Index as follows:

$$\mathrm{I_{uf}} = \sqrt{\frac{\sum_{p=1}^{n_p}\left(f_p^{res}\right)^2 / n_p}{\sum_{c=1}^{n_c}(f_c)^2 / n_c}} \tag{46}$$

where f_p^{res} is the resultant force (i.e. out-of-balance force) acting on particle p and f_c is the contact force for contact c, and there are n_p particles and n_c contacts in the system. Ng et al. (2014) defined a variation of $\mathrm{I_{uf}}$, called the unbalanced force ratio (UFR), as

$$\mathrm{UFR} = \frac{\sum_{p=1}^{n_p}\left|f_p^{res}\right| / n_p}{\sum_{c=1}^{n_c}|f_c| / n_c} \tag{47}$$

This index shows the relative magnitude of the average out-of-balance forces in

order for the quantification of the equilibrium state. A small UFR value, for example one less than 1%, indicates that the quasi-static conditions are fulfilled.

Table 8 presents the UFR values of the models averaged between 0% and 50% applied strain. Models D-0, D-2, and D-2e had the same UFR, which was equal to 0.1%, whereas D-1 and D-1e showed a relatively higher UFR of 15.2%. This indicated that the quasi-static conditions had been violated due to a higher dimensionless strain rate. Moreover, D-2 and D-2e both experienced a higher dimensionless strain rate than D-0. However, D-2 and D-2e yielded the same UFR as Model D-0. Whereas the numerator of the UFR fraction in Eq. (47) was large due to the higher dimensionless strain rate, the denominator was increased due to the higher dimensionless contact forces. These higher dimensionless forces, in turn, resulted from the higher extent of particle overlaps. The simultaneous increase in both the numerator and denominator of the UFR fraction yielded a relatively low value for the UFR, which, in this case, happened to be the same as the UFR of the baseline model.

Table 8 Unbalanced Force Ratio for the models in Series (3)

Model	UFR
D-0	0.1%
D-1	15.2%
D-1e	15.2%
D-2	0.1%
D-2e	0.1%

Since it appeared that the most significant difference between Models D-0 and D-2 lay in their volumetric behavior, it seemed reasonable to compare an overall measure associated with the volumetric response of each model with that from a similar experimental test to determine which of the models produced behavior that was closer to

the actual response of granular material. For this purpose, the bulk shear moduli of the assemblies were examined.

The tangent bulk shear modulus is defined as

$$G_{Bulk} = \frac{\Delta\tau}{\Delta\gamma} \tag{48}$$

where τ is the shear stress of the assembly that builds up at a shear strain of γ. The shear stress can be calculated by halving the difference between the major and minor principle stresses of the assembly, that is,

$$\tau = \frac{\sigma_1 - \sigma_3}{2} \tag{49}$$

The shear strain is

$$\gamma = \varepsilon_1 - \varepsilon_3 \tag{50}$$

where ε_1 and ε_3 are the overall strains of the assembly in the major and the minor directions, respectively.

Using Eq. (48), the tangent bulk shear moduli of Models D-0 and D-2 were calculated and presented against the applied axial strain ε_1 in Fig. 8. The fluctuations were filtered in Fig. 8 to smooth out the curves. The average grain diameter, D_{50}, the coefficient of uniformity, C_u, the sphericity parameter, S, and the roundness parameter, R, of the grains of in Models D-0 and D-2 are presented in Table 9. So are the maximum values of the bulk shear modulus obtained from Fig. 8.

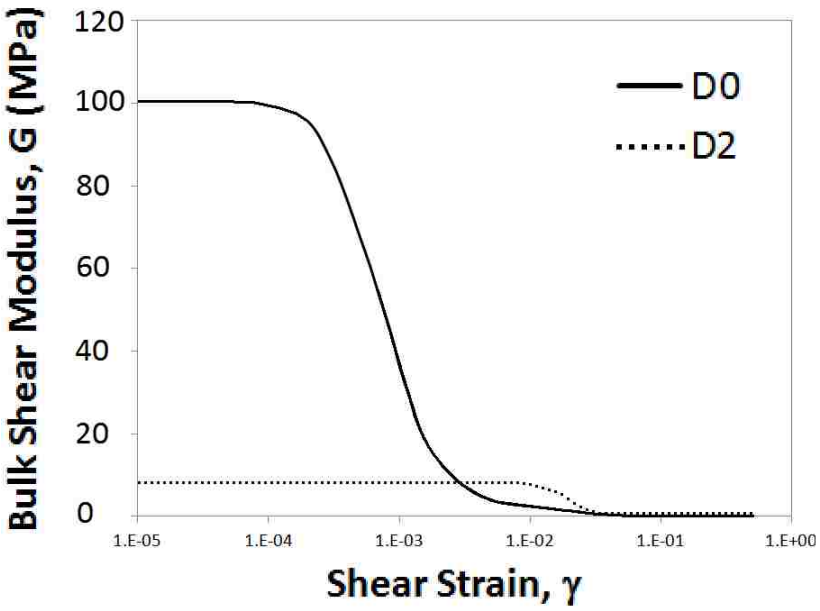

Fig. 8 Bulk shear modulus of Models D-0 and D-2 versus applied shear strain

Table 9 Maximum bulk shear modulus and specs of Models D-0 and D-2, and an actual test

Model	$(G_{Bulk})_{max}$ (MPa)	D_{50} (mm)	C_u	S	R	Initial Void Ratio, e_0	ρ (g/cm^3)
D-0	101	0.45	1	0.83	1	0.645	2.65
D-2	8.4	0.45	1	0.83	1	0.645	2.65
Actual Test	122	0.60	1.2	0.9	0.9	0.645	2.65

In Table 9, the bulk shear modulus and the specifications of an actual test specimen extracted from Cho et al. (2006) are also presented. The material specs of the actual test specimen correspond to ASTM C-778, standard Ottawa sand #20/30, which is very similar in material properties to Models D-0 and D-2. According to Cho et al. (2006), the shear wave velocity for the Ottawa sand #20/30 can be calculated as follows:

$$V_s = 72.7 \left(\frac{\sigma_m}{\text{kPa}}\right)^{0.223} \tag{51}$$

where σ_m is the initial mean stress of the sample. As $\sigma_m = 390$ kPa for D-0 and D-2, the

expected shear wave velocity from Eq. (52) was $V_s = 275\ \mathrm{m/s}$. The bulk shear modulus can be obtained from the following:

$$G_{Bulk} = \rho_{Bulk} V_s^2 \tag{52}$$

where ρ_{Bulk} is the bulk density of the sample.

$$\rho_{Bulk} = \frac{\rho}{1 + e_0} \tag{53}$$

ρ and e_0 are the particle density and the initial void ratio of the samples, respectively. As $\rho = 2.65\ \mathrm{g/mm^3}$ and $e_0 = 0.645$, we got $\rho_{Bulk} = 1611\ \mathrm{kg/m^3}$. Then, from Eqs (52) and (53), the bulk shear modulus for the actual sample, which had the specs of the Ottawa sand #20/30 listed in Table 9 with a void ratio of $e_0 = 0.645$ and a grain density of $\rho = 2.65\ \mathrm{g/mm^3}$, was expected to be $(G_{Bulk})_{max} = 122\ \mathrm{MPa}$. This result matched Model D-0 closely, indicating that the unscaled model represented a stiffness close to that of the actual test. However, the bulk shear modulus of Model D-2 was far below this value, suggesting that stiffness scaling produces models with substantially softer behavior than actual experiments.

It was observed that manipulations of the input parameters (i.e. the density and elastic modulus of the particles) resulted in a change in the mechanical behavior unless the dimensionless equivalents of the parameters were kept constant. When the dimensionless input parameters were kept constant, the number of computation cycles was the same and the analysis runtime did not vary. Therefore, there is no point in applying the scaling methods.

As O'Sullivan (2011) has correctly pointed out, to reduce the runtime of simulations, instead of utilizing scaling methods which are questionable, *"it seems preferable to maximize the rate of deformation in the simulations while ensuring that the simulations remain quasi-static by carefully monitoring the applied and internal stresses in the specimen."*

3.6. Summary

In this chapter, a set of dimensionless parameters and formulations was introduced for DEM analyses where the mass damping ratio and the dimensionless strain rate are inversely proportional to the critical time increment of the granular assembly and the dimensionless stress is the stress normalized by the elastic modulus. The dimensionless formulation was derived for a single particle and validated through drained and undrained numerical tests.

Using the proposed formulation, the number of independently influencing parameters is reduced if the model is represented in this system. Using these parameters, the responses of the models in the dimensionless scale are independent of the particles' density, stiffness (via the elastic modulus), and the length scale for the particle sizes. That is, any two models which have the same dimensionless strain rate and initial geometry (and, therefore, the same initial dimensionless stress state) with the same mass damping ratio, as defined herein, exhibit identical behavior in terms of dimensionless measures (such as the mobilized friction angle of the assembly and stresses normalized by the elastic modulus) even though they may have different parameters in regular scales. The analytical derivations were verified using the numerical models.

It was demonstrated that a model with a specific damping ratio and a specific dimensionless strain rate shows unique mechanical behavior independent of the selected density and elastic modulus value for the particles in a DEM model.

It was shown that the damping ratio is a better basis than the mass damping coefficient for selecting a proper value for artificial mass damping that is used in DEM analyses. This parameter affects the mechanical behavior of the models. Thus, it should be selected carefully and excessive amounts should be avoided to prevent incorrect responses. Hence, the determination of the optimum value for the damping ratio is necessary.

It was demonstrated that the dimensionless strain rate correlates with the mechanical behavior of the models better than the regular strain rate when density, elastic modulus, and particle sizes are selected arbitrarily. Likewise, dimensionless stress is better than regular stress for the purpose of comparison when different elastic modului are used. An excessively high dimensionless strain rate may affect the mechanical response adversely such that a loose sample may behave like a dense sample and exhibit the unstable type of behavior that is due to the erroneous violation of the quasi-static conditions. Therefore, it is necessary to determine a suitable dimensionless value of strain rate for preserving the quasi-static conditions.

In addition, in test Series (2), it was observed that, when the product of the damping ratio and the dimensionless strain rate is constant for a specific model (but with various parameters and different mass damping ratios and dimensionless strain rates), the mechanical behavior turns out to be very similar in qualitative and quantitative terms. However, this observation is limited to the studied range of the parameters, and the

analytical reason behind it should be explored before it is put into practice.

If the density is increased as practiced in the density scaling approach, the resulting model will be equivalent to a model with the original density and an increased strain rate. As a result the UFR will be higher. This means that the unbalanced forces of the particles will be higher relative to the overall stress of the assembly, which may violate the quasi-static conditions. If the strain rate is reduced to get the same UFR as that of the model with the original density, no speed-up will be gained.

When stiffness of the contact is reduced by reducing the elastic modulus of the particles as practiced in the stiffness scaling approach, the resulting model will be equivalent to a model with the original elastic modulus with a higher strain rate and confining pressure than those of the model with the original elastic modulus. The increase in the confining stress is due to the increase in the contact forces, which, in turn, results from the increase in the contact overlaps. If the contact overlaps increase excessively, the calculated contact forces through the Hertz model are not valid as it assumes small deformations. Moreover, the particles are expected to break under excessively high contact forces, thus, the crushing mechanism should be modeled as well.

On the other hand, the unbalanced forces increase due to the increase in the strain rate. Hence, the UFR remains the same or even reduces depending upon the amount of the reduction of the elastic modulus and whether the quasi-static conditions are maintained. However, the fabric is different from that of the original model. Therefore, a different behavior from that in an experimental test with similar specifications is observed. Furthermore, the bulk shear modulus of the assembly is significantly lower than that of experimental results, whereas that of the model with the original elastic

modulus approximately matches experimental results. This means that the model with reduced stiffness shows an incorrectly softer mechanical response than the experiment despite speeding up of the simulation.

Consequently, the use of neither of the scaling techniques is recommended. However, if a density or an elastic modulus different from the properties of the actual grains is used, the dimensionless strain rate and dimensionless stress should be kept the same as those of the unscaled model.

The runtime is proportional to the number of time-steps in a DEM analysis. Furthermore, the number of time-steps is directly proportional to the final strain and inversely proportional to the time-step fraction and the dimensionless strain rate. Therefore, if these three parameters are kept constant, it is not possible to reduce the runtime by manipulating the input parameters.

The only legitimate ways to reduce the runtime for a quasi-static DEM analysis are by improving the numerical algorithms, employing parallel processing, using faster computers, and increasing the dimensionless strain rate as long as the quasi-static conditions are maintained. Therefore, the limiting dimensionless strain rate value above which compliance with the quasi-static conditions fails should be determined.

CHAPTER 4

Sample Preparation and Friction Coefficient

4.1. Overview

An automatic algorithm is introduced for the systematic sample preparation in discrete element modeling. This algorithm is aimed at preparing samples with arbitrary particle-size distributions of ellipsoids with desired confining pressures and void ratios by adjusting the inter-particle friction coefficient in the sample preparation stage. The performance of the proposed algorithm was examined, and the effect of the friction coefficient on making samples with mono-sized particles and with different void ratios was assessed.

4.2. Necessary Considerations for Sample Preparation

Since the invention of the discrete elements method (DEM), preparing necessary samples has been a challenging task and is at least as costly as main simulations. Among those models, preparing simulated samples of granular soils has been more challenging, particularly in soil samples comprising particles with different shapes and sizes. The particles are situated in certain arrangements within the body of soil specimens. Furthermore, every soil sample undergoes a certain in situ pressure naturally and has a specific void ratio.

Many attempts have been made to prepare more realistic samples. However, a sample with properties close to a real specimen is not necessarily a practical sample. For example, nowadays some methods can scan the 3D shapes of the particles. Due to the

unique shape of every particle and the presence of numerous particles in each sample, it is not feasible to extract the geometric information of every single grain. Furthermore, if one managed to prepare such information for a finite soil sample, it would take too much time to run a numerical simulation using the existing computational hardware and thus is not practical.

In addition, if one gets particles out of their original positions to scan their shapes, the original fabric will be destroyed, and the behavior of the reconstituted sample may be different from that of the original one because it is almost impossible to restore the initial fabric once it is disturbed. It should also be mentioned that there is no rigorous solution for the contact mechanics of irregularly shaped particles.

Considering the above-mentioned problems, most researchers prefer to stay away from the actual particle shapes and stick with simplified models such as spheres, ellipsoids, super-ellipsoids, tetrahedrons, polyhedrons, and so on. Among these shapes, the sphere, due to its simplicity, has been the most widely used. However, it is obvious that spheres cannot represent soil particles due to their oversimplification in general (e.g., particle shape) and low resistance against rotation in particular.

Ellipsoids are an alternative shape to simulate less angular soil particles (e.g., Ottawa sand). One of the advantages of the ellipsoid shape is that it does not have any singular point, and thus contact mechanics can be applied to it with higher confidence. This type of element has been implemented in some DEM codes, such as ELLIPSE3D, which is developed at the University of New Mexico (Lin & Ng, 1995) and was used in the present study. It is important to choose a suitable aspect ratio for the particles in order to resemble the actual particles as much as possible. To reduce the number of input

parameters, a spheroidal particle shape is used, which is an ellipsoid with two equal semi-diameters in minor directions. The aspect ratio of particles is defined as the ratio of the major diameter to the minor diameters of the particle.

Some problems such as segregation and presence of the idle particles (sometime called rattlers or floaters) may be encountered as well. Particle size distribution (PSD) of the samples has a key role in selecting a sample preparation method. Based on PSD, granular materials can be categorized into well-graded and poorly graded types. In preparing a gap-graded sample, segregation and presence of floaters are the major problems. If gravity is not applied for such samples, smaller particles float within the voids between the larger ones without making any load-bearing contacts. If gravity is applied, segregation occurs where small particles migrate toward the bottom of the sample. Hence, the preparation of gap-graded samples requires specific considerations.

Among the major sample preparation methods mentioned in Chapter 2, ballistic deposition, gravitational, and uniaxial compaction methods are not capable of making dense samples. Gravitational methods cannot be implemented with a periodic boundary condition. The Lily-pond model only makes samples with an identical size. Tessellation methods cannot make samples with a specific grain size distribution, and they cannot make loose samples. According to Bagi (2005), this method makes loose packing in the vicinity of boundaries that end up with non-homogeneous samples. Furthermore, the radius expansion method was meant for making dense packing of spheres in its original form.

As mentioned in Chapter 2, isotropic compaction methods are widely used for sample preparation. They create the particles in a container larger than the final sample

size, and then the sample is compressed in all directions to achieve the desired pressure. In these methods, segregation does not occur due to lack of gravity. Isotropic compaction methods are performed through various approaches with different stages. However, these methods are relatively slow. Also, due to the application of the force-controlled routines that densify the initial cloud of randomly generated particles, the final samples may be distorted from the initial desired aspect ratio of sample dimensions.

Another input parameter is the number of the particles in a sample. Plassiard et al. (2009) created four samples of identical size but with different numbers of particles (i.e., 10,000, 20,000, 50,000, and 90,000 particles). They demonstrated that the obtained mechanical response is independent of the mean size of the particles and of the characteristic size of the samples. Therefore, using about 10,000 particles in the samples still seems reasonable to avoid size effects on the behavior of the numerical media.

Regarding every application, samples may be created under various boundary conditions, such as rigid, membrane, axisymmetric, periodic, and hybrid. For rigid boundaries, the enclosing planes are assumed to be rigid, and the membrane can be applied using different techniques, such as shell elements, or by simulating hydrostatic pressure (Lin & Ng, 1995). The periodic cell method, which is used in this study, removes the boundary effect and allows users to create smaller samples that require less simulation runtime (Cundall, 1988; Thornton, 2000; Ng, 2004). It should be mentioned that the three-phase method, proposed in the next section, can be implemented using rigid or membrane boundaries as well.

It is noteworthy to mention that binary-mixture samples with distinct differences between two particles sizes require more particles to capture the true mechanical

response. Also, the strain field is not uniform in this type of materials; hence, the periodic boundaries are not applicable. However, the study of binary mixtures is out of scope of this research.

4.3. Three-Phase Method

A three-phase method is explained to overcome the above-mentioned drawbacks, based on the same concept as isotropic compaction. The samples required throughout the present study are made by the automatic algorithm that saves a lot of time for DEM users and reduces human error.

First, particles are created in a space larger than the final sample with no contacts, in the so-called particle generation phase. Then, to achieve the final sample, the created particle cloud undergoes two more phases – namely, the shrinkage phase and the compression phase, respectively.

4.3.1. Particle Generation Phase

In this phase, based on the desired particle size distribution, the particles are created in a sufficiently large rectangular cuboid-shaped container that can accommodate all particles without developing any overlap or contact to each other. The position and orientation of the particles are generated by a random function called random seeds. Note that in order to minimize the initial size of the container, and thereby minimize the computational cost, it is preferred to first create large particles and then create smaller particles within the voids. It should be mentioned that the container sizes have to be proportional to the desired sizes of the final sample so that by applying equal strain

measures in all directions, one may achieve the final size of the sample.

In this phase, the desired void ratio range is applied by selecting an appropriate internal friction angle between the particles, μ. The higher the friction angle, the harder their movement with respect to each other, and the higher the void ratio as a result. In this study, the friction coefficient ranges from 0 to 0.50. The upper limit was selected for two reasons: according to Huang et al. (2014), using a friction coefficient higher than 0.5 results in a non-physical response. On the other hand, the inter-particle friction coefficient in the final granular assembly will be set to $\mu = 0.5$. Using a friction coefficient for the final sample higher than the value that will be used during the shearing tests is not suitable, since it produces strong tangential contacts that are broken after lowering the friction coefficient (Barreto et al., 2008).

4.3.2. Shrinkage Phase

The shrinkage phase is a displacement-controlled phase. In this phase, the same strain increments are applied to all three dimensions of the sample at each time step at inward directions. As the container shrinks, particles start to contact each other, and these contacts develop a pressure within the sample. However, by numerical cycling the sample in the absence of dimension change, the developed pressure diminishes which is due to breaking the meta-stable contacts by rearranging the particles. This operation, which is employed to stabilize the sample, is called “balancing”.

The remaining pressure is a criterion to determine when the sample is ready to be transferred to the next stage – that is, as soon as the pressure in any direction exceeds the user-defined target confining pressure, the strain rate is declined. In the next step, the

strain rate is halved, and so on. Thornton and Antony (2000) mentioned a similar approach in gradual reduction of the strain rate as the sample moves closer to the target stress level, yet through a stress-controlled simulation.

Since the state of the sample is evaluated only at the end of any fixed number of cycling intervals, it is important to keep the last good configuration of the sample so that if the confining pressure may exceed the target pressure in any of the three directions, the previous state can be restored. The excessive pressure can be released by moving the boundary in the outward direction. However, this makes the sample overconsolidated by leaving irreversible tangential contact forces. Therefore, the unwanted overconsolidation can be avoided by preserving the previous state of the sample.

Our strain-controlled procedure helps to increase the sample preparation speed, since when the voids are larger, a higher strain rate is applied, and when the voids decrease, the strain rate is lowered. This reduction of the strain rate continues until a minimum strain rate limit is met. From this point forward, the strain rate remains constant. The application of the displacement-controlled shrinkage in this phase significantly reduces the computational cost by speeding up the simulation process.

4.3.3. Compression Phase

In the beginning of this phase, the friction angle is set to its final value, $\mu = 0.5$. In contrast to the shrinkage phase, in this phase, change in the container size is applied by a force-controlled procedure through a servo-mechanism.

This phase aims to achieve a specific predetermined confining pressure equally in all three directions. Also, it is desired that the particles stop vibrating and equilibrium state is

achieved for the sample. In the other words, the dynamic forces must be considerably less than static forces. For this purpose, we use the Unbalanced Force Ratio defined by Ng (2006), as follows:

$$\text{URF} = \frac{\sum_1^{n_b}(out\ of\ balance\ forces)^2 \div n_b}{\sum_1^{n_c}(contact\ forces)^2 \div n_c} \tag{54}$$

where n_b and n_c are the number of particles and number of contacts, respectively.

When this index is less than 0.1%, we assume that the sample is in static equilibrium. Unlike the shrinkage phase, the exerted compression rate is calculated using a force-controlled mechanism in this phase through a servo-control technique. In force-controlled mechanisms, the displacement applied on the boundaries is updated in every time step using feedback received from the previous step so the stress can approach the desired value.

Similar to what was explained in the shrinkage phase, cycling the sample in the absence of a dimension change, i.e. balancing, allows the sample to get closer to a static equilibrium state by dissipating the excessive kinetic energy. Compressing the sample to a predefined confining stress by a servo-controlled algorithm and performing a balancing stage alternatively until the associated desired criteria are met leads the sample to its final ready-to-use state.

One may avoid applying the shrinkage phase and apply only the compression phase right after the particle generation phase. However, this is not recommended for two reasons: First, the compression procedure is slower than shrinkage due to the trial-and-error nature associated with the servo-control. When there are a lot of voids in the sample in the initial configuration and there are few contacts between particles, the stress is much

lower than the goal pressure, thus, there is no need for a force/stress-controlled algorithm that takes longer.

Second, the sole compression may undesirably and significantly change the initial aspect ratios of the sample container box, whereas the shrinkage may not. Before enough contacts have developed in the sample and a load-bearing structure is created, application of a stress-controlled algorithm significantly distorts the shape of samples, particularly if a low inter-particle friction coefficient is applied. However, after sufficient contacts are developed, the compression phase has insignificant influence on the final sizes of the sample.

4.3.4. Sample Preparation Algorithms

Even though the concept of the aforementioned procedure is simple, it involves a lot of detail and takes a long time to perform manually, especially if the number of particles is high. This makes sample preparation cumbersome that may introduce human error, especially when many consistent samples need to be created. Therefore, a standardized approach is necessary to prepare samples that can work automatically. This approach guarantees the repeatable creation of identical samples by using the same input and control parameters and by following the same procedure.

Fig. 9 and Fig. 10 show the flowcharts used for the shrinkage phase and the compression phase. The flowcharts illustrate the detailed steps, conditions, connections between every two steps, and default values used in the present study. These charts are implemented in ELLIPSE3D and may ease the programming task for the mentioned sample preparation methods in other DEM programs. Note that the time-step ratio was set

to $C_t = \frac{\Delta t}{\Delta t_c} = 0.1$ in all sample preparation phases.

4.3.5. Material Properties

The following properties were used for sample preparation:

Density $\rho = 2650\ \text{kg/m}^3 = 2.65\ \text{mg/mm}^3$

Shear Modulus $G = 30\ \text{GPa} = 3 \times 10^7\ \text{mN/mm}^2$

Poisson's Ratio $\nu = 0.30$

Final inter-particle friction coefficient $\mu = 0.50$

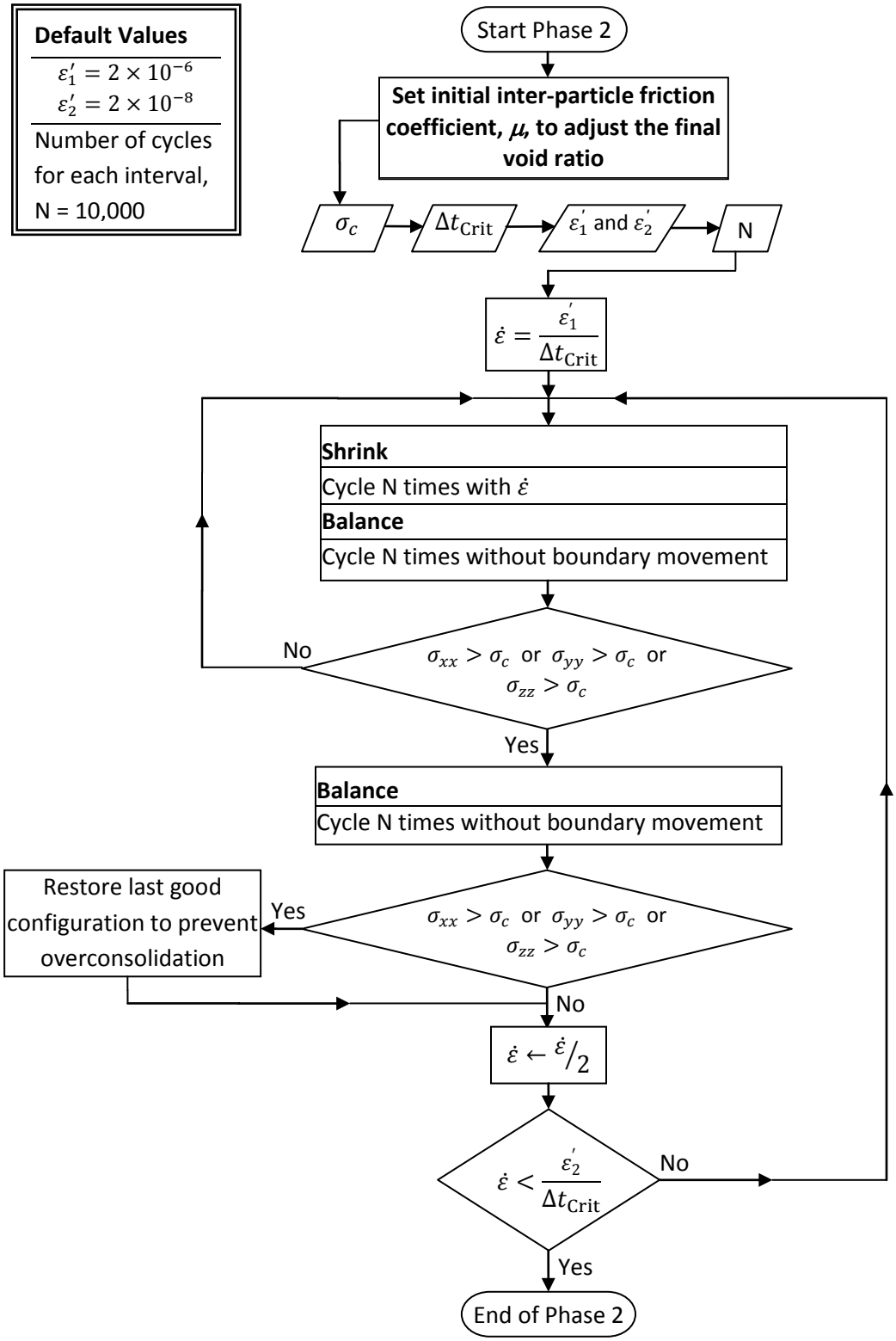

Fig. 9 Flowchart of Shrinkage Phase

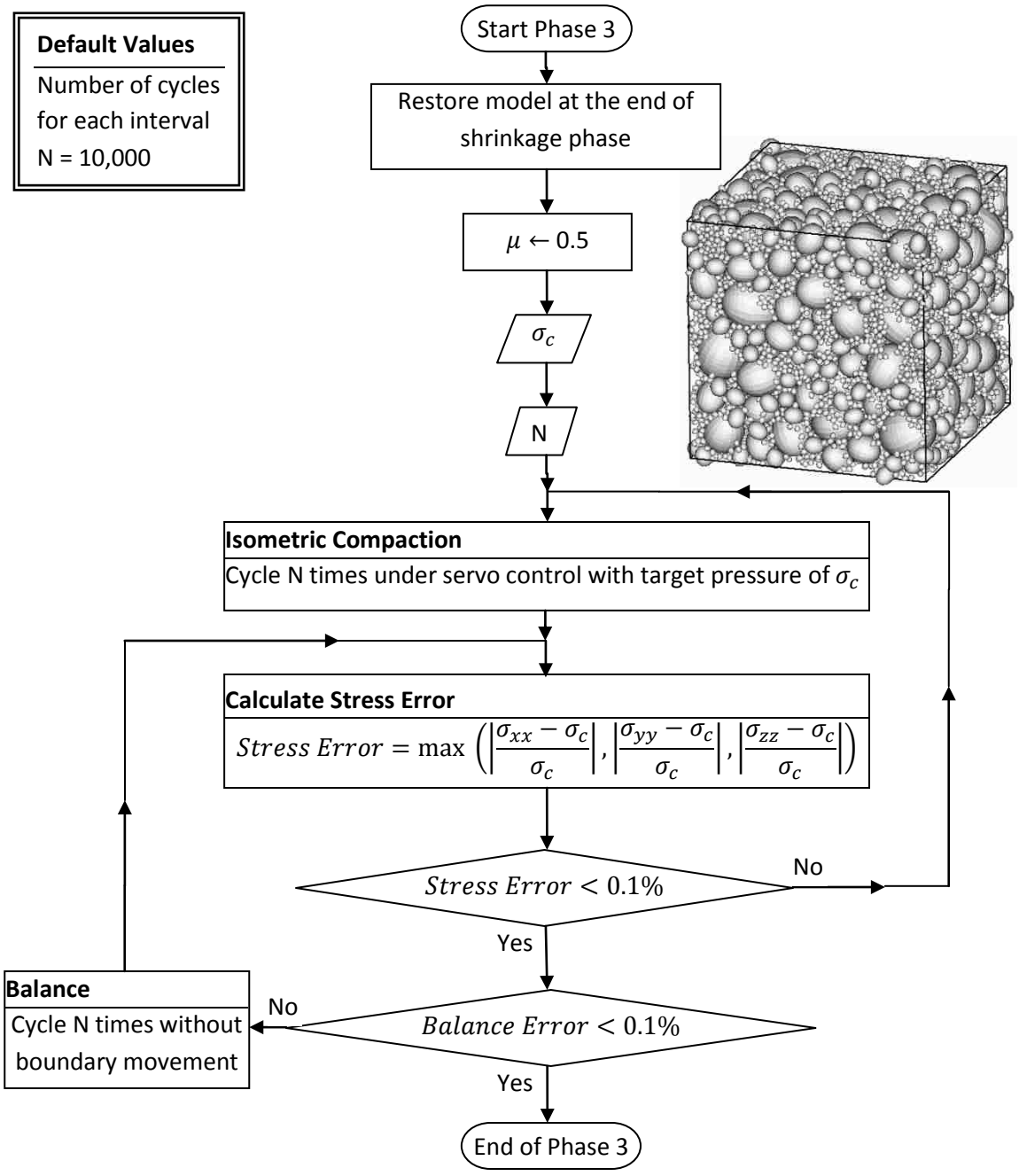

Fig. 10 Flowchart of Compression Phase

4.4. Sample Preparation Program

The particles were of prolate ellipsoidal (spheroid) shape. The aspect ratio of particles was selected to be 1.2. In order to have a smooth behavioral curve (e.g., stress-strain) in the output, the total number of particles was selected to be 10,000 particles. The initial box sizes were minimized by trial and error so the box could enclose all particles. The reason to choose the smallest initial box size is that it takes less time to create the sample in this way since the size is closer to the final size and thus requires less numerical cycles.

Using the proposed algorithm, 112 mono-dispersed samples with the major size of particles (major semi-diameter) equal to 0.48 mm were created to study the effect of using different inter-particle friction coefficients in the shrinkage phase on the properties of the final samples. Four different confining pressures – 39, 390, 3900 and 39,000 kPa – were applied. The samples were created using 28 different friction coefficients ranging from 0 to 0.5, as presented in Table 49 of Appendix 7.

4.5. Results of Sample Preparation

The void ratios of the prepared samples are shown in Table 49 of Appendix 7. The variation of the void ratio with the friction coefficient that was used in the shrinkage phase is shown in Fig. 11 for the four different confining pressures. There is a clear correlation between the void ratio and the friction coefficient in the shrinkage phase, μ_1, at each confining pressure. As the friction coefficient increases, the void ratio increases. Below $\mu_1 = 0.03$ and above $\mu_1 = 0.47$, there is no significant change in the void ratio. This means that $\mu_1 = 0.03$ produces the densest sample and $\mu_1 = 0.47$ creates the loosest

sample. A friction coefficient lower than $\mu_1 = 0.03$ does not lead to a denser sample, but this small value speeds up the shrinkage phase by playing a stabilizing role on the tangential contacts.

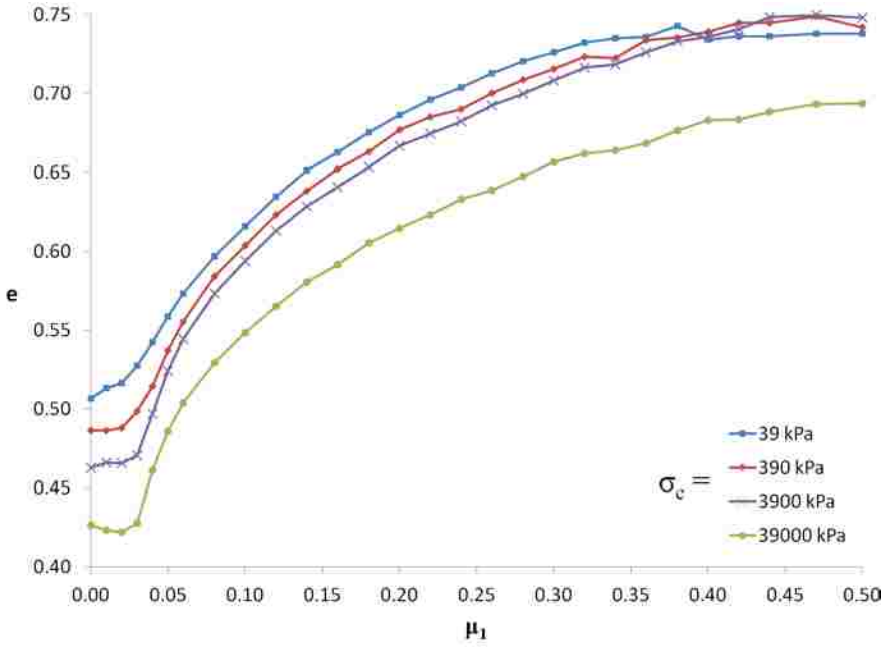

Fig. 11 Variation of void ratio with the friction coefficient at four different confining pressures

In addition, it is evident that by increasing the confining pressure, a denser sample is obtained. This is also evident in Fig. 12; this figure indicates that the effect of confining pressure on the void ratio is more noticeable at higher friction coefficients that produce looser samples.

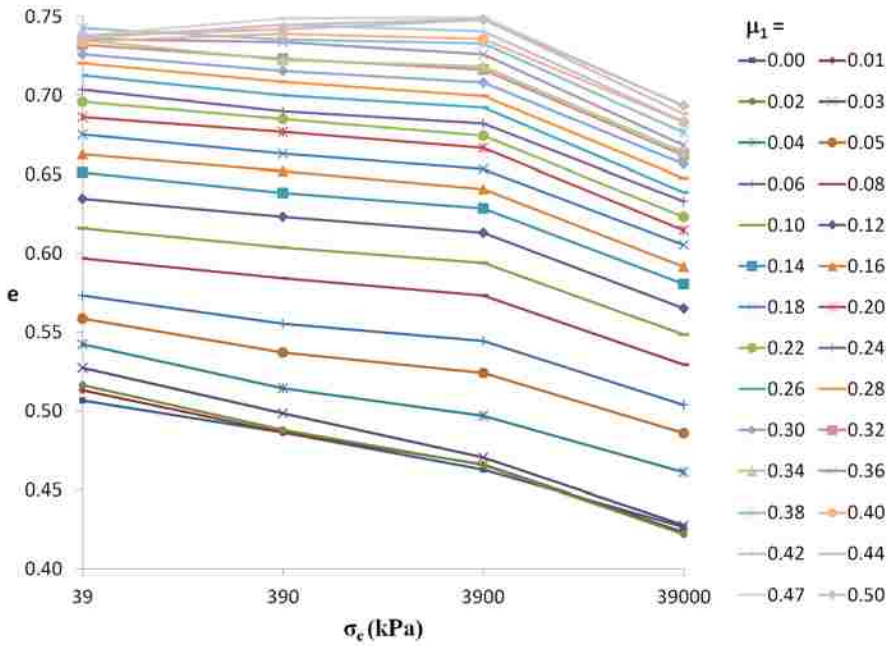

Fig. 12 Effect of confining pressure on void ratio at different friction coefficients

(Connecting lines are drawn for visibility)

The relative densities of the achieved samples were calculated using the minimum and maximum void ratios for each confining stress. Fig. 13 shows the variation of the relative density with the confining stress, indicating that relative density for the samples created with a specific friction coefficient is almost constant with variation of the confining pressure, other than the small deviations for the samples with very low confining pressure equal to 39 kPa. Fig. 14 shows the variation of the relative density with the friction coefficient for the four confining pressures. For practical purposes, the locus of the relative density as a function of the friction coefficient in the shrinkage phase for $\mu_1 \geq 0.03$ can be approximated with the following empirical equation:

$$D_r = -0.4(1 + \ln\ \mu_1) \tag{55}$$

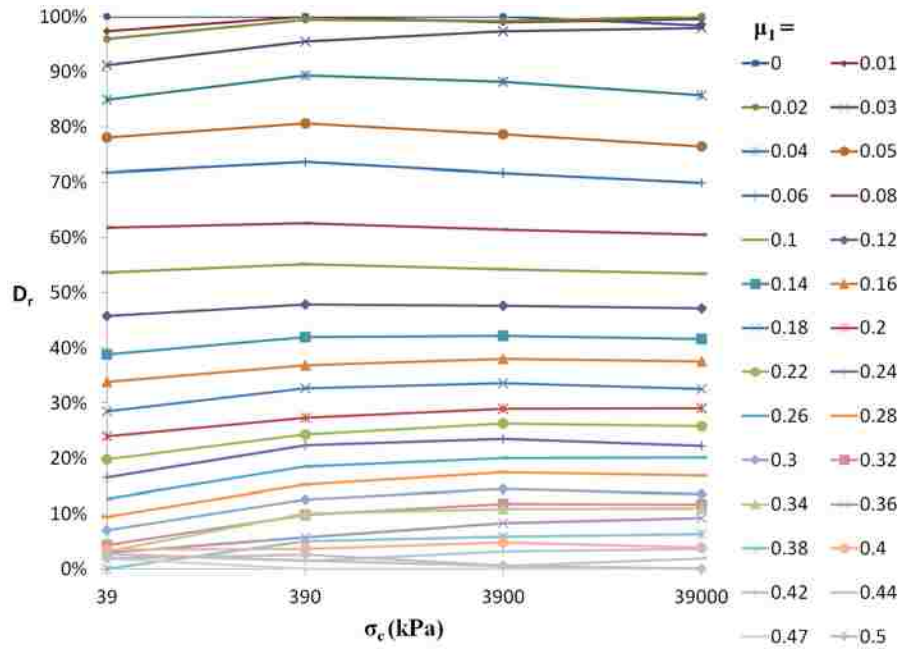

Fig. 13 Variation of relative density with the friction coefficient in the shrinkage phase

(Connecting lines are drawn for visibility)

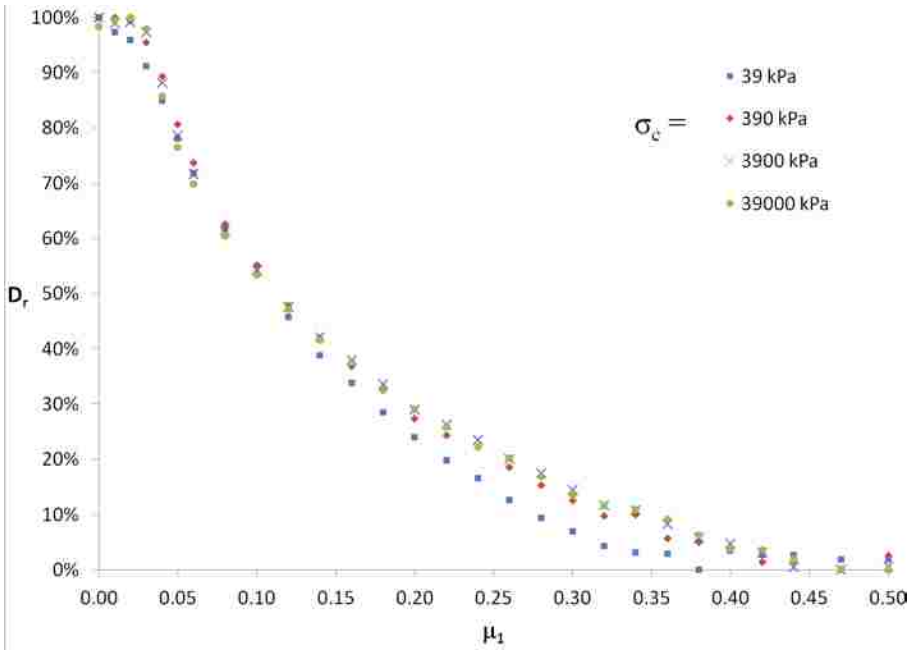

Fig. 14 Variation of relative density with the friction coefficient for three confining pressures

As defined in the literature, the mechanical coordination number is the average number of contacts of each particle – that is, the number of contacts divided by the number of particles. In order to calculate a correct coordination number, both idle particles and idle contacts should be excluded. Every particle with fewer than three contacts is counted as an idle particle. Particles with no contact are rattlers, particles with one contact are unstable, and particles with two contacts are metastable. Particles with three or more contacts in a 3D model are stable and actively participate in the load-bearing structure. Idle contacts are the contacts linked to one or two idle particles. However, identification of the idle particles needs to be done iteratively; when some of the particles are excluded as idle particles, their associated contacts are considered idle and are thus excluded. Some other particles may then lose their contacts and need to be considered idle. This procedure should be repeated until no more idle particles are identified. This procedure to calculate the correct coordination number was implemented in the program. A similar non-iterative approach was suggested by Thornton and Sun (1993) and Thornton (2000), among others.

In Fig. 15, the mechanical coordination number of the samples is shown versus the friction coefficient in the shrinkage phase. It is observed that for $\mu_1 \geq 0.03$, the coordination number declines with the increase of μ_1, and the coordination number for the higher confining stresses is higher. In Fig. 16, the variation of the coordination number with relative density is displayed for the four different confining stresses. It shows that as the relative density increases, the coordination number increases. Strong linear correlations are observed between the coordination number and the relative density at every confining pressure by excluding very low and very high relative densities.

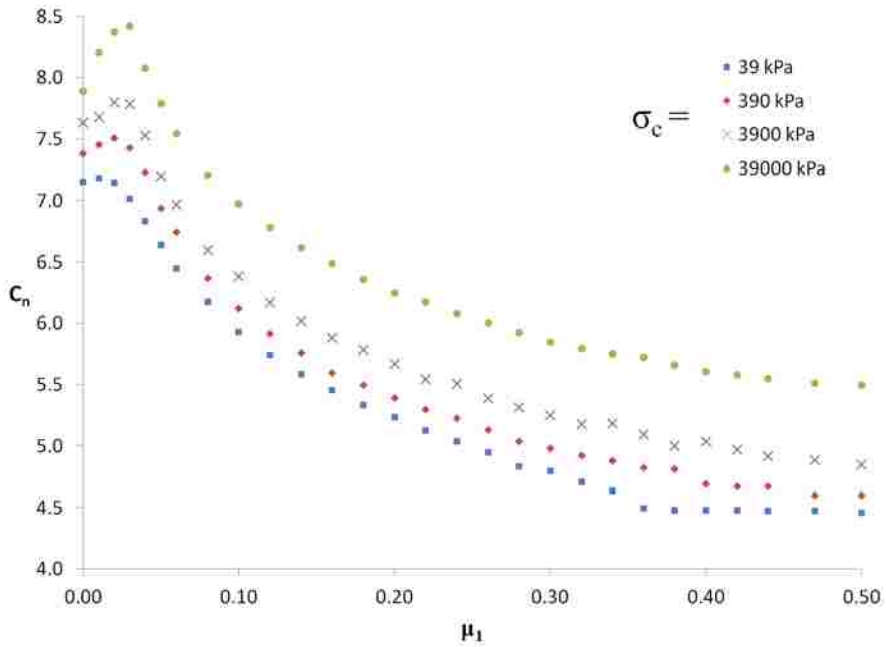

Fig. 15 Variation of coordination number with the friction coefficient in shrinkage phase

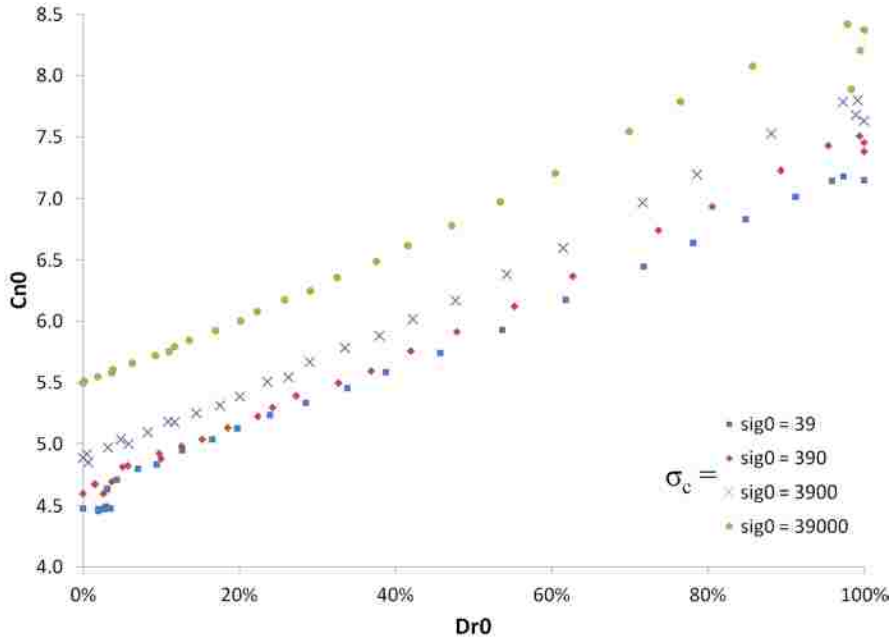

Fig. 16 Variation of coordination number with relative density for four different confining pressures

Fig. 17 shows the ratio of idle particles by weight that exist in the samples versus the friction coefficient in the shrinkage phase of the sample preparation for the four different confining pressures. It is evident that when $\mu_1 \leq 0.03$ is used, which indicates dense samples, no or few idle particles are present. As μ_1 increases, the idle particle percentage increases and plateaus at higher friction coefficients. Also, the idle particle percentage increases with increase in the confining pressure.

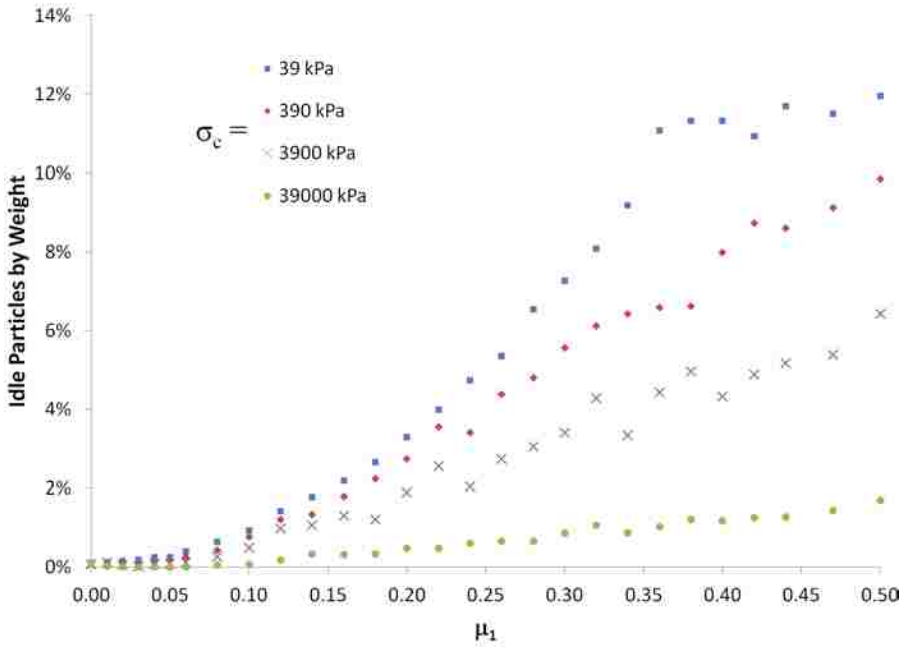

Fig. 17 Weight percentage of idle particles versus friction coefficient in shrinkage phase

4.6. Summary

This chapter presented a robust three-phase sample-preparation method. This method can be used with any particle shape and any predefined particle size distribution, unlike most of the existing methods. This method was then tested, and demonstrated the ability to successfully create DEM samples. Our method, which was inspired by the isotropic compaction method, is able to make samples with predefined aspect ratios for the container, unlike its predecessor. In addition, it works faster than isotropic compaction due to the displacement-controlled shrinkage phase.

At four different confining pressures, strong correlations were found between void ratios of samples and the inter-particle friction coefficients used in the shrinkage phase of the sample preparation. As the friction coefficient increases, the void ratio increases. A friction coefficient between 0.03 (for the densest sample) and 0.47 (for the loosest sample) is advisable. Relative density showed a strong correlation with the friction coefficient regardless of the confining pressure. For practical purposes, an empirical equation was presented that can be used to predict the value of the necessary friction coefficient to achieve a sample with a desired relative density. However, the use of this equation should be limited to the mono-dispersed samples with ellipsoidal particles that have an aspect ratio of 1.20.

CHAPTER 5

Mass-Proportional Damping

5.1. Overview

A new damping model was introduced and compared to the conventional mass-damping model. The comparison was conducted using an existing index and a new index proposed here. These indices indicate the equilibrium state of a sample. Two samples of different particle size distributions were created and were subjected to the triaxial compression loading test in drained conditions. Simulations of fourteen different damping ratios, ranging from 0 to 5%, and four different dimensionless strain rates, ranging from 10^{-8} to 10^{-5}, were carried out. The damping ratio that resulted in minimum unbalanced force, so-called optimum damping ratio, was determined based on the proposed index for the models simulated by the conventional and new damping systems. Finally, the efficiency of the new damping model was compared to that of the conventional damping model in terms of maintaining equilibrium conditions.

5.2. Damping in DEM

In the discrete element method, a Coulomb friction mechanism is used to model the tangential component of the contact forces that damp out the excessive vibrations by dissipating energy. However, the mechanism of the Coulomb friction stops dissipating energy if the normal contact force exceeds a threshold and the contact sticks. In other words, the shear component of the contact force has to be greater than a threshold value

for the contact to start sliding and dissipating energy. The normal component of the contact force does not have a damping mechanism itself.

Moreover, there is an inherent computational damping that is encountered using finite difference methods to solve the differential equations numerically (as in DEM), which is related to the interpolation scheme and the discretization refinement. This damping is called algorithmic damping, referring to Thomas (2013) and Newmark (1959). However, it is not associated with any input parameter and thus is not controllable.

Therefore, it is inevitable to apply an artificial damping to attain the equilibrium, especially for modeling quasi-static loading conditions. Since there is no physical justification for this type of damping, the damping value should be kept as small as possible so the interference is as low as possible in the response of the DEM models of particulate matters. Therefore, a minimum damping ratio that effectively minimizes the excessive particle oscillations and enhances the equilibrium state of the assembly, the so-called optimum damping ratio, has to be determined.

Damping has been implemented into the DEM through different methods, such as local contact damping and mass-proportional global damping. The global mass damping was used in this study. In addition, a size dependent mass damping was introduced.

5.2.1. Conventional Mass-Proportional Damping

The conventional mass damping, hereafter referred to as the old damping (OD), was explained in detail in Section 3.2.2 and Appendix 2.

The damping constant in translational motion of particle *i* is determined in

proportion to the particle mass, m_i, giving the so-called mass-proportional damping:

$$c_i = \alpha_i m_i \tag{56}$$

where α_i is the coefficient of mass-proportional damping.

We have showed that α_i can be related to the damping ratio, ξ:

$$\alpha_i = 2\omega_i \xi \tag{57}$$

where ω_i is the natural frequency of particle i. In practice, an equal value for the damping coefficient, α_0, is used for different-sized particles in an assembly:

$$\alpha_0 = 2\omega_{max} \xi \tag{58}$$

where ω_{max} is the highest natural frequency of the entire assembly that is approximated by the natural frequency of the smallest particle in the assembly:

$$\omega_{max} = \frac{1}{R_{min}} \sqrt{\frac{E}{\rho}} \tag{59}$$

where R_{min} is the radius of the smallest particle, and E and ρ are the elastic modulus and the density of particles.

It means that α_0 is intended to target the highest natural frequency occurring in the assembly, which is attributable to the smallest particle. Using Eqs. (59) and (60) the following equation is obtained:

$$\alpha_0 = \frac{2\xi}{R_{min}} \sqrt{\frac{E}{\rho}} \tag{60}$$

Therefore, the damping term in the equilibrium equation of all the particles –i.e., Eq. (94) – becomes:

$$c_i = \alpha_0 m_i \tag{61}$$

5.2.2. Proposed Size-Dependent Mass Damping

Instead of targeting the highest frequency in the assembly by using the natural frequency of the smallest particle, the aim is to customize the damping to each individual particle in the assembly based on the particle size. The new damping model is called size-dependent mass-proportional damping, as it was still proportional to the mass of each particle. Eqs. (94) and (98) are still in effect. However, ω_i is calculated for particle i, based on the particle radius, R_i, as follows:

$$\omega_i = \frac{1}{R_i}\sqrt{\frac{E}{\rho}} \tag{62}$$

Using Eqs. (98) and (99), the customized mass-proportional damping coefficient for particle i, α_i, is determined as follows:

$$\alpha_i = \frac{2\xi_i}{R_i}\sqrt{\frac{E}{\rho}} \tag{63}$$

In the above equation, the damping ratio is denoted with an i subscript to differentiate it from that of the conventional damping model. It is interesting to know that how much damping is applied in the conventional damping model in terms of ξ_i to a particle with a radius equal to R_i. Note that $\xi_i = c_i/c_{c_i}$ (c_{c_i} is the critical damping of particle i) whereas ξ is not necessarily equal to c_i/c_{c_i}, because ξ is equal to the actual damping ratio only for the smallest particle for which $R_i = R_{min}$.

Assuming a constant damping coefficient of $\alpha_0 = \frac{2\xi_0}{R_{min}}\sqrt{\frac{E}{\rho}}$ is equally applied to all of the particles with different sizes; by letting $\alpha_i = \alpha_0$ and using Eqs. (61) and (64) one obtains:

$$\xi_i = \frac{R_i}{R_{min}} \xi_0 \tag{64}$$

As ξ_0 is constant, Eq. (65) indicates that the actual damping ratio for the conventional damping model is proportional to the particle radius, R_i. As the particle radius increases, the damping ratio increases. However, the small particles move and vibrate faster than the large particles in a collision between small and large particles, and thus it is incorrect to assign a greater damping ratio to large particles. In the conventional mass-damping model, larger particles have a greater damping ratio than smaller ones, but, the proposed size-dependent mass-damping model overcomes this issue by allocating an equal damping ratio to all particles with different sizes. This damping model is denoted as new damping (ND) in our simulations.

5.3. Indices for Monitoring the Equilibrium State

Any damping model aims to fulfill the equilibrium state of the particles as fast as possible. To assess the equilibrium state in an assembly, the Itasca Consulting Group (2007) recommended monitoring the magnitude of the particles' unbalanced forces by comparing them to the contact forces to ensure that the out-of-balance forces are relatively small. For this purpose, a quantifiable measure is needed, so some indices have been devised to achieve this goal. In the present study, two indices were used to evaluate the performance of the conventional and the newly introduced mass-damping systems in preserving the equilibrium state.

5.3.1. Unbalanced Force Indices

Several dimensionless indices have been defined in DEM to evaluate the equilibrium state of the particular assemblies. The unbalanced force index was proposed by Ng (2006), as follows:

$$\mathrm{I_{uf}} = \sqrt{\frac{\sum_{p=1}^{n_p}\left(f_p^{res}\right)^2 / n_p}{\sum_{c=1}^{n_c}(f_c)^2 / n_c}} \tag{65}$$

where f_p^{res} is the resultant force of the contact forces (i.e., out-of-balance force) acting on particle p, and f_c is the contact force for contact c, while there are n_p particles and n_c contacts in the system. A variation of I_{uf}, called unbalanced force ratio (UFR), was introduced by Ng et al. (2014) as:

$$\mathrm{UFR} = \frac{\sum_{p=1}^{n_p}\left|f_p^{res}\right| / n_p}{\sum_{c=1}^{n_c}|f_c| / n_c} \tag{66}$$

This index shows the relative magnitude of the average out-of-balance forces to quantify the equilibrium state. I_{uf} and UFR are statistical indices and are defined based on the observation. In the present study, a new index was introduced for comparison purposes. The new index is called moment index. The moment index is based on the unbalanced moments of particle, which is not covered in UFR.

5.3.2. Moment Index

The moment index is the ratio of the sum of the magnitudes of the unbalanced moments of the particles per volume of the assembly to the magnitude of the octahedral stress of the assembly.

$$I_{Mom} = \frac{\sum_{p=1}^{n_p} |M_p|}{V|\sigma_{oct}|} \tag{67}$$

M^p is the unbalanced moment of particle p, n_p is the number of total particles, V is the volume of the sample, including the volume occupied by the particles and the inter-particle voids, and σ_{oct} is the octahedral stress of the assembly defined by

$$\sigma_{oct} = \frac{1}{\sqrt{3}}(\sigma_1 \hat{e}_1 + \sigma_2 \hat{e}_2 + \sigma_3 \hat{e}_3) \tag{68}$$

where σ_i is the stress in the i^{th} principal direction, $\hat{e}_i$.

The moment index is dimensionless and independent of the choice of density, elastic modulus of the particles, and characteristic size of the assembly.

Itasca Consulting Group (2007) recommends monitoring the magnitude of the unbalanced forces of the particles to the magnitude of the contact forces in order to ensure that the equilibrium state is reached. Obviously, I_{uf} and UFR, in Eqs. (66) and (67), fulfill this condition. The moment index is very similar to the I_{uf} in the formulation, as the unbalanced moments of a particle are the products of the unbalanced forces of the particle and the vectors directed from the center of the particle to the contact point.

On the other hand, the components of the stress tensor, from which the octahedral stress is built, are the sum of the products of the contact forces of the particles and the branch vectors divided by the volume of the assembly (See Eq. (79)). Instead of the vector sum of the particle moments, adding the magnitudes of the unbalanced moments in the numerator preserves the unbalanced moment of each particle in the formulation by preventing the particles from negating the vector components of each other's moments.

5.3.3. Inertia Index

Similar to the moment index, the inertia index was developed based on the inertia term in the rotational equation of motion, $I_i\ddot{\theta}_i$, where I_i is the moment of inertia and $\ddot{\theta}_i$ is the angular acceleration of particle i. This index, which aims to monitor the quasi-static state of models, is:

$$I_{in} = \frac{\sum_{p=1}^{n_p} |I_p \ddot{\theta}_p|}{V|\sigma_{oct}|}$$

5.4. Numerical Tests

The numerical tests were conducted to evaluate the efficiency of the introduced size-dependent damping model – proposed to achieve a better equilibrium state (i.e. less moment index) – and compare it to the conventional one. Another objective was to assess the functionality of the proposed moment index and compare it to that of the unbalanced force ratio. In addition, it was intended to determine an appropriate damping value for the conventional and size-dependent mass-damping models for shearing at different strain rates.

The response of the models using the conventional and the size-dependent damping models for a mono-dispersed sample would be the same, so in order to study the effect of the particle-size difference on the performance of the conventional and size-dependent mass-damping models, two poly-dispersed samples with 8,000 particles, A and B, with different particle size distributions (PSD) were created using the algorithm introduced in Chapter 4.

The PSDs of the samples A and B are shown in Table 10 and Table 11, respectively,

as well as in Fig. 18. Sample A was well-graded with particles that were distributed within a wide range of particle sizes from d_{min}=2.13mm to d_{max}=16.03mm, resulting in a size disparity ratio equal to d_{max}/d_{min}=7.53. Note that the particle size is nominal and refers to the diameter of a sphere with volume equal to the volume of the particle. Sample B had a narrower particle size distribution ranging from d_{min}=11.69^{mm} to d_{max}=16.03^{mm} and resulting in a size disparity ratio equal to d_{max}/d_{min} =1.37. The initial void ratios of Samples A and B were 0.419 and 0.632, respectively.

Table 10 Particle sizes and particle size distribution of Sample A

Particle Type Number	Particle Aspect Ratio	Minor Radii (mm)	Major Radius (mm)	Particle Nominal Size (mm)	Number of Particles	Weight Ratio	Accumulated Weight Ratio
1	1.2	1.0	1.2	2.13	7284	10%	10%
2	1.3	3.0	3.9	6.55	498	20%	30%
3	1.4	5.0	7.0	11.19	150	30%	60%
4	1.5	7.0	10.5	16.03	68	40%	100%

Table 11 Particle sizes and particle size distribution of Sample B

Particle Type Number	Particle Aspect Ratio	Minor Radii (mm)	Major Radius (mm)	Particle Nominal Size (mm)	Number of Particles	Weight Ratio	Accumulated Weight Ratio
1	1.2	5.5	6.6	11.69	1448	10%	10%
2	1.3	6.0	7.8	13.10	2056	20%	30%
3	1.4	6.5	9.1	14.54	2252	30%	60%
4	1.5	7.0	10.5	16.03	2244	40%	100%

The input parameters of the samples can be found in Table 12. As shown in this table, 14 different damping ratios ranging from 0 to 5% were applied in the models in order to determine the optimum damping values for each damping model. Moreover, the samples were sheared at four different dimensionless strain rates, equal to $10^{-8}, 10^{-7}, 10^{-6}$, and 10^{-5}, and up to 10% strain in the major loading direction in order

to study the damping effect at different deformation rates.

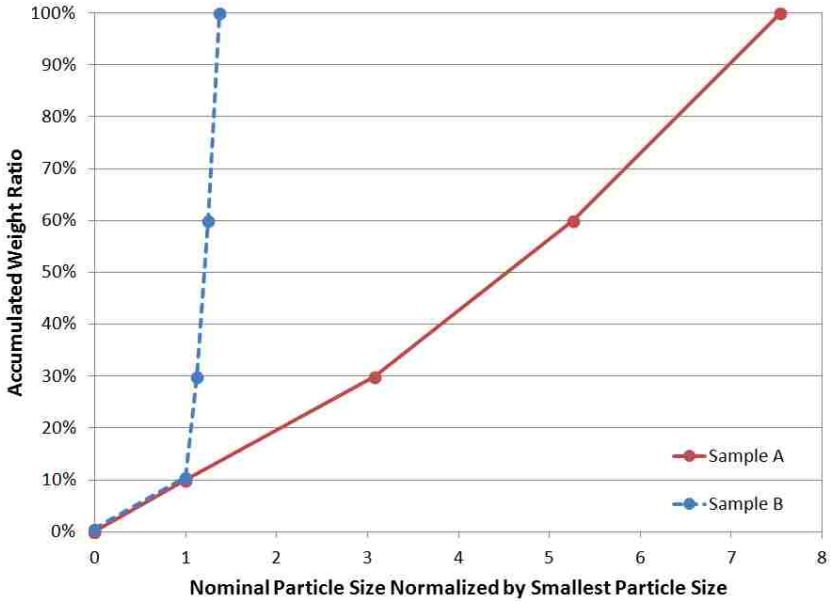

Fig. 18 Relative particle size distribution of Samples A and B

As a database, Table 50 of Appendix 8 provides the peak strength of each model in terms of the mobilized angle of friction of an assembly, ϕ_{max}, the strain measure at which the peak strength occurs, ε_{Peak}, the unbalanced force ratio, UFR, and the moment index, I_{Mom}, as well as the total kinetic energy of the particles, including the translational and the rotational components in each model, E_{Kin}. By monitoring the strain of the peak strengths, it was ensured that the peak states had been captured before the loading ends at 10% strain. Note that both the index values and the kinetic energy in Table 50 were evaluated at 250 points (i.e., one point for every 0.04% strain) and averaged between 0 and 10% strain.

The following is the naming convention for the models. {Mn-DD-n.nn}

M: model name (A or B)

n: deformation speed (5 for $\varepsilon' = 10^{-5}$, 6 for $\varepsilon' = 10^{-6}$, 7 for $\varepsilon' = 10^{-7}$, and 8 for $\varepsilon' = 10^{-8}$)

DD: damping type (ND = new damping model, OD = old damping model, and WD = without damping, i.e., $\xi = 0$)

n.nn: damping ratio in terms of percent (i.e., 100ξ)

Table 12 Features of the simulation code and input parameters of Samples A and B

Computation Code	ELLIPSE3D
Particle Shape	Ellipsoid
Contact Laws	Simplified Hertz-Mindlin
Boundary Conditions	Periodic
Aspect Ratios of Sample (Cuboid)	1, 1, 1
Sample Preparation Approach	Automatic Three-Phase Method
Initial Stress State of Samples	$\sigma_{11} = \sigma_{22} = \sigma_{33}$ = 390 kPa
Poisson's Ratio (ν)	0.3
Inter-particle Friction Coefficient in Shrinkage Phase of Sample Preparation (μ_0)	0.2
Inter-Particle Friction Coefficient in Loading Stage (μ)	0.5
Time Step Ratio (c_t)	0.32
Density, ρ (mg/mm^3)	2.65
Elastic Modulus, E, (mN/mm^2)	7.8×10^7

5.5. Interpretation of the Numerical Test Results

Comparison of the UFR and I_{Mom} values using the data in Table 50 of Appendix 8 indicates that the two indices yield values close to each other and show similar trends with changes of damping ratio, ξ, and the dimensionless strain rate, ε'; that is, when UFR increases, I_{Mom} increases and vice versa. For example, for a specific sample with a specific damping ratio using the same damping model, an increase of the shearing rate increases both indices. Altogether, the values of the two indices are very close for the models with Sample A, whereas I_{Mom} yields smaller values for the models with Sample B (2 to 3 times smaller) with respect to the values of the UFR. In Fig. 19 where the UFR and moment index of two sample models are shown, the two indices exhibit the same pattern.

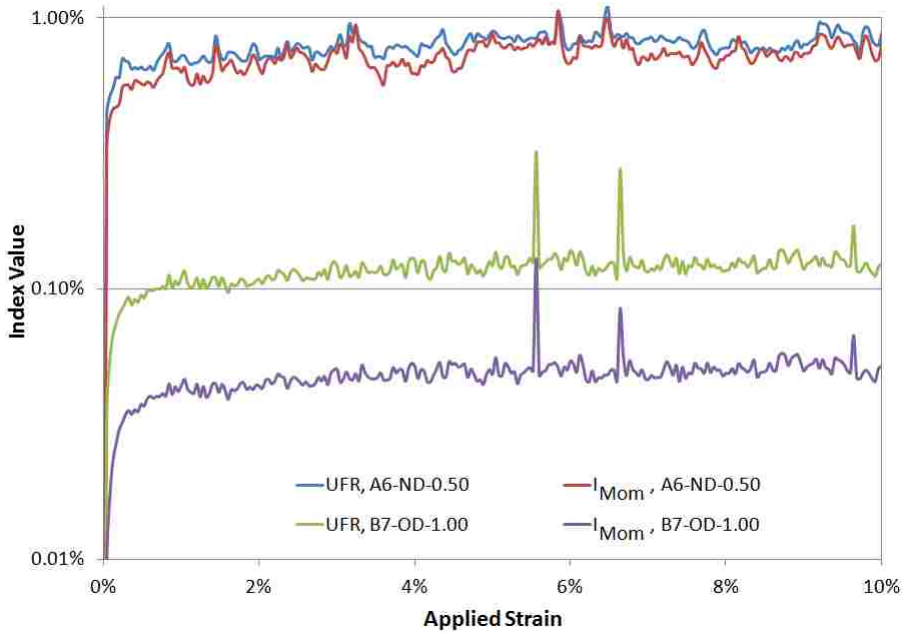

Fig. 19 Evolution of UFR and moment index with the applied strain for two sample models

Fig. 20 shows the moment index values that were obtained for Sample A with the old damping model and different damping ratios at different loading speeds. It is evident that at every dimensionless strain rate, with the increase of the damping ratio from 0, the index value decreases from its value at $\xi = 0$ to a minimum value specific to that strain rate. This minimum value of the damping ratio is called the optimum damping ratio, ξ_{opt}. From this point on, with further increase of the damping ratio, the moment index increases. It indicates that $\xi = \xi_{opt}$ is the best damping ratio value to maintain the equilibrium state in the assembly.

The existence of an optimum damping value for each loading speed is also observed for Sample B with the old damping model, as illustrated in Fig. 21. As shown in Fig. 22 and Fig. 23, the same applies to Samples A and B, respectively, with the new damping model. In addition, in Fig. 20, Fig. 21, Fig. 22, and Fig. 23, the optimum damping ratio for each loading speed was determined by fitting a smooth curve to the data points, and the index values were interpolated at the optimum damping points. The optimum damping ratios for Samples A and B at different loading speeds and using the conventional and the size-dependent mass-damping models based on the moment index have been collected in Fig. 24.

Fig. 24 indicates that at low deformation rates that suit the quasi-static regime, the optimum damping ratios for Samples A and B using the new damping model are about 0.5% and 0.4%, respectively, whereas using the old damping model for Samples A and B at low speeds, the optimum damping ratios are about 0.25% to 0.35%. It was learned that the value of the optimum damping ratio depends on the particle size distribution, and this

agrees with the results of Zhou et al. (2016) from the experimental tests. With the old damping model, a wider PSD required less damping, whereas a narrower PSD required a higher damping ratio. Using the new damping model, conversely, a higher damping ratio is required for a narrow PSD, and a lower damping ratio is needed for a wide PSD; thus, the damping model affects the choice of damping ratio.

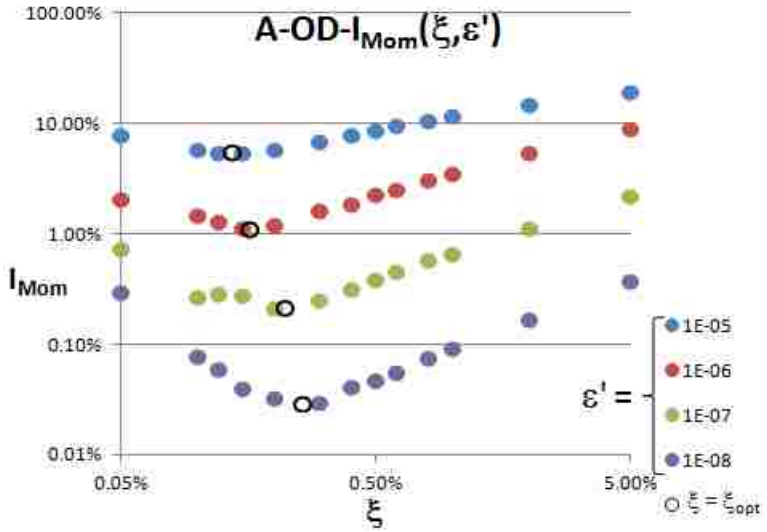

Fig. 20 Moment index for Sample A with old damping model and different damping ratios at different dimensionless strain rates (log–log scale)

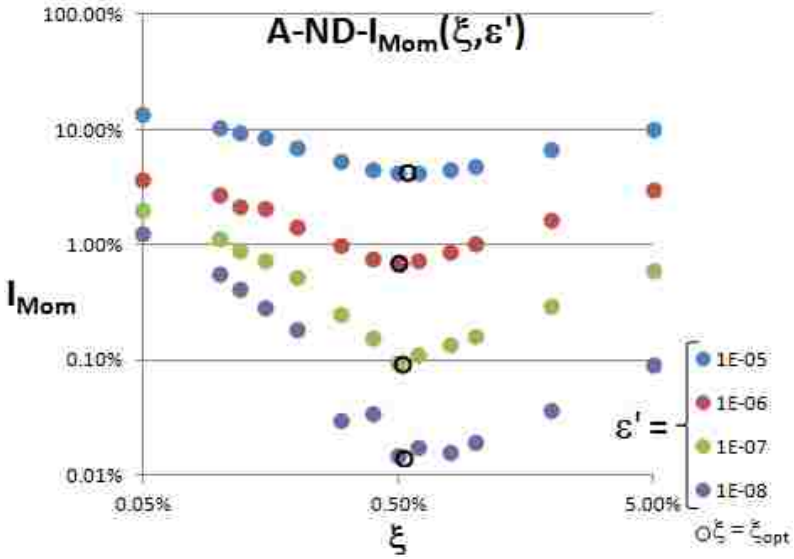

Fig. 21 Moment index for Sample B with old damping model and different damping ratios at different dimensionless strain rates (log–log scale)

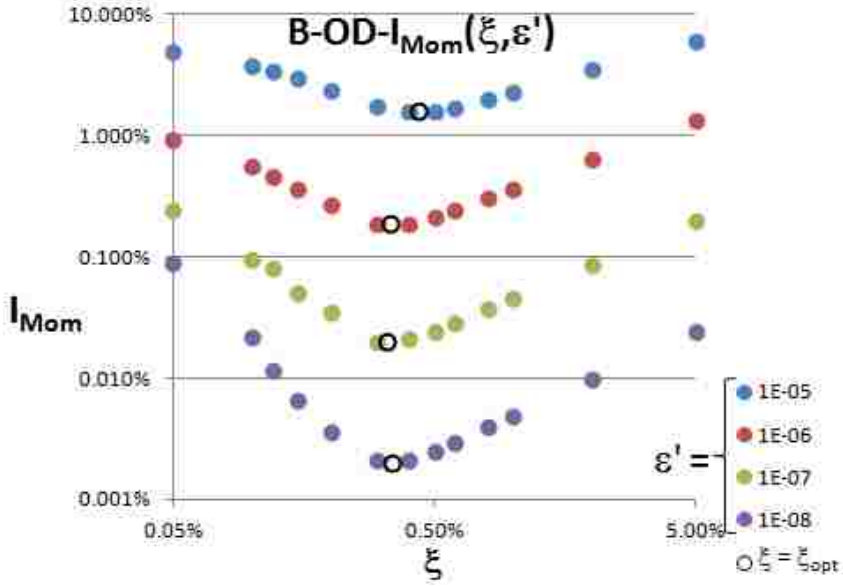

Fig. 22 Moment index for Sample A with new damping model and different damping ratios at different dimensionless strain rates (log–log scale)

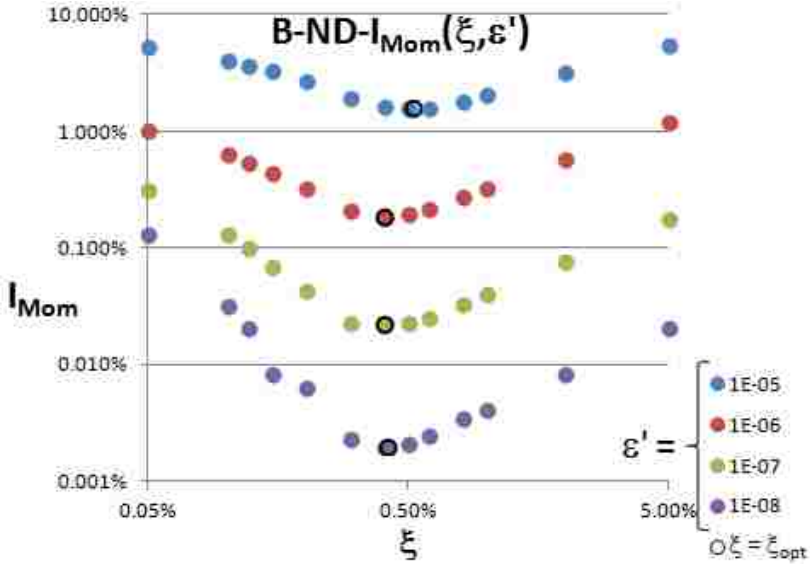

Fig. 23 Moment index for Sample B with new damping model and different damping ratios at different dimensionless strain rates (log–log scale)

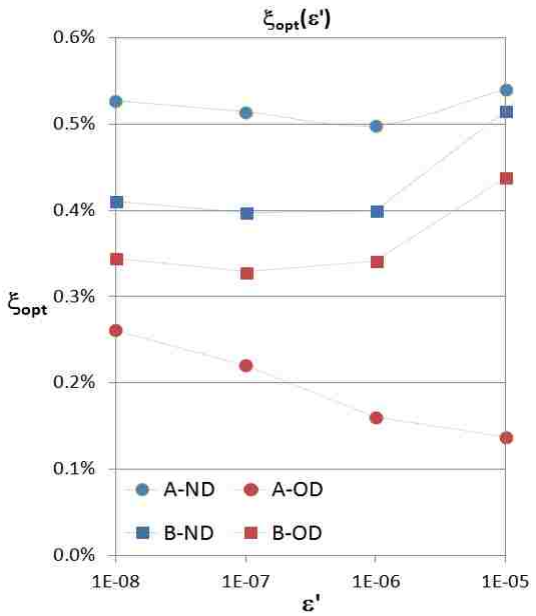

Fig. 24 Optimum damping ratios of Samples A and B versus dimensionless strain rate using old and new damping models based on moment index (semi-log scale)
(Connecting lines are drawn for visibility)

Moreover, it was known that the optimum damping ratio value is almost independent of the strain rate at lower strain rates for the new damping model. Using the old damping model, Sample B, which has a narrower PSD (a lower particle size disparity), mostly needs the same damping ratio at different loading speeds, whereas Sample A needs more damping at lower loading speeds. Furthermore, for Sample B, which has particle sizes within a narrow range, the optimum damping ratios at different strain rates are close for the new and the old damping models, as expected.

In Fig. 20, Fig. 21, Fig. 22, and Fig. 23, it is evident that at lower strain rates, I_{Mom} values grow faster about the optimum damping ratio noticing the log scale. Therefore, it is important to pick an appropriate damping ratio in quasi-static simulations where a relatively low strain rate is applied.

For comparison, Fig. 25 displays the UFR values versus the various damping ratios

for Sample A at different deformation rates using the new damping model. As mentioned before, a very high degree of similarity is observed between the moment index and the unbalanced force ratio, qualitatively and quantitatively. Alternatively, the optimum damping ratio value can be determined based on UFR, as shown in Fig. 26. It is evident that the optimum damping values, which are calculated based on the UFR and I_{Mom}, are very close, especially at the lower strain rates usually intended for maintaining the quasi-static conditions.

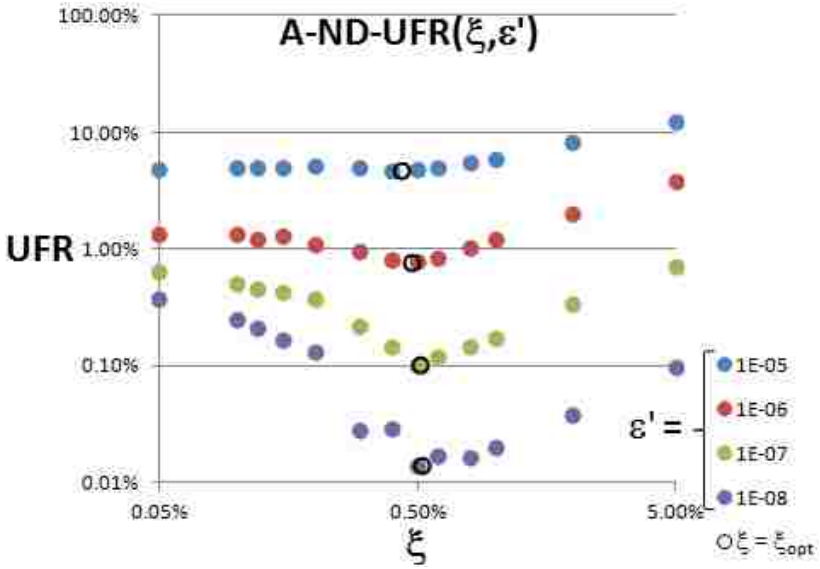

Fig. 25 Unbalanced force ratio for Sample A with new damping model and different damping ratios at different dimensionless strain rates (log–log scale)

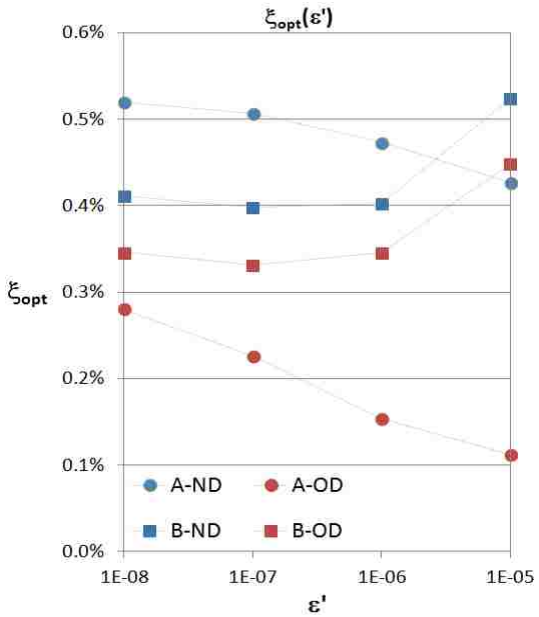

Fig. 26 Optimum damping ratios of Samples A and B versus dimensionless strain rate using old and new damping models based on unbalanced force ratio (semi-log scale)
(Connecting lines are drawn for visibility)

Fig. 27, Fig. 28, Fig. 29, and Fig. 30 display the kinetic energy of Samples A and B versus the damping ratio for the models with the old and new damping systems at different dimensionless strain rates. The kinetic energy, E_{Kin}, was calculated by summing up the translational and the rotational kinetic energies of all of the particles in each sample. It is observed that as ε' increases, E_{Kin} increases in all of the models. On the other hand, E_{Kin} decreases with the increase of ξ. There is no change in the trend of kinetic energy at $\xi = \xi_{opt}$. Therefore, E_{Kin} does not provide any information about the equilibrium state of the models.

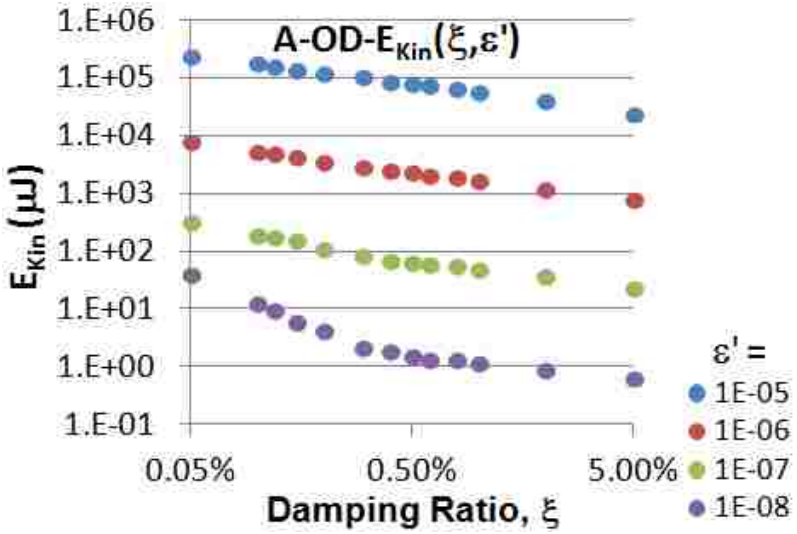

Fig. 27 Kinetic energy of models versus damping ratio with old damping model at different dimensionless loading rates for Sample A (log–log scale)

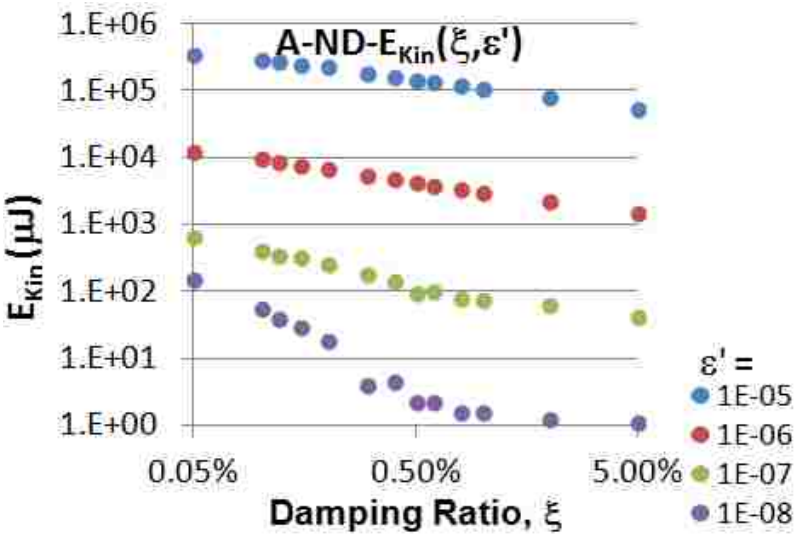

Fig. 28 Kinetic energy of models versus damping ratio with new damping model at different dimensionless loading rates for Sample A (log–log scale)

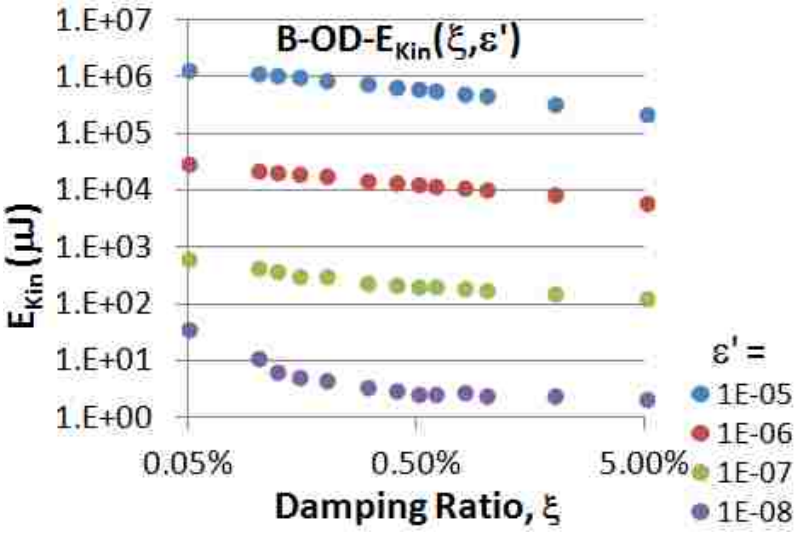

Fig. 29 Kinetic energy of models versus damping ratio with old damping model at different loading rates for Sample B (log–log scale)

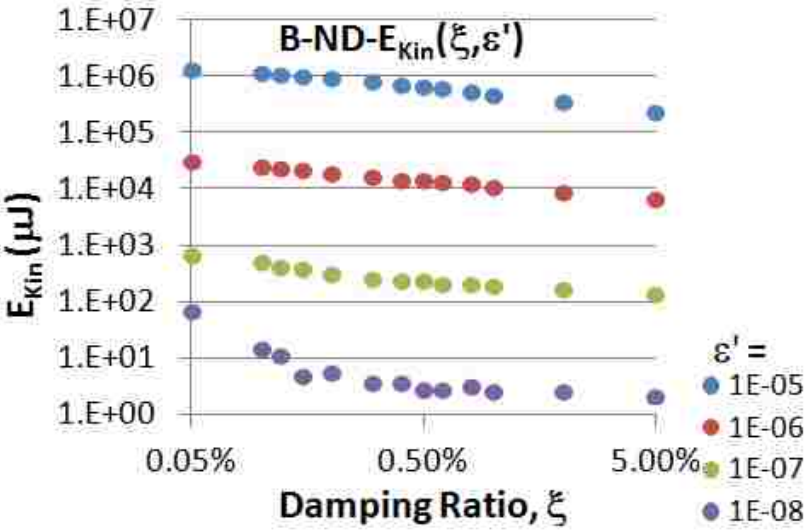

Fig. 30 Kinetic energy of models versus damping ratio with new damping model at different dimensionless loading rates for Sample B (log–log scale)

In Fig. 31, Fig. 32, Fig. 33, and Fig. 34, the variation of the inertia index with damping ratio using the old and the new damping models are presented for Samples A and B at different dimensionless strain rates. As expected, the moment index and the inertia index have the same values at zero damping ratio. As the damping ratio increases

at each dimensionless strain rate, the inertia index decreases monotonically. With the increase of the strain rate, the inertia index increases. Hence, the trends observed for the inertia index are similar to those of the kinetic energy, and no information is provided about the optimum damping ratio by the inertia index either. Furthermore, the inertia index in all cases has a value less than the moment index. Therefore, by monitoring the moment index and keeping it small, one can ensure than the inertia index is small as well.

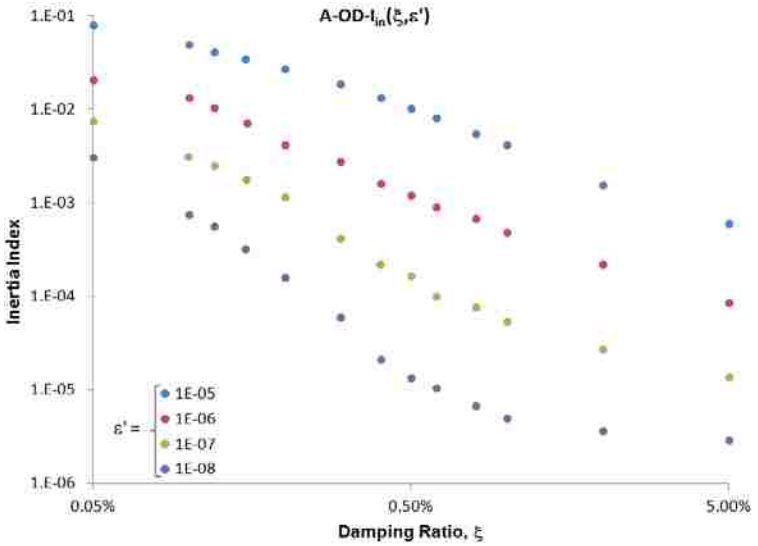

Fig. 31 Inertia index of models versus damping ratio with old damping model at different dimensionless loading rates for Sample A (log–log scale)

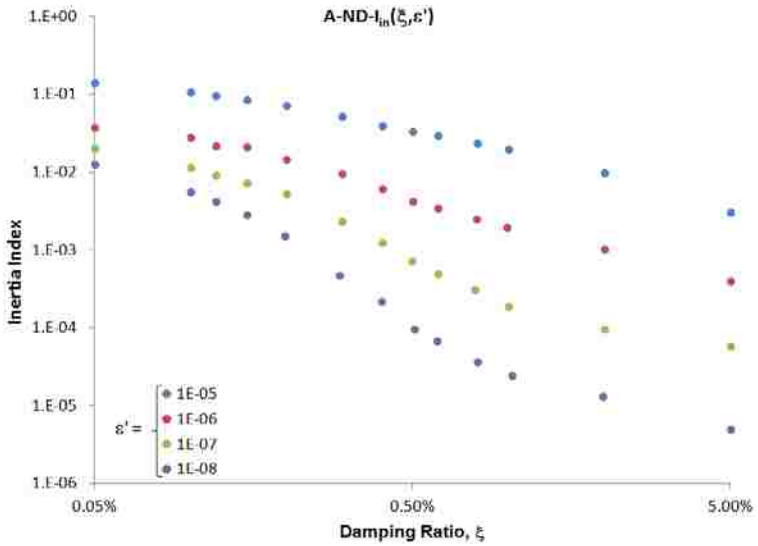

Fig. 32 Inertia index of models versus damping ratio with old damping model at different dimensionless loading rates for Sample B (log–log scale)

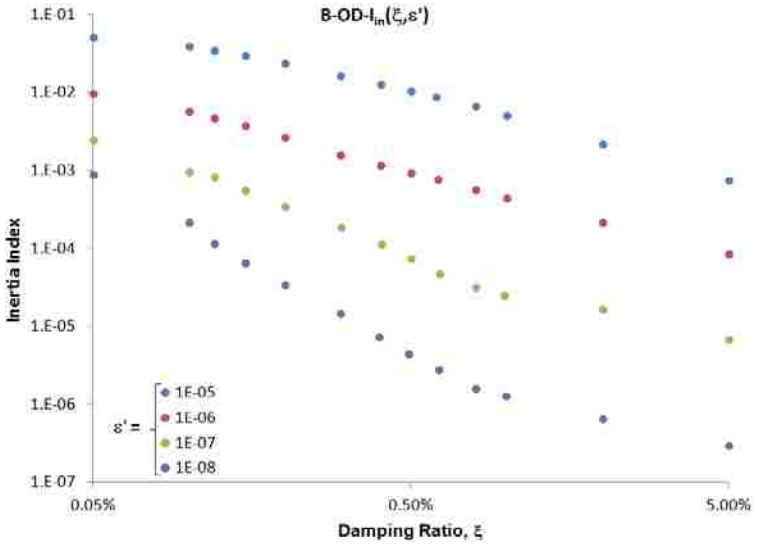

Fig. 33 Inertia index of models versus damping ratio with new damping model at different dimensionless loading rates for Sample A (log–log scale)

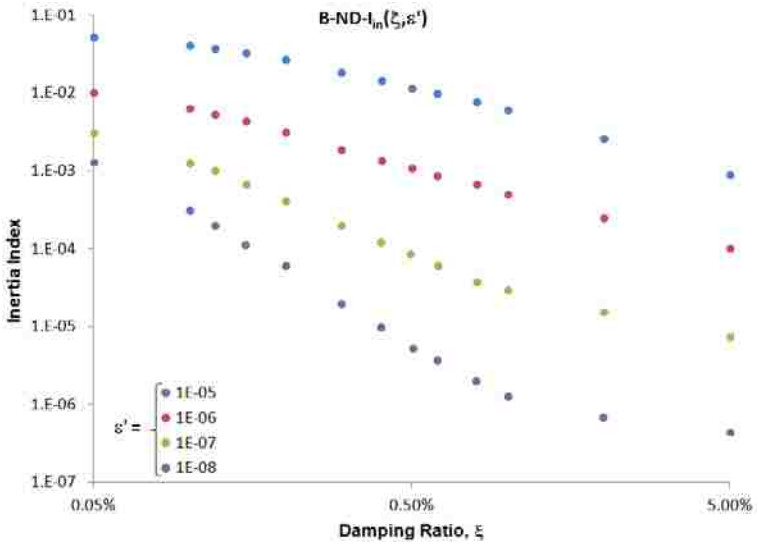

Fig. 34 Inertia index of models versus damping ratio with new damping model at different dimensionless loading rates for Sample B (log–log scale)

Fig. 35 shows the moment index values at the optimum damping ratios versus the dimensionless strain rates for Samples A and B using the old and new damping models. Strong linear relationships can be interpreted in the log–log scale (i.e., power fit in normal scales) between I_{Mom} and ε' at $\xi = \xi_{opt}$ for Samples A and B using the old and the new damping models. This equation is still in effect for $\xi > \xi_{opt}$. However, for $\xi < \xi_{opt}$, the linear relationship is not valid. It is clear that the moment index increases with the increase of the dimensionless strain rate. Moreover, in Fig. 35, it is evident that the moment index values for Sample B at different strain rates are almost identical using the old and new damping models as expected because of the lower particle size differences. However, the moment index values at $\xi = \xi_{opt}$ for Sample A using the old and new damping models at different loading speeds differ. The new damping model results in a lower moment index for Sample A, indicating that the performance of the new damping model was better than that of the old damping model in preserving the equilibrium state where the particle-size disparity is high.

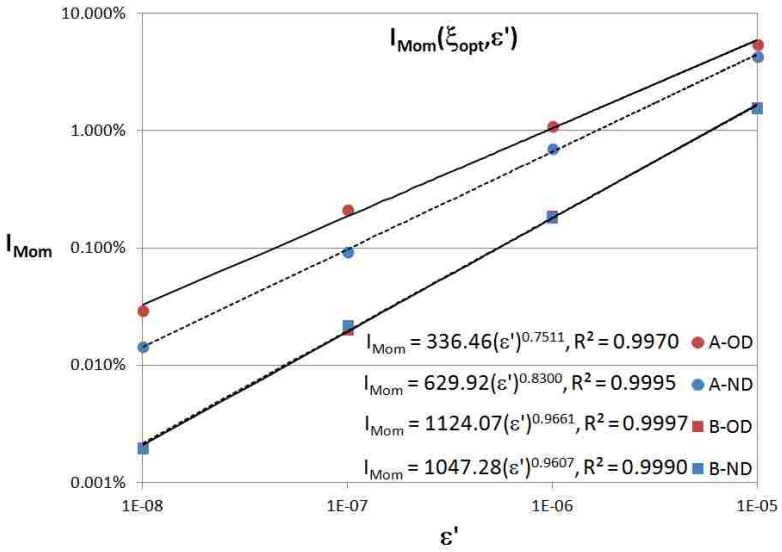

Fig. 35 Moment index at $\xi = \xi_{opt}$ for Samples A and B using old and new damping models at different dimensionless loading rates (log–log scale)

We defined quasi-static dimensionless strain rate, ε'_{QS}, as the highest dimensionless strain rate above which the quasi-static condition is violated. To have the quasi-static condition fulfilled, the loading rate has to be small so that no large inertial forces can build up in the model. It is important to determine the largest strain rate at which the quasi-static condition can be maintained so that one can perform the simulation in the shortest runtime possible. According to Eq. (28) in Chapter 3, the out-of-balance force of each particle in every direction is equal to the sum of the inertial force and the damping force of the particle in that direction. By monitoring the unbalanced forces of the particles, one needs to ensure that the inertial forces are relatively small when they are compared to the contact forces of particles. Alternatively, the unbalanced moments of particles can be examined. For this purpose, we monitor the value of the moment index. We assume that the quasi-static condition is maintained if $I_{mom} \leq 0.1\%$. Hence, we define ε'_{QS} as the strain rate corresponding to $I_{Mom} = 0.1\%$.

Since there is a strong correlation between I_{Mom} and ε'_{QS} when $\xi = \xi_{opt}$, we can calculate ε'_{QS} from this relationship by letting $I_{Mom} = 0.1\%$. In this way, the quasi-static strain rates of Samples A and B with the old and new damping models are calculated and shown in Table 13. Apparently, ε'_{QS} is almost equal for Sample B with the old and new damping models. This was expected because the particles of Sample B are distributed in a narrow size range, and thus the new size-dependent damping model cannot make a big difference. However, the quasi-static strain rate for Sample A with the new damping model is 2.35 times of the quasi-static strain rate with the old damping model. This means that where using the old damping model, the required runtime to perform a simulation on Sample A is 23.5 days, for example, to keep the moment index below 0.1%, the same can be accomplished in 10 days using the new damping model. This is a significant improvement over the conventional mass-damping model for speeding up the DEM simulations when the sample contains particles with a large size disparity. In addition, it is evident that the size disparity has an adverse effect on ε'_{QS} with both damping models, because Sample A with a large size disparity has a smaller ε'_{QS} than Sample B with small size disparity.

Table 13 Quasi-static strain rates and optimum damping ratios of Samples A and B with old and new damping models

Sample	**Damping Model**	ξ_{opt}	ε'_{QS}	Relative Improvement
A	OD	0.23%	4.38×10^{-8}	1
A	ND	0.51%	1.03×10^{-7}	2.35
B	OD	0.34%	5.46×10^{-7}	1
B	ND	0.40%	5.42×10^{-7}	0.99

It was aimed to compare the responses of Sample A obtained using the old and new damping models with the optimum damping ratios at quasi-static strain rates that were determined with each damping models, separately, i.e., Models A-QS-OD-OPT and A-QS-ND-OPT, respectively. The damping ratios and the dimensionless strain rates of the two models are shown in Table 14. Note that the model A-QS-ND-OPT already existed in the database, so only A-QS-ND-OPT was simulated.

Table 14 Strain rates and damping ratios for models of Sample A with old and new damping models selected for comparison

Model	ε'	ξ
A-QS-OD-OPT	4×10^{-8}	0.25%
A-QS-ND-OPT	1×10^{-7}	0.50%

Fig. 36 and Fig. 37 show the friction angle and the volumetric strain of the two models that evolved with the applied strain where very close behavioral curves are observed for the two models. Therefore, using the new size dependent mass-damping model reproduces the response obtained using the old damping model, but in less runtime.

In Fig. 38, the variations of the peak friction angles of models with the dimensionless strain rate are shown for four sample models, A-OD-0.20, A-ND-0.50, B-OD-0.30, and B-ND-0.40. It is clear that the friction angles of the assemblies increase as the dimensionless strain rate increases in all of the models with a constant damping ratio. Moreover, as shown in Fig. 39, Fig. 40, Fig. 41, and Fig. 42, ϕ_{Peak} of Samples A and B with both of the damping models increases with the increase of the damping ratio. The

increase is more noticeable for the models that were subjected to higher deformation rates. Furthermore, the variation of the strength parameter, ϕ_{Peak}, with $\xi\varepsilon'$ values in semi-log scales is shown for Samples A and B with the old and the new damping models in Fig. 43, Fig. 44, Fig. 45, and Fig. 46. It is evident that, at low $\xi\varepsilon'$ values, ϕ_{Peak} is almost constant as $\xi\varepsilon'$ increases, ϕ_{Peak} increases. With further increases of $\xi\varepsilon'$, the increase of ϕ_{Peak} accelerates more. Interestingly, the increase of ϕ_{Peak} with the increase of $\xi\varepsilon'$ occurs monotonically, indicating that the increase of ϕ_{Peak} with the increase of ξ and the increase of ϕ_{Peak} with the increase of ε' occurs at the same rate. Therefore, it is concluded that ϕ_{Peak} is a function of $\xi\varepsilon'$.

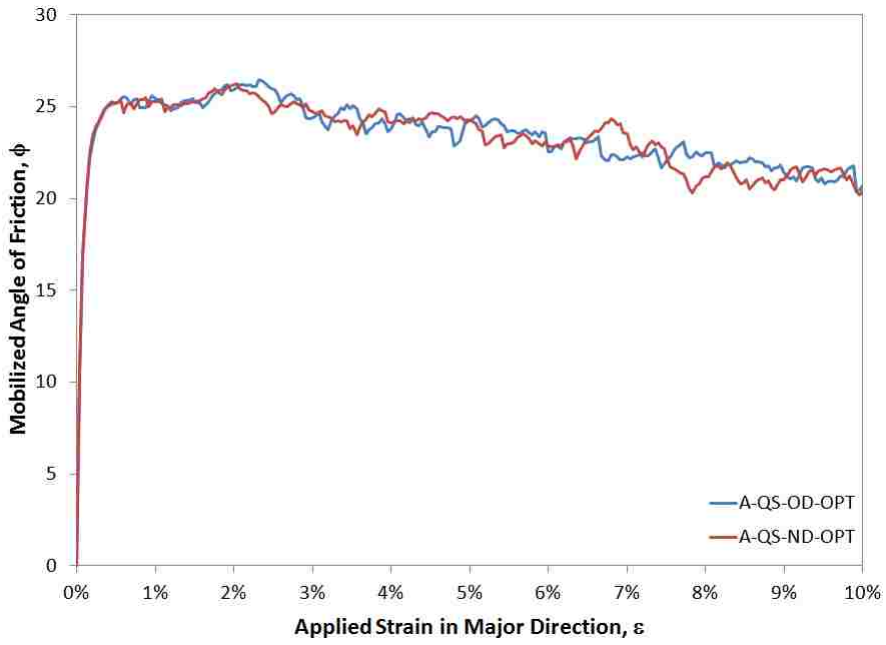

Fig. 36 Friction angle evolved with applied strain for Sample A with old and new damping models with optimum damping ratio at quasi-static strain rates

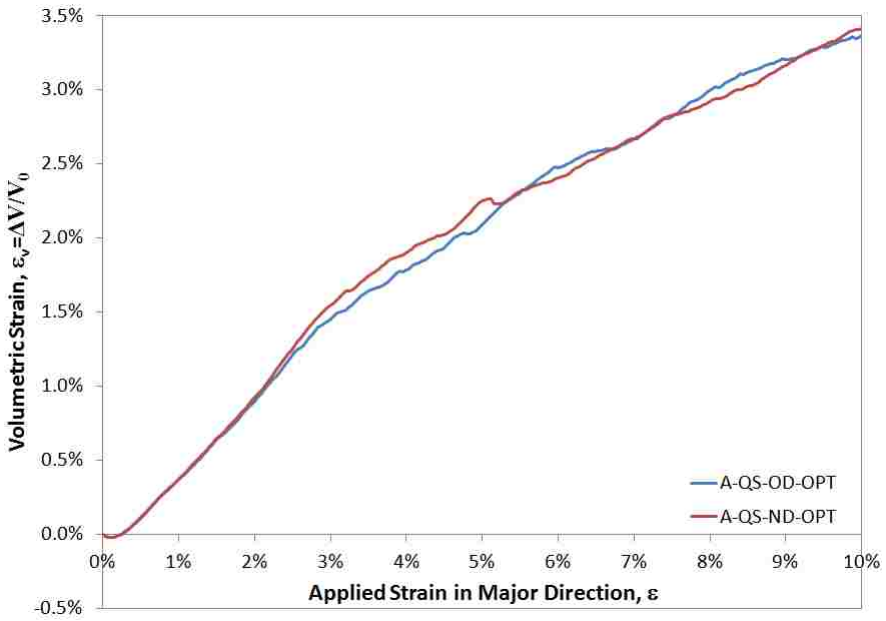

Fig. 37 Volumetric strain evolved with applied strain for Sample A with old and new damping models with optimum damping ratio at quasi-static strain rates

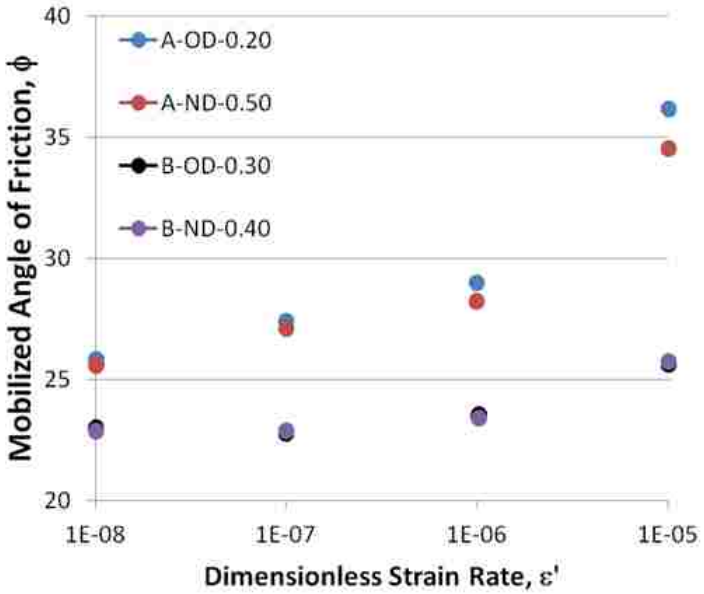

Fig. 38 Friction angle versus dimensionless strain rate for Samples A and B with old and new damping models with damping ratios close to the optimum damping ratios (semi-log scale)

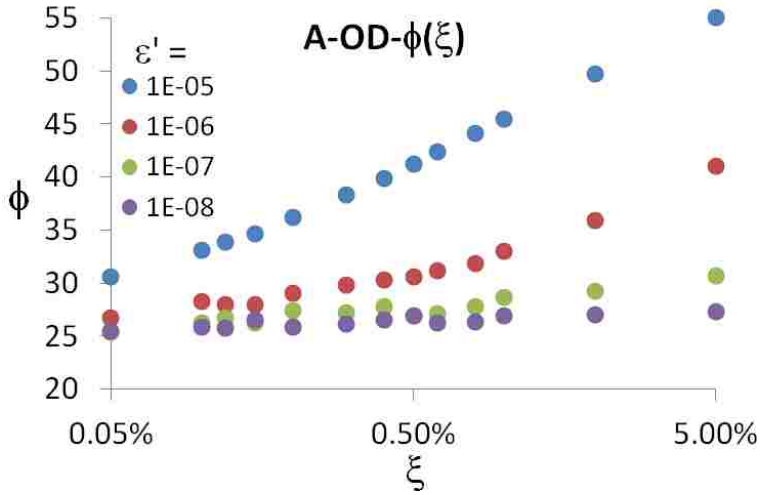

Fig. 39 Friction angle for Sample A with old damping model versus various damping ratio values at different dimensionless strain rates (semi-log scale)

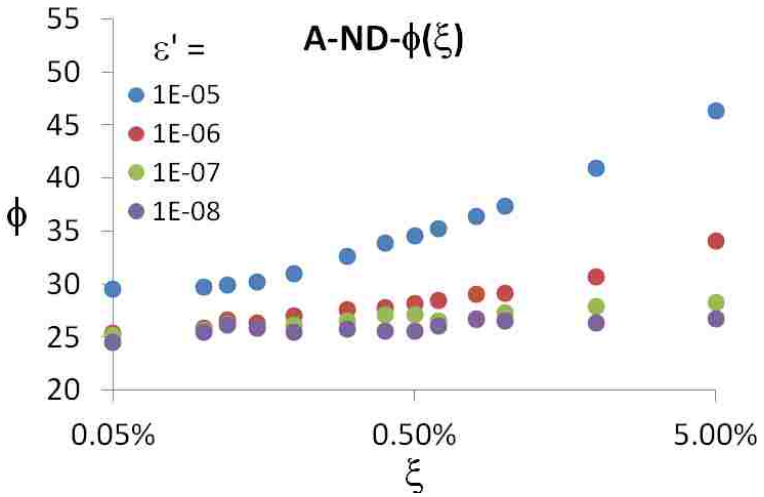

Fig. 40 Friction angle for Sample A with new damping model versus various damping ratio values at different dimensionless strain rates (semi-log scale)

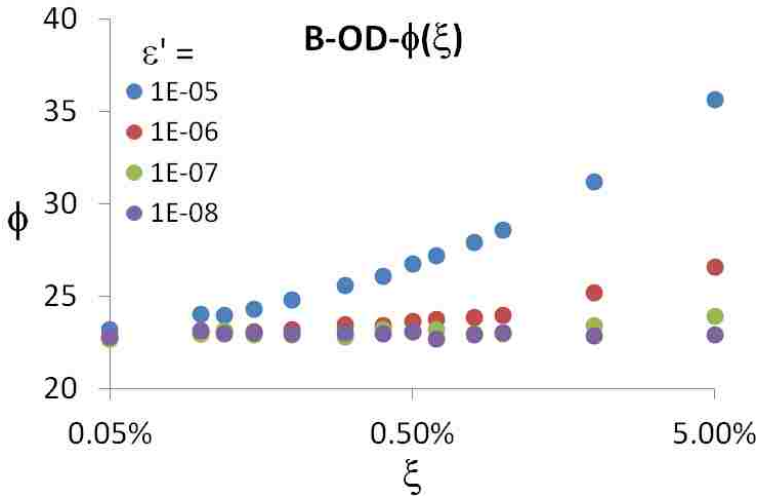

Fig. 41 Friction angle for Sample B with old damping model versus various damping ratio values at different dimensionless strain rates (semi-log scale)

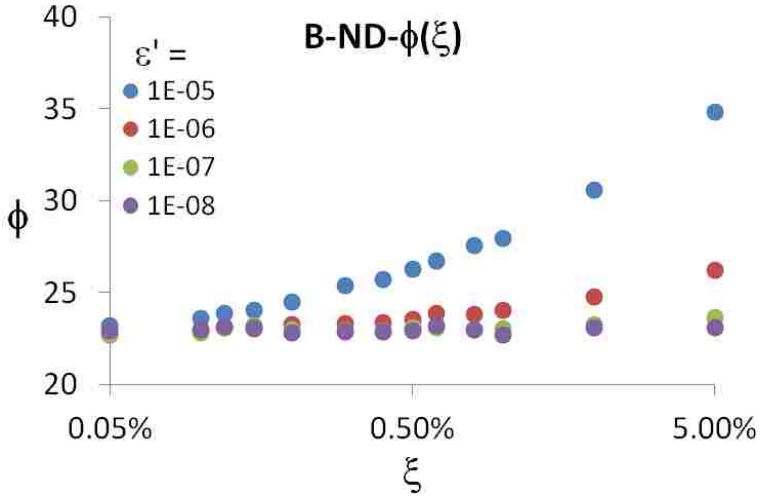

Fig. 42 Friction angle for Sample B with new damping model versus various damping ratio values at different dimensionless strain rates (semi-log scale)

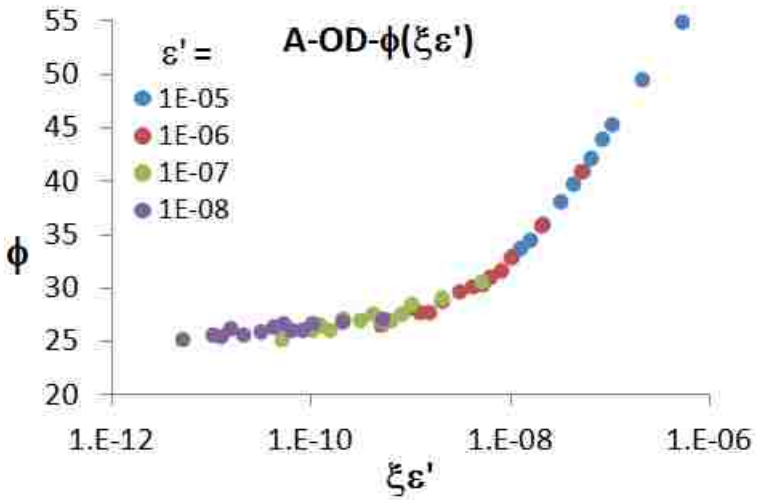

Fig. 43 Friction angle for Sample A with old damping model versus various values of product of damping ratio and dimensionless strain rate (semi-log scale)

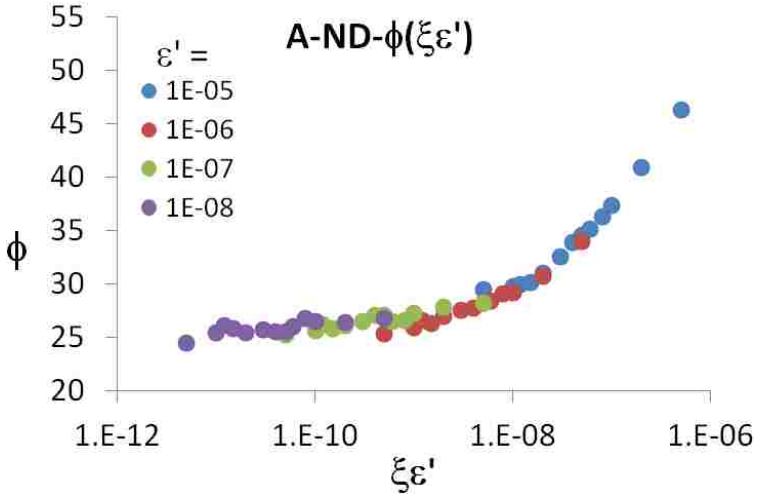

Fig. 44 Friction angle for Sample A with new damping model versus various values of product of damping ratio and dimensionless strain rate (semi-log scale)

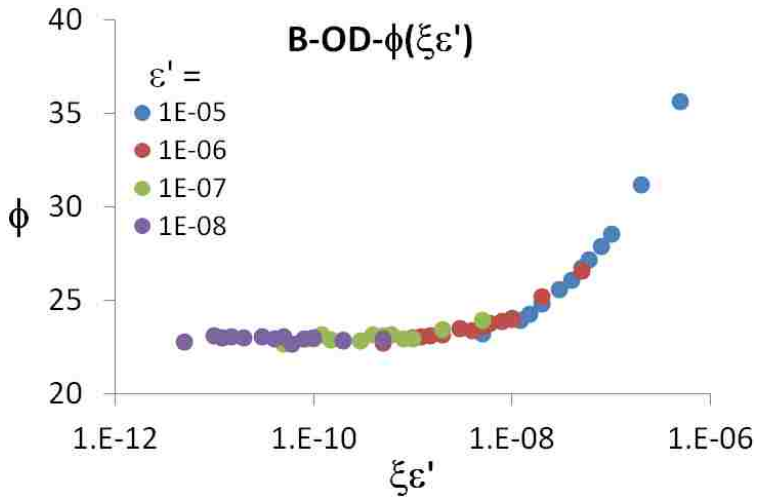

Fig. 45 Friction angle for Sample B with old damping model versus various values of product of damping ratio and dimensionless strain rate (semi-log scale)

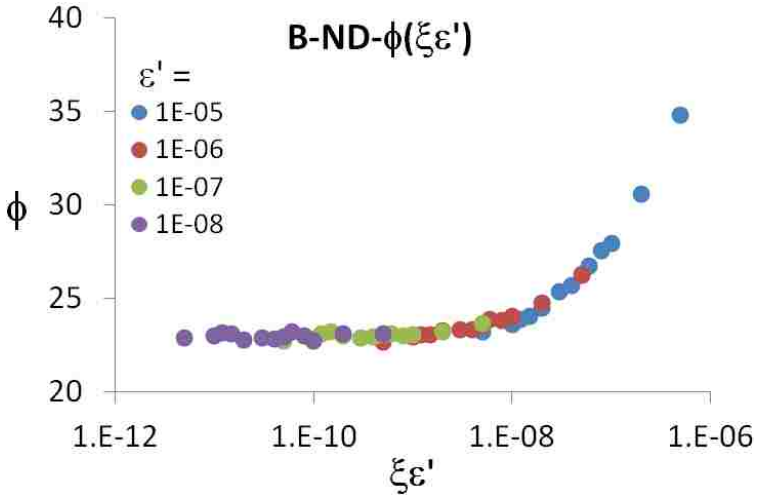

Fig. 46 Friction angle for Sample B with new damping model versus various values of product of damping ratio and dimensionless strain rate (semi-log scale)

I_{Mom} is also a function of $\xi\varepsilon'$. This is evident in Fig. 47, Fig. 48, Fig. 49, and Fig. 50. In these figures the data points of the models with $\xi \geq \xi_{opt}$ are marked with circles.

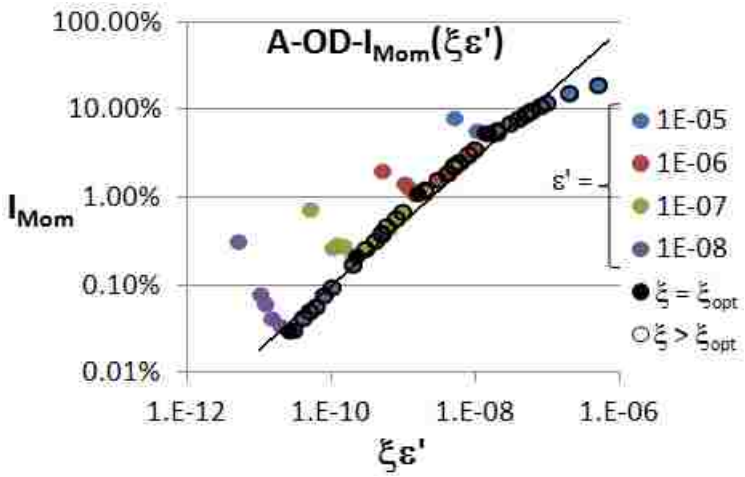

Fig. 47 Moment index for Sample A with old damping model versus values of product of damping ratio and dimensionless strain rate (log-log scale)

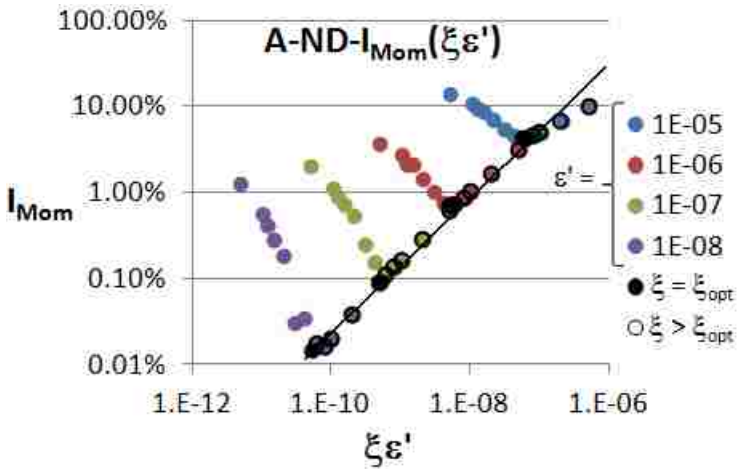

Fig. 48 Moment index for Sample A with new damping model versus values of product of damping ratio and dimensionless strain rate (log-log scale)

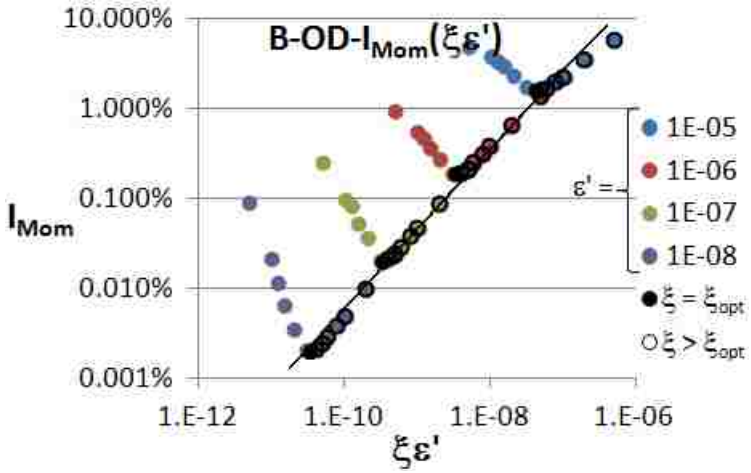

Fig. 49 Moment index for Sample B with old damping model versus values of product of damping ratio and dimensionless strain rate (log-log scale)

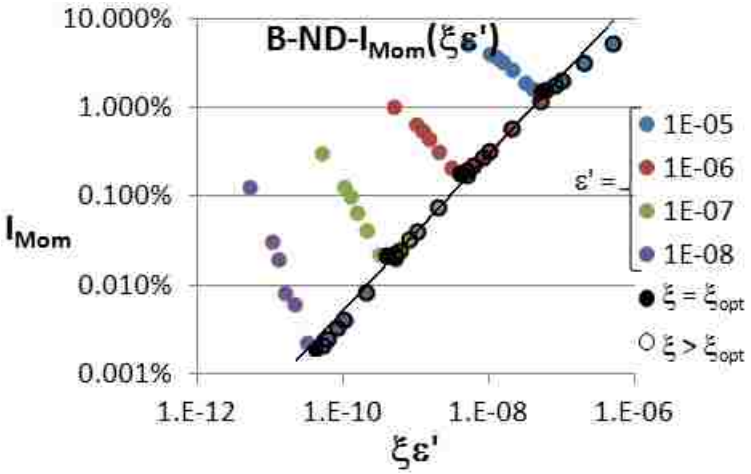

Fig. 50 Moment index for Sample B with new damping model versus values of product of damping ratio and dimensionless strain rate (log-log scale)

In Fig. 51, Fig. 52, Fig. 53, and Fig. 54, the variation of $\tan\phi_{Peak}$ is shown versus the moment index. In this figure the data points of the models which have a damping ratio higher than the optimum damping ratio are marked with circles. It is evident that when the damping ratio is less than the optimum damping ratio the peak friction angle is lower and the moment index value is significantly higher. This applies to both samples

with both damping models at any strain rate. Moreover, it is observed that for the data points associated with models with $\xi \geq \xi_{opt}$ and any strain rate the locus of the points is a straight line that can be described in the following form.

$$\tan\phi = \tan\phi_{QS} + k.I_{Mom} \tag{69}$$

da Cruz et al. (2005) in 2D simulations of the direct shear test using discs observed a similar relationship that is between the friction coefficient of the samples, $\mu = \frac{\tau}{\sigma}$ (τ and σ are shear and normal stress values at the shear surface, respectively), and the inertial number, I, in the form of $\mu = \mu_0 + K.I$ where μ_0 is the minimum value of the friction coefficient that occurs in quasi-static conditions. A definition for the inertial number can be found in Chapter 2. A relationship similar to the latter equation was also reported by Kuwano et al. (2013) from experimental tests on both spherically and angularly shaped quartz particles.

By letting $I_{Mom} = 0$ in Eq. (70) one gets $\phi = \phi_{QS}$. Since the imbalance is almost zero at $\phi = \phi_{QS}$, ϕ_{QS} is called quasi-static peak friction angle. If $I_{Mom} > 0$ and $\xi > \xi_{opt}$, the value obtained for the peak friction angle is higher than ϕ_{QS}, else if $I_{Mom} > 0$ and $\xi < \xi_{opt}$, the value obtained for the peak friction angle is lower than ϕ_{QS}, and thus it is incorrect.

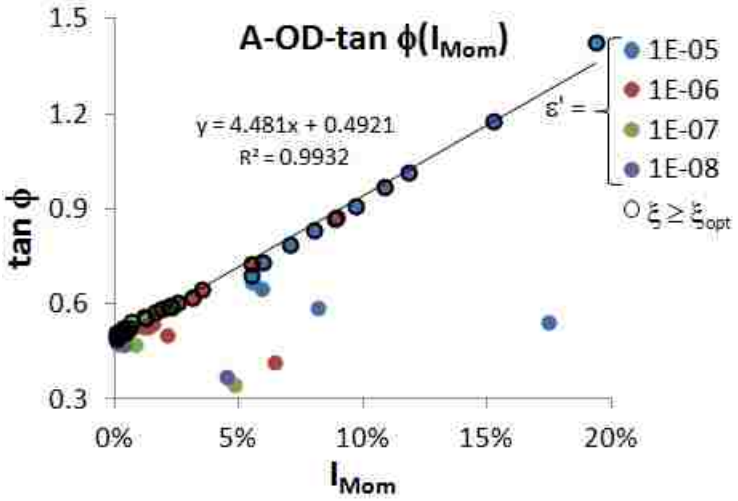

Fig. 51 Peak friction coefficient of assembly versus moment index for Sample A with old damping model at different dimensionless strain rates

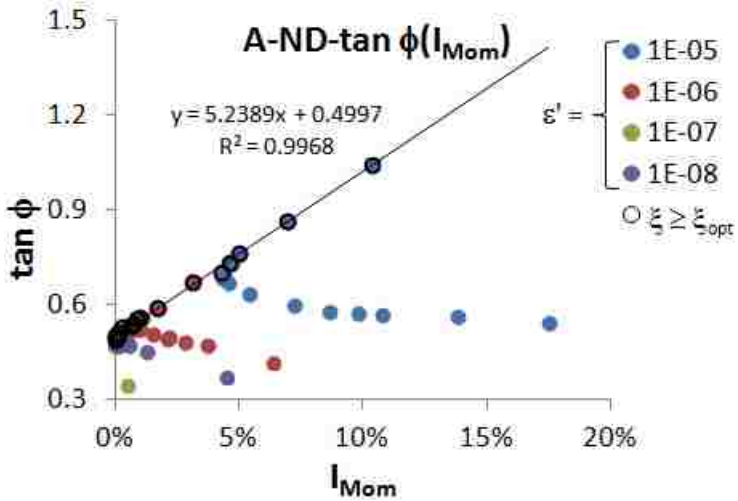

Fig. 52 Peak friction coefficient of assembly versus moment index for Sample A with new damping model at different dimensionless strain rates

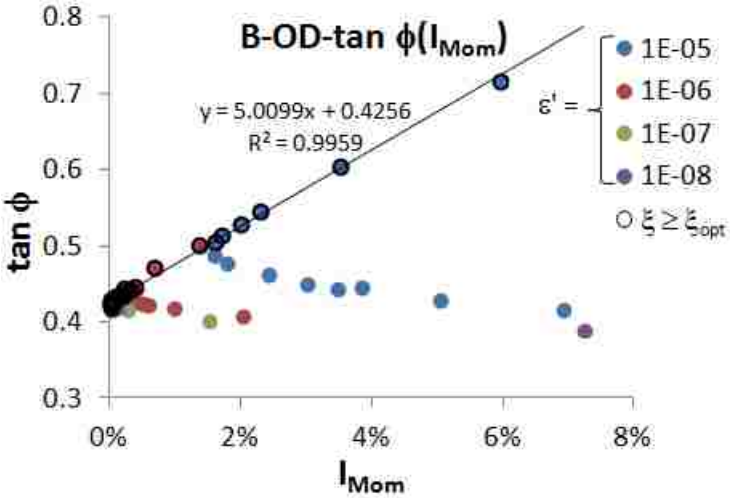

Fig. 53 Peak friction coefficient of assembly versus moment index for Sample B with old damping model at different dimensionless strain rates

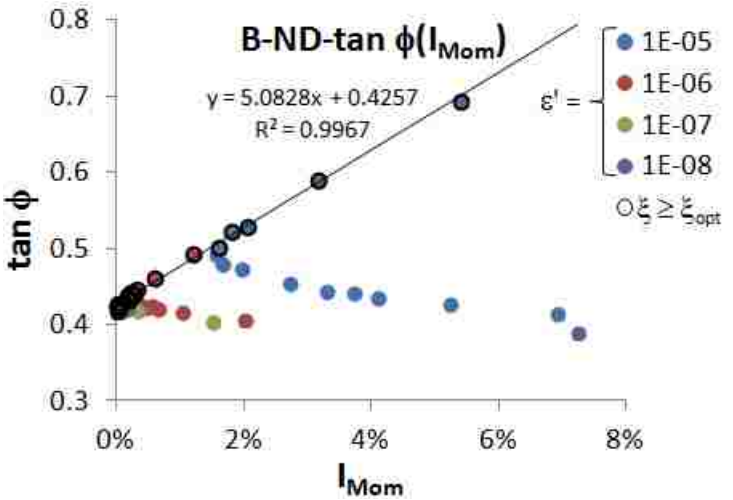

Fig. 54 Peak friction coefficient of assembly versus moment index for Sample B with new damping model at different dimensionless strain rates

Usually, the quasi-static strain-rate limit is significantly small and leads to long simulation runtimes. If the peak friction coefficient of an assembly of particles is aimed to be determined at quasi-static conditions, instead of the application of the quasi-static strain rate to the model, one can alternatively run several simulations in drained conditions with different damping ratios with a certain strain rate selected significantly higher than the quasi-static strain rate. Then, the optimum damping ratio is determined at

that strain rate. After that, a straight line can be passed through the data points of $\xi \geq \xi_{opt}$ in the chart of $\tan\phi_{Peak}$ versus I_{Mom}. By letting $I_{Mom} = 0$ in the equation of this line, the intercept value is obtained that is the "quasi-static" peak friction coefficient.

For example, this procedure was followed for A-OD and A-ND models with $\varepsilon' = 10^{-6}$, and for B-OD and B-ND models with $\varepsilon' = 10^{-5}$. These dimensionless strain rate values are significantly higher than ε'_{QS} values of the models presented in Table 13. The approximated peak friction angles – shown in Table 15 next to the values that were directly obtained from the simulations – indicate a remarkable accuracy that is sufficient for practical uses.

Table 15 Approximate friction angle of Samples A and B at quasi-static strain rates using old and new damping models with optimum damping ratios and the values from independent simulations

	ϕ_{QS} (degree)		
Model	**Test**	**Approx.**	**Error**
A-OD	26.5	26.6	0.4%
A-ND	26.0	26.6	2.3%
B-OD	23.2	23.3	0.4%
B-ND	22.9	23.2	1.3%

In the second series of the numerical tests in Chapter 3, it was observed that when $\xi\varepsilon'$ was equal for the models made from a sample that were subjected to the undrained loading conditions with different ξ and ε' values, the obtained mechanical behaviors of the models were the same. However, it was emphasized that the observation was limited to a certain range of the parameters. Here, it is aimed to track the same phenomenon for the models in this chapter under the drained loading conditions. The data in Table 50 are reorganized, by bundling the samples with equal $\xi\varepsilon'$ values in the same groups, and presented in Table 16, Table 17, Table 18, and Table 19. The highlighted rows indicate

the models with $\xi \geq \xi_{opt}$ in each group. Evidently, the highlighted models in each group exhibit the same behavior as indicated by comparing ϕ_{max}, ε_{Peak}, and I_{Mom} values in the table.

Table 16 List of models with equal $\xi\varepsilon'$ value for Sample A with old damping model. Highlighted rows indicate models with damping ratios greater than or equal to the optimum damping ratio.

ξε'	Model	ξ_{opt}	ξ	ε'	ϕ_{max}	ε_{Peak}	I_{Mom}	UFR	E_{kin} (μJ)	E_{kin}/ε'^2 (μJ)
0E+00	A5-WD-0.00	0.137%	0.00%	1E-05	28.54	0.24%	17.466%	5.074%	5.32E+05	5.32E+15
	A6-WD-0.00	0.160%	0.00%	1E-06	22.66	0.84%	6.361%	1.421%	2.53E+04	2.53E+16
	A7-WD-0.00	0.220%	0.00%	1E-07	19.13	1.00%	4.770%	0.839%	2.02E+03	2.02E+17
	A8-WD-0.00	0.261%	0.00%	1E-08	20.52	10.00%	4.481%	0.642%	9.04E+02	9.04E+18
5E-11	A7-OD-0.05	0.220%	0.05%	1E-07	25.38	2.16%	0.753%	0.352%	3.29E+02	3.29E+16
	A8-OD-0.50	0.261%	0.50%	1E-08	26.91	2.44%	0.049%	0.038%	1.56E+00	1.56E+16
1E-10	A7-OD-0.10	0.220%	0.10%	1E-07	26.21	2.48%	0.276%	0.226%	1.92E+02	1.92E+16
	A8-OD-1.00	0.261%	1.00%	1E-08	26.90	1.88%	0.093%	0.074%	1.15E+00	1.15E+16
2E-10	A7-OD-0.20*	0.220%	0.20%	1E-07	27.35	2.28%	0.219%	0.197%	1.12E+02	1.12E+16
	A8-OD-2.00	0.261%	2.00%	1E-08	26.98	2.12%	0.171%	0.139%	9.12E-01	9.12E+15
5E-10	A6-OD-0.05	0.160%	0.05%	1E-06	26.68	2.40%	2.074%	0.961%	7.88E+03	7.88E+15
	A7-OD-0.50	0.220%	0.50%	1E-07	26.93	2.12%	0.392%	0.329%	6.80E+01	6.80E+15
	A8-OD-5.00	0.261%	5.00%	1E-08	27.23	1.92%	0.378%	0.322%	6.43E-01	6.43E+15
1E-09	A6-OD-0.10	0.160%	0.10%	1E-06	28.27	2.24%	1.494%	1.051%	5.58E+03	5.58E+15
	A7-OD-1.00	0.220%	1.00%	1E-07	28.59	2.16%	0.673%	0.578%	5.00E+01	5.00E+15
2E-09	A6-OD-0.20	0.160%	0.20%	1E-06	28.98	2.44%	1.214%	1.066%	3.72E+03	3.72E+15
	A7-OD-2.00	0.220%	2.00%	1E-07	29.19	2.24%	1.163%	1.034%	3.80E+01	3.80E+15
5E-09	A5-OD-0.05	0.137%	0.05%	1E-05	30.52	2.32%	8.114%	3.039%	2.33E+05	2.33E+15
	A6-OD-0.50	0.160%	0.50%	1E-06	30.57	2.16%	2.263%	2.043%	2.43E+03	2.43E+15
	A7-OD-5.00	0.220%	5.00%	1E-07	30.67	2.04%	2.204%	2.067%	2.35E+01	2.35E+15
1E-08	A5-OD-0.10	0.137%	0.10%	1E-05	33.08	1.92%	5.864%	3.220%	1.78E+05	1.78E+15
	A6-OD-1.00	0.160%	1.00%	1E-06	32.94	1.92%	3.500%	3.314%	1.67E+03	1.67E+15
2E-08	A5-OD-0.20	0.137%	0.20%	1E-05	36.17	2.12%	5.947%	4.650%	1.25E+05	1.25E+15
	A6-OD-2.00	0.160%	2.00%	1E-06	35.92	2.04%	5.501%	5.252%	1.24E+03	1.24E+15
5E-08	A5-OD-0.50	0.137%	0.50%	1E-05	41.15	2.28%	8.894%	8.457%	8.10E+04	8.10E+14
	A6-OD-5.00	0.160%	5.00%	1E-06	41.00	2.28%	8.837%	8.601%	7.99E+02	7.99E+14

*$\xi \geq \xi_{opt}$ is approximately fulfilled.

Table 17 List of models with equal $\xi\varepsilon'$ value for Sample A with new damping model. Highlighted rows indicate models with damping ratios greater than or equal to the optimum damping ratio.

$\xi\varepsilon'$	Model	ξ_{opt}	ξ	ε'	ϕ_{max}	ε_{Peak}	I_{Mom}	UFR	E_{kin} (μJ)	E_{kin}/ε'^2 (μJ)
0E+00	A5-WD-0.00	0.54%	0.00%	1.E-05	28.54	0.24%	17.466%	5.074%	5.32E+05	5.32E+15
	A6-WD-0.00	0.50%	0.00%	1.E-06	22.66	0.84%	6.361%	1.421%	2.53E+04	2.53E+16
	A7-WD-0.00	0.51%	0.00%	1.E-07	19.13	1.00%	4.770%	0.839%	2.02E+03	2.02E+17
	A8-WD-0.00	0.53%	0.00%	1.E-08	20.52	10.00%	4.481%	0.642%	9.04E+02	9.04E+18
5E-11	A7-ND-0.05	0.51%	0.05%	1.E-07	25.20	1.92%	1.990%	0.659%	6.44E+02	6.44E+16
	A8-ND-0.50	0.53%	0.50%	1.E-08	25.56	1.96%	0.015%	0.014%	2.33E+00	2.33E+16
1E-10	A7-ND-0.10	0.51%	0.10%	1.E-07	25.64	0.76%	1.126%	0.515%	4.03E+02	4.03E+16
	A8-ND-1.00	0.53%	1.00%	1.E-08	26.50	2.68%	0.020%	0.021%	1.55E+00	1.55E+16
2E-10	A7-ND-0.20	0.51%	0.20%	1.E-07	26.12	2.36%	0.528%	0.386%	2.53E+02	2.53E+16
	A8-ND-2.00	0.53%	2.00%	1.E-08	26.34	2.52%	0.038%	0.039%	1.30E+00	1.30E+16
5E-10	A6-ND-0.05	0.50%	0.05%	1.E-06	25.35	1.72%	3.702%	1.369%	1.22E+04	1.22E+16
	A7-ND-0.50*	0.51%	0.50%	1.E-07	27.05	2.28%	0.094%	0.103%	9.49E+01	9.49E+15
	A8-ND-5.00	0.53%	5.00%	1.E-08	26.74	2.52%	0.092%	0.101%	1.11E+00	1.11E+16
1E-09	A6-ND-0.10	0.50%	0.10%	1.E-06	25.87	1.84%	2.811%	1.357%	9.68E+03	9.68E+15
	A7-ND-1.00	0.51%	1.00%	1.E-07	27.28	1.88%	0.162%	0.178%	7.51E+01	7.51E+15
2E-09	A6-ND-0.20	0.50%	0.20%	1.E-06	26.95	2.40%	1.492%	1.124%	6.98E+03	6.98E+15
	A7-ND-2.00	0.51%	2.00%	1.E-07	27.83	2.24%	0.294%	0.343%	6.20E+01	6.20E+15
5E-09	A5-ND-0.05	0.54%	0.05%	1.E-05	29.49	0.24%	13.801%	4.832%	3.49E+05	3.49E+15
	A6-ND-0.50	0.50%	0.50%	1.E-06	28.16	2.28%	0.713%	0.785%	4.26E+03	4.26E+15
	A7-ND-5.00	0.51%	5.00%	1.E-07	28.23	2.24%	0.613%	0.714%	4.18E+01	4.18E+15
1E-08	A5-ND-0.10	0.54%	0.10%	1.E-05	29.73	0.24%	10.750%	4.983%	3.02E+05	3.02E+15
	A6-ND-1.00	0.50%	1.00%	1.E-06	29.16	2.36%	1.039%	1.250%	3.14E+03	3.14E+15
2E-08	A5-ND-0.20	0.54%	0.20%	1.E-05	30.98	1.80%	7.216%	5.246%	2.32E+05	2.32E+15
	A6-ND-2.00	0.50%	2.00%	1.E-06	30.66	1.96%	1.701%	2.056%	2.24E+03	2.24E+15
5E-08	A5-ND-0.50*	0.54%	0.50%	1.E-05	34.51	2.12%	4.311%	4.786%	1.53E+05	1.53E+15
	A6-ND-5.00	0.50%	5.00%	1.E-06	33.99	2.04%	3.125%	3.812%	1.51E+03	1.51E+15

*$\xi \geq \xi_{opt}$ is approximately fulfilled.

Table 18 List of models with equal $\xi\varepsilon'$ value for Sample B with old damping model. Highlighted rows indicate models with damping ratios greater than or equal to the optimum damping ratio.

$\xi\varepsilon'$	Model	ξ_{opt}	ξ	ε'	ϕ_{max}	ε_{Peak}	I_{Mom}	UFR	E_{kin} (μJ)	E_{kin}/ε'^2 (μJ)
0E+00	B5-WD-0.00	0.44%	0.00%	1.E-05	22.55	3.32%	6.908%	17.187%	1.63E+06	1.63E+16
	B6-WD-0.00	0.34%	0.00%	1.E-06	22.16	6.60%	2.017%	4.603%	4.61E+04	4.61E+16
	B7-WD-0.00	0.33%	0.00%	1.E-07	21.93	1.12%	1.492%	2.744%	3.57E+03	3.57E+17
	B8-WD-0.00	0.34%	0.00%	1.E-08	21.35	9.16%	7.242%	17.083%	3.30E+04	3.30E+20
5E-11	B7-OD-0.05	0.33%	0.05%	1.E-07	22.65	2.52%	0.247%	0.559%	6.16E+02	6.16E+16
	B8-OD-0.50	0.34%	0.50%	1.E-08	23.06	4.12%	0.002%	0.006%	2.67E+00	2.67E+16
1E-10	B7-OD-0.10	0.33%	0.10%	1.E-07	22.93	2.40%	0.099%	0.245%	4.38E+02	4.38E+16
	B8-OD-1.00	0.34%	1.00%	1.E-08	23.00	3.48%	0.005%	0.012%	2.56E+00	2.56E+16
2E-10	B7-OD-0.20	0.33%	0.20%	1.E-07	22.88	3.60%	0.037%	0.094%	3.20E+02	3.20E+16
	B8-OD-2.00	0.34%	2.00%	1.E-08	22.82	5.08%	0.010%	0.024%	2.52E+00	2.52E+16
5E-10	B6-OD-0.05	0.34%	0.05%	1.E-06	22.70	5.04%	0.957%	2.409%	2.94E+04	2.94E+16
	B7-OD-0.50	0.33%	0.50%	1.E-07	23.09	3.52%	0.025%	0.062%	2.17E+02	2.17E+16
	B8-OD-5.00	0.34%	5.00%	1.E-08	22.92	5.60%	0.024%	0.059%	2.17E+00	2.17E+16
1E-09	B6-OD-0.10	0.34%	0.10%	1.E-06	22.96	3.12%	0.574%	1.488%	2.33E+04	2.33E+16
	B7-OD-1.00	0.33%	1.00%	1.E-07	22.95	2.00%	0.047%	0.116%	1.85E+02	1.85E+16
2E-09	B6-OD-0.20	0.34%	0.20%	1.E-06	23.16	2.52%	0.275%	0.697%	1.84E+04	1.84E+16
	B7-OD-2.00	0.33%	2.00%	1.E-07	23.41	3.40%	0.089%	0.220%	1.59E+02	1.59E+16
5E-09	B5-OD-0.05	0.44%	0.05%	1.E-05	23.20	3.24%	5.029%	12.793%	1.29E+06	1.29E+16
	B6-OD-0.50	0.34%	0.50%	1.E-06	23.60	3.88%	0.219%	0.535%	1.32E+04	1.32E+16
	B7-OD-5.00	0.33%	5.00%	1.E-07	23.90	3.20%	0.205%	0.502%	1.28E+02	1.28E+16
1E-08	B5-OD-0.10	0.44%	0.10%	1.E-05	24.02	3.56%	3.846%	9.919%	1.13E+06	1.13E+16
	B6-OD-1.00	0.34%	1.00%	1.E-06	23.98	2.60%	0.381%	0.930%	1.08E+04	1.08E+16
2E-08	B5-OD-0.20	0.44%	0.20%	1.E-05	24.79	3.44%	2.411%	6.231%	9.05E+05	9.05E+15
	B6-OD-2.00	0.34%	2.00%	1.E-06	25.19	4.04%	0.671%	1.640%	8.57E+03	8.57E+15
5E-08	B5-OD-0.50	0.44%	0.50%	1.E-05	26.74	3.36%	1.610%	3.938%	6.28E+05	6.28E+15
	B6-OD-5.00	0.34%	5.00%	1.E-06	26.56	3.00%	1.361%	3.332%	6.08E+03	6.08E+15

Table 19 List of models with equal $\xi\varepsilon'$ value for Sample B with new damping model. Highlighted rows indicate models with damping ratios greater than or equal to the optimum damping ratio.

$\xi\varepsilon'$	Model	ξ_{opt}	ξ	ε'	ϕ_{max}	ε_{Peak}	I_{Mom}	UFR	E_{kin} (μJ)	E_{kin}/ε'^2 (μJ)
0E+00	B5-WD-0.00	0.52%	0.00%	1.E-05	22.55	3.32%	6.908%	17.187%	1.63E+06	1.63E+16
	B6-WD-0.00	0.40%	0.00%	1.E-06	22.16	6.60%	2.017%	4.603%	4.61E+04	4.61E+16
	B7-WD-0.00	0.40%	0.00%	1.E-07	21.93	1.12%	1.492%	2.744%	3.57E+03	3.57E+17
	B8-WD-0.00	0.41%	0.00%	1.E-08	21.35	9.16%	7.242%	17.083%	3.30E+04	3.30E+20
5E-11	B7-ND-0.05	0.40%	0.05%	1.E-07	22.69	3.76%	0.308%	0.647%	6.48E+02	6.48E+16
	B8-ND-0.50	0.41%	0.50%	1.E-08	22.93	3.32%	0.002%	0.005%	2.75E+00	2.75E+16
1E-10	B7-ND-0.10	0.40%	0.10%	1.E-07	22.81	3.16%	0.129%	0.306%	5.15E+02	5.15E+16
	B8-ND-1.00	0.41%	1.00%	1.E-08	22.71	3.64%	0.004%	0.010%	2.68E+00	2.68E+16
2E-10	B7-ND-0.20	0.40%	0.20%	1.E-07	22.99	4.56%	0.043%	0.108%	3.15E+02	3.15E+16
	B8-ND-2.00	0.41%	2.00%	1.E-08	23.10	2.52%	0.008%	0.021%	2.64E+00	2.64E+16
5E-10	B6-ND-0.05	0.40%	0.05%	1.E-06	22.66	3.96%	1.021%	2.563%	2.98E+04	2.98E+16
	B7-ND-0.50	0.40%	0.50%	1.E-07	23.06	4.04%	0.023%	0.057%	2.29E+02	2.29E+16
	B8-ND-5.00	0.41%	5.00%	1.E-08	23.10	3.44%	0.021%	0.051%	2.17E+00	2.17E+16
1E-09	B6-ND-0.10	0.40%	0.10%	1.E-06	22.91	3.76%	0.648%	1.682%	2.45E+04	2.45E+16
	B7-ND-1.00	0.40%	1.00%	1.E-07	23.05	2.80%	0.040%	0.100%	1.92E+02	1.92E+16
2E-09	B6-ND-0.20	0.40%	0.20%	1.E-06	23.28	4.76%	0.326%	0.838%	1.91E+04	1.91E+16
	B7-ND-2.00	0.40%	2.00%	1.E-07	23.23	3.76%	0.077%	0.190%	1.64E+02	1.64E+16
5E-09	B5-ND-0.05	0.52%	0.05%	1.E-05	23.22	3.20%	5.228%	13.277%	1.32E+06	1.32E+16
	B6-ND-0.50	0.40%	0.50%	1.E-06	23.53	2.96%	0.201%	0.493%	1.41E+04	1.41E+16
	B7-ND-5.00	0.40%	5.00%	1.E-07	23.66	2.92%	0.177%	0.441%	1.35E+02	1.35E+16
1E-08	B5-ND-0.10	0.52%	0.10%	1.E-05	23.58	2.64%	4.110%	10.591%	1.16E+06	1.16E+16
	B6-ND-1.00	0.40%	1.00%	1.E-06	24.05	3.32%	0.329%	0.809%	1.12E+04	1.12E+16
2E-08	B5-ND-0.20	0.52%	0.20%	1.E-05	24.48	3.32%	2.717%	7.051%	9.52E+05	9.52E+15
	B6-ND-2.00	0.40%	2.00%	1.E-06	24.75	3.68%	0.586%	1.449%	9.09E+03	9.09E+15
5E-08	B5-ND-0.50*	0.52%	0.50%	1.E-05	26.28	4.04%	1.567%	3.888%	6.67E+05	6.67E+15
	B6-ND-5.00	0.40%	5.00%	1.E-06	26.22	3.68%	1.202%	2.959%	6.48E+03	6.48E+15

*$\xi \geq \xi_{opt}$ is approximately fulfilled.

For example, the responses of Models B5-OD-0.05, B6-OD-0.50, and B7-OD-5.00, which have equal $\xi\varepsilon'$ value of 5×10^{-9}, are presented in Fig. 55, Fig. 56, Fig. 57, Fig. 58, and Fig. 59. Note that for Model B5-OD-0.05, we have $\xi < \xi_{opt}$, while for Models B6-OD-0.50 and B7-OD-5.00 we have $\xi > \xi_{opt}$. Fig. 55 shows that B6-OD-0.50 and B7-OD-5.00 produce the same maximum friction angle, while B5-OD-0.05 shows a lower peak friction angle. Fig. 56 shows that B6-OD-0.50 and B7-OD-5.00 exhibit almost the same volumetric behavior, while B5-OD-0.05 shows less dilative behavior. Fig. 57 indicates that B6-OD-0.50 and B7-OD-5.00 show the same coordination number whereas B5-OD-0.05 shows a lower coordination number. Fig. 58 shows that B5-OD-0.05 has a much higher moment index than B6-OD-0.50 and B7-OD-5.00, which exhibit equal moment indices.

In Table 18, it is evident that the kinetic energy is distinctively different for the three models. However, Fig. 59 indicates that the normalized kinetic energy values by the square of the dimensionless strain rates are virtually the same for the three models, implying that in each model, the particle velocities are proportional to the square of the dimensionless strain rate of that model with the same coefficient of proportionality. This is despite the fact that Model B5-OD-0.05, with a damping ratio less than the optimum value, displays a remarkably different behavior from B6-OD-0.50 and B7-OD-5.00. The same phenomenon is also observed for the other models belonging to the same group in Table 16, Table 17, Table 18, and Table 19 for both samples with both damping models.

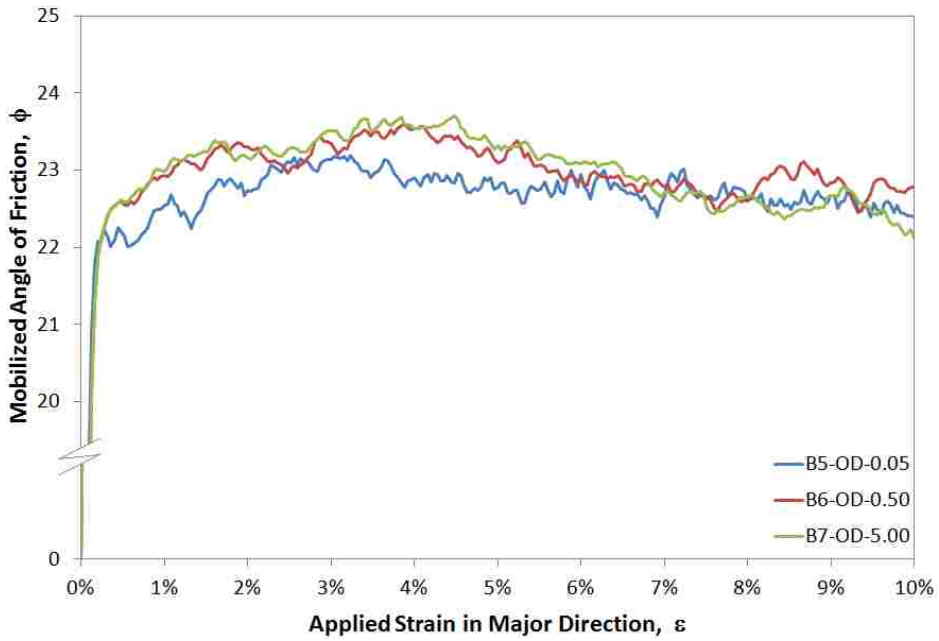

Fig. 55 Friction angle of models with equal $\xi\varepsilon'$ values evolved with applied strain. Blue indicates the model with $\xi < \xi_{opt}$; red and green indicate the models with $\xi > \xi_{opt}$.

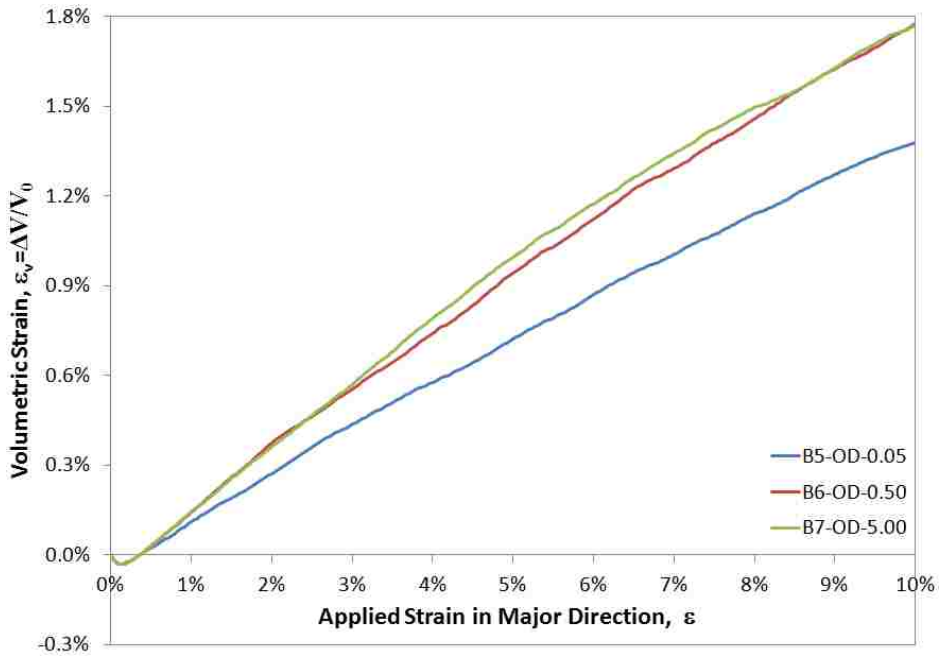

Fig. 56 Volumetric strain of models with equal $\xi\varepsilon'$ values evolved with applied strain. Blue indicates the model with $\xi < \xi_{opt}$; red and green indicate the models with $\xi > \xi_{opt}$.

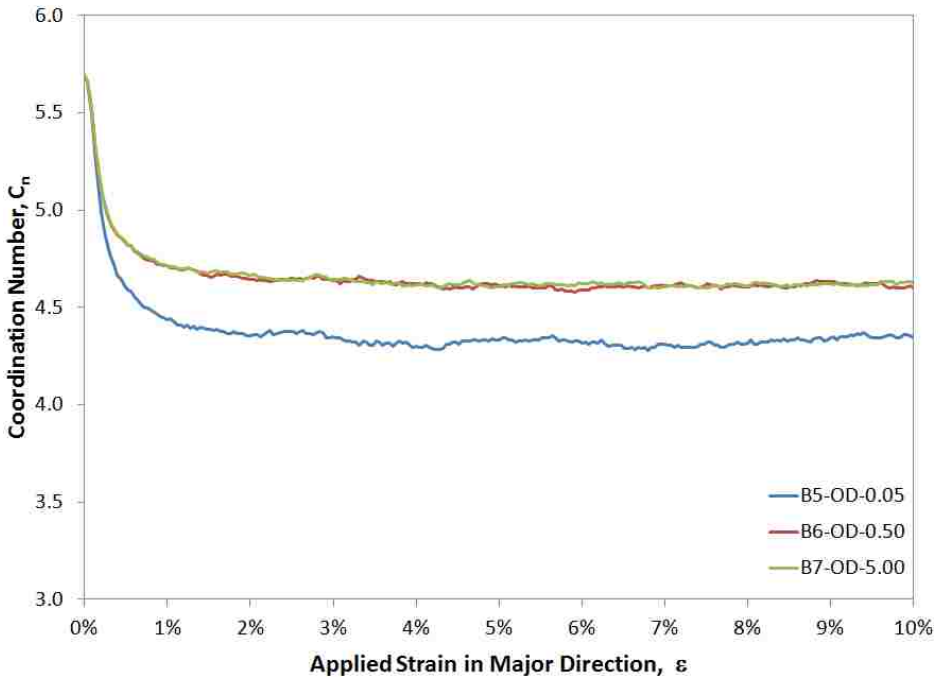

Fig. 57 Coordination number of models with equal $\xi\varepsilon'$ values evolved with applied strain. Blue indicates the model with $\xi < \xi_{opt}$; red and green indicate the models with $\xi > \xi_{opt}$.

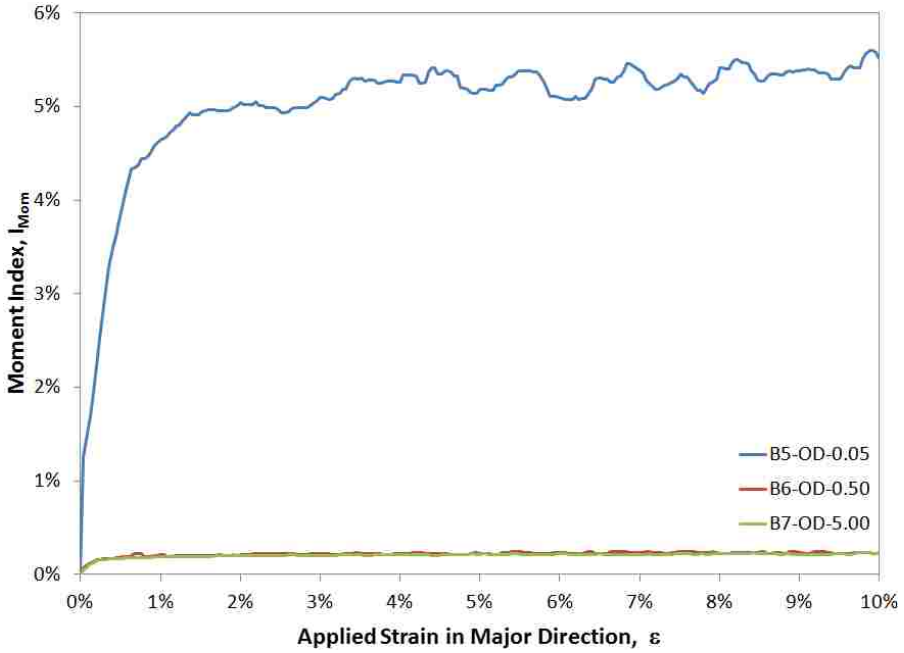

Fig. 58 Moment index of models with equal $\xi\varepsilon'$ values evolved with applied strain. Blue indicates the model with $\xi < \xi_{opt}$; red and green indicate the models with $\xi > \xi_{opt}$.

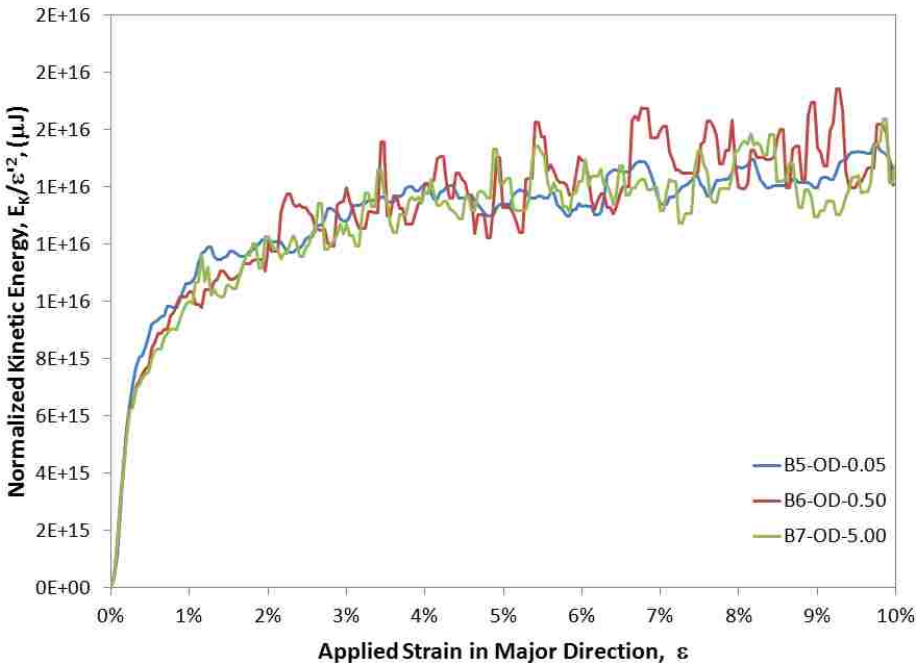

Fig. 59 Kinetic energy normalized by the squared of the dimensionless strain rate for models with equal $\xi\varepsilon'$ values evolved with applied strain. Blue indicates the model with $\xi < \xi_{opt}$; red and green indicate the models with $\xi > \xi_{opt}$.

Therefore, it is concluded that two models with equal values of the product of damping ratio and dimensionless strain rate produce the same response if they are subjected to the damping ratios greater than the optimum damping ratios of each strain rate. However, the particle velocities differ in such models; the model with a higher strain rate has higher particle velocities, and the normalized particle velocities by the square of dimensionless strain rate of each model are the same. Therefore, a model with a dimensionless strain rate equal to ε' and a damping ratio of ξ, excessively higher than the optimum damping ratio, ξ_{opt}, is equivalent to a model with the optimum damping ratio and a higher dimensionless strain rate equal to $\xi\varepsilon'/\xi_{opt}$. On the other hand, a model with a damping ratio that is less than the optimum damping ratio results in a worse equilibrium state than the model with the optimum damping ratio and a lower strength. Consequently,

the determination of the optimum damping ratio in order for the application in DEM models is critical, particularly for the quasi-static analyses.

O'Sullivan (2002) recommended setting the damping to zero during the loading stage. In Fig. 60, Fig. 61, Fig. 62, Fig. 63, Fig. 64, and Fig. 65, the responses of Sample A with zero and 0.2% damping ratio using the old damping model are shown at a strain rate equal to 10^{-8}. Note that $\xi = 0.20\%$ is adequately close to the optimum damping ratio of this model at $\varepsilon' = 10^{-8}$, which is 0.23%. Also, the dimensionless strain rate of 10^{-8} is considered quasi-static, since the upper limit of the dimensionless quasi-static strain rate for this model is 4.38×10^{-8}, as presented in Table 13. Thus, the quasi-static condition is maintained in Model A8-OD-0.20, and the response can be regarded as valid.

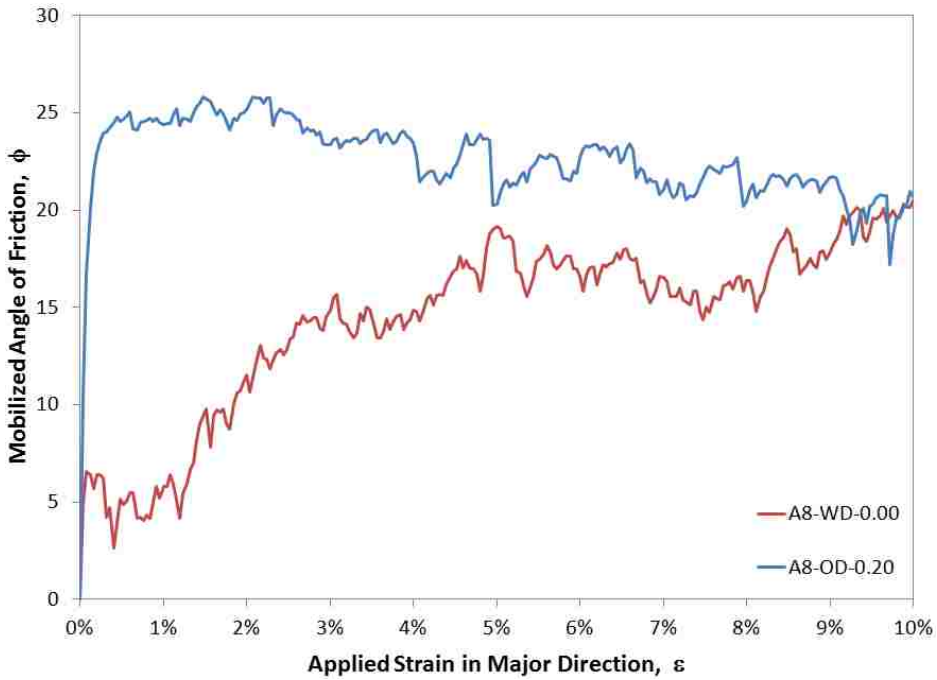

Fig. 60 Friction angle evolved with applied strain for Sample A using old damping model with optimum damping and without damping at quasi-static strain rate

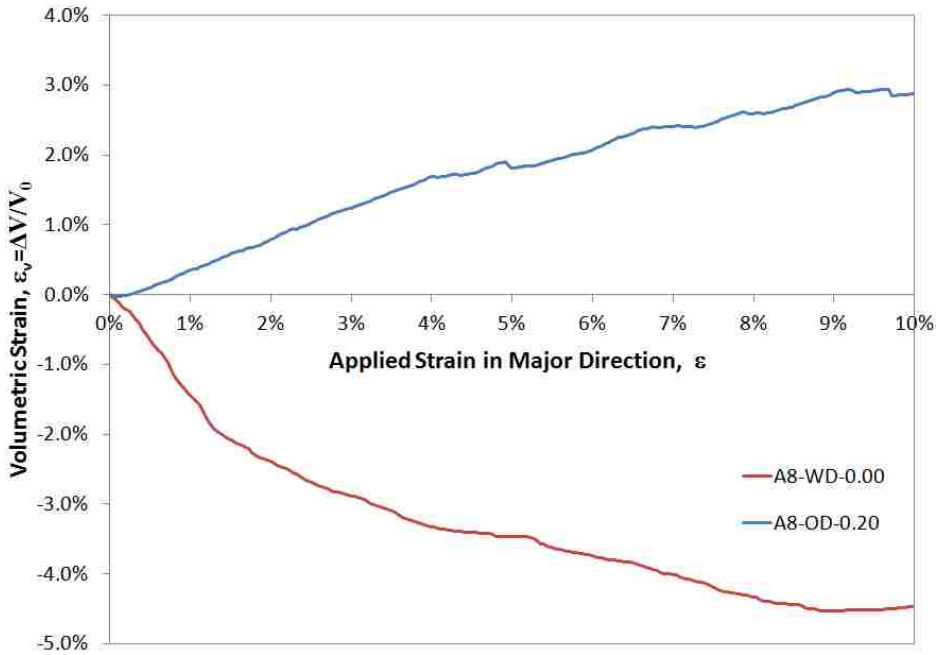

Fig. 61 Volumetric strain evolved with applied strain for Sample A using old damping model with optimum damping and without damping at quasi-static strain rate

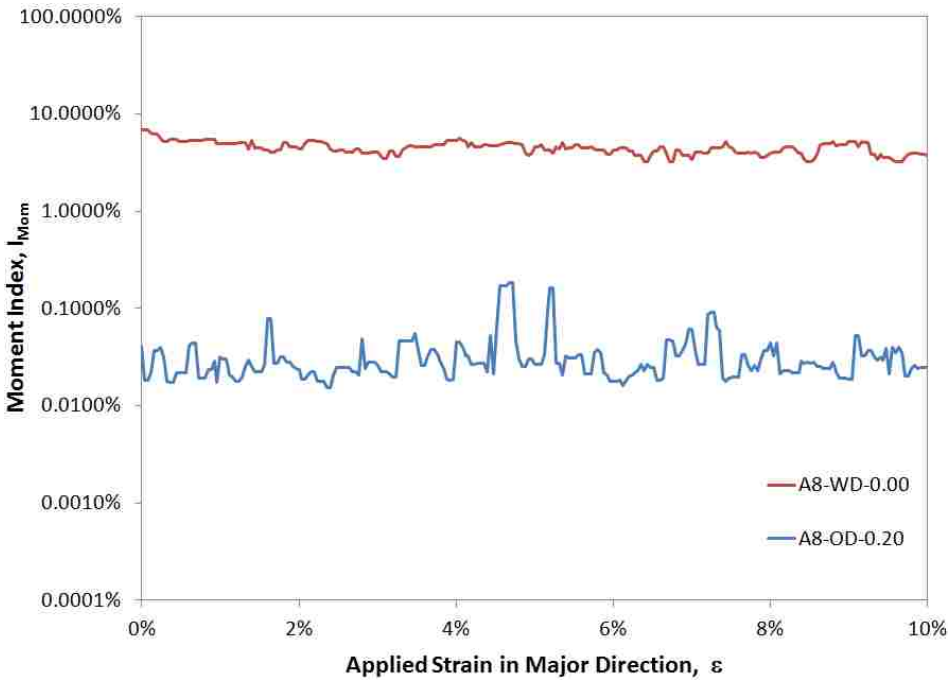

Fig. 62 Moment index evolved with applied strain for Sample A using old damping model with optimum damping and without damping at quasi-static strain rate

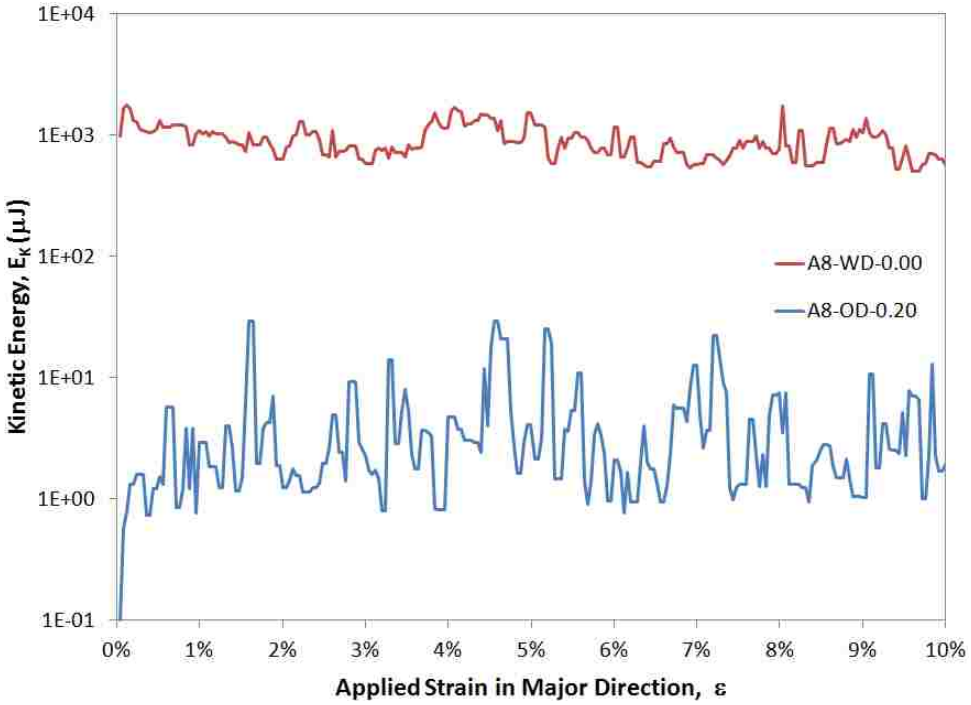

Fig. 63 Kinetic energy evolved with applied strain for Sample A using old damping model with optimum damping and without damping at quasi-static strain rate

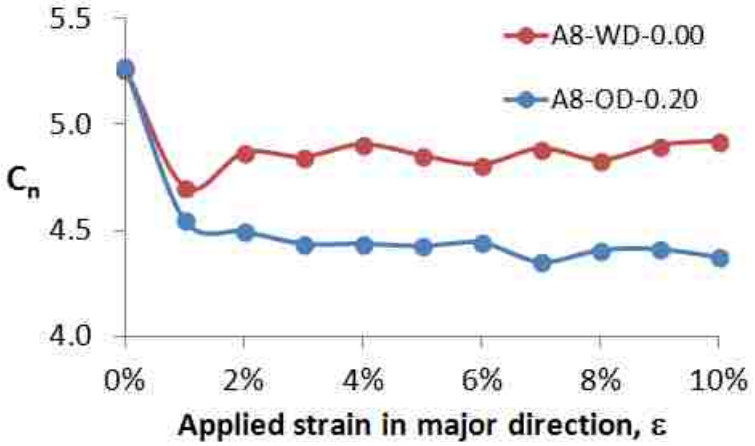

Fig. 64 Coordination number evolved with applied strain for Sample A using old damping model with optimum damping and without damping at quasi-static strain rate

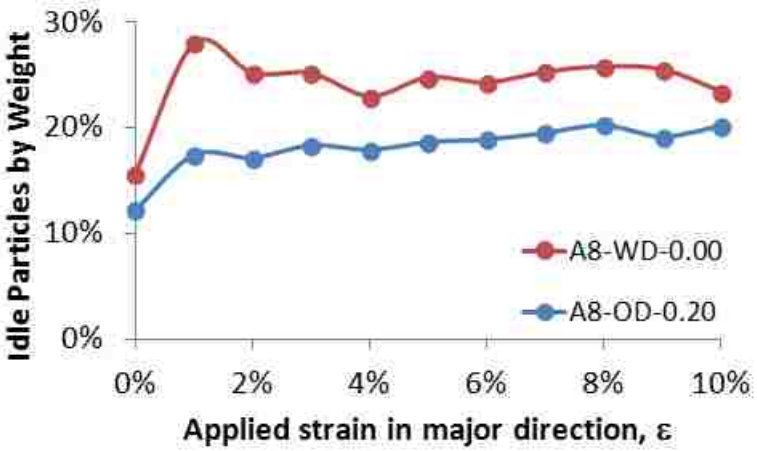

Fig. 65 Idle particles by weight evolved with applied strain for Sample A using old damping model with optimum damping and without damping at quasi-static strain rate

It is observed that if $\xi = 0$ is used, as in Model A8-WD-0.00, the stress-strain behavior becomes much softer, ϕ_{Peak} value becomes less than ϕ_{QS}, I_{Mom} value increases and the imbalance rises, the volumetric behavior becomes contractive rather than dilative, kinetic energy increases as particle velocities increase, the coordination number increases, and the ratio of the idle particles by weight increase. Therefore, setting the damping ratio to zero is not recommended for non-spherical particles as used in the present study.

5.6. Testing the Proposed Damping-Based Approach for Predicting Peak Friction coefficient

Two extra poly-disperse samples of 10,000 particles with different particle size distributions – with properties listed in Table 20, Table 21, Table 22, and Table 23 – were created to test the ability of the proposed approach to approximately predict the "quasi-static" peak friction angle; 18 new simulations were carried out. This approach

was presented in Section 5.5. The initial inter-particle friction of $\mu_0 = 0.4$ was selected. Unlike Samples A and B, Samples C and D are loose, as indicated by the void ratio values presented in Table 21.

Table 20 Properties common between Models C and D

Computation Code	ELLIPSE3D
Particle Shape	Ellipsoid
Aspect Ratio of Particles (R_1/R_2)	1.20
Contact Laws	Simplified Hertz-Mindlin
Boundary Conditions	Periodic
Aspect Ratios of Sample (Cuboid)	1, 1, 1
Sample Preparation Method	Automatic Two-Phase Method
Damping Model	Size Dependent Mass Damping
Number of Particles (n_p)	10,000
Density, ρ (mg/mm^3)	2.65
Elastic Modulus (E) (kPa)	7.2×10^7
Poisson's Ratio (ν)	0.2
Friction Coefficient in Sample Preparation Stage (μ_0), Sample Compaction	0.4 (Loose sample)
Inter-Particle Friction Coefficient in Loading Stage (μ)	0.5
Time Step Ratio (c_t)	0.32
Initial Stress State of Samples	$\sigma_{11} = \sigma_{22} = \sigma_{33} = 288$kPa
Initial Dimensionless Mean Stress ($\bar{\sigma}_{m,ini}$)	-4×10^{-6}
Loading Path	Drained
Final Strain (ε)	50%

Table 21 Unique properties of Samples C and D

Sample Name	C	D
Particle Size Distribution (PSD)	PSD-C	PSD-D
Initial Void Ratio (e_{ini})	0.4987	0.5159

Table 22 Particle size distribution of Sample C

Particle Type Number	Minor Radii (mm)	Major Radius (mm)	Particle Nominal Size (mm)	Number of Particles	Weight Ratio	Accumulated Weight Ratio
1	0.50	0.60	1.06	9234	10%	10%
2	1.50	1.80	3.19	513	15%	25%
3	2.50	3.00	5.31	148	20%	45%
4	3.50	4.20	7.44	67	25%	70%
5	4.50	5.40	9.56	38	30%	100%

Table 23 Particle size distribution of Sample D

Particle Type Number	Minor Radii (mm)	Major Radius (mm)	Particle Nominal Size (mm)	Number of Particles	Weight Ratio	Accumulated Weight Ratio
1	0.75	0.90	1.59	7937	23%	23%
2	1.25	1.50	2.66	1565	21%	44%
3	2.00	2.40	4.25	364	20%	64%
4	3.00	3.60	6.38	102	19%	83%
5	4.25	5.10	9.03	32	17%	100%

In order to estimate the peak friction angle of the assemblies in quasi-static conditions, a relatively high dimensionless strain rate of $\varepsilon' = 10^{-6}$ was selected for both samples. Using the size-dependent damping model, different damping ratios ranging from 0.05% to 10% were applied and the samples were subjected to triaxial loading in drained conditions by keeping the lateral stress at 288 kPa. The output data points were acquired at every 0.04% strain. The moment index values were averaged from the initial condition up to the point associated with the peak friction angle. Applying a relatively high strain of 50% in the major direction ensured that the maximum friction angle was mobilized in each sample.

The moment index values and peak friction angles obtained for each damping ratio are presented in Table 24 and Table 25 for Samples C and D, respectively, and the

variation of the moment index with the damping ratio is shown in Fig. 66 and Fig. 67. The optimum value for the damping ratio was determined for each sample by interpolation and is shown in Table 26. It was observed that the minimum imbalance (in terms of the moment index) is achieved at about $\xi = 0.5\%$ for both samples, which is similar to Models A and B with the new damping model.

Table 24 Moment index and mobilized friction angle for Sample C with different damping ratios at $\varepsilon' = 10^{-6}$

ξ	0.05%	0.10%	0.20%	0.40%	0.50%	1.00%	2.00%	5.00%	10.00%
I_{Mom}	5.22%	3.53%	1.88%	1.23%	1.24%	1.79%	2.28%	3.89%	5.64%
ϕ_{Peak} (degree)	22.47	23.99	22.88	22.90	23.29	24.43	26.27	30.56	34.63

Table 25 Moment index and mobilized friction angle for Sample D with different damping ratios at $\varepsilon' = 10^{-6}$

ξ	0.05%	0.10%	0.20%	0.40%	0.50%	1.00%	2.00%	5.00%	10.00%
I_{Mom}	3.07%	2.01%	1.14%	0.64%	0.62%	0.84%	1.32%	2.22%	3.34%
ϕ_{Peak} (degree)	21.18	20.64	21.10	20.90	21.42	22.32	23.61	25.97	29.30

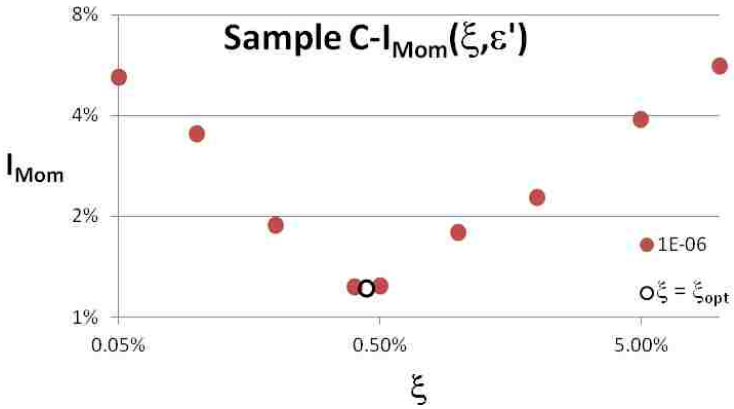

Fig. 66 Moment index versus damping ratio for Sample C

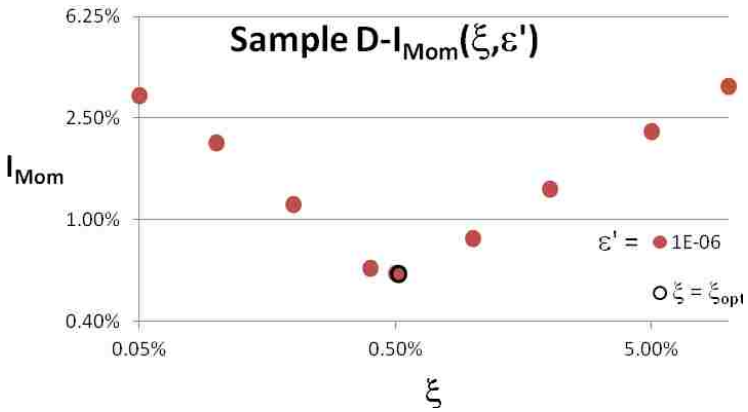

Fig. 67 Moment index versus damping ratio for Sample D

Table 26 Optimum damping ratio for Models C and D at $\varepsilon' = 10^{-6}$

Sample	ξ_{opt}
C	0.441%
D	0.509%

The peak friction coefficient of each assembly versus the moment index value is shown in Fig. 68 and Fig. 69. The trends observed for Samples C and D are similar to those of Samples A and B. For $\xi \geq \xi_{opt}$, a straight line was fitted to data points for each sample, as shown in Fig. 68 and Fig. 69. The coefficients of determination (R^2 values in Fig. 68 and Fig. 69) are very close to unity, indicating that the locus of the data points are sufficiently close to a straight line. The intercept values of the lines (i.e., $\tan\phi$ at $I_{Mom} = 0$) indicate the approximate peak friction coefficients of the samples at quasi-static strain rates, as presented in Table 30

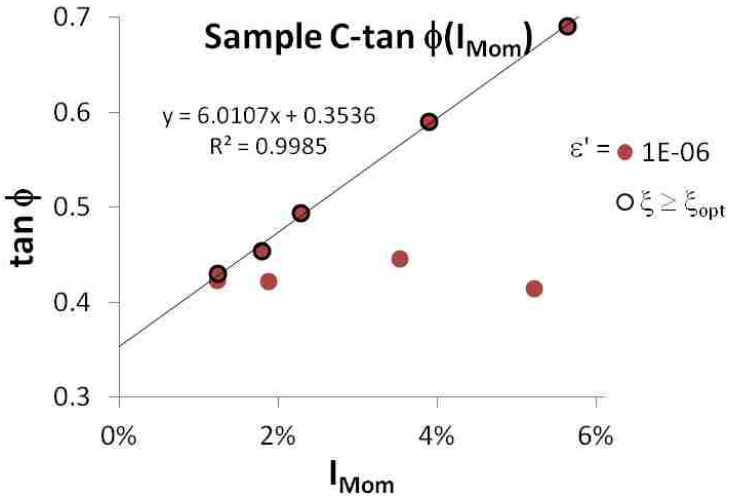

Fig. 68 Peak friction coefficient of assembly versus moment index and interpretation of quasi-static friction coefficient for Sample C

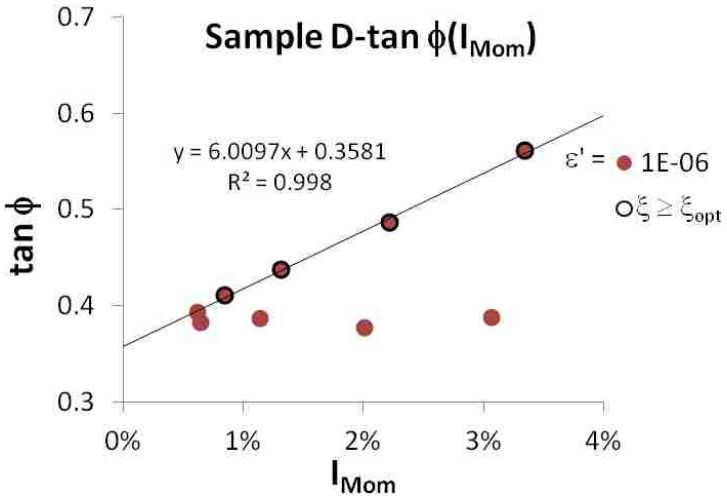

Fig. 69 Peak friction coefficient of assembly versus moment index and interpretation of quasi-static friction coefficient for Sample D

It should be mentioned that in the first try, the damping ratio was selected in a range from 0.05% to 0.8%. The first try was not good, since the data points in the $\tan\phi - I_{Mom}$ curves were not adequately spaced apart and the line fitting was not successful. Therefore, it is important to choose relatively high damping ratios for the purpose of the approximation.

Moreover, the peak friction angles were determined through a direct approach for each model. Samples C and D were subjected to the dimensionless strain rates of 10^{-5}, 10^{-6}, 10^{-7}, and 10^{-8} with $\xi = 0.5\%$. The moment index values and peak friction angles obtained for each sample at each strain rate are presented in Table 27 and Table 28.

Table 27 Peak friction angle and moment index values for different strain rates with $\xi = 0.5\%$ for Sample C

ε'	10^{-5}	10^{-6}	10^{-7}	10^{-8}
I_{Mom}	6.118%	1.238%	0.200%	0.024%
ϕ_{Peak} (degree)	31.07	23.29	22.32	21.42

Table 28 Peak friction angle and moment index values for different strain rates with $\xi = 0.5\%$ for Sample D

ε'	10^{-5}	10^{-6}	10^{-7}	10^{-8}
I_{Mom}	2.978%	0.618%	0.084%	0.011%
ϕ_{Peak} (degree)	26.34	21.42	20.68	20.20

The moment index versus dimensionless strain rate is shown in log–log scale in Fig. 70 and Fig. 71 for Samples C and D. A straight line was fitted to the data points, which is equivalent to power curves in the normal scales. The dimensionless quasi-static strain rates were determined for each sample based on the $I_{Mom} = 0.1\%$ criterion. The ε'_{QS} values are shown in Table 29 to be compared with the strain rate selected for the approximation procedure, $\varepsilon' = 10^{-6}$. The moment index values are less than 0.1% at $\varepsilon' = 10^{-8}$ for both samples. Thus, the peak friction angles associated with $\varepsilon' = 10^{-8}$ were selected to be compared with the values obtained using the approximation approach.

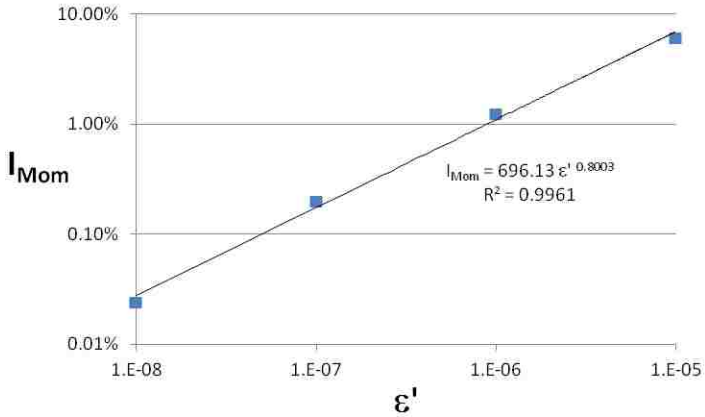

Fig. 70 Average moment index versus dimensionless strain rate for Sample C to interpret the quasi-static strain rate

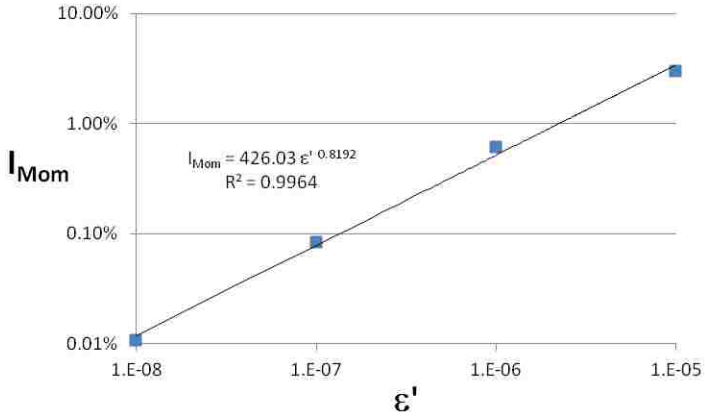

Fig. 71 Average moment index versus dimensionless strain rate for Sample D to interpret the quasi-static strain rate

Table 29 Dimensionless quasi-static rates of Models C and D and runtime saving amount with respect to the selected dimensionless strain rate for approximation, i.e., $\varepsilon' = 10^{-6}$

Sample	ε'_{QS}	Runtime Saving
C	5×10^{-8}	20 times
D	1.3×10^{-7}	8 times

Table 30 presents the approximate peak friction coefficients and the peak friction coefficient values obtained from the direct method. The errors are relatively small. Sample C was subjected to a strain rate 20 times greater than the quasi-static strain rate

that produced 9.1% error, whereas Sample D was subjected to a strain rate eight times greater than its quasi-static strain rate, that yielded only 2.5% error.

Table 30 Peak friction angle of Models C and D using direct and approximate methods

Sample	Exact $\phi_{Peak_{QS}}$	Predicted $\phi_{Peak_{QS}}$	Relative Error
C	21.42	19.47	-9.1%
D	20.20	19.70	-2.5%

Altogether, the proposed approximation approach to predict the peak friction angles of assemblies was tested on Samples A, B, C, and D, which had different particle size distributions and different relative densities. Due to significant runtime saving the outcome seems satisfactory for engineering applications.

5.7. Summary

A new damping model – namely, size-dependent mass-proportional damping – was proposed. For the samples with high particle size disparity, the new damping model indicated a superior performance over the conventional mass damping by exhibiting a lower imbalance at any specific strain rate with respect to the conventional mass-damping model. This helps to elevate the upper limiting quasi-static strain rate, and thus reduces necessary runtime. In the quasi-static loading conditions, the new damping model provided the same behaviors as those simulations using the conventional mass-damping model.

A new index was proposed to quantify the equilibrium state of DEM models – namely, the moment index. The performance of the new index was tested and compared

to an existing index, UFR. The proposed moment index is comparable to UFR in performance.

The optimum mass-damping ratio at a specific strain rate was defined as the mass-damping ratio at which the imbalance of models was minimized. At any specific strain rate, there is a damping value, the optimum damping, above and below which the imbalance state is heightened. The optimum damping ratio was determined for two samples that sheared at different strain rates using either the conventional or the size-dependent mass-damping models.

The optimum damping ratio showed a slight dependency on the particle size distribution of samples and the strain rate at which the samples were sheared. The optimum damping values for the conventional and new damping models at low deformation rates are 0.3% and 0.5%, respectively, for both samples. The value of the optimum damping ratio for the new damping model is slightly higher than that of the old damping model.

It was learned that the equilibrium state of a model worsens as the strain rate increases. A clear power relationship was observed between the moment index value and the strain rate for the models with damping ratios greater than the optimum damping ratio. The moment index that quantifies the imbalance measure of the models depends not only on the strain rate but also on the damping ratio.

The quasi-static strain rate was defined as the upper limit of strain rate for quasi-static simulations using the moment index. The moment index reaches the minimum value at the optimum damping value, so in order to determine the quasi-static strain rate to minimize simulation runtimes, the optimum damping ratio also has to be applied. In

addition, it was found that the quasi-static strain rate is lower for samples with high particle size disparity.

No clear link was detected between the imbalance state of models and the kinetic energy of the particles. The kinetic energy decreases with the increase of the damping ratio and with the decrease of the strain rate monotonically; thus, the kinetic energy cannot spot the optimum damping value and provides no information on the equilibrium state of the models.

It was noticed that when the damping ratio is less than the optimum value, the models behave differently from the models using the optimum damping values. Setting the damping ratio to zero or selecting an excessively low damping ratio for non-spherical particles, as modeled in the present study, results in a lower strength, worse equilibrium state, more contractive volumetric response, higher kinetic energy, and greater number of idle particles in the assembly; therefore, setting the damping ratio to a value lower than the optimum damping ratio is not recommended.

It was observed that the peak friction angle of the assemblies increases with the increase of the strain rate and the damping ratio. Moreover, the peak friction angle is proportional to the product of the damping ratio and the dimensionless strain rate, $\xi\varepsilon'$. However, at very low $\xi\varepsilon'$ values, the peak friction angle is almost constant.

A linear relationship was observed between the peak friction coefficient and the moment index for the models that had a damping ratio above the optimum value. Upon knowing this, an approximation approach was established to estimate the peak friction coefficient by using results of simulations at significantly higher strain rates, necessitating shorter runtimes.

In agreement with the results in Chapter 3, it was discovered that when the product of the damping ratio and the strain rate is constant for a specific model and the damping ratio is greater than the optimum value, the models with any combinations of damping ratio and strain rate present the same mechanical behavior (except for the particle velocities). Therefore, selecting a damping ratio that is excessively higher than the optimum value is equivalent to shearing the same sample at a higher strain rate with the optimum damping ratio, which should be avoided.

CHAPTER 6

Quasi-Static Strain Rate

6.1. Overview

The quasi-static (referred to as QS for brevity hereafter) strain rate is a strain rate above which the loading conditions cannot be considered quasi-static. The determination of the highest strain rate under which QS conditions are attainable is beneficial for reducing simulation runtimes. This upper strain-rate limit is called the QS strain rate and denoted by $\dot{\varepsilon}_{QS}$ in this study.

da Cruz et al. (2005) proposed an equation to predict the QS strain rate based on the observations from simulations as follows:

$$I = \dot{\varepsilon} d_{\mathrm{Avg}} \sqrt{\frac{\rho}{\sigma_m}} \tag{70}$$

where I is the inertial number, $\dot{\varepsilon}$ is the shearing strain rate, ρ is the particle density, σ_m is the mean stress in the assembly, and d_{Avg} is the average particle diameter. For a simulation to meet the QS conditions, I should be a very small number relative to unity, giving an indication that the inertial forces are significantly lower than the contact forces. For example, Macaro and Utili (2012) considered $I \leq 2 \times 10^{-4}$ for QS conditions.

Perez et al. (2016) reported that $I \leq 2.5 \times 10^{-3}$ satisfies the QS conditions where the critical state values are needed to be measured and stated that, for this purpose, the inertial number is independent of the initial state of samples and the type of tests, e.g. drained and undrained. Therefore, the inertial number is not suited for finding an

appropriate QS strain rate where determining the peak friction angle is aimed, since the peak friction angle is known to be dependent on the initial state of samples. In this case, the predicting equation has to be a function of a parameter related to the initial state, for example, void ratio. On the other hand, Modense et al. (2012) mentioned a sensitivity of the QS strain rate to the particle-size distribution (PSD), which is not covered in the inertial number, explicitly.

In this chapter, determining the QS strain rate that guarantees the correctness of the material behavior at peak state as well as at the critical state is aimed. The QS strain rate should be a function of the initial mean stress of assemblies, the initial void ratio, and the PSD.

For this purpose, first, the methodology is explained. Then, a criterion for the QS strain-rate limit is proposed using the moment index. After that, by conducting a parametric study, the correlations between the QS strain rate and the selected parameters of the models are studied for each parameter, separately, and the variation trend of the QS strain rate with each parameter is identified independently. Then, a direct equation is proposed to predict $\dot{\varepsilon}_{QS}$ quantitatively based on those parameters by combining the individual trends, and its prediction ability is validated by a leave-out sample. Furthermore, the predictions of the proposed equations are compared with those of the inertial number. Finally, two more methods, in addition to the one introduced in Chapter 5, are proposed to predict the peak friction angle using the findings in this chapter.

6.2. Limitations and Methodology

In this study, the following restrictions are applied: boundary conditions are periodic; thus, the sample size is not expected to influence, and the number of particles in each sample is constant. The loading is axisymmetric in triaxial drained conditions. The effects of the inter-particle contact laws, Poisson's ratio, and damping are not considered. A minimal constant mass proportional damping ratio is applied, which is equal to 0.3% for the (OD) models and 0.5% for the (ND) models after Chapter 5.

Regarding the dimensionless DEM scheme in Chapter 3, the effects of density and the elastic modulus of particles are removed by performing the study on the dimensionless parameters and determining the dimensionless QS strain rate, ε'_{QS}, instead of $\dot{\varepsilon}_{QS}$. This remarkably helps in limiting the parametric study and reducing the number of necessary simulations by eliminating the need to consider three major parameters: ρ, E, and absolute particle sizes.

Therefore, the effects of the initial void ratio, e_0, and the initial dimensionless mean stress, $\bar{\sigma}_0$, of the samples and the particle-size distribution will be studied. A characteristic parameter, Δ, is used to incorporate the effect of the PSD of the samples; that is, the dimensionless parameter, Δ, will represent the PSD.

Hence, the possible effective parameters that remain are e_0, $\bar{\sigma}_0$, and Δ. Therefore, we expect that ε'_{QS} will be a function of e_0, $\bar{\sigma}_0$, and Δ. The aim is to specify the function. Assuming that the effects of the involved parameters are independent from each other for simplicity, the following equation will be fitted, and the unknown exponents and the coefficient will be determined:

$$\varepsilon'_{QS} = K e_0^a \, \bar{\sigma}_0^b \, \Delta^c \tag{71}$$

Throughout this chapter, curve fitting was done by minimizing the residual sum of squares where needed.

The predictions of Eq. (72) will be compared with the predictions of the inertial number. Using Eq. (71), recalling $\dot{\varepsilon} = \varepsilon'/\Delta t_c$, $\Delta t_c = d_{\min}\sqrt{\rho/E}$, and $\sigma_m = \bar{\sigma}_0 E$ from Chapter 3, and by defining dispersity index in the form of $\Delta = \frac{d_{\text{Avg}}}{d_{\min}}$, the following dimensionless form of the inertial number is deduced:

$$\varepsilon' = I\frac{\sqrt{\bar{\sigma}_0}}{\Delta} \tag{72}$$

In Eq. (73), by setting the inertial number, I, to its value at QS, the resulting strain rate will be approximate ε'_{QS} that the inertial number predicts.

6.3. Definition of Maximum Quasi-Static Strain Rate

QS solutions are aimed to approximate the static behavior where a static solution is not available, such as using DEM. No quantifiable criteria exist for the QS conditions in the literature. However, a parametric study can be useful to determine the maximum strain rate that does not violate the quasi-static conditions. The peak shear strength has dependence against the applied strain rate. As the strain rate decreases, the peak shear strength decreases. Nevertheless, below a certain strain rate, the peak shear strength does not decrease anymore. The strain rate for quasi-static simulations can then be chosen as high as the generated inertial effects do not cause more than a specific error on the shear strength.

To ensure the satisfaction of the QS condition, one can alternatively lower the strain

rate such that the inertial effects do not exceed a specific limit. A fulfilled equilibrium state means that the inertial effects are small enough. The moment index is used in this chapter. As shown in Chapter 5, as the strain rate is reduced, the moment index value, I_{Mom}, decreases. In the present study, to meet the QS conditions, the strain rate will be lowered such that the moment index does not exceed 0.1%. That is, ε'_{QS} is defined as the strain rate at which the moment index yields a value equal to 0.1%. The moment index was known to depend on the damping ratio as well. To minimize the moment index at a specific strain rate, the selected damping ratio should be equal to the optimum damping ratio. For the OD and ND damping models, the optimum damping ratios were determined to be about 0.3% and 0.5%, respectively, which were nearly independent of the applied strain rate. After ε'_{QS} was determined based on the $I_{Mom} = 0.1\%$ criterion, we will make sure that the error that is obtained for the peak friction coefficient (or angle) does not exceed a small value.

6.4. Numerical Tests Schedule

To study the effects of the parameters on ε'_{QS}, 18 samples with 10,000 particles were created. The samples cover wide ranges of initial void ratio, confining stress, and particle-size distributions were covered. The properties of the samples can be found in Table 31 to Table 39. One more sample was created and left out for the evaluation of the proposed equations. The naming convention for the samples is $n_\sigma n_\mu n_\Delta$, where n_σ represents the confining stress, σ_c, n_μ denotes the friction coefficient in the second phase of the sample preparation, μ_0, and n_Δ indicates the PSD type.

Table 31 Features of the simulation code and common input parameters

Computation Code	ELLIPSE3D
Particle Shape	Spheroid
Aspect Ratio of Particles	1.20
Number of Particles in each Sample	10,000
Contact Laws	Simplified Hertz-Mindlin
Boundary Conditions	Periodic
Aspect Ratios of Sample (Cuboid)	1, 1, 1
Sample Preparation Approach	Automatic Three-Phase Method
Initial Stress State	$\sigma_{11} = \sigma_{22} = \sigma_{33}$
Poisson's Ratio (ν)	0.2
Inter-Particle Friction Coefficient in Loading Stage (μ)	0.5
Time Step Ratio (c_t)	0.32
Density, ρ (mg/mm^3)	2.65
Elastic Modulus, E, (mN/mm^2)	7.2×10^7
Damping Ratio for OD Series, (ξ)	0.3%
Damping Ratio for ND Series, (ξ)	0.5%
Loading Path	Drained
Final Strain (ε)	25%

Table 32 Particle sizes and particle-size distribution of Type 0, $\Delta = 1$

Particle Type Number	Minor Radii (mm)	Major Radius (mm)	Particle Nominal Size (mm)	Number of Particles	Weight Ratio	Accumulated Weight Ratio
1	1.0	1.2	1.06	10,000	100%	100%

Table 33 Particle sizes and particle-size distribution of Type 1, $\Delta = 6.00$

Particle Type Number	Minor Radii (mm)	Major Radius (mm)	Particle Nominal Size (mm)	Number of Particles	Weight Ratio	Accumulated Weight Ratio
1	1.0	1.2	1.06	9,234	10%	10%
2	3.0	3.6	3.19	513	15%	25%
3	5.0	6.0	5.31	148	20%	45%
4	7.0	8.4	7.44	67	25%	70%
5	9.0	10.8	9.56	38	30%	100%

Table 34 Particle sizes and particle-size distribution of Type 2, $\Delta = 2.84$

Particle Type Number	Minor Radii (mm)	Major Radius (mm)	Particle Nominal Size (mm)	Number of Particles	Weight Ratio	Accumulated Weight Ratio
1	1.5	1.8	1.59	7,937	23%	23%
2	2.5	3.0	2.66	1,565	21%	44%
3	4.0	4.8	4.25	364	20%	64%
4	6.0	7.2	6.38	102	19%	83%
5	8.5	10.2	9.03	32	17%	100%

Table 35 Particle sizes and particle-size distribution of Type 3, $\Delta = 1.28$

Particle Type Number	Minor Radii (mm)	Major Radius (mm)	Particle Nominal Size (mm)	Number of Particles	Weight Ratio	Accumulated Weight Ratio
1	10.0	12.0	10.63	990	5%	5%
2	11.0	13.2	11.69	1,488	10%	15%
3	12.0	14.4	12.75	2,292	20%	35%
4	13.0	15.6	13.81	2,704	30%	65%
5	14.0	16.8	14.88	2,526	35%	100%

Table 36 Particle sizes and particle-size distribution of Type 4, $\Delta = 4.00$

Particle Type Number	Minor Radii (mm)	Major Radius (mm)	Particle Nominal Size (mm)	Number of Particles	Weight Ratio	Accumulated Weight Ratio
1	1.0	1.2	1.06	9,186	20%	20%
2	2.5	3.0	2.66	588	20%	40%
3	4.0	4.8	4.25	144	20%	60%
4	5.5	6.6	5.84	55	20%	80%
5	7.0	8.4	7.44	27	20%	100%

Table 37 Particle sizes and particle-size distribution of Type 5, $\Delta = 2.75$

Particle Type Number	Minor Radii (mm)	Major Radius (mm)	Particle Nominal Size (mm)	Number of Particles	Weight Ratio	Accumulated Weight Ratio
1	1.0	1.2	1.06	9,843	51%	51%
2	3.0	3.6	3.19	107	15%	66%
3	4.5	5.4	4.78	28	13%	79%
4	5.5	6.6	5.84	13	11%	90%
5	6.0	7.2	6.38	9	10%	100%

Table 38 Particle sizes and particle-size distribution of Type T, $\Delta = 6.15$

Particle Type Number	Minor Radii (mm)	Major Radius (mm)	Particle Nominal Size (mm)	Number of Particles	Weight Ratio	Accumulated Weight Ratio
1	1.0	1.2	1.06	9,601	15%	15%
2	3.5	4.2	3.72	299	20%	35%
3	6.0	7.2	6.38	59	20%	55%
4	8.0	9.6	8.50	25	20%	75%
5	10.0	12.0	10.63	16	25%	100%

Four values were selected for σ_c ranging from 74 to 5,760 kPa. μ_0 was assigned four values ranging from 0.05 to 0.4 to yield samples of different void ratios, e_0. In Chapter 4, we showed a one-to-one correlation between e_0 and relative density with μ_0. Six particle-size distributions, shown in Fig. 72, were designed, and their specs are presented in Table 32, Table 33, Table 34, Table 35, Table 36, Table 37, and Table 38. They represent well-graded and poorly graded granular material, noting that PSD type 0 is monosized. Every PSD is represented by a characteristic value, Δ, which will be defined later. The values of $\bar{\sigma}_0$ (dimensionless form of σ_c), e_0, and Δ are provided in Table 39 for the samples. In addition, those values of the test sample (TTT) are presented in Table 39.

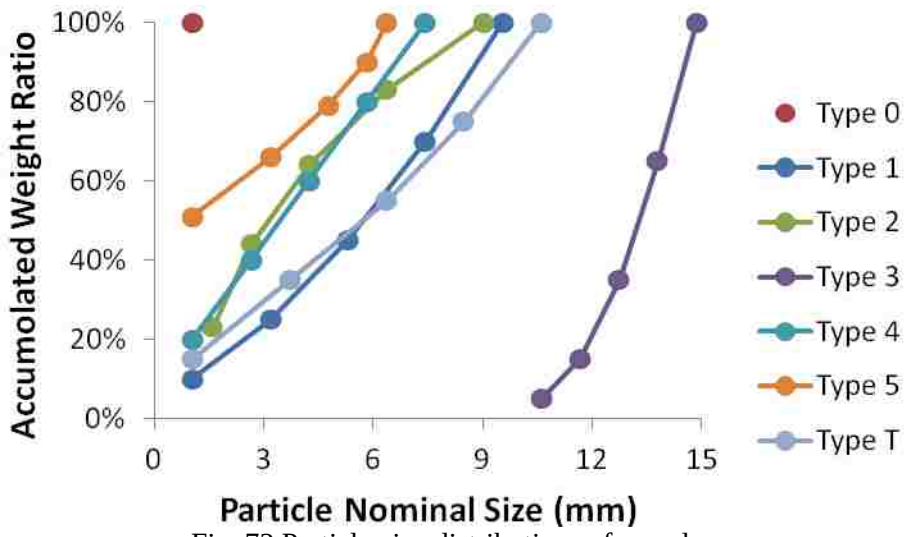

Fig. 72 Particle-size distributions of samples

The samples were subjected to the drained conditions and loaded up to 25% strain in the vertical direction to ensure the mobilization of peak shear strength of the assemblies. To study the effect of the damping model on ε'_{QS}, two damping models, ND and OD, were applied. The naming convention of the models is {Sample Name}{Damping Model}{Dimensionless Strain Rate}, as used in Table 51 of Appendix 9. To determine ε'_{QS}, the dimensionless strain rate, ε', was allocated nine values ranging from 2×10^{-8} to 1×10^{-5}. The peak friction angle, ϕ_{max}, and the moment index values, I_{Mom}, of the models are presented in Table 51. Note that I_{Mom} was averaged from $\varepsilon = 0$ through ε_{peak} to preserve the effect of the initial state that influences the peak state.

Table 39 Input parameters of samples (ND and OD)

Sample	Inter-particle friction coefficient in the second phase of sample preparation, μ_0	Initial Void Ratio, e_0	Initial Dimensionless Mean Stress, $\bar{\sigma}_0$	Initial Mean Stress, σ_0 (kPa)	Dispersity Index, Δ
121	0.10	0.356	1×10^{-6}	72	6.000
122	0.10	0.412	1×10^{-6}	72	2.837
211	0.05	0.312	4×10^{-6}	288	6.000
212	0.05	0.370	4×10^{-6}	288	2.837
220	0.10	0.606	4×10^{-6}	288	1.000
221	0.10	0.343	4×10^{-6}	288	6.000
222	0.10	0.406	4×10^{-6}	288	2.837
223	0.10	0.596	4×10^{-6}	288	1.280
224	0.10	0.336	4×10^{-6}	288	4.000
225	0.10	0.410	4×10^{-6}	288	2.750
231	0.20	0.401	4×10^{-6}	288	6.000
232	0.20	0.450	4×10^{-6}	288	2.837
241	0.40	0.469	4×10^{-6}	288	6.000
242	0.40	0.505	4×10^{-6}	288	2.837
321	0.10	0.334	2×10^{-5}	1,440	6.000
322	0.10	0.400	2×10^{-5}	1,440	2.837
421	0.10	0.325	8×10^{-5}	5,760	6.000
422	0.10	0.394	8×10^{-5}	5,760	2.837
TTT	0.14	0.312	1×10^{-5}	720	6.150

6.5. Relationship between I_{Mom} and ε'

The general form of the relationship between I_{Mom} and ε' and the damping ratio, ξ, was presented in Chapter 5 in the form of a power function, $I_{Mom} = a(\xi\varepsilon')^b$. In this chapter, ξ is constant, so the relationship can be simplified to the following form:

$$I_{Mom} = a_I \varepsilon'^{b_I} \tag{73}$$

As mentioned in the methodology section, ε'_{QS} was determined assuming $I_{QS} = 0.1\%$. I_{QS} is the value of the moment index that corresponds to ε'_{QS} by our definition. By this definition, ε'_{QS} was determined for each sample using the interpolation approach and

presented in Table 40 and Table 41.

To further examine the correctness of a power function form for the relationship between I_{Mom} and ε', this type of curve was fitted to the data points and the parameters a_I and b_I were determined and presented in Table 40 and Table 41 along with the coefficient of determination, R^2. An R^2 value approaching unity indicates the goodness of the selected function, meaning that a power function suits for this purpose. The variation of the moment index versus the strain rate is shown for the models in Fig. 73 and Fig. 74 in a log-log scale. The fact that the trends approximate straight lines in a log-log scale is another indication of the appropriateness of the selected function.

Table 40 Power fit parameters and coefficients of determination for the (ND) models and ε'_{QS} for $I_{QS} = 0.1\%$

Model	a	b	R^2	ε'_{QS}
121ND	335	0.70	0.9984	2.14E-08
122ND	232	0.73	0.9973	8.31E-08
211ND	1815	0.92	0.9998	1.97E-07
212ND	1566	0.97	0.9973	4.10E-07
220ND	3131	1.05	0.9955	6.46E-07
221ND	791	0.84	0.9993	9.59E-08
222ND	1278	0.93	0.9906	2.54E-07
223ND	3664	1.04	0.9776	4.62E-07
224ND	1726	0.93	0.9892	1.79E-07
225ND	2129	0.99	0.9790	3.89E-07
231ND	636	0.81	0.9871	6.17E-08
232ND	815	0.89	0.9918	1.94E-07
241ND	410	0.76	0.9858	4.57E-08
242ND	460	0.82	0.9705	1.20E-07
321ND	1534	0.98	0.9988	4.56E-07
322ND	730	0.98	0.9991	1.00E-06
421ND	52	0.79	0.9980	9.60E-07
422ND	240	0.97	0.9967	2.48E-06
TTTND	1050	0.91	0.9997	2.71E-07

Table 41 Power fit parameters and coefficients of determination for the (OD) models and ε'_{QS} for $I_{QS} = 0.1\%$

Model	a	b	R^2	ε'_{QS}
121OD	27	0.46	0.9852	4.82E-09
122OD	1260	0.84	0.9712	5.86E-08
211OD	1410	0.85	0.9173	6.24E-08
212OD	863	0.90	0.9992	2.51E-07
220OD	14523	1.14	0.9731	5.43E-07
221OD	555	0.76	0.8947	3.14E-08
222OD	2633	0.96	0.9439	1.90E-07
223OD	6211	1.08	0.9809	5.06E-07
224OD	1802	0.90	0.9433	1.13E-07
225OD	3896	1.01	0.9779	2.76E-07
231OD	419	0.72	0.9198	2.17E-08
232OD	770	0.85	0.9907	1.02E-07
241OD	206	0.66	0.9469	1.21E-08
242OD	518	0.80	0.9593	7.45E-08
321OD	822	0.89	0.9857	1.97E-07
322OD	217	0.87	0.9895	7.00E-07
421OD	259	0.89	0.9955	7.40E-07
422OD	17	0.72	0.9991	1.34E-06
TTTOD	570	0.81	0.9722	9.08E-08

Assuming that I_{Mom} is a power function of ε', users can approximate ε'_{QS} using two or more data points with significantly higher strain rates to save runtime, instead of a trial and error. For example, ε'_{QS} was approximated for the ND models using two and three data points of the highest strain rates in the present study. The results are presented in Table 42 and seem adequately close for practical applications. Less error is observed on average using three points compared to two points.

Table 42 Approximate quasi-static strain rate using two and three points for the (ND) models

Model	ε'_{qs}	2pt Approx	3pt Approx
121ND	2.14E-08	4.8E-09	1.05E-08
122ND	8.31E-08	1.9E-08	3.04E-08
211ND	1.97E-07	1.4E-07	1.52E-07
212ND	4.10E-07	2.4E-07	3.43E-07
220ND	6.46E-07	3.9E-07	5.57E-07
221ND	9.59E-08	8.7E-08	7.77E-08
222ND	2.54E-07	1.9E-07	1.61E-07
223ND	4.62E-07	3.2E-07	2.49E-07
224ND	1.79E-07	1.8E-07	1.97E-07
225ND	3.89E-07	3.3E-07	2.69E-07
231ND	6.17E-08	3.3E-08	4.34E-08
232ND	1.94E-07	1.7E-07	1.69E-07
241ND	4.57E-08	2.3E-08	3.00E-08
242ND	1.20E-07	6.2E-08	5.95E-08
321ND	4.56E-07	6.6E-07	5.23E-07
322ND	1.00E-06	1.3E-06	1.00E-06
421ND	9.60E-07	1.3E-06	1.02E-06
422ND	2.48E-06	2.4E-06	2.48E-06
TTTND	2.71E-07	2.9E-07	2.57E-07
Average Error		33%	24%

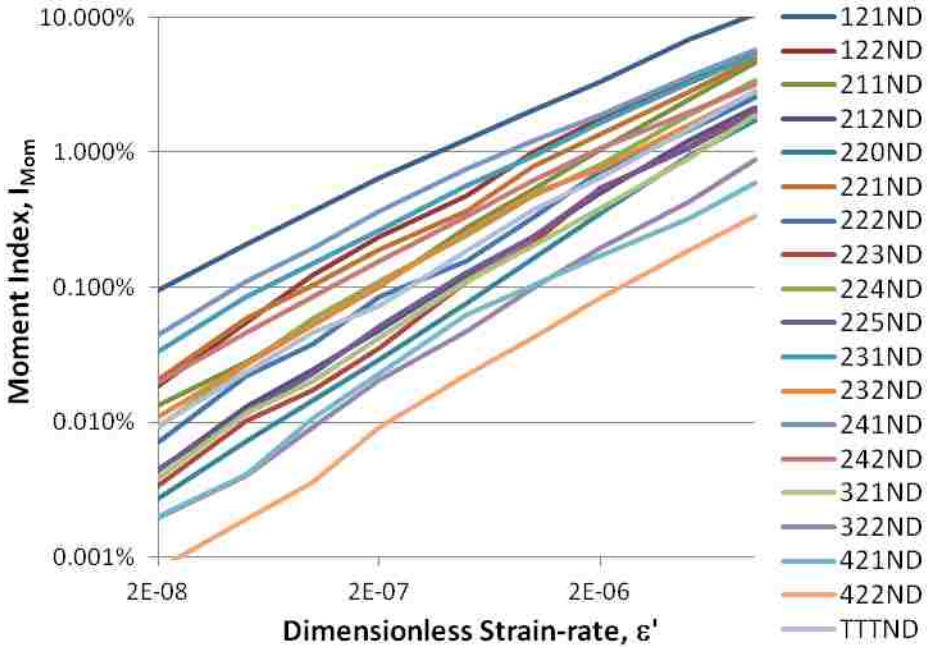

Fig. 73 Variation of moment index with the dimensionless strain rate for the (ND) models

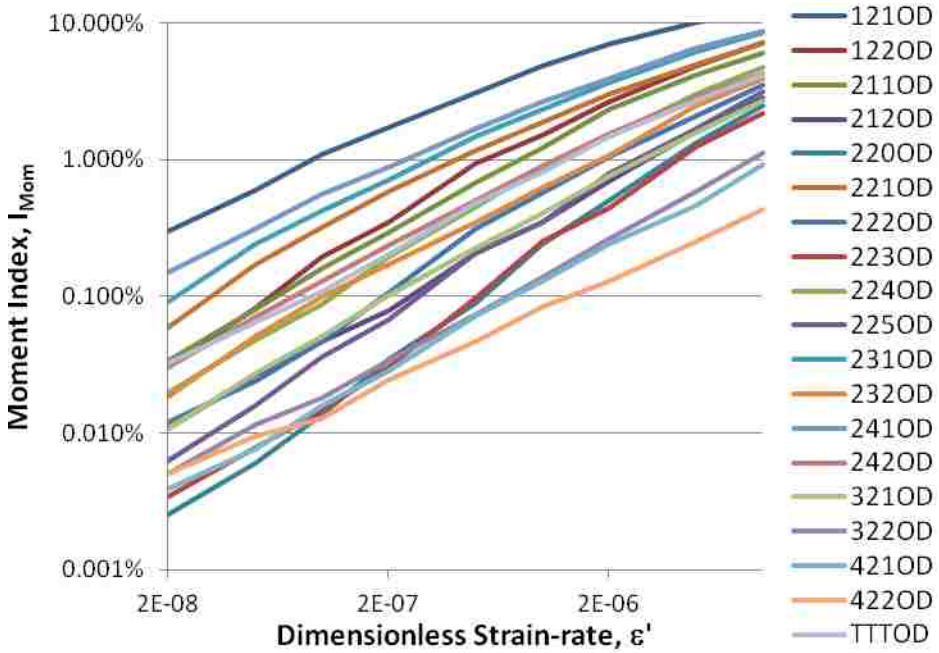

Fig. 74 Variation of moment index with the dimensionless strain rate for the (OD) models

6.6. Relationship between $\tan \phi_{max}$ and I_{Mom}

As shown in Chapter 5, a linear relationship exists between $\mu = \tan \phi$ and I_{Mom}:

$$\tan \phi = \tan \phi_0 + k I_{Mom} \tag{74}$$

A similar relationship was observed by da Cruz et al. (2005) between μ and the inertial number, I, in the simulations of direct shear tests in the form of $\mu = \mu_0 + kI$. To further study the correctness of Eq. (75), the variation of $\tan \phi$ against I_{Mom} is shown in Fig. 75 and Fig. 76, where the curves are very close to straight lines. The parameters of the fitted lines, that is, $\tan \phi_0$ and k, are presented in Table 43, as well as the coefficients of determination. R^2 values are close to unity, which indicates the suitability of the linear assumption for the relationship between $\mu = \tan \phi$ and I_{Mom}. Note that ϕ_0 can be interpreted as the QS friction angle since when $I_{Mom} = 0$, Eq. (75) results in $\phi_{max} = \phi_0$. $I_{Mom} \approx 0$ occurs when the inertia-induced stresses/forces approach zero compared with the static stresses/forces.

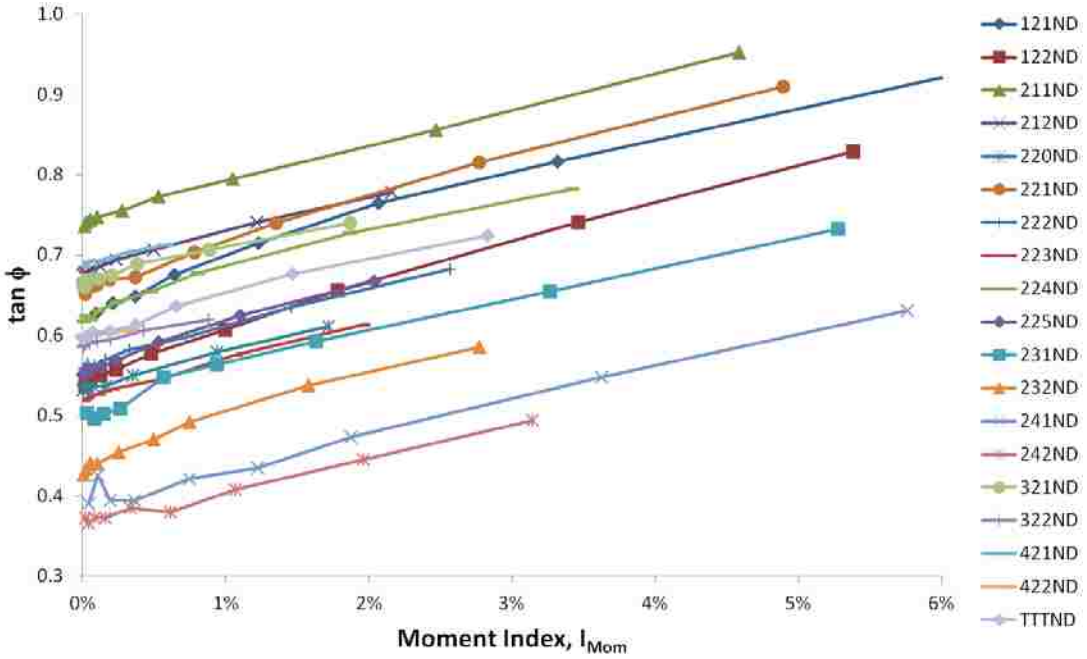

Fig. 75 Peak friction coefficient versus moment index for the (ND) models

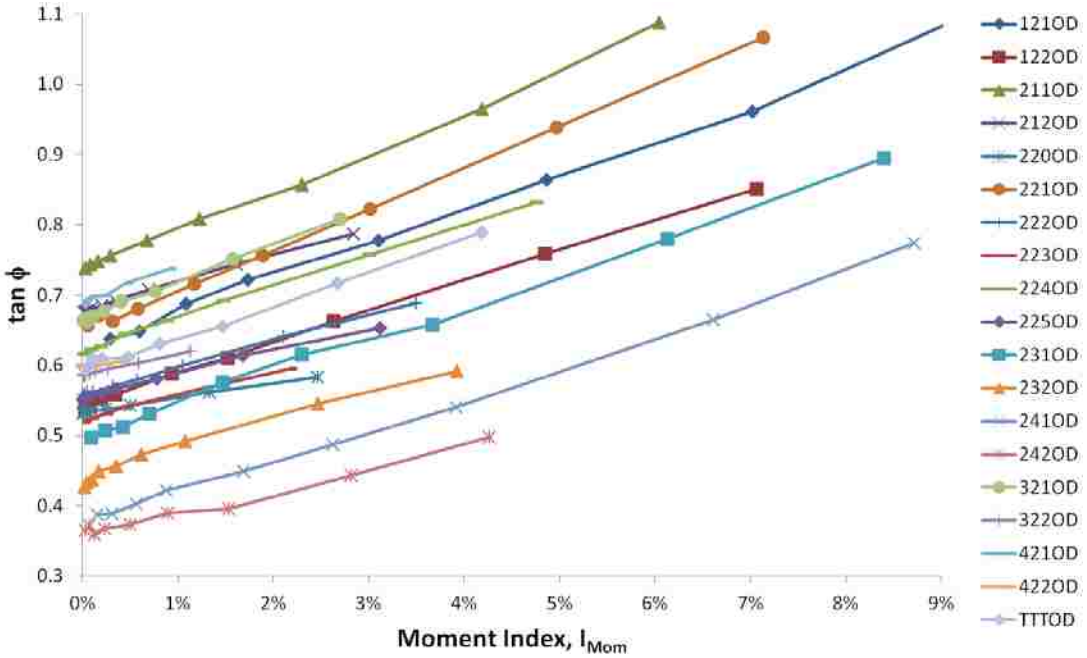

Fig. 76 Peak friction coefficient versus moment index for the (OD) models

Table 43 Linear fit parameters of (ϕ vs. I_{Mom}) for the (ND) and (OD) models and the corresponding coefficients of determination

Model	tan ϕ_0	k	R^2	Model	tan ϕ_0	k	R^2
121ND	0.64	5.05	0.9916	**121OD**	0.61	5.53	0.9904
122ND	0.55	5.43	0.9940	**122OD**	0.54	4.42	0.9990
211ND	0.74	4.62	0.9971	**211OD**	0.74	5.65	0.9977
212ND	0.68	4.74	0.9903	**212OD**	0.68	3.96	0.9957
220ND	0.53	4.69	0.9964	**220OD**	0.53	2.09	0.9970
221ND	0.66	5.30	0.9942	**221OD**	0.65	5.80	0.9986
222ND	0.56	4.83	0.9952	**222OD**	0.56	3.78	0.9985
223ND	0.52	4.79	0.9955	**223OD**	0.52	3.47	0.9941
224ND	0.63	4.83	0.9766	**224OD**	0.62	4.54	0.9973
225ND	0.55	5.80	0.9891	**225OD**	0.55	3.32	0.9944
231ND	0.51	4.47	0.9776	**231OD**	0.50	4.69	0.9973
232ND	0.44	5.67	0.9770	**232OD**	0.44	4.10	0.9788
241ND	0.39	4.15	0.9787	**241OD**	0.38	4.45	0.9979
242ND	0.37	3.98	0.9874	**242OD**	0.36	3.07	0.9800
321ND	0.67	4.12	0.9722	**321OD**	0.66	5.41	0.9972
322ND	0.59	3.82	0.9807	**322OD**	0.59	3.07	0.9971
421ND	0.69	4.32	0.9566	**421OD**	0.69	5.20	0.9805
422ND	0.60	2.33	0.9870	**422OD**	0.60	1.43	0.8990
TTTND	0.60	4.64	0.9860	**TTTOD**	0.60	4.56	0.9940

6.7. Relationship between tan ϕ_{max} and ε'

The evolution of the mobilized friction angle with the applied strain for Sample 220 at different strain rates using the ND damping model is shown in Fig. 77 and Fig. 78, for instance. It indicates that as the strain rate decreases, the friction angle decreases and finally converges to a constant value. The variations of the peak friction coefficient of the samples with the applied strain rate are shown in Fig. 79, Fig. 80, Fig. 81, and Fig. 82. In Fig. 80 and Fig. 82, where the horizontal axes are in the logarithmic scale, plateaus are observed at very small strain rates, which indicate the convergence to the QS state.

Using Eqs. (74) and (75), a relationship between tan ϕ_{max} and ε' can be established in the following form if $a_\phi = k a_I$ and $b_\phi = b_I$.

$$\tan\phi_{max} = \tan\phi_0 + a_\phi \varepsilon'^{b_\phi} \tag{75}$$

To verify whether the above equation applies, R^2 values were calculated and presented in Table 40 and Table 41. R^2 values approaching unity agree the assumptions for the relationship.

Eq. (76) – if rearranged – is similar to the Cowper-Symonds model (1957), which is frequently used to describe viscoelastic effects on the shear strength:

$$q_{max} = q_0 \left[1 + \left(\frac{\dot{\varepsilon}}{D}\right)^n\right] \tag{76}$$

where q_{max} is the shear strength at the strain rate of $\dot{\varepsilon}$, q_0 is the QS value of the shear strength, and n and D are the fit parameters.

Since the exponent b_ϕ in Eq. (76) is less than unity, according to Table 44 and Table 45, a shear-thinning type of viscoelastic behavior is implied for the particulate models in this study.

The extra peak friction angle that is obtained by applying ε'_{QS} (using $I_{QS} = 0.1\%$ criterion), that is, $\Delta\phi_{QS} = \phi_{QS} - \phi_0$, can be calculated using Eq. (76) as follows:

$$\Delta\phi_{QS} = \tan^{-1}\left(\tan\phi_0 + a_\phi {\varepsilon'_{QS}}^{b_\phi}\right) - \phi_0 \tag{77}$$

To ensure that by applying ε'_{QS}, the ϕ_{max} values obtained from the simulations, i.e. ϕ_{QS}, are sufficiently close to ϕ_0, the extra friction angles, $\Delta\phi_{QS}$, were calculated and presented in Table 44 and Table 45. The average error on the peak friction angles of all models is about 0.2°, which is small enough to consider the quasi-static values. Therefore, $I_{QS} = 01.\,\%$ is an appropriate assumption to determine ε'_{QS}.

Table 44 Parameters of the Cowper-Symonds models and coefficients of determination for the (ND) models and the extra friction angle at $\varepsilon' = \varepsilon'_{QS}$ with respect to the quasi-static friction angle for $I_{QS} = 0.1\%$

Model	$a_\phi = k a_I$	$b_\phi = b_I$	$\tan\phi_0$	R^2	ϕ_0 (degrees)	$\Delta\phi_{QS}$ (degrees)
121ND	1688	0.70	0.64	0.9953	32.5	0.29
122ND	1262	0.73	0.55	0.9873	28.6	0.40
211ND	8383	0.92	0.74	0.9971	36.6	0.21
212ND	7421	0.97	0.68	0.9809	34.2	0.19
220ND	14671	1.05	0.53	0.9870	28.0	0.21
221ND	4188	0.84	0.66	0.9907	33.3	0.21
222ND	6170	0.93	0.56	0.9808	29.3	0.19
223ND	17566	1.04	0.52	0.9704	27.5	0.19
224ND	8335	0.93	0.63	0.9588	32.0	0.17
225ND	12349	0.99	0.55	0.9549	29.0	0.23
231ND	2843	0.81	0.51	0.9539	26.8	0.20
232ND	4624	0.89	0.44	0.9559	23.6	0.25
241ND	1703	0.76	0.39	0.9677	21.4	0.22
242ND	1834	0.82	0.37	0.9671	20.1	0.19
321ND	6327	0.98	0.67	0.9752	33.7	0.15
322ND	2787	0.98	0.59	0.9821	30.4	0.15
421ND	226	0.79	0.69	0.9586	34.5	0.15
422ND	558	0.97	0.60	0.9806	30.9	0.09
TTTND	4875	0.91	0.60	0.9882	30.9	0.20

Table 45 Parameters of the Cowper-Symonds models and coefficients of determination for the (OD) models and the extra friction angle at $\varepsilon' = \varepsilon'_{QS}$ with respect to the quasi-static friction angle for $I_{QS} = 0.1\%$

Model	$a_\phi = ka_I$	$b_\phi = b_I$	$\tan\phi_0$	R^2	ϕ_0 (degrees)	$\Delta\phi_{QS}$ (degrees)
121OD	148	0.46	0.61	0.9964	31.5	0.88
122OD	5572	0.84	0.54	0.9629	28.5	0.20
211OD	7969	0.85	0.74	0.9316	36.4	0.21
212OD	3418	0.90	0.68	0.9926	34.1	0.16
220OD	30356	1.14	0.53	0.9656	28.0	0.10
221OD	3218	0.76	0.65	0.8996	33.0	0.28
222OD	9965	0.96	0.56	0.9352	29.2	0.16
223OD	21556	1.08	0.52	0.9645	27.5	0.15
224OD	8181	0.90	0.62	0.9307	31.8	0.20
225OD	12951	1.01	0.55	0.9645	28.9	0.14
231OD	1967	0.72	0.50	0.9200	26.4	0.28
232OD	3158	0.85	0.44	0.9581	23.7	0.17
241OD	917	0.66	0.38	0.9574	20.6	0.29
242OD	1589	0.80	0.36	0.9631	19.8	0.16
321OD	4444	0.89	0.66	0.9799	33.6	0.20
322OD	665	0.87	0.59	0.9889	30.3	0.13
421OD	1349	0.89	0.69	0.9829	34.6	0.19
422OD	25	0.72	0.60	0.8941	30.9	0.06
TTTOD	2599	0.81	0.60	0.9757	30.8	0.20

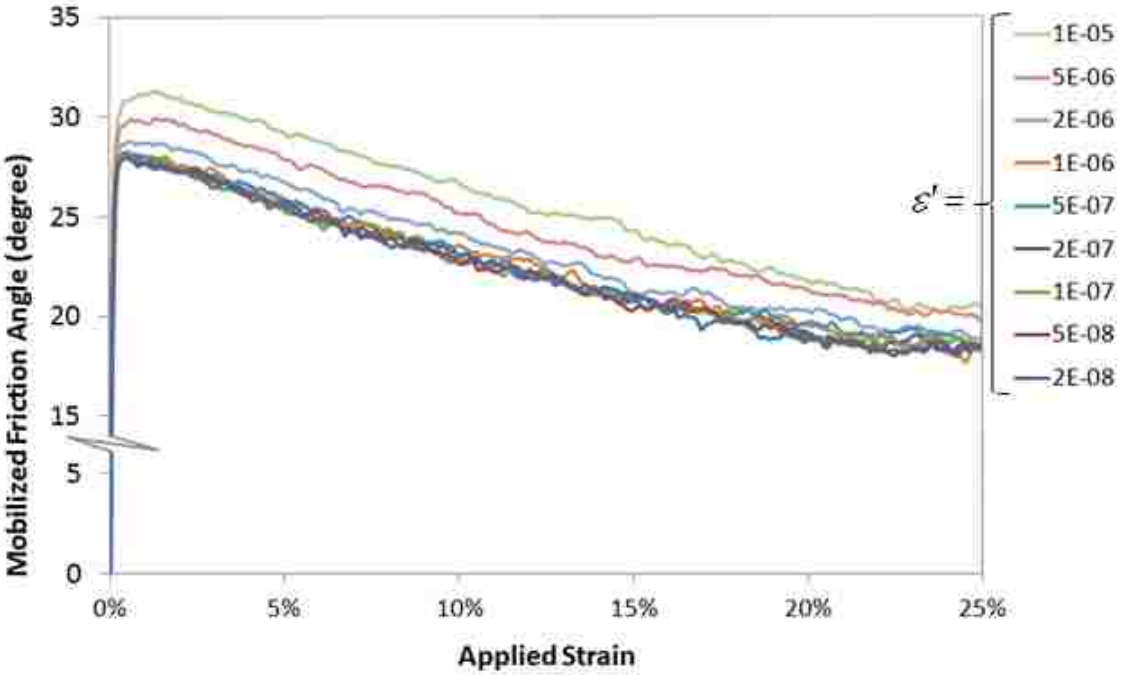

Fig. 77 Friction angle evolved with the applied strain at different strain rates for Sample 220 using the ND damping model

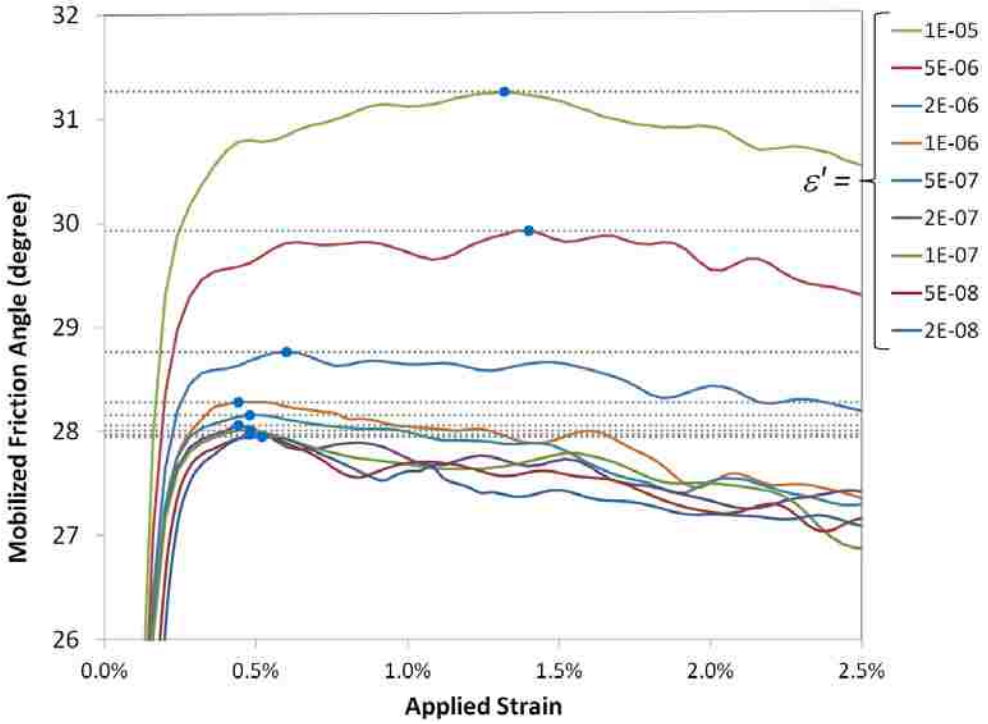

Fig. 78 Friction angle evolved with the applied strain at different strain rates for Sample 220 using the ND damping model (the peak section is zoomed)

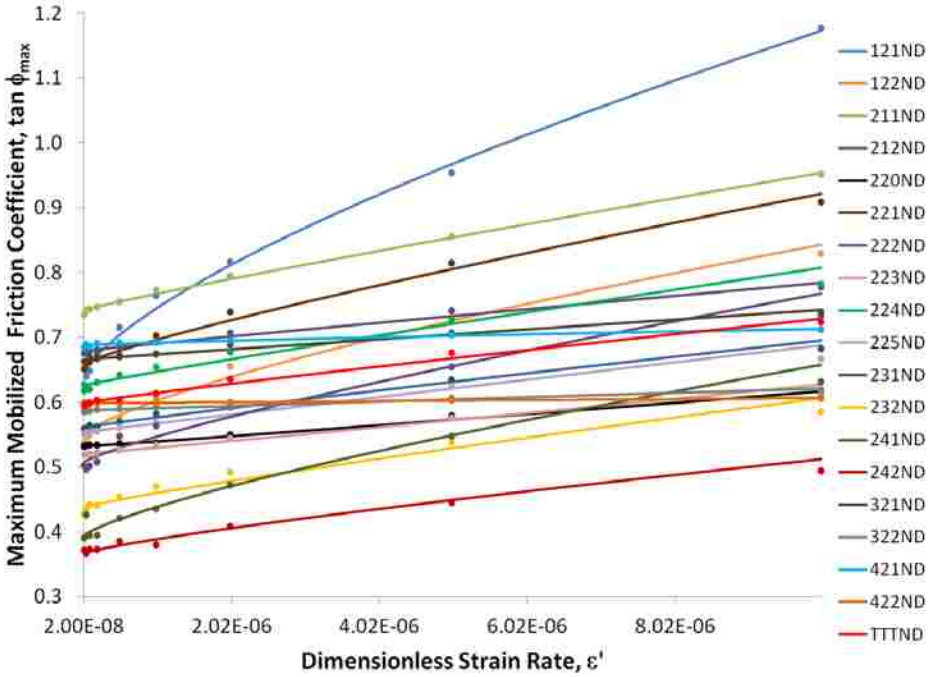

Fig. 79 Variation of the peak friction angle of the (ND) models with the dimensionless strain rate (markers are actual data; continuous lines are fitted curves)

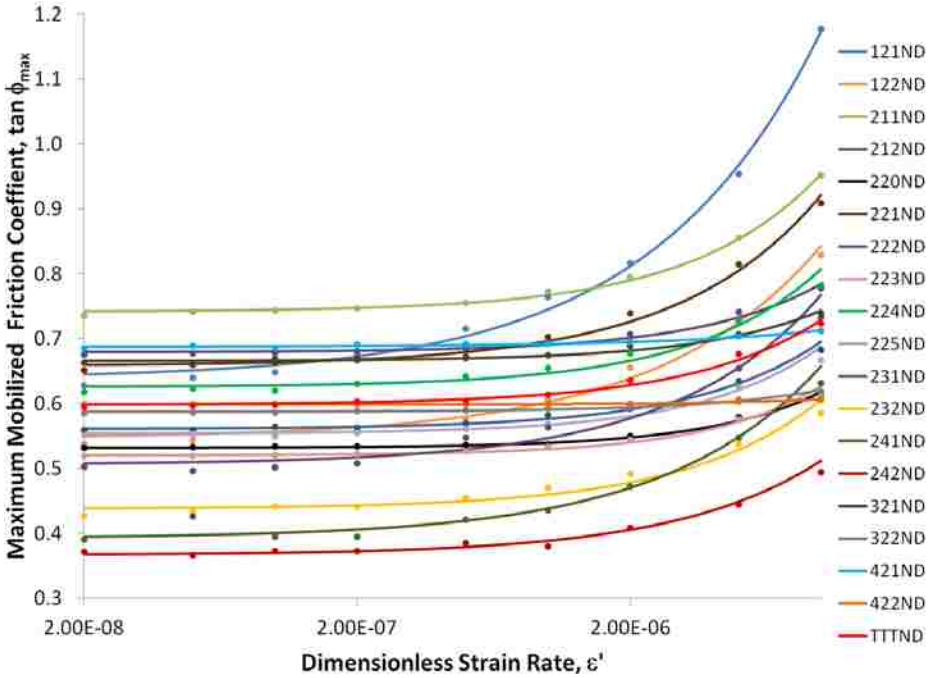

Fig. 80 Variation of the peak friction angle of the (ND) models with the dimensionless strain rate in log scale (markers are actual data; continuous lines are fitted curves)

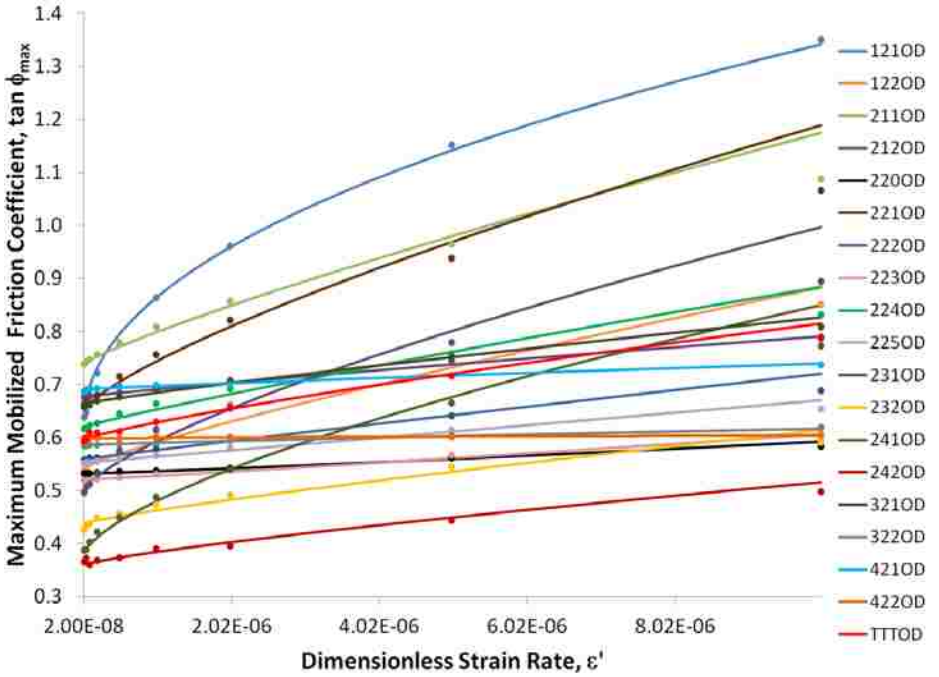

Fig. 81 Variation of the peak friction angle of the (OD) models with the dimensionless strain rate (markers are actual data; continuous lines are fitted curves)

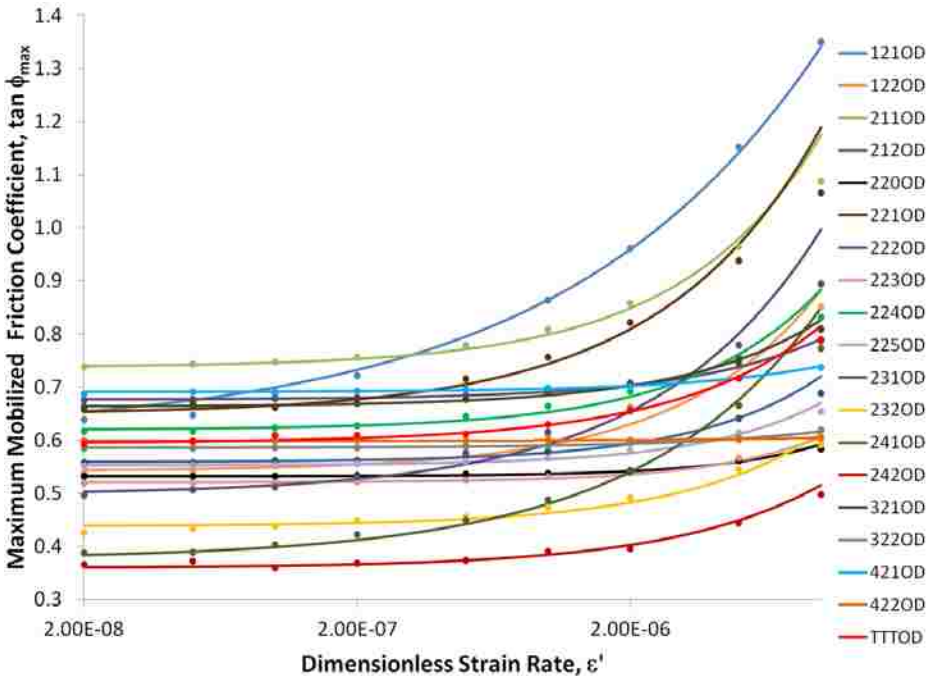

Fig. 82 Variation of the peak friction angle of the (OD) models with the dimensionless strain rate in a log-normal scale (markers are actual data; continuous lines are fitted curves)

In Fig. 83, $\Delta\phi_{QS}$ is shown against $\varepsilon'/\varepsilon'_{QS}$, where a linear relationship is observed in log-log scales. As ε' exceeds ε'_{QS}, the error of the peak friction angle, that is, $\Delta\phi_{QS}$, increases. However, where ε' is less than ε'_{QS}, the difference is satisfactorily small.

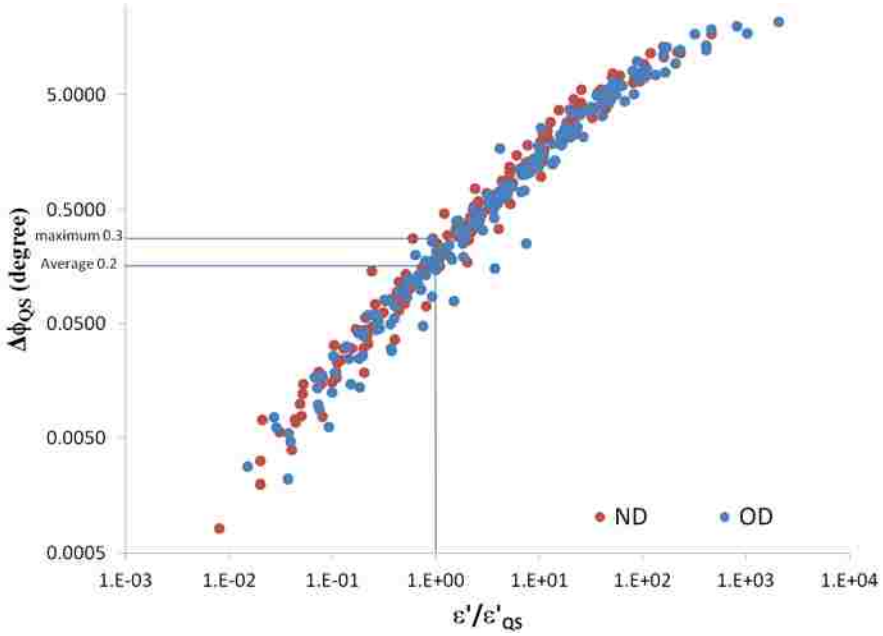

Fig. 83 Extra friction angle with respect to the quasi-static friction angle at different strain rates that are normalized by the quasi-static strain rates for all models ($I_{QS} = 0.1\%$)

6.8. Relationship between ε'_{QS} and e_0

To study the effect of the initial void ratio, e_0, on ε'_{QS}, two series of the samples were examined. In the first series, the PSD is of Type 1, while in the second series, the PSD is of Type 2, as indicated in Table 33 and Table 34, respectively. In both series, the initial dimensionless mean stress, that is, the dimensionless confining stress, is $\bar{\sigma}_0 = 4 \times 10^{-6}$. In each series, the PSD and $\bar{\sigma}_0$ are constant and e_0 differs. The samples in the first series are 211, 221, 231, and 241, and in the second series, 212, 222, 232, and 242. The variation of ε'_{QS} versus e_0 is shown for both series in Fig. 84 and Fig. 85, where ε'_{QS} is observed to decrease with the increase in e_0. This relationship can be approximately

expressed by a power function with an exponent equal to –4, which is displayed by trend lines in Fig. 84 and Fig. 85. R^2 values suggest the appropriateness of the approximations. Since the exponents of both power functions are equal to –4, the effect of e_0 on ε'_{QS} is implied to be independent of the PSD. Therefore,

$$\varepsilon'_{QS} \propto e_0^{b_e} \; ; \quad b_e = -4 \tag{78}$$

The inertial number does not indicate any relationship between ε'_{QS} and e_0.

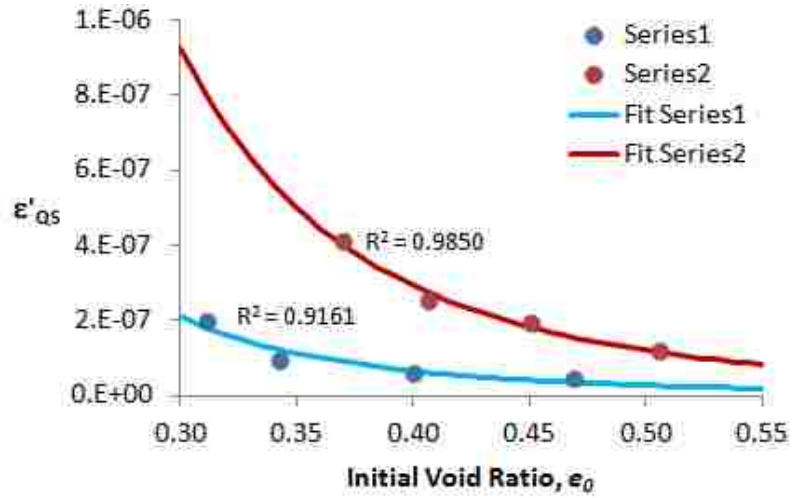

Fig. 84 Variation of ε'_{QS} with the initial void ratio for the (ND) models; $I_{QS} = 0.1\%$

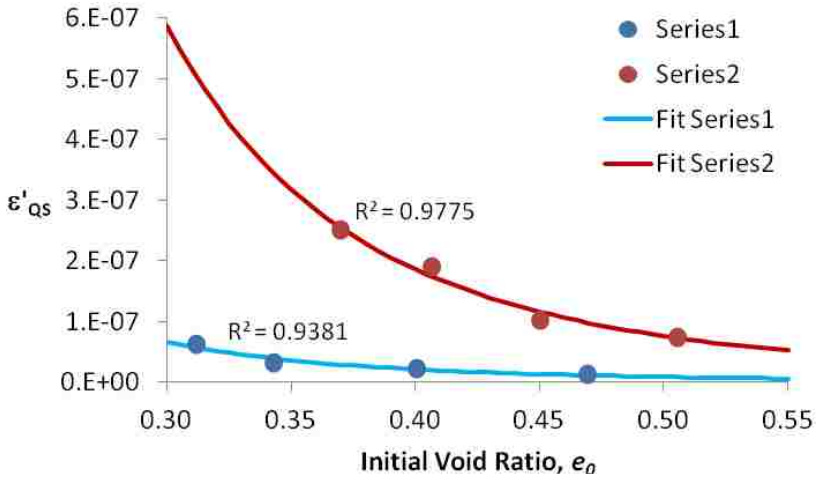

Fig. 85 Variation of ε'_{QS} with the initial void ratio for the (OD) models; $I_{QS} = 0.1\%$

6.9. Relationship between ε'_{QS} and $\bar{\sigma}_0$

In this section, the relationship between ε'_{QS} and the dimensionless confining stress, $\bar{\sigma}_0$, is studied. For this purpose, keeping e_0 and PSD constant and only varying $\bar{\sigma}_0$ would be better. However, creating samples with different confining pressures with equal void ratios was intense. As shown in the previous section, the relationship between ε'_{QS} and e_0 can be approximated by Eq. (79) for different PSDs. Therefore, to neutralize the effect of e_0, the relationship between $\varepsilon'_{QS}/e_0^{b_e}$ and $\bar{\sigma}_0$ was studied instead, for simplicity, assuming that this relationship is independent of the effect of e_0 on ε'_{QS}.

Two series with different PSDs were tested: Series 1 with PSD Type 1 consists of Samples 121, 221, 321, and 421; and Series 2 with PSD Type 2 consists of Samples 122, 222, 322, and 422. The variation of $\varepsilon'_{QS}/e_0^{b_e}$ against $\bar{\sigma}_0$ is shown in Fig. 86 and Fig. 87, where as $\bar{\sigma}_0$ increases, $\varepsilon'_{QS}/e_0^{b_e}$ is observed to increase as well. This relationship can be represented by a power function with an exponent equal to 0.67 for both series. R^2 values are very close to unity, which indicates the suitableness of the proposed relationship. Again, the effect of $\bar{\sigma}_0$ on ε'_{QS} was deduced independent of the PSD as the exponents were equal for both series. Hence, it is concluded that $\varepsilon'_{QS}/e_0^{b_e} \propto \bar{\sigma}_0^{\,0.67}$ or

$$\varepsilon'_{QS} \propto \bar{\sigma}_0^{\,b_\sigma} \quad ; \quad b_\sigma = 0.67 \tag{79}$$

This outcome is similar to the inertial number that predicts $\varepsilon'_{QS} \propto \bar{\sigma}_0^{\,0.5}$.

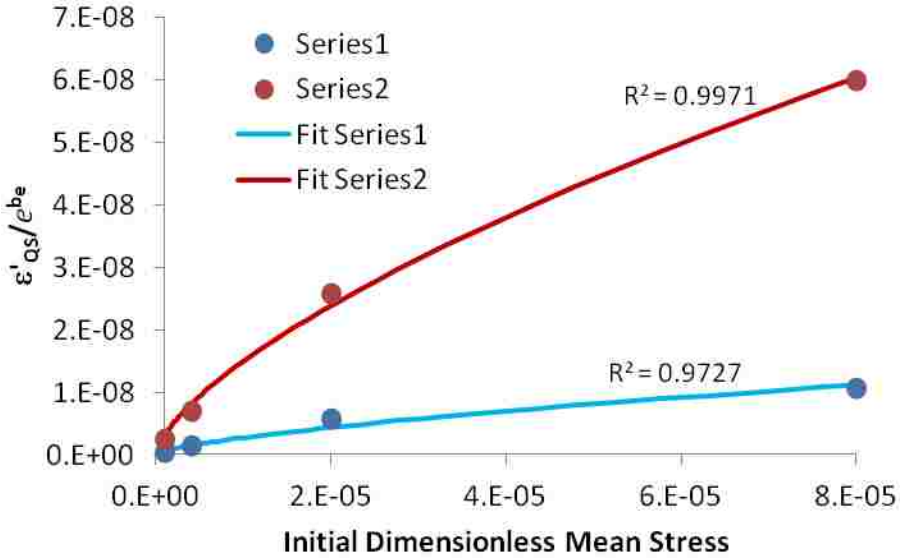

Fig. 86 Variation of the normalized ε'_{QS} with $\bar{\sigma}_0$ for the (ND) models; $I_{QS} = 0.1\%$

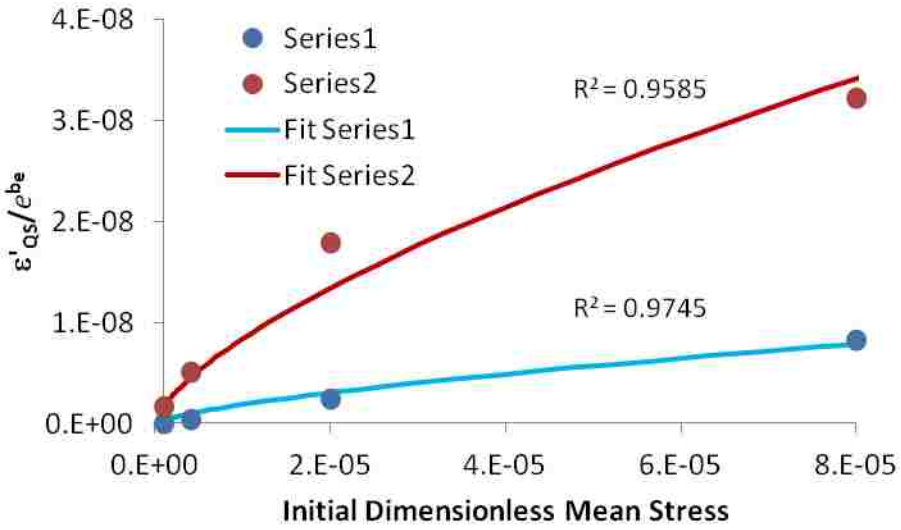

Fig. 87 Variation of the normalized ε'_{QS} with $\bar{\sigma}_0$ for the (OD) models; $I_{QS} = 0.1\%$

6.10. Relationship between ε'_{QS} and Δ

The effect of the PSD on ε'_{QS} was studied. For this purpose, a characteristic value was needed to represent the PSD. Several dimensionless parameters were created and tested, including the coefficient of curvature, C_c, and the coefficient of uniformity, C_u.

The best correlation was observed between ε'_{QS} and Δ, defined in the following form. Note that this parameter better suits for discretized PSDs.

$$\Delta = \frac{d_{\text{Avg}}}{d_{\text{min}}} \tag{80}$$

d_{min} and d_{Avg} are the nominal size of the smallest particle and the average nominal particle size by weight for the assembly of particles, respectively. The nominal size of a particle is defined as the diameter of a particle with the volume of a sphere equal to that of the particle. Δ was named dispersity index and can vary from unity, for a monosized PSD, to infinity in theory. Similar parameters, termed polydispersity indices, are found in chemistry and material sciences. However, the definition in Eq. (81) is preferred as it appears in the dimensionless formulation of the inertial number in Eq. (73).

To study the effect of Δ on ε'_{QS}, six samples (220, 221, 222, 223, 224, and 225) were used for which $\mu_0 = 0.10$ and $\bar{\sigma}_0 = 4 \times 10^{-6}$ were constant. Building samples with an equal void ratio using different PSDs was difficult. Hence, as mentioned in the previous section, the effect of e_0 was removed by considering the relationship between $\varepsilon'_{QS}/e_0^{b_e}$ and Δ instead of ε'_{QS} and Δ, assuming that the effect of e_0 on ε'_{QS} is independent of the effect of the PSD on ε'_{QS}.

The relationship is displayed in Fig. 88 and Fig. 89, where $\varepsilon'_{QS}/e_0^{b_e}$ is observed to decrease as Δ increases. However, the decrease has a faster rate for the models with the (OD) damping model. This relationship can be represented by a power function whose exponent, b_Δ, is 2.0 for the (ND) models where it is 2.5 for the (OD) models. R^2 values close to unity indicate the appropriateness of the selected function.

Thus, it is concluded that $\varepsilon'_{QS}/e_0^{b_e} \propto \Delta^{b_\Delta}$ or

$$\varepsilon'_{QS} \propto \Delta^{b_\Delta} \; ; \quad \begin{cases} b_\Delta = -2.0 \text{ for ND} \\ b_\Delta = -2.5 \text{ for OD} \end{cases} \tag{81}$$

It is worthy to mention that the inertial number predicts that $\varepsilon'_{QS} \propto \Delta^{-1}$.

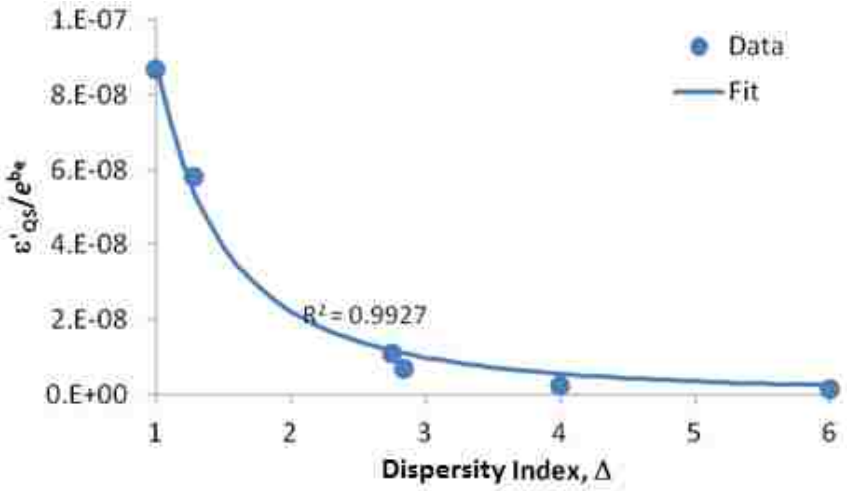

Fig. 88 Variation of the normalized ε'_{QS} with the dispersity index for the (ND) models; $I_{QS} = 0.1\%$

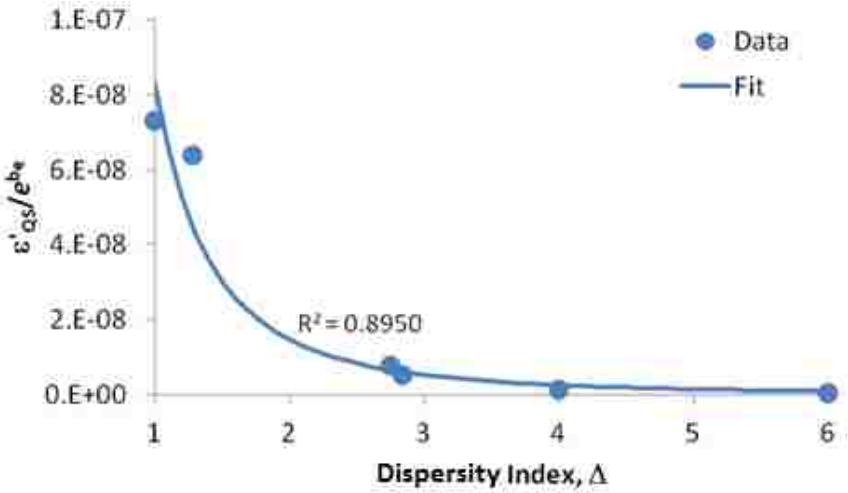

Fig. 89 Variation of the normalized ε'_{QS} with the dispersity index for the (OD) models; $I_{QS} = 0.1\%$

6.11. Dimensionless Forms of the Predicting Equations

The variation trends of ε'_{QS} with e_0, $\bar{\sigma}_0$, and Δ were identified in Sections 6.8, 6.9, and 6.10, referring to Eqs. (79), (80), and (82), respectively. Therefore, ε'_{QS} can be expressed proportional to the product of the terms, that is, $\varepsilon'_{QS} \propto e_0^{b_e} \bar{\sigma}_0^{\,b_\sigma} \Delta^{b_\Delta}$, or

$$\varepsilon'_{QS} = K e_0^{b_e} \bar{\sigma}_0^{\,b_\sigma} \Delta^{b_\Delta} \; ; \begin{cases} b_e = -4 \\ b_\sigma = 0.67 \\ \begin{cases} b_\Delta = -2.0 \;\; \text{for ND} \\ b_\Delta = -2.5 \;\; \text{for OD} \end{cases} \end{cases} \tag{82}$$

The K coefficient was determined by minimizing the error through the least squares method. Thus, the dimensionless forms of the proposed equations for the $I_{QS} = 0.1\%$ condition become as follows:

$$\begin{cases} \varepsilon'_{QS} = 2.7 \times 10^{-4} e_0^{-4} \bar{\sigma}_0^{\,0.67} \Delta^{-2} \;\; ; & \text{for the ND model} \\ \varepsilon'_{QS} = 2.7 \times 10^{-4} e_0^{-4} \bar{\sigma}_0^{\,0.67} \Delta^{-2.5}; & \text{for the OD model} \end{cases} \tag{83}$$

6.12. Test of the Proposed Equations on a Leave-Out Sample

The TTT sample is a test sample that was not used in any of the equations. With the $I_{QS} = 0.1\%$ criterion, the ε'_{QS} obtained from the simulations is 2.71×10^{-7} using the ND damping model and 9.08×10^{-8} using the OD damping model, according to Table 40 and Table 41, respectively. The values of e_0, $\bar{\sigma}_0$, and Δ for this sample are given in Table 39. Using Eq. (84), ε'_{QS} is obtained to be 3.36×10^{-7} and 1.36×10^{-7} for the ND and OD models, respectively, which indicate 24% and 49% error, respectively, compared with the values obtained directly from the simulations. The errors indicate that the proposed equations can be useful in practical applications.

6.13. Generalized Forms of the Proposed Equations

As shown in Section 6.5, the relationship between the moment index and ε' is a power function in the form of $I_{Mom} = a_I \varepsilon'^{b_I}$ according to Eq. (74). Assuming $I_{Mom} = I_{QS}$, one gets $\varepsilon' = \varepsilon'_{QS}$, or $I_{QS} = a_I \varepsilon'^{\,b_I}_{QS}$, or $\varepsilon'_{QS} = \left(\frac{I_{QS}}{a_I}\right)^{\frac{1}{b_I}}$ as a result. In the latter equation, evidently, by considering a greater value for I_{QS}, a greater ε'_{QS} is obtained. The assumption of $I_{QS} = 0.1\%$ was observed to result in very small deviations from the peak friction angles of the QS state, about 0.2° on average. If a lower precision is desired, a greater value for I_{QS} can be chosen to establish the QS state, which leads to a greater ε'_{QS} and a shorter runtime. Therefore, Eq. (84) can be modified to incorporate the assumptions of different I_{QS} criteria. Referring to Table 40 and Table 41, the b exponent differs for different samples. For the ND and OD models, $0.70 < b_I < 1.14$ and $0.47 < b_I < 1.04$ are observed, respectively. By conservatively assuming $b_I = 1$, the following equations are obtained for the case of $I_{QS} > 0.1\%$:

$$\begin{cases} \varepsilon'_{QS} = 0.27 e_0^{-4} \bar{\sigma}_0^{\,0.67} \Delta^{-2} I_{QS} \ ; & \text{for the ND model} \\ \varepsilon'_{QS} = 0.27 e_0^{-4} \bar{\sigma}_0^{\,0.67} \Delta^{-2.5} I_{QS}; & \text{for the OD model} \end{cases} \tag{84}$$

Using $\varepsilon'_{QS} = \dot{\varepsilon}_{QS} \Delta t_c$, $\Delta t_c = d_{\min}\sqrt{\rho/E}$, $\bar{\sigma}_0 = \sigma_c/E$, and $\Delta = \frac{d_{\text{Avg}}}{d_{\min}}$, Eq. (85) can be generalized to the following dimensional forms:

$$\begin{cases} \dot{\varepsilon}_{QS} = \dfrac{0.27 d_{\min} \sigma_c^{0.67} I_{QS}}{d_{\text{Avg}}^2 \rho^{0.5} E^{0.17} e_0^4} \ ; & \text{for the ND model} \\ \dot{\varepsilon}_{QS} = \dfrac{0.27 d_{\min}^{1.5} \sigma_c^{0.67} I_{QS}}{d_{\text{Avg}}^{2.5} \rho^{0.5} E^{0.17} e_0^4}; & \text{for the OD model} \end{cases} \tag{85}$$

6.14. Comparison of the ND and OD damping models in terms of ε'_{QS}

Since all the 19 samples were examined using both damping models, ND and OD, we aimed to determine the improvement on ε'_{QS} that is achieved using the damping model that was introduced in Chapter 5, that is, the ND model, with respect to the conventional mass damping model, that is, the OD model. The ratio, $\frac{(\varepsilon'_{QS})_{ND}}{(\varepsilon'_{QS})_{OD}}$, indicates the speed gain that the ND model provides over the OD damping model. In other words, it tells us how higher the strain rate can be using the ND model compared with the OD model to yield the same moment index of 0.1%.

By dividing the proposed relationships in Eq. (84), the speed gain is expected to be about $\frac{(\varepsilon'_{QS})_{ND}}{(\varepsilon'_{QS})_{OD}} = \sqrt{\Delta}$, which indicates that the higher is the dispersity index of the PSD of a sample, the higher is the benefit that one can get from using the ND model in terms of simulation speed. The exact speed gain values are presented in Table 46 as well as in Fig. 90 for the samples. The improvements are minimal for Samples 220 (monosized with $\Delta = C_u = 1$) and 223 (narrow PSD with $\Delta = 1.3$ and $C_u = 1.2$), indicating nearly no improvements, while greater improvements (about four times) are observed for the samples with large dispersity indices, Samples 121 and 241 (both with $\Delta = 6$ and $C_u = 2.6$), for example.

Table 46 Improvement of the quasi-static strain rates of the models using the (ND) damping model with respect to the (OD) damping model ($I_{QS} = 0.1\%$)

Model	**121**	**122**	**211**	**212**	**220**	**221**	**222**	**223**	**224**	**225**	**231**	**232**	**241**	**242**	**321**	**322**	**421**	**422**	**TTT**
Δ	6.0	2.8	6.0	2.8	1.0	6.0	2.8	1.3	4.0	2.8	6.0	2.8	6.0	2.8	6.0	2.8	6.0	2.8	6.2
$\frac{(\varepsilon'_{QS})_{ND}}{(\varepsilon'_{QS})_{OD}}$	4.4	1.4	3.2	1.6	1.2	3.1	1.3	0.9	1.6	1.4	2.8	1.9	3.8	1.6	2.3	1.4	1.3	1.9	3.0

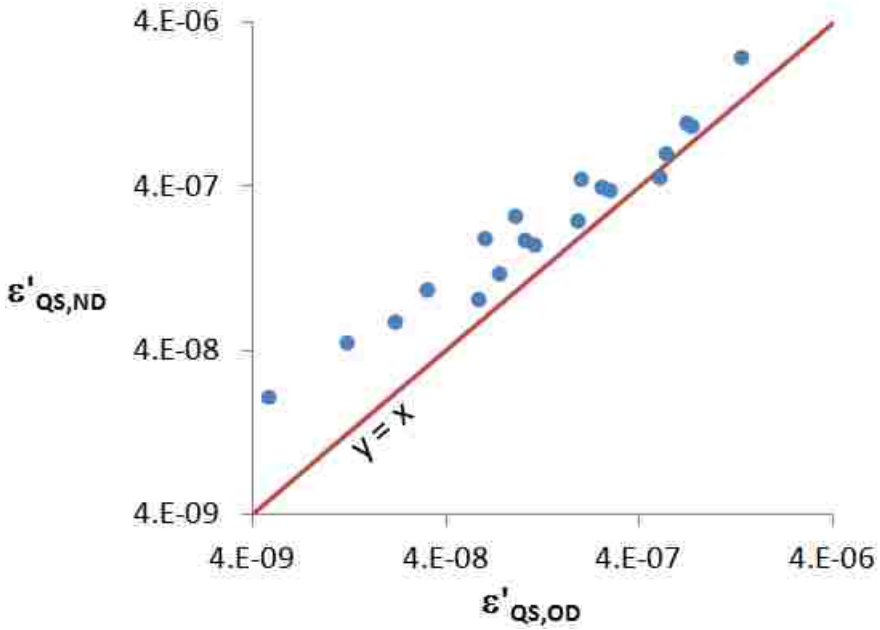

Fig. 90 Quasi-static strain rates of the models using the (ND) damping model versus the (OD) damping model ($I_{QS} = 0.1\%$)

6.15. Comparison of the Proposed Equations and Inertial Number

In this section, the predictive ability of the proposed equations, that is, Eq. (84), was compared with that of the inertial number, that is, using Eq. (73). Note that I is not specified by da Cruz et al. (2005); however, Macaro and Utili (2012) recommended $I \leq 2 \times 10^{-4}$. To conduct a fair comparison, I was determined by finding the best fit of Eq. (73) to the ε'_{QS} values that were deduced directly from the simulations based on the

$I_{QS} = 0.1\%$ criterion. For the samples using the ND and OD models, I was found to be 5.8×10^{-4} and 3.7×10^{-4}, respectively.

Using Eq. (73) with the calculated inertial numbers, the quasi-static strain rates, ε'_{QS}, were specified and presented against the exact ε'_{QS} values from the simulations along with the predictions of the proposed equations in Fig. 91 and Fig. 92 for the ND and OD models, respectively. R^2 of the predicted values of ε'_{QS} obtained from Eq. (84) for the ND series is 0.97, while it is 0.80 using the inertial number. R^2 of the predictions of Eq. (84) for the OD series is 0.92, while it is 0.89 using the inertial number. In terms of relative error, our equation yields 24% and 38% error for all the models on average for the ND and OD models, respectively, whereas the average errors resulted using the inertial number are 98% and 202%, respectively.

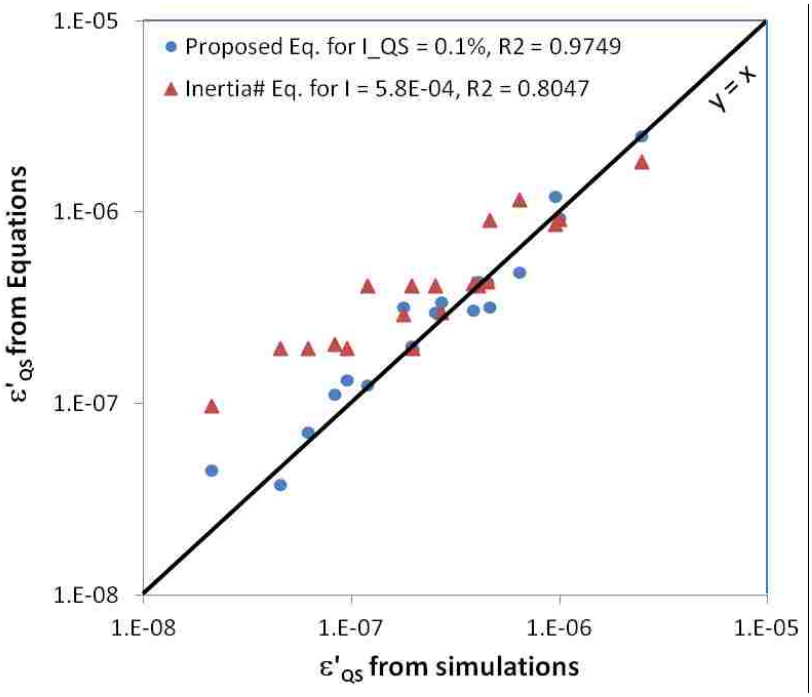

Fig. 91 Predictions of ε'_{QS} using the proposed equation and inertia number for the (ND) models compared with ε'_{QS} from simulations

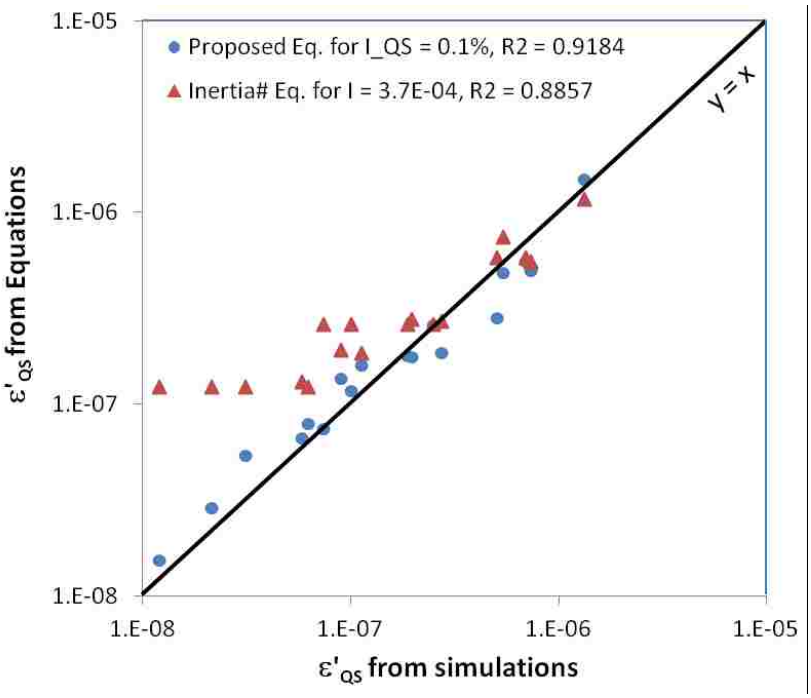

Fig. 92 Predictions of ε'_{QS} using the proposed equation and inertia number for the (OD) models compared with ε'_{QS} from simulations

6.16. Approximation Methods for Prediction of the Quasi-Static Friction Coefficient

Chapter 5 suggests a method to approximate the QS friction angle of particulate assemblies using the results of simulations with a constant high strain rate and different damping ratios. In this chapter, two more methods are proposed based on simulations with different high strain rates. The results of three dimensionless strain rates (1×10^{-5}, 5×10^{-6}, and 2×10^{-6}) are used to obtain the QS peak friction angle.

In the first method, Eq. (76), is used. This model has three parameters, $\tan\phi_0$, a_ϕ, and b_ϕ, which were determined by three $(\varepsilon', \phi_{\text{peak}})$ data points. These calculations involved solving nonlinear systems of equations using the Newton-Raphson method. After fitting Eq. (74) to the three data points, this equation was used to predict ϕ_{peak} at $\varepsilon' = 0$, that is, ϕ_{QS}.

In the second method, Eq. (75) is used. Two parameters, $\tan\phi_0$ and k, are determined from the three $(\varepsilon', \phi_{\text{peak}})$ data points by least squares fitting. Then, the resulting equation can be used to predict ϕ_{peak} at $I_{Mom} = 0$, that is, ϕ_{QS}.

The peak friction coefficients predicted using these two methods were compared with the exact $\tan\phi_{QS}$ values from the simulations (corresponding to $I_{Mom} = 0.1\%$) and are presented in Table 47, where the second method exhibits less error on average.

Table 47 Peak friction angle approximation for the (ND) models using (a) $\tan\phi$ vs. ε' curve with three points, and (b) $\tan\phi$ vs. I_{Mom} curve with three points

Model	$\tan\phi_{QS}$	Approximation Method	
		(a)	(b)
121ND	0.61	12.6%	-0.5%
122ND	0.54	-13.2%	4.6%
211ND	0.74	1.1%	0.8%
212ND	0.68	-6.3%	1.2%
220ND	0.53	-6.1%	0.6%
221ND	0.65	-2.8%	3.0%
222ND	0.56	-1.5%	0.9%
223ND	0.52	-4.5%	0.1%
224ND	0.62	-6.6%	3.6%
225ND	0.55	-1.1%	2.3%
231ND	0.50	1.4%	4.6%
232ND	0.44	-13.4%	5.2%
241ND	0.38	-15.0%	1.3%
242ND	0.36	0.6%	-0.7%
321ND	0.66	2.2%	1.6%
322ND	0.59	-1.9%	0.3%
421ND	0.69	-1.6%	0.3%
422ND	0.60	-1.2%	0.0%
TTTND	0.60	-3.7%	2.5%
Average Error		**5.1%**	**1.8%**

6.17. Summary

A total of 342 numerical triaxial tests in drained conditions, including 19 samples, two damping models, and nine strain rates, were carried out to determine the quasi-static strain rate and the effects of the initial void ratio, confining stress, and particle-size distribution on the quasi-static strain rate.

The strain rate corresponding to the moment index value of $I_{QS} = 0.1\%$ was proposed as a criterion to determine the quasi-static strain rate. This criterion was shown to lead to small errors for the peak friction angles of particulate assemblies, less than 0.5°, with respect to the quasi-static friction angles, which is sufficient for practical applications. The greater was the selected strain rate than the quasi-static strain rate, the greater was the peak friction angle than the quasi-static peak friction angle.

The power function was used to describe the relationship between the moment index and strain rate. This power function can be used to estimate the quasi-static strain rate. The predicted quasi-static strain rates matched the quasi-static strain rates obtained directly from the simulations with sufficient precision for use in practice.

Based on observation, a power function can describe the relationship between the moment index and the strain rate. Also, a linear relationship between the peak friction coefficient and the corresponding moment index value was observed, which is in agreement with the observations of da Cruz et al. (2005). Furthermore, a model was deduced to describe the relationship between the peak friction coefficient and strain rate, which is in agreement with the viscoelastic model of Cowper and Symonds (1957). This well-known model remarkably matched the data in the present study and proved its capability in describing the shear-thinning behavior of particulate media.

The study of the relationship between the quasi-static strain rate and the initial void ratio showed a correlation that can be expressed by a power function with a negative exponent. The inertial number (da Cruz et al., 2005) that is independent of the void ratio lacks this feature and thus suits for the prediction of the quasi-static strain rate that is only suitable for determining critical state values.

A relationship between the quasi-static strain rate and confining pressure (i.e., initial mean stress) was observed. This direct correlation can be expressed by a power function with an exponent equal to 0.67.

The quasi-static strain rate was shown to depend on the particle-size distribution. An inverse correlation in the form of a power function was observed between the quasi-static strain rate and the proposed dispersity index, Δ, which is a characteristic value to represent the particle-size distribution. For the abovementioned power function, the exponent was determined to be equal to 2, for ND damping model, and 2.5 for OD model.

By combining the identified trends found for the relationship of the quasi-static strain rate with the initial void ratio, the dimensionless confining pressure, and the dispersity index and determining the unknown coefficient, the predictive equations were proposed to estimate the dimensionless quasi-static strain rate of samples using the ND and OD damping models with the $I_{QS} = 0.1\%$ criterion. The equations were generalized for $I_{QS} > 0.1\%$ and presented in dimensional forms for practical applications.

The quasi-static strain rates were estimated by the proposed equations for a leave-out sample and compared with the quasi-static strain rates obtained from simulations using

the ND and OD damping models. The comparison showed that the predicted values were accurate enough for practical uses. Moreover, the inertial number was tuned for the models, and the predictions of the inertial number were compared with those of the proposed equations where the proposed equations showed better performances in terms of coefficient of determination and relative error.

The ND and OD damping models were compared in terms of the quasi-static strain rate, and the size-dependent ND model demonstrated improvement over the conventional OD model. The ND model improves the quasi-static strain rate by $\sqrt{\Delta}$ times. The wider is the particle-size distribution, the higher is the increase in the quasi-static strain rate by using the ND damping model. As Δ is equal or greater than unity, the ND model yields less moment index (i.e., less imbalance) than the conventional mass-damping model.

In addition to the damping-based approximation method that was introduced in Chapter 5 for the prediction of the peak friction coefficients of granular assemblies at the quasi-static state, two more methods were introduced. The first method was based on the relationship between the peak friction coefficient of the assembly and the strain rate. The second method was based on the linear relationship between the peak friction coefficient and the moment index. Three or more simulations are needed at high strain rates to use these methods. The outcomes of both methods were reasonable for the models in this study; however, the second method involves less mathematics and the results were more accurate.

Chapter 7

Conclusions and Future Works

7.1. Overview

Particulate media are encountered in many engineering applications. The discrete element method has proved its ability in capturing the complex behavior of particulate media. Input parameters greatly affect the DEM simulations results. If inappropriate values are selected, the outcomes of simulations may involve unrealistic responses, which may result in incorrect interpretations and problematic designs. Hence, it is important to select appropriate models and suitable values for the parameters. Where a Hertzian contact model and a mass-damping model are adopted, some of the parameters are the density, elastic modulus, and characteristic size of particles, as well as the damping coefficient or ratio, strain rate, and time step.

7.2. Major Findings

In the following section, the major findings of this study are presented:

1. When the strain rate and damping coefficient are defined inversely proportional to a characteristic time of a model (for which a nominal critical time step is adopted), it was shown that the responses in the dimensionless units are independent of the selected values for density, elastic modulus, and characteristic size of particles. The dimensionless units were built based on a characteristic length and time measures of samples. In this

system, the density, elastic modulus, and characteristic length have only scaling effects on the results.

2. The dimensionless strain rate, , and the mass-damping ratio extremely affect the behavior of models. For instance, a loose sample with a high strain rate or a high damping ratio in undrained conditions can develop a response similar to that of a dense sample. Thus, it is of great importance to select appropriate values for the dimensionless strain rate and the damping ratio.

3. The density scaling and stiffness scaling techniques were assessed. It was learned that the increase in the density and size of particles are equivalent to the increase of the dimensionless strain rate and damping ratio if the dimensionless strain rate and damping coefficient are kept constant.

The reduction of elastic modulus has the same effect. Also, if the confining pressure and void ratio are kept constant, the dimensionless stress, i.e., stress normalized by the elastic modulus, increases as well.

Scaling up the density and/or particle sizes result in aggravating the equilibrium state. However, scaling down the elastic modulus has an insignificant effect on the equilibrium state of samples when inertia-induced forces are compared to the static forces; however, it changes the mechanical behavior of samples, which is not desired. Therefore, the application of the scaling techniques is not recommended.

4. For a sample with any combination of damping ratio and strain rate, when the product of the damping ratio and the strain rate is constant, and the damping ratio is greater than a

specific limit, which is called optimum damping, the same mechanical behavior is observed. That is, if the damping ratio is greater than the optimum damping ratio, further increase in the damping ratio has the same effect as the increase in the strain rate with the same factor. Thus, applying large amount of damping ratio is not recommended, as it worsens the equilibrium state.

5. An automatic algorithm was devised to create samples with desired confining pressures and compactness. Samples with different void ratios can be created using this algorithm by adjusting the inter-particle friction coefficient. A friction coefficient less than or equal to 0.03 yields the densest samples, while 0.47 or greater yields the loosest samples. It was known that the relative density of the produced samples strongly correlated with the inter-particle friction coefficient regardless of the applied confining stress. Therefore, the inter-particle friction coefficient can be adjusted accordingly to achieve samples with desired relative densities.

6. A new mass-damping model, namely the size-dependent mass-damping model, which is similar to the conventional model, was introduced. In the new damping model, the damping coefficient is adjusted to each particle based on the size and natural frequency of each particle to yield equal damping ratios for all particles. This model, which is in agreement with the damping model proposed by Munjiza et al. (1998) and whose exponent is set to 0.5, improves the equilibrium state and enables users to apply higher strain rates, thereby reducing runtimes, especially for samples with wide particle-size distributions.

7. An indicator was proposed for quantitative evaluation of the equilibrium state of samples, namely moment index. The moment index was defined as a measure of the unbalanced stresses divided by magnitude of the octahedral stress of a sample. A lower moment index value indicates a better equilibrium state and approach to the quasi-static conditions.

8. The optimum damping ratio was defined as a damping ratio such that the moment index is minimized at a specific strain rate. At any specific strain rate, a damping ratio equal to zero results in a high value for the moment index. As damping ratio is increased from zero, the moment index decreases and reaches its minimum value. The damping ratio corresponding to the minimum moment index was defined as optimum damping ratio. With further increase in the damping ratio, the moment index increases. Samples with damping ratios less than the optimum damping ratio indicate higher imbalance, lower peak friction angle, higher amounts of idle particles, and more contractive behavior. Therefore, setting the damping ratio less than the optimum damping ratio is not recommended. It was observed that the peak friction coefficient of an assembly is a function of the product of damping ratio and strain rate. Increasing the damping ratio or the strain rate excessively results in unrealistic increase of the peak shear strength, thus should be avoided.

7.2.1. Constitutive Equations

Three constitutive equations were observed in this research. The imbalance in terms

of the moment index was shown to depend on the strain rate as well as the damping ratio. For any sample, a relationship was observed between the moment index value and product of the damping ratio and the strain rate when the damping ratio is greater than or equal to the optimum damping ratio. This relationship can be expressed well by a power function, i.e.,

$$I_{Mom} = a_I(\xi\varepsilon')^{b_I}; \quad \xi \geq \xi_{opt} \tag{86}$$

Therefore, with a constant damping ratio equal to the optimum value, the strain rate can be determined at which the moment index yields a specific value. The quasi-static strain rate was defined as the strain rate that corresponds to the moment index of $I_{QS} = 0.1\%$. It was shown that at the above-defined strain rate, the resulting peak friction angle converges to a minimum value within maximum 0.5° error, which indicates the quasi-static conditions are fulfilled.

The peak friction coefficient, $\mu = \tan\phi_{peak}$, shows a linear relationship with the moment index:

$$\tan\phi_{peak} = \tan\phi_{QS} + kI_{Mom} \tag{87}$$

where ϕ_{QS} is the peak friction angle at the quasi-static state, and k is a constant specific to every sample. This equation, which agrees with findings of da Cruz et al. (2005), indicates that the greater the moment index is, the greater is the peak friction coefficient compared to the peak friction coefficient at quasi-static state.

Combining Eqs. (98) and (88), the relationship between the peak friction coefficient and the damping ratio and dimensionless strain rate is obtained as follows:

$$\tan\phi_{peak} = \tan\phi_{QS} + a_{\phi}(\xi\varepsilon')^{b_{\phi}} \quad (88)$$

where $a_{\phi} = ka_I$ and $b_{\phi} = b_I$. Eq. (89), which is similar to the model of Cowper-Symonds (1957), can represent the viscoelastic behavior of non-cohesive particulate assemblies very well. As b_{ϕ} is less than unity, a shear-thinning behavior is perceived.

7.2.2. Approximation Methods

Two methods were proposed to estimate the quasi-static strain rate, and three methods were presented to approximate the peak friction coefficient of particulate samples.

Approximation of Quasi-Static Strain Rate Using High Strain Rate Simulations

By setting the damping ratio to a value greater than or equal to the optimum damping ratio, Eq. (98) simplifies to $I_{Mom} = a\varepsilon'^{b}$. By conducting two or three simulations at high strain rates and measuring the moment index values, a and b parameters can be specified by conducting a linear regression. Then, the quasi-static strain rate can be estimated by letting $I_{Mom} = I_{QS}$.

Prediction of Quasi-Static Strain Rate without Simulation

The effects of density, elastic modulus, and characteristic size of particles on the quasi-static strain rate were ruled out by employing the dimensionless scheme. Then, the dimensionless quasi-static strain rate, ε'_{QS}, was shown to depend on the initial void ratio, e_0, dimensionless confining pressure, $\bar{\sigma}_0$ (i.e., confining pressure normalized by the

elastic modulus), and the particle-size distribution of samples.

The relationship of ε'_{QS} with e_0 can be approximated by a power function whose exponent is equal to -4. As e_0 increases, ε'_{QS} decreases. The relationship of ε'_{QS} with $\bar{\sigma}_0$ can be approximated by a power function whose exponent is equal to 0.67. As $\bar{\sigma}_0$ increases, ε'_{QS} increases. In order to determine the relationship between ε'_{QS} and particle-size distribution, a characteristic parameter is needed. It was shown that the dispersity index, which was defined as the ratio of the average of particle sizes by weight to the minimum particle size, i.e., $\Delta = \frac{d_{\text{Avg}}}{d_{\min}}$, suits this aim. The relationship between ε'_{QS} and Δ can be expressed by a power function approximately. However, the exponent was different for the conventional and the size-dependent damping models. The exponent was determined equal to -2 and -2.5 for those damping models, respectively. The wider the particle-size distribution of sample, the greater the dispersity index and the lower ε'_{QS}.

By combining the individual relationships of ε'_{QS} with e_0, $\bar{\sigma}_0$, and Δ, dimensionless equations were proposed to predict ε'_{QS} for $I_{QS} = 0.1\%$. Then, these equations were generalized for $I_{QS} > 0.1\%$, and the dimensional forms were presented for the conventional and size-dependent mass-damping models as follows:

$$\begin{cases} \dot{\varepsilon}_{QS} = \dfrac{0.27 d_{\min} \sigma_c^{0.67} I_{QS}}{d_{\text{Avg}}^2 \rho^{0.5} E^{0.17} e_0^4} \;\; ; \;\; \text{for ND model} \\ \dot{\varepsilon}_{QS} = \dfrac{0.27 d_{\min}^{1.5} \sigma_c^{0.67} I_{QS}}{d_{\text{Avg}}^{2.5} \rho^{0.5} E^{0.17} e_0^4} ; \quad \text{for OD model} \end{cases} \tag{89}$$

The cross-validation through the comparison of the resulting values using the predictive equations with the values obtained from the simulations for a leave-out sample

was carried out. Moreover, the comparison of the values obtained using the predictive equation with those using the inertial number (da Cruz et al., 2005) demonstrated the superiority of the proposed equations. In addition, it was shown that the size-dependent damping model improves the quasi-static strain rate by $\sqrt{\Delta}$ times approximately. Note that the dispersity index is always greater or equal to unity.

First Approximation Method for Peak Friction Coefficient based on Damping

The relationship between the peak friction coefficient and the moment index, i.e., Eq. (88), is used in this method. A few simulations (three or more) are performed at a selected high strain rate with different damping ratios greater than or equal to the optimum damping ratio, and the peak friction coefficients and the moment index values are measured. Then, using a linear regression and regarding the fact that ε' is constant, Eq. (88) is fitted and ϕ_{QS} is obtained.

Second Approximation Method for Peak Friction Coefficient based on Strain Rate

The relationship between the peak friction coefficient and the moment index, i.e., Eq. (88), is used in this method as well. A few simulations (three or more) are performed using a constant damping ratio greater than or equal to the optimum damping ratio at different high strain rates, and the peak friction coefficients and moment index values are measured. Then, using a linear regression and regarding the fact that ξ is constant, Eq. (88) is fitted and ϕ_{QS} is obtained.

Third Approximation Method of Peak Friction Coefficient using Viscoelastic Model

The relationship between the peak friction coefficient and strain rate, i.e., Eq. (89), is used in this method. A few simulations (three or more) are performed using the optimum damping ratio at different high strain rates, and the peak friction coefficients are measured. Then, using the least squares method and regarding the fact that ξ is constant, Eq. (89) is fitted and ϕ_{QS} is obtained. Note that this method involves nonlinear regression and results in a lower precision than the previous method.

7.3. Suggestions for Future Works

Following are some suggestions for future studies that we believe may help to get a deeper insight into the discrete element modeling and improve DEM efficiency in the applications through selecting suitable models and parameters.

1. Constant $\xi\varepsilon'$ phenomenon

It was observed that for a specific model with a constant product of damping ratio and strain rate (if the damping ratio is greater than or equal to the optimum damping ratio), any combination of the damping ratio and strain rate results in an identical mechanical response except for resulting in different particle velocities. This was observed in the numerical tests of the present study; however, the analytical reason behind that was not known. Finding the analytical reason can be very valuable

2. Comparison of different damping models

Two mass-proportional damping models were tested and compared. The proposed size-dependent model, in comparison to the conventional mass-damping model,

demonstrated improvement in the equilibrium state of samples and enabled the application of higher strain rates while maintaining the quasi-static conditions. Other damping models exist that work in the contact level rather than the particle level, e.g., the local hysteretic damping model (Cundall, 1987), in which the damping forces of contacts are proportional to the contact force, and the local viscous damping model (Cleary, 2000), where the damping forces of contact are proportional to the relative velocity of contacting particles. In these local models, contact damping forces are summed and added to the equilibrium equations of the particles. It is suggested to compare these models to the size-dependent damping model in terms of the equilibrium state using the moment index. Also, determining suitable damping amounts for these models in terms of damping ratio can be beneficial.

3. Determining suitable damping ratio and strain rate for undrained conditions

The optimum damping ratio and quasi-static strain rate were determined for simulations in drained conditions. Suitable parameters may differ for testing in drained and undrained conditions. Drained tests are usually carried out by applying very low strain rates to simulate long-term loading conditions in quasi-static state, whereas undrained tests simulate the effect of short-term loads, such as earthquakes and landslides, and cannot be considered quasi-static, as particle velocities are relatively high, and thus, the inertia induced effects cannot be neglected. It was shown that damping ratio and strain rate may affect material response significantly, such that, for example, a loose sample may behave like a dense sample if a high strain rate or damping ratio is applied. Therefore, determining a suitable damping ratio and strain rate to be used in tests with undrained conditions is of a great value.

APPENDICES

Appendix 1. Relationship between Critical Time Step and Characteristic Time

Appendix 2. Definition of Damping Ratio for Mass-Proportional Damping

Appendix 3. Dimensionless Forces and Moments are independent of ρ, E, and L_0.

Appendix 4. Dimensionless Stress is independent of ρ, E, and L_0.

Appendix 5. Constant Strain Rate Boundary Conditions in Dimensionless DEM

Appendix 6. Derivation of Dimensionless DEM Formulation

Appendix 7. Sample Preparation Results

Appendix 8. Output parameters of models in Chapter 5

Appendix 9. Output parameters of models in Chapter 6

Appendix 1. Relationship between Critical Time Step and Characteristic Time

Most DEM codes use either the central difference time integration algorithm or a slightly modified version of it to solve the governing equations, i.e. Eqs. (42) and (43). The time increment used in this method must be smaller than the critical time step to avoid numerical instability. The critical time step is related to the highest natural frequency of the system, ω_{max}, via the following equation (Belytschko, 1983):

$$\Delta t_c = \frac{2}{\omega_{max}} \tag{90}$$

Different approaches, such as that shown in Table 48, have been proposed to estimate the critical time increment. Our critical time step is calculated as follows (Šmilauer and Chareyre, 2010):

$$\Delta t_c = 2R_{min}\sqrt{\frac{\rho}{E}} \tag{91}$$

Based on our choice of the characteristic length in Eq. (15), we get

$$\Delta t_c = T_0 \tag{92}$$

Table 48 Estimate of critical time step for central difference time integration in DEM

Reference	Equation	Estimation Base	Comments
Sheng et al. (2004)	$\Delta t_c = \frac{\pi R_{min}}{\alpha}\sqrt{\frac{\rho}{G}}$	Rayleigh wave speed	$G = \frac{E}{2(1+\nu)}$ † $\alpha \simeq 0.163\nu + 0.8766$
Šmilauer and Chareyre (2010)	$\Delta t_c = l_{min}\sqrt{\frac{\rho}{E}}$	Sonic speed	$l_{min} = \begin{cases} 2R_{min}; \text{for periodic BC} \\ R_{min}; \text{for rigid BC} \end{cases}$

† ν is Poisson's ratio and G is the shear modulus of the particles.

Appendix 2. Definition of Damping Ratio for Mass-Proportional Damping

The damping constant in translational motion can be determined in terms of mass, giving the so-called mass-proportional damping:

$$c_i = \alpha_i m_i \tag{93}$$

where α_i is the coefficient of mass-proportional damping.

According to the classical dynamics, the critical damping of the particle, c_i^c, is defined as:

$$c_i^c = 2m_i\omega_i \tag{94}$$

where ω_i is natural frequency of the particle *i*.

Damping can be expressed in terms of the critical damping and a damping ratio as

$$c_i = c_i^c\,\xi \tag{95}$$

where ξ is the mass-proportional damping ratio, which is equal for all of the particles in an assembly.

Eqs. (95) and (96) give

$$c_i = 2m_i\omega_i\xi \tag{96}$$

Eqs. (97) and (94) give

$$\alpha_i = 2\omega_i\xi \tag{97}$$

There is no universal closed-form solution for computing the exact ω_i for particulate assemblies. Using Eqs. (91) and (92), the highest natural frequency of the entire assembly is approximated as follows:

$$\omega_{max} = \frac{1}{R_{min}}\sqrt{\frac{E}{\rho}} \tag{98}$$

In practice, a constant value, α_0, is used for mass-proportional damping in an assembly for all of the particles of different sizes, i.e.

$$\alpha_0 = 2\omega_0\xi \tag{99}$$

Letting $\omega_0 = \omega_{max}$ means that this damping is customized for the highest natural frequency of the assembly, which is attributable to the smallest particle. With this assumption, and using Eq. (99), one gets:

$$\alpha_0 = \frac{2\xi}{R_{min}}\sqrt{\frac{E}{\rho}} \tag{100}$$

Recalling Eqs. (15) and (16), we have

$$\alpha_0 = \frac{4\xi}{T_0} \tag{101}$$

Also, α_0 is used for the rotational degrees of freedom as in Eq. (28).

Appendix 3. Dimensionless Forces and Moments are independent of ρ, E, and L_0.

In Eq. (37), the contact force of the adjacent particle *j* that acts on the particle *i* is the vector sum of the normal and tangential components of the contact force, respectively, i.e.

$$F_{ij}^{c} = F_{ij}^{n} + F_{ij}^{t} \tag{102}$$

In this study, the Hertzian contact model is used for the normal component of the contact force, F_{ij}^{n}, whose magnitude, $\left|F_{ij}^{n}\right|$, can be calculated using the following equation:

$$\left|\Delta_{ij}\right|^{3} = \frac{9\left|F_{ij}^{n}\right|^{2}}{16R_{ij}^{*}E_{ij}^{*\,2}} \tag{103}$$

In this equation, Δ_{ij} is the overlap vector developed between contacting particles, *i* and *j*. The equivalent particle radius, R_{ij}^{*}, and the effective elastic modulus, E_{ij}^{*}, for the contact between particle *i* and particle *j* are given by:

$$R_{ij}^{*} = \frac{R_i R_j}{R_i + R_j} \tag{104}$$

where R_i is the average radius of particle *i* and

$$\frac{1}{E_{ij}^{*}} = \frac{1-\nu_i^2}{E_i} + \frac{1-\nu_j^2}{E_j} \tag{105}$$

ν_i is the Poisson's ratio of the material of particle *i*. If the material properties of the particles are the same, i.e. $E_i = E_j = E$ and $\nu_i = \nu_j = \nu$, employing Eq. (106), the following expression can be used for the effective elastic modulus:

$$E^{*} = E_{ij}^{*} = \frac{E}{2(1-\nu^2)} \tag{106}$$

Then, Eq. (104) can be rewritten using Eq. (105) and (107) as follows:

$$\left|F_{ij}^{n}\right| = \frac{2E}{3(1-\nu^2)}\sqrt{\frac{R_i R_j \left|\Delta_{ij}\right|^3}{R_i + R_j}} \tag{107}$$

We define a dimensionless counterpart for the normal component of the contact force, whose magnitude is given as follows:

$$\left|\bar{F}_{ij}^{n}\right| = \frac{2}{3(1-\nu^2)}\sqrt{\frac{\bar{R}_i \bar{R}_j \left|\bar{\Delta}_{ij}\right|^3}{\bar{R}_i + \bar{R}_j}} \tag{108}$$

In Eq. (109), the dimensionless radius of the particles *i* and *j* and their dimensionless overlap are given by the following equations, respectively:

$$\bar{R}_i = \frac{R_i}{L_0} \tag{109}$$

$$\bar{\Delta}_{ij} = \frac{\Delta_{ij}}{L_0} \tag{110}$$

Using Eq. (108) and (109), one gets

$$\left|F_{ij}^{n}\right| = EL_0^2\left|\bar{F}_{ij}^{n}\right| \tag{111}$$

Therefore,

$$F_{ij}^{n} = EL_0^2\bar{F}_{ij}^{n} \tag{112}$$

$\left|\bar{F}_{ij}^{n}\right|$ in Eq. (109) is constant as $\bar{R}_i$, $\bar{R}_j$, and $\bar{\Delta}_{ij}$ are constant according to the assumption of a constant initial dimensionless geometry in Section 3.4, and ν is a dimensionless constant. Thus, $\bar{F}_{ij}^{n}$ is constant in Eq. (113).

Eq. (113) can also be used if the linear contact model is utilized. In that case, the normal stiffness must be expressed in the form of $K_n = k_n E R_0$, where k_n is a dimensionless coefficient. Then the dimensionless normal contact force will be $\bar{F}_{ij}^{n} =$

$k_n \bar{\Delta}_{ij}$.

A simplified tangential contact force model based on Mindilin and Deresiewicz (1953) with a truncation that justifies Coulomb-type friction (Lin and Ng, 1997) is used in this study:

$$F_{ij}^t = \sum_{t=t_1}^{t_2} K_{ij}^t(t)\, \Delta_{ij}^t(t)\,, \qquad \left|F_{ij}^t\right| \le \mu \left|F_{ij}^n\right| \tag{113}$$

Note that the tangential force has to be calculated incrementally as it is path dependent. In Eq. (114), t_1 and t_2 are the time at which contact begins and the current time, respectively. $\Delta_{ij}^t(t)$ is the tangential projection of the contact overlap increment at time *t*, and $K_{ij}^t(t)$ is the tangential stiffness of the contact at *t*, which is given by the following equation by suppressing the time argument (t).

$$K_{ij}^t = \frac{2(1-\nu)}{(2-\nu)} K_{ij}^n \tag{114}$$

where K_{ij}^n is the normal contact stiffness and is given by

$$K_{ij}^n = \frac{\mathrm{d}\left|F_{ij}^n\right|}{\mathrm{d}\left|\Delta_{ij}\right|} \tag{115}$$

or

$$K_{ij}^n = \frac{E}{(1-\nu^2)} \sqrt{\frac{R_i R_j \left|\Delta_{ij}\right|}{R_i + R_j}} \tag{116}$$

Eq. (115) and (117) give

$$K_{ij}^t = \frac{2E}{(2-\nu)(1+\nu)} \sqrt{\frac{R_i R_j \left|\Delta_{ij}\right|}{R_i + R_j}} \tag{117}$$

Substituting Eq. (118) in Eq. (114) gives

$$F_{ij}^{t} = \frac{2E}{(2-\nu)(1+\nu)}\sqrt{\frac{R_i R_j}{R_i+R_j}}\sum_{t=t_1}^{t_2}\Delta_{ij}^{t}(t)\sqrt{\left|\Delta_{ij}(t)\right|}\,, \qquad \left|F_{ij}^{t}\right| \leq \mu\left|F_{ij}^{n}\right| \tag{118}$$

We define the following dimensionless tangential force:

$$\bar{F}_{ij}^{t} = \frac{2}{(2-\nu)(1+\nu)}\sqrt{\frac{\bar{R}_i \bar{R}_j}{\bar{R}_i+\bar{R}_j}}\sum_{\tau=\tau_1}^{\tau_2}\bar{\Delta}_{ij}^{t}(\tau)\sqrt{\left|\bar{\Delta}_{ij}(\tau)\right|}\,, \qquad \left|\bar{F}_{ij}^{t}\right| \leq \mu\left|\bar{F}_{ij}^{n}\right| \tag{119}$$

Using Eqs. (110) to (112) and (120) and (119) and letting $\Delta_{ij}^{t} = L_0\bar{\Delta}_{ij}^{t}$ gives the following relationship, which is comparable to Eq. (113):

$$F_{ij}^{t} = EL_0^2\bar{F}_{ij}^{t} \tag{120}$$

Similar to $\bar{F}_{ij}^{n}$, $\bar{F}_{ij}^{t}$ is constant according to the assumptions.

We define the dimensionless contact force as:

$$\bar{F}_{ij}^{c} = \bar{F}_{ij}^{n} + \bar{F}_{ij}^{t} \tag{121}$$

We have shown that $\bar{F}_{ij}^{n}$ and $\bar{F}_{ij}^{t}$ in Eqs. (113) and (121), respectively, are constant. Therefore, $\bar{F}_{ij}^{c}$ is constant as well. Using Eqs. (103), (113), (121), and (122), the following equation is obtained:

$$F_{ij}^{c} = EL_0^2\bar{F}_{ij}^{c} \tag{122}$$

Thus, the sum of the contact forces acting on particle *i* becomes

$$\sum_{j=1}^{n_i}F_{ij}^{c} = EL_0^2\sum_{j=1}^{n_i}\bar{F}_{ij}^{c} \tag{123}$$

or

$$F_i^p = EL_0^2 \bar{F}_i^p \tag{124}$$

where $\bar{F}_i^p$ is constant based on the assumptions.

In Eq. (38), $M_{ij}^c = R_{ij}^c \times F_{ij}^c$ is the moment due to the contact that particle *j* applies, acting on particle *i*, in which R_{ij}^c is the vector directed from the centroid of particle *i* to the center of the interface area of contact with particle *j*. Using Eq. (123) and letting $R_{ij}^c = L_0 \bar{R}_{ij}^c$ and $\bar{M}_{ij}^c = \bar{R}_{ij}^c \times \bar{F}_{ij}^c$, the sum of the contact moments acting on particle *i*, i.e. $\sum_{j=1}^{n_i} M_{ij}^c$, is decomposed into its dimensional and dimensionless parts:

$$\sum_{j=1}^{n_i} M_{ij}^c = EL_0^3 \sum_{j=1}^{n_i} \bar{M}_{ij}^c \tag{125}$$

Therefore,

$$M_i^p = EL_0^3 \bar{M}_i^p \tag{126}$$

Note that $\bar{M}_i^p$ is also constant according to the assumptions.

We have shown that dimensionless forces and moments depend solely on dimensionless geometry and are invariant with respect to ρ, E, and L_0.

Appendix 4. Dimensionless Stress is independent of ρ, E, and L_0.

The stress developed within an assembly of particles in the *ij*-plane, σ_{ij} (i.e. the *ij* component of the stress tensor), is calculated using the following equation:

$$\sigma_{ij} = \frac{1}{V}\sum_{c=1}^{n_c} L_i^c F_j^c \tag{127}$$

where V is the volume of the assembly, including the voids, n_c is the number of the contacts, and L_i^c is the projection of L^c in the *i*-direction. That is, $L_i^c = L^c \cdot \hat{e}_i$, where L^c is called the branch vector of the contact, *c*, that connects the centroids of the two particles in contact, with $\hat{e}_i$ being the unit vector of the *i*-direction. F_j^c is the projection of F^c in the *j*-direction, i.e. $F_j^c = F^c \cdot \hat{e}_j$, in which F^c is the force of contact *c*.

By substituting the dimensionless volume from Eq. (18), the dimensionless contact branch length with $\bar{L}^c = L^c/L_0$, and the dimensionless contact force with $\bar{F}^c = F^c/EL_0^2$ in Eq. (128), one gets

$$\sigma_{ij} = \frac{E}{\bar{V}}\sum_{c=1}^{n_c} \bar{L}_i^c \bar{F}_j^c \tag{128}$$

We define a dimensionless stress tensor $\bar{\sigma}_{ij}$ as

$$\bar{\sigma}_{ij} = \frac{1}{\bar{V}}\sum_{c=1}^{n_c} \bar{L}_i^c \bar{F}_j^c \tag{129}$$

Therefore, the relationship between the stress tensor and its dimensionless counterpart is established as follows:

$$\sigma_{ij} = \bar{\sigma}_{ij} E \tag{130}$$

Appendix 5. Constant Strain Rate Boundary Conditions in Dimensionless DEM

Boundary conditions (BC) can be either periodic or rigid in type.

If the periodic BC are used, the position of every particle, x_i, is updated at each time step, Δt, by:

$$x_i = X_i + \left(\hat{I} + \dot{\varepsilon}\, \Delta t\right) x_i^{old} \tag{131}$$

where x_i^{old} is the position vector of the particle at the end of the previous time step.

In practice, the time step is a fraction of the critical time increment, i.e.

$$\Delta t = c_t \Delta t_c \tag{132}$$

where c_t, the time step ratio, is a constant less than one. Šmilauer and Chareyre (2010) recommend that $c_t = 0.3$. Using Eqs. (31), (32), (93), (132), and (133), we get:

$$x_i/L_0 = \bar{X}_i + \left(\hat{I} + c_t \varepsilon'\right) x_i^{old}/L_0 \tag{133}$$

By defining the dimensionless positions, $\bar{x}_i = x_i/\mathrm{L}_0$ and $\bar{x}_i^{old} = x_i^{old}/L_0$, the following expression is derived for the periodic BC in the natural units:

$$\bar{x}_i = \bar{X}_i + \left(\hat{I} + c_t \varepsilon'\right) \bar{x}_i^{old} \tag{134}$$

If the rigid BC are used, positions of the walls, x_w, are updated at each time step by

$$x_w = \left(\hat{I} + \dot{\varepsilon}\, \Delta t\right) x_w^{old} \tag{135}$$

where x_w^{old} is the position vector of the walls at the end of the previous time step.

Using Eqs. (31), (93), (133), and (136), we get:

$$x_w/L_0 = \left(\hat{I} + c_t \varepsilon'\right) x_w^{old}/L_0 \tag{136}$$

By defining the dimensionless wall positions, $\bar{x}_w = x_w/L_0$ and $\bar{x}_w^{old} = x_w^{old}/L_0$, the following expression is derived for the rigid BC in the natural units:

$$\bar{x}_w = \left(\hat{I} + c_t \varepsilon'\right) \bar{x}_w^{old} \tag{137}$$

Appendix 6. Derivation of Dimensionless DEM Formulation

All of the coefficients on the left-hand side and the entire right-hand side of Eq. (44) are constant. Hence, $\bar{X}_i$, $\bar{X}_i'$, and $\bar{X}_i''$ are invariant with respect to ρ, E, and L_0. Therefore, the dimensionless displacement and, consequently, the position, velocity, and acceleration of particle *i* due to equilibrium are invariant with respect to those parameters at the end of the first time step, right before the application of the additional displacement, which is induced by a uniform strain rate field.

Similarly, all of the coefficients on the left-hand side and the entire right-hand side of Eq. (45) are constant. Hence, θ_i, θ_i', and θ_i'' are invariant with respect to ρ, E, and L_0. The rotation and, thereby, the orientation and the dimensionless angular velocity and acceleration of particle *i* due to equilibrium are invariant with respect to those parameters at the end of the first time step, right before the application of the boundary conditions that the strain rate field induces. Now, the boundary conditions need to be examined:

ε_0', referring to the assumptions, is constant. Also, $\bar{x}_i^{old} = x_i^{old}/L_0$ is constant based on the assumption of a constant dimensionless initial geometry. As c_t is the same for dimensional and dimensionless cases, and regarding Eq. (17), one time step in the regular time scale, Δt, corresponds to one time step in the dimensionless time scale, $\Delta\tau$. Thus, the n^{th} cycle in the dimensionless time scale and the n^{th} cycle in the dimensional time scale are correlated. To update the boundary conditions, the dimensionless position of particle *i* is calculated through Eq. (135) or (138). As $\bar{X}_i$, which comes from Eq. (44), is invariant with respect to ρ, E, and L_0, $\bar{x}_i$ is also invariant with respect to those parameters at the end of the first time step.

Since this is true for all of the particles in the assembly, the dimensionless geometry of the problem (i.e. the positions and overlaps that L_0 normalizes) is independent of ρ, E, and L_0 at the end of the first time step. Therefore, the dimensionless geometry at every time step is not a function of ρ, E, and L_0. The independence of the normalized movements of particles passes to the next time step and goes on in the subsequent time increments. This applies to the moments and rotational degrees of freedom as well.

In other words, any typical particle in the problem at a specific time step has constant dimensionless overlaps in Eqs. (109) and (120), which, in turn, yield constant dimensionless forces in Eq. (44) and dimensionless moments in Eq. (45). These are the forces and moments that run the equations of motion. Therefore, the dimensionless geometry remains unchanged with ρ, E, and L_0 at every time increment.

Eqs. (44), (45), and (135) or (138) apply to all of the particles in the assembly. As characteristic time and length are the same for the force and moment equilibrium equations of all particles, they move at the same pace. Therefore, their dimensionless positions and orientation with respect to each other, and the overall dimensionless geometry will remain invariant with respect to the scaling parameters, ρ, E, and L_0, at any time step.

Appendix 7. Sample Preparation Results

Table 49 Void ratios of samples created with the automatic three-phase algorithm

μ_1	$\sigma_c = 39$ kPa	$\sigma_c = 390$ kPa	$\sigma_c = 3900$ kPa	$\sigma_c = 39000$ kPa
0.00	0.507	0.486	0.463	0.427
0.01	0.513	0.486	0.466	0.423
0.02	0.516	0.488	0.465	0.422
0.03	0.527	0.498	0.471	0.428
0.04	0.542	0.514	0.497	0.461
0.05	0.558	0.537	0.524	0.486
0.06	0.573	0.555	0.544	0.504
0.08	0.597	0.584	0.573	0.529
0.10	0.616	0.604	0.594	0.548
0.12	0.635	0.623	0.613	0.565
0.14	0.651	0.638	0.629	0.581
0.16	0.663	0.652	0.641	0.591
0.18	0.675	0.663	0.653	0.605
0.20	0.686	0.677	0.667	0.615
0.22	0.696	0.685	0.674	0.623
0.24	0.703	0.690	0.682	0.633
0.26	0.712	0.700	0.692	0.639
0.28	0.720	0.709	0.699	0.647
0.30	0.726	0.715	0.708	0.657
0.32	0.732	0.723	0.716	0.662
0.34	0.735	0.722	0.718	0.664
0.36	0.736	0.733	0.726	0.668
0.38	0.742	0.735	0.733	0.676
0.40	0.734	0.739	0.736	0.683
0.42	0.736	0.745	0.740	0.683
0.44	0.736	0.745	0.748	0.688
0.47	0.738	0.749	0.750	0.693
0.50	0.738	0.742	0.748	0.693

Appendix 8. Output parameters of models in Chapter 5

Table 50 Output parameters of models

#	Model	ε_{Peak}	ϕ_{max} (degree)	UFR	I_{Mom}	E_{Kin} (μJ)
1	A5-ND-0.05	0.24%	29.49	4.832%	13.801%	3.49E+05
2	A5-ND-0.10	0.24%	29.73	4.983%	10.750%	3.02E+05
3	A5-ND-0.12	0.32%	29.89	4.930%	9.760%	2.79E+05
4	A5-ND-0.15	0.32%	30.13	5.005%	8.638%	2.58E+05
5	A5-ND-0.20	1.80%	30.98	5.246%	7.216%	2.32E+05
6	A5-ND-0.30	2.04%	32.57	4.943%	5.393%	1.93E+05
7	A5-ND-0.40	2.08%	33.84	4.755%	4.557%	1.69E+05
8	A5-ND-0.50	2.12%	34.51	4.786%	4.311%	1.53E+05
9	A5-ND-0.60	2.16%	35.17	4.947%	4.326%	1.41E+05
10	A5-ND-0.80	2.20%	36.32	5.493%	4.652%	1.25E+05
11	A5-ND-1.00	2.12%	37.36	5.939%	4.999%	1.11E+05
12	A5-ND-2.00	2.32%	40.90	8.290%	6.944%	8.21E+04
13	A5-ND-5.00	2.80%	46.30	12.205%	10.355%	5.38E+04
14	A5-OD-0.05	2.32%	30.52	3.039%	8.114%	2.33E+05
15	A5-OD-0.10	1.92%	33.08	3.220%	5.864%	1.78E+05
16	A5-OD-0.12	2.04%	33.87	3.157%	5.497%	1.62E+05
17	A5-OD-0.15	1.84%	34.64	3.682%	5.462%	1.42E+05
18	A5-OD-0.20	2.12%	36.17	4.650%	5.947%	1.25E+05
19	A5-OD-0.30	2.16%	38.30	6.260%	7.034%	1.03E+05
20	A5-OD-0.40	2.28%	39.85	7.501%	7.990%	8.95E+04
21	A5-OD-0.50	2.28%	41.15	8.457%	8.894%	8.10E+04
22	A5-OD-0.60	2.32%	42.31	9.259%	9.672%	7.44E+04
23	A5-OD-0.80	2.52%	44.07	10.647%	10.833%	6.50E+04
24	A5-OD-1.00	2.84%	45.42	11.707%	11.827%	5.79E+04
25	A5-OD-2.00	2.92%	49.66	14.930%	15.232%	4.10E+04
26	A5-OD-5.00	3.24%	54.99	18.500%	19.380%	2.44E+04
27	A5-WD-0.00	0.24%	28.54	5.074%	17.466%	5.32E+05
28	A6-ND-0.05	1.72%	25.35	1.369%	3.702%	1.22E+04
29	A6-ND-0.10	1.84%	25.87	1.357%	2.811%	9.68E+03
30	A6-ND-0.12	1.60%	26.59	1.237%	2.171%	8.70E+03
31	A6-ND-0.15	2.12%	26.27	1.301%	2.124%	7.84E+03
32	A6-ND-0.20	2.40%	26.95	1.124%	1.492%	6.98E+03
33	A6-ND-0.30	2.28%	27.57	0.980%	1.028%	5.45E+03
34	A6-ND-0.40	1.76%	27.77	0.823%	0.773%	4.99E+03
35	A6-ND-0.50	2.28%	28.16	0.785%	0.713%	4.26E+03
36	A6-ND-0.60	2.20%	28.44	0.864%	0.754%	3.91E+03
37	A6-ND-0.80	2.08%	29.05	1.040%	0.893%	3.40E+03
38	A6-ND-1.00	2.36%	29.16	1.250%	1.039%	3.14E+03
39	A6-ND-2.00	1.96%	30.66	2.056%	1.701%	2.24E+03

Table 50 Output parameters of models (Cont.)

#	Model	ε_{Peak}	ϕ_{max} (degree)	UFR	I_{Mom}	E_{Kin} (μJ)
40	A6-ND-5.00	2.04%	33.99	3.812%	3.125%	1.51E+03
41	A6-OD-0.05	2.40%	26.68	0.961%	2.074%	7.88E+03
42	A6-OD-0.10	2.24%	28.27	1.051%	1.494%	5.58E+03
43	A6-OD-0.12	2.24%	27.93	1.054%	1.294%	5.11E+03
44	A6-OD-0.15	2.64%	27.93	0.923%	1.113%	4.43E+03
45	A6-OD-0.20	2.44%	28.98	1.066%	1.214%	3.72E+03
46	A6-OD-0.30	1.96%	29.81	1.408%	1.607%	2.99E+03
47	A6-OD-0.40	2.08%	30.27	1.732%	1.896%	2.63E+03
48	A6-OD-0.50	2.16%	30.57	2.043%	2.263%	2.43E+03
49	A6-OD-0.60	2.00%	31.10	2.375%	2.522%	2.16E+03
50	A6-OD-0.80	2.08%	31.78	2.850%	3.071%	1.92E+03
51	A6-OD-1.00	1.92%	32.94	3.314%	3.500%	1.67E+03
52	A6-OD-2.00	2.04%	35.92	5.252%	5.501%	1.24E+03
53	A6-OD-5.00	2.28%	41.00	8.601%	8.837%	7.99E+02
54	A6-WD-0.00	0.84%	22.66	1.421%	6.361%	2.53E+04
55	A7-ND-0.05	1.92%	25.20	0.659%	1.990%	6.44E+02
56	A7-ND-0.10	0.76%	25.64	0.515%	1.126%	4.03E+02
57	A7-ND-0.12	2.36%	26.20	0.463%	0.900%	3.41E+02
58	A7-ND-0.15	1.84%	25.78	0.436%	0.727%	3.22E+02
59	A7-ND-0.20	2.36%	26.12	0.386%	0.528%	2.53E+02
60	A7-ND-0.30	2.08%	26.51	0.227%	0.251%	1.78E+02
61	A7-ND-0.40	2.08%	27.10	0.149%	0.157%	1.44E+02
62	A7-ND-0.50	2.28%	27.05	0.103%	0.094%	9.49E+01
63	A7-ND-0.60	1.88%	26.52	0.124%	0.114%	1.01E+02
64	A7-ND-0.80	1.88%	26.56	0.151%	0.137%	8.22E+01
65	A7-ND-1.00	1.88%	27.28	0.178%	0.162%	7.51E+01
66	A7-ND-2.00	2.24%	27.83	0.343%	0.294%	6.20E+01
67	A7-ND-5.00	2.24%	28.23	0.714%	0.613%	4.18E+01
68	A7-OD-0.05	2.16%	25.38	0.352%	0.753%	3.29E+02
69	A7-OD-0.10	2.48%	26.21	0.226%	0.276%	1.92E+02
70	A7-OD-0.12	2.28%	26.73	0.265%	0.294%	1.80E+02
71	A7-OD-0.15	1.28%	26.18	0.269%	0.284%	1.65E+02
72	A7-OD-0.20	2.28%	27.35	0.197%	0.219%	1.12E+02
73	A7-OD-0.30	1.96%	27.16	0.224%	0.257%	8.70E+01
74	A7-OD-0.40	2.68%	27.73	0.278%	0.323%	7.37E+01
75	A7-OD-0.50	2.12%	26.93	0.329%	0.392%	6.80E+01
76	A7-OD-0.60	1.72%	27.11	0.371%	0.458%	6.32E+01
77	A7-OD-0.80	2.20%	27.74	0.492%	0.580%	5.72E+01
78	A7-OD-1.00	2.16%	28.59	0.578%	0.673%	5.00E+01
79	A7-OD-2.00	2.24%	29.19	1.034%	1.163%	3.80E+01
80	A7-OD-5.00	2.04%	30.67	2.067%	2.204%	2.35E+01

Table 50 Output parameters of models (Cont.)

#	Model	ε_{Peak}	ϕ_{max} (degree)	UFR	I_{Mom}	E_{Kin} (μJ)
81	A7-WD-0.00	1.00%	19.13	0.839%	4.770%	2.02E+03
82	A8-ND-0.05	2.92%	24.45	0.377%	1.258%	1.50E+02
83	A8-ND-0.10	2.88%	25.41	0.260%	0.565%	5.84E+01
84	A8-ND-0.12	2.00%	26.09	0.218%	0.426%	4.04E+01
85	A8-ND-0.15	2.00%	25.82	0.173%	0.288%	3.04E+01
86	A8-ND-0.20	1.56%	25.45	0.136%	0.189%	1.90E+01
87	A8-ND-0.30	2.28%	25.71	0.029%	0.031%	4.17E+00
88	A8-ND-0.40	2.48%	25.51	0.029%	0.035%	4.51E+00
89	A8-ND-0.50	1.96%	25.56	0.014%	0.015%	2.33E+00
90	A8-ND-0.60	2.00%	26.01	0.018%	0.018%	2.25E+00
91	A8-ND-0.80	2.24%	26.73	0.017%	0.016%	1.64E+00
92	A8-ND-1.00	2.68%	26.50	0.021%	0.020%	1.55E+00
93	A8-ND-2.00	2.52%	26.34	0.039%	0.038%	1.30E+00
94	A8-ND-5.00	2.52%	26.74	0.101%	0.092%	1.11E+00
95	A8-OD-0.05	2.32%	25.41	0.147%	0.308%	3.92E+01
96	A8-OD-0.10	1.72%	25.80	0.070%	0.079%	1.26E+01
97	A8-OD-0.12	1.64%	25.70	0.061%	0.061%	9.82E+00
98	A8-OD-0.15	2.68%	26.48	0.044%	0.041%	6.17E+00
99	A8-OD-0.20	1.48%	25.82	0.032%	0.034%	4.26E+00
100	A8-OD-0.30	1.68%	26.07	0.026%	0.031%	2.16E+00
101	A8-OD-0.40	2.24%	26.52	0.032%	0.042%	1.84E+00
102	A8-OD-0.50	2.44%	26.91	0.038%	0.049%	1.56E+00
103	A8-OD-0.60	1.80%	26.22	0.046%	0.058%	1.40E+00
104	A8-OD-0.80	2.36%	26.30	0.062%	0.076%	1.35E+00
105	A8-OD-1.00	1.88%	26.90	0.074%	0.093%	1.15E+00
106	A8-OD-2.00	2.12%	26.98	0.139%	0.171%	9.12E-01
107	A8-OD-5.00	1.92%	27.23	0.322%	0.378%	6.43E-01
108	A8-WD-0.00	10.00%	20.52	0.642%	4.481%	9.04E+02
109	B5-ND-0.05	3.20%	23.22	13.277%	5.228%	1.32E+06
110	B5-ND-0.10	2.64%	23.58	10.591%	4.110%	1.16E+06
111	B5-ND-0.12	3.52%	23.88	9.642%	3.725%	1.09E+06
112	B5-ND-0.15	4.96%	24.03	8.531%	3.285%	1.04E+06
113	B5-ND-0.20	3.32%	24.48	7.051%	2.717%	9.52E+05
114	B5-ND-0.30	4.08%	25.35	5.010%	1.954%	8.21E+05
115	B5-ND-0.40	3.24%	25.69	4.162%	1.658%	7.39E+05
116	B5-ND-0.50	4.04%	26.28	3.888%	1.567%	6.67E+05
117	B5-ND-0.60	3.36%	26.70	3.947%	1.598%	6.19E+05
118	B5-ND-0.80	2.96%	27.57	4.444%	1.803%	5.46E+05
119	B5-ND-1.00	2.64%	27.93	5.066%	2.043%	4.96E+05
120	B5-ND-2.00	4.32%	30.55	7.864%	3.155%	3.63E+05
121	B5-ND-5.00	3.80%	34.80	13.625%	5.401%	2.39E+05

Table 50 Output parameters of models (Cont.)

#	Model	ε_{Peak}	ϕ_{max} (degree)	UFR	I_{Mom}	E_{Kin} (μJ)
122	B5-OD-0.05	3.24%	23.20	12.793%	5.029%	1.29E+06
123	B5-OD-0.10	3.56%	24.02	9.919%	3.846%	1.13E+06
124	B5-OD-0.12	4.04%	23.94	8.974%	3.469%	1.07E+06
125	B5-OD-0.15	2.20%	24.27	7.784%	2.999%	1.00E+06
126	B5-OD-0.20	3.44%	24.79	6.231%	2.411%	9.05E+05
127	B5-OD-0.30	4.52%	25.55	4.491%	1.784%	7.85E+05
128	B5-OD-0.40	3.36%	26.04	3.943%	1.598%	6.92E+05
129	B5-OD-0.50	3.36%	26.74	3.938%	1.610%	6.28E+05
130	B5-OD-0.60	3.28%	27.18	4.178%	1.709%	5.78E+05
131	B5-OD-0.80	3.04%	27.87	4.876%	1.988%	5.12E+05
132	B5-OD-1.00	2.84%	28.56	5.592%	2.287%	4.64E+05
133	B5-OD-2.00	3.56%	31.16	8.689%	3.523%	3.38E+05
134	B5-OD-5.00	3.52%	35.63	14.874%	5.958%	2.22E+05
135	B5-WD-0.00	3.32%	22.55	17.187%	6.908%	1.63E+06
136	B6-ND-0.05	3.96%	22.66	2.563%	1.021%	2.98E+04
137	B6-ND-0.10	3.76%	22.91	1.682%	0.648%	2.45E+04
138	B6-ND-0.12	3.76%	23.06	1.429%	0.548%	2.30E+04
139	B6-ND-0.15	3.52%	23.03	1.158%	0.446%	2.16E+04
140	B6-ND-0.20	4.76%	23.28	0.838%	0.326%	1.91E+04
141	B6-ND-0.30	4.68%	23.31	0.530%	0.212%	1.66E+04
142	B6-ND-0.40	5.96%	23.34	0.453%	0.183%	1.46E+04
143	B6-ND-0.50	2.96%	23.53	0.493%	0.201%	1.41E+04
144	B6-ND-0.60	4.56%	23.86	0.548%	0.221%	1.34E+04
145	B6-ND-0.80	3.84%	23.80	0.680%	0.275%	1.21E+04
146	B6-ND-1.00	3.32%	24.05	0.809%	0.329%	1.12E+04
147	B6-ND-2.00	3.68%	24.75	1.449%	0.586%	9.09E+03
148	B6-ND-5.00	3.68%	26.22	2.959%	1.202%	6.48E+03
149	B6-OD-0.05	5.04%	22.70	2.409%	0.957%	2.94E+04
150	B6-OD-0.10	3.12%	22.96	1.488%	0.574%	2.33E+04
151	B6-OD-0.12	3.92%	23.05	1.247%	0.479%	2.15E+04
152	B6-OD-0.15	3.80%	23.09	0.976%	0.378%	2.06E+04
153	B6-OD-0.20	2.52%	23.16	0.697%	0.275%	1.84E+04
154	B6-OD-0.30	4.48%	23.47	0.474%	0.193%	1.55E+04
155	B6-OD-0.40	4.80%	23.40	0.476%	0.195%	1.42E+04
156	B6-OD-0.50	3.88%	23.60	0.535%	0.219%	1.32E+04
157	B6-OD-0.60	4.52%	23.75	0.617%	0.252%	1.28E+04
158	B6-OD-0.80	3.32%	23.86	0.773%	0.316%	1.15E+04
159	B6-OD-1.00	2.60%	23.98	0.930%	0.381%	1.08E+04
160	B6-OD-2.00	4.04%	25.19	1.640%	0.671%	8.57E+03
161	B6-OD-5.00	3.00%	26.56	3.332%	1.361%	6.08E+03
162	B6-WD-0.00	6.60%	22.16	4.603%	2.017%	4.61E+04

Table 50 Output parameters of models (Cont.)

#	Model	ε_{Peak}	ϕ_{max} (degree)	UFR	I_{Mom}	E_{Kin} (μJ)
163	B7-ND-0.05	3.76%	22.69	0.647%	0.308%	6.48E+02
164	B7-ND-0.10	3.16%	22.81	0.306%	0.129%	5.15E+02
165	B7-ND-0.12	4.56%	23.08	0.247%	0.101%	4.17E+02
166	B7-ND-0.15	4.76%	23.22	0.174%	0.068%	3.73E+02
167	B7-ND-0.20	4.56%	22.99	0.108%	0.043%	3.15E+02
168	B7-ND-0.30	4.84%	22.89	0.057%	0.023%	2.56E+02
169	B7-ND-0.40	3.20%	22.91	0.055%	0.022%	2.44E+02
170	B7-ND-0.50	4.04%	23.06	0.057%	0.023%	2.29E+02
171	B7-ND-0.60	6.44%	23.07	0.062%	0.025%	2.05E+02
172	B7-ND-0.80	2.68%	23.00	0.082%	0.033%	2.00E+02
173	B7-ND-1.00	2.80%	23.05	0.100%	0.040%	1.92E+02
174	B7-ND-2.00	3.76%	23.23	0.190%	0.077%	1.64E+02
175	B7-ND-5.00	2.92%	23.66	0.441%	0.177%	1.35E+02
176	B7-OD-0.05	2.52%	22.65	0.559%	0.247%	6.16E+02
177	B7-OD-0.10	2.40%	22.93	0.245%	0.099%	4.38E+02
178	B7-OD-0.12	4.00%	23.14	0.214%	0.084%	3.94E+02
179	B7-OD-0.15	5.96%	22.88	0.134%	0.053%	3.09E+02
180	B7-OD-0.20	3.60%	22.88	0.094%	0.037%	3.20E+02
181	B7-OD-0.30	5.52%	22.81	0.051%	0.021%	2.46E+02
182	B7-OD-0.40	4.48%	23.17	0.054%	0.022%	2.26E+02
183	B7-OD-0.50	3.52%	23.09	0.062%	0.025%	2.17E+02
184	B7-OD-0.60	3.52%	23.17	0.073%	0.030%	2.05E+02
185	B7-OD-0.80	4.40%	22.94	0.095%	0.039%	1.98E+02
186	B7-OD-1.00	2.00%	22.95	0.116%	0.047%	1.85E+02
187	B7-OD-2.00	3.40%	23.41	0.220%	0.089%	1.59E+02
188	B7-OD-5.00	3.20%	23.90	0.502%	0.205%	1.28E+02
189	B7-WD-0.00	1.12%	21.93	2.744%	1.492%	3.57E+03
190	B8-ND-0.05	5.44%	22.89	0.391%	0.129%	6.74E+01
191	B8-ND-0.10	4.04%	22.98	0.062%	0.032%	1.56E+01
192	B8-ND-0.12	4.44%	23.16	0.043%	0.020%	1.12E+01
193	B8-ND-0.15	5.56%	23.07	0.020%	0.008%	4.98E+00
194	B8-ND-0.20	3.40%	22.79	0.017%	0.006%	5.64E+00
195	B8-ND-0.30	2.80%	22.88	0.006%	0.002%	3.80E+00
196	B8-ND-0.40	3.12%	22.84	0.005%	0.002%	3.63E+00
197	B8-ND-0.50	3.32%	22.93	0.005%	0.002%	2.75E+00
198	B8-ND-0.60	4.08%	23.22	0.006%	0.003%	2.74E+00
199	B8-ND-0.80	3.28%	22.97	0.009%	0.003%	3.19E+00
200	B8-ND-1.00	3.64%	22.71	0.010%	0.004%	2.68E+00
201	B8-ND-2.00	2.52%	23.10	0.021%	0.008%	2.64E+00
202	B8-ND-5.00	3.44%	23.10	0.051%	0.021%	2.17E+00
203	B8-OD-0.05	4.24%	22.77	0.256%	0.088%	3.64E+01

Table 50 Output parameters of models (Cont.)

#	Model	ε_{Peak}	ϕ_{max} (degree)	UFR	I_{Mom}	E_{Kin} (μJ)
204	B8-OD-0.10	3.16%	23.12	0.046%	0.022%	1.17E+01
205	B8-OD-0.12	2.04%	22.98	0.027%	0.012%	6.57E+00
206	B8-OD-0.15	6.32%	23.02	0.016%	0.007%	5.46E+00
207	B8-OD-0.20	9.60%	22.96	0.009%	0.004%	4.60E+00
208	B8-OD-0.30	3.80%	23.02	0.005%	0.002%	3.65E+00
209	B8-OD-0.40	3.96%	22.95	0.005%	0.002%	3.05E+00
210	B8-OD-0.50	4.12%	23.06	0.006%	0.002%	2.67E+00
211	B8-OD-0.60	7.16%	22.66	0.007%	0.003%	2.73E+00
212	B8-OD-0.80	3.40%	22.92	0.010%	0.004%	2.85E+00
213	B8-OD-1.00	3.48%	23.00	0.012%	0.005%	2.56E+00
214	B8-OD-2.00	5.08%	22.82	0.024%	0.010%	2.52E+00
215	B8-OD-5.00	5.60%	22.92	0.059%	0.024%	2.17E+00
216	B8-WD-0.00	9.16%	21.35	17.083%	7.242%	3.30E+04

Appendix 9. Output parameters of models in Chapter 6

Table 51 Output parameters of the (ND) and (OD) models

#	Model	ε_{peak}	ϕ_{max}	I_{Mom}	#	Model	ε_{peak}	ϕ_{max}	I_{Mom}
1	121ND1e-5	0.20%	49.64	10.464%	172	121OD1e-5	1.24%	53.46	12.560%
2	121ND1e-6	1.64%	37.37	2.067%	173	121OD1e-6	2.76%	40.81	4.865%
3	121ND1e-7	1.48%	32.97	0.369%	174	121OD1e-7	1.76%	34.51	1.085%
4	121ND2e-6	1.56%	39.22	3.320%	175	121OD2e-6	2.92%	43.86	7.020%
5	121ND2e-7	1.48%	34.02	0.644%	176	121OD2e-7	1.48%	35.80	1.728%
6	121ND2e-8	1.29%	32.11	0.094%	177	121OD2e-8	1.25%	32.53	0.296%
7	121ND5e-6	0.16%	43.65	6.863%	178	121OD5e-6	1.20%	49.03	10.121%
8	121ND5e-7	1.16%	35.56	1.230%	179	121OD5e-7	0.96%	37.88	3.105%
9	121ND5e-8	1.46%	32.60	0.209%	180	121OD5e-8	1.26%	32.93	0.595%
10	122ND1e-5	0.84%	39.66	5.384%	181	122OD1e-5	0.60%	40.40	7.070%
11	122ND1e-6	0.56%	31.24	0.994%	182	122OD1e-6	0.84%	31.42	1.522%
12	122ND1e-7	0.40%	28.79	0.124%	183	122OD1e-7	0.44%	28.89	0.195%
13	122ND2e-6	0.76%	33.25	1.780%	184	122OD2e-6	1.04%	33.52	2.633%
14	122ND2e-7	0.44%	29.13	0.235%	185	122OD2e-7	0.36%	29.17	0.345%
15	122ND2e-8	0.13%	28.25	0.018%	186	122OD2e-8	0.17%	28.28	0.030%
16	122ND5e-6	0.52%	36.51	3.462%	187	122OD5e-6	1.52%	37.19	4.852%
17	122ND5e-7	0.28%	29.98	0.480%	188	122OD5e-7	1.28%	30.43	0.940%
18	122ND5e-8	0.22%	28.51	0.055%	189	122OD5e-8	0.18%	28.45	0.082%
19	211ND1e-5	0.28%	43.59	4.587%	190	211OD1e-5	0.88%	47.40	6.045%
20	211ND1e-6	0.40%	37.68	0.530%	191	211OD1e-6	0.40%	38.95	1.223%
21	211ND1e-7	0.32%	36.63	0.053%	192	211OD1e-7	0.32%	36.78	0.158%
22	211ND2e-6	0.40%	38.48	1.052%	193	211OD2e-6	0.80%	40.59	2.300%
23	211ND2e-7	0.32%	36.75	0.102%	194	211OD2e-7	0.32%	37.09	0.290%
24	211ND2e-8	0.33%	36.31	0.013%	195	211OD2e-8	0.33%	36.43	0.033%
25	211ND5e-6	0.52%	40.55	2.468%	196	211OD5e-6	0.96%	43.98	4.185%
26	211ND5e-7	0.36%	37.04	0.275%	197	211OD5e-7	0.36%	37.85	0.673%
27	211ND5e-8	0.34%	36.53	0.028%	198	211OD5e-8	0.34%	36.61	0.081%
28	212ND1e-5	0.44%	37.87	2.161%	199	212OD1e-5	0.52%	38.18	2.838%
29	212ND1e-6	0.36%	34.77	0.236%	200	212OD1e-6	0.36%	34.70	0.345%
30	212ND1e-7	0.40%	34.15	0.024%	201	212OD1e-7	0.48%	34.12	0.047%
31	212ND2e-6	0.40%	35.24	0.496%	202	212OD2e-6	0.40%	35.28	0.690%
32	212ND2e-7	0.40%	34.22	0.048%	203	212OD2e-7	0.44%	34.21	0.079%
33	212ND2e-8	0.33%	34.01	0.004%	204	212OD2e-8	0.45%	34.02	0.011%
34	212ND5e-6	0.56%	36.53	1.221%	205	212OD5e-6	0.48%	36.68	1.606%
35	212ND5e-7	0.40%	34.44	0.122%	206	212OD5e-7	0.48%	34.41	0.206%

Table 51 Output parameters of the (ND) and (OD) models (Cont.)

#	Model	ε_{peak}	ϕ_{max}	I_{Mom}	#	Model	ε_{peak}	ϕ_{max}	I_{Mom}
36	212ND5e-8	0.50%	34.09	0.013%	207	212OD5e-8	0.50%	34.09	0.027%
37	220ND1e-5	1.28%	31.44	1.719%	208	220OD1e-5	0.80%	30.26	2.464%
38	220ND1e-6	0.60%	28.23	0.239%	209	220OD1e-6	0.60%	28.23	0.239%
39	220ND1e-7	0.48%	28.08	0.015%	210	220OD1e-7	0.44%	28.05	0.014%
40	220ND2e-6	0.60%	28.81	0.349%	211	220OD2e-6	0.52%	28.48	0.501%
41	220ND2e-7	0.52%	28.10	0.029%	212	220OD2e-7	0.56%	28.08	0.034%
42	220ND2e-8	0.45%	27.98	0.003%	213	220OD2e-8	0.49%	28.00	0.003%
43	220ND5e-6	1.88%	30.06	0.937%	214	220OD5e-6	1.28%	29.33	1.327%
44	220ND5e-7	0.52%	28.20	0.075%	215	220OD5e-7	0.56%	28.20	0.089%
45	220ND5e-8	0.50%	28.03	0.007%	216	220OD5e-8	0.46%	28.03	0.006%
46	221ND1e-5	1.44%	42.27	4.894%	217	221OD1e-5	1.60%	46.84	7.139%
47	221ND1e-6	1.64%	35.09	0.783%	218	221OD1e-6	1.88%	37.07	1.892%
48	221ND1e-7	1.76%	33.53	0.104%	219	221OD1e-7	1.88%	33.51	0.321%
49	221ND2e-6	1.08%	36.46	1.349%	220	221OD2e-6	2.04%	39.42	3.016%
50	221ND2e-7	1.48%	33.77	0.189%	221	221OD2e-7	1.96%	34.21	0.583%
51	221ND2e-8	1.17%	33.08	0.021%	222	221OD2e-8	0.81%	33.30	0.059%
52	221ND5e-6	1.48%	39.18	2.773%	223	221OD5e-6	1.60%	43.17	4.974%
53	221ND5e-7	0.72%	33.90	0.370%	224	221OD5e-7	1.84%	35.58	1.170%
54	221ND5e-8	1.82%	33.45	0.058%	225	221OD5e-8	1.86%	33.86	0.171%
55	222ND1e-5	1.80%	34.30	2.567%	226	222OD1e-5	1.68%	34.55	3.493%
56	222ND1e-6	0.60%	30.18	0.329%	227	222OD1e-6	1.48%	30.07	0.570%
57	222ND1e-7	0.56%	29.43	0.038%	228	222OD1e-7	0.52%	29.33	0.047%
58	222ND2e-6	1.36%	30.86	0.725%	229	222OD2e-6	1.68%	30.96	1.048%
59	222ND2e-7	1.52%	29.36	0.085%	230	222OD2e-7	0.40%	29.33	0.082%
60	222ND2e-8	0.65%	29.19	0.007%	231	222OD2e-8	0.89%	29.16	0.012%
61	222ND5e-6	0.88%	32.40	1.459%	232	222OD5e-6	1.84%	32.68	2.104%
62	222ND5e-7	0.56%	29.66	0.158%	233	222OD5e-7	1.24%	29.71	0.315%
63	222ND5e-8	0.66%	29.21	0.022%	234	222OD5e-8	0.42%	29.18	0.024%
64	223ND1e-5	2.32%	31.50	1.962%	235	223OD1e-5	1.60%	30.73	2.175%
65	223ND1e-6	0.76%	28.09	0.212%	236	223OD1e-6	1.36%	27.94	0.252%
66	223ND1e-7	0.36%	27.50	0.017%	237	223OD1e-7	0.36%	27.47	0.014%
67	223ND2e-6	1.52%	28.56	0.538%	238	223OD2e-6	0.84%	28.38	0.442%
68	223ND2e-7	0.40%	27.58	0.035%	239	223OD2e-7	0.40%	27.54	0.030%
69	223ND2e-8	0.37%	27.45	0.003%	240	223OD2e-8	0.69%	27.46	0.003%
70	223ND5e-6	1.84%	29.93	1.075%	241	223OD5e-6	1.80%	29.52	1.242%
71	223ND5e-7	0.96%	27.79	0.110%	242	223OD5e-7	0.72%	27.70	0.098%
72	223ND5e-8	0.74%	27.43	0.010%	243	223OD5e-8	0.50%	27.46	0.008%

Table 51 Output parameters of the (ND) and (OD) models (Cont.)

#	Model	ε_{peak}	ϕ_{max}	I_{Mom}	#	Model	ε_{peak}	ϕ_{max}	I_{Mom}
73	224ND1e-5	0.84%	38.01	3.423%	244	224OD1e-5	0.64%	39.76	4.762%
74	224ND1e-6	0.80%	33.22	0.476%	245	224OD1e-6	0.84%	33.57	0.884%
75	224ND1e-7	0.80%	31.78	0.059%	246	224OD1e-7	0.36%	31.90	0.087%
76	224ND2e-6	0.44%	34.11	0.803%	247	224OD2e-6	0.64%	34.68	1.482%
77	224ND2e-7	0.80%	32.22	0.110%	248	224OD2e-7	0.52%	32.06	0.192%
78	224ND2e-8	0.49%	31.69	0.009%	249	224OD2e-8	0.41%	31.66	0.020%
79	224ND5e-6	0.76%	36.02	1.867%	250	224OD5e-6	0.76%	37.13	3.009%
80	224ND5e-7	0.76%	32.68	0.240%	251	224OD5e-7	0.68%	32.79	0.453%
81	224ND5e-8	0.78%	31.93	0.027%	252	224OD5e-8	0.42%	31.65	0.048%
82	225ND1e-5	0.52%	33.68	2.037%	253	225OD1e-5	0.84%	33.15	3.120%
83	225ND1e-6	0.40%	29.63	0.237%	254	225OD1e-6	0.40%	29.52	0.349%
84	225ND1e-7	0.36%	28.94	0.023%	255	225OD1e-7	0.36%	28.93	0.036%
85	225ND2e-6	0.48%	30.58	0.534%	256	225OD2e-6	0.44%	30.16	0.785%
86	225ND2e-7	0.36%	29.01	0.052%	257	225OD2e-7	0.44%	29.02	0.068%
87	225ND2e-8	0.37%	28.85	0.004%	258	225OD2e-8	0.37%	28.86	0.006%
88	225ND5e-6	0.48%	31.99	1.101%	259	225OD5e-6	0.64%	31.56	1.678%
89	225ND5e-7	0.52%	29.31	0.128%	260	225OD5e-7	0.40%	29.24	0.206%
90	225ND5e-8	0.38%	28.93	0.012%	261	225OD5e-8	0.38%	28.93	0.016%
91	231ND1e-5	4.36%	36.22	5.278%	262	231OD1e-5	4.00%	41.80	8.398%
92	231ND1e-6	3.16%	29.39	0.940%	263	231OD1e-6	3.72%	31.61	2.300%
93	231ND1e-7	3.44%	26.65	0.149%	264	231OD1e-7	3.24%	27.12	0.424%
94	231ND2e-6	3.24%	30.64	1.632%	265	231OD2e-6	3.64%	33.35	3.667%
95	231ND2e-7	3.44%	26.93	0.266%	266	231OD2e-7	3.04%	27.99	0.703%
96	231ND2e-8	2.81%	26.69	0.033%	267	231OD2e-8	1.41%	26.38	0.092%
97	231ND5e-6	5.80%	33.20	3.266%	268	231OD5e-6	3.72%	37.93	6.127%
98	231ND5e-7	3.20%	28.70	0.568%	269	231OD5e-7	3.08%	29.92	1.468%
99	231ND5e-8	5.26%	26.39	0.084%	270	231OD5e-8	2.98%	26.88	0.243%
100	232ND1e-5	3.84%	30.33	2.774%	271	232OD1e-5	4.08%	30.58	3.921%
101	232ND1e-6	4.12%	25.17	0.495%	272	232OD1e-6	1.24%	25.33	0.616%
102	232ND1e-7	1.16%	23.82	0.052%	273	232OD1e-7	3.24%	23.62	0.099%
103	232ND2e-6	1.12%	26.18	0.748%	274	232OD2e-6	1.08%	26.16	1.073%
104	232ND2e-7	1.04%	23.77	0.092%	275	232OD2e-7	0.96%	24.19	0.144%
105	232ND2e-8	0.97%	23.11	0.011%	276	232OD2e-8	1.13%	23.10	0.018%
106	232ND5e-6	2.16%	28.27	1.581%	277	232OD5e-6	4.32%	28.61	2.466%
107	232ND5e-7	2.88%	24.43	0.251%	278	232OD5e-7	1.36%	24.51	0.349%
108	232ND5e-8	1.18%	23.46	0.027%	279	232OD5e-8	2.14%	23.44	0.050%
109	241ND1e-5	5.92%	32.25	5.760%	280	241OD1e-5	1.44%	37.71	8.713%

Table 51 Output parameters of the (ND) and (OD) models (Cont.)

#	Model	ε_{peak}	ϕ_{max}	I_{Mom}	#	Model	ε_{peak}	ϕ_{max}	I_{Mom}
110	241ND1e-6	13.32%	23.52	1.226%	281	241OD1e-6	3.28%	25.98	2.624%
111	241ND1e-7	17.24%	21.52	0.193%	282	241OD1e-7	13.48%	21.94	0.559%
112	241ND2e-6	2.08%	25.30	1.873%	283	241OD2e-6	3.20%	28.38	3.910%
113	241ND2e-7	18.96%	21.54	0.362%	284	241OD2e-7	2.00%	22.87	0.876%
114	241ND2e-8	23.80%	21.34	0.045%	285	241OD2e-8	23.08%	21.17	0.149%
115	241ND5e-6	4.64%	28.72	3.625%	286	241OD5e-6	5.36%	33.63	6.608%
116	241ND5e-7	15.80%	22.85	0.748%	287	241OD5e-7	2.60%	24.20	1.686%
117	241ND5e-8	21.06%	23.06	0.109%	288	241OD5e-8	24.90%	21.25	0.312%
118	242ND1e-5	3.64%	26.28	3.144%	289	242OD1e-5	3.00%	26.45	4.263%
119	242ND1e-6	12.96%	20.80	0.613%	290	242OD1e-6	15.56%	21.30	0.895%
120	242ND1e-7	16.24%	20.43	0.085%	291	242OD1e-7	11.08%	19.76	0.130%
121	242ND2e-6	12.96%	22.19	1.065%	292	242OD2e-6	15.80%	21.60	1.531%
122	242ND2e-7	13.92%	20.44	0.157%	293	242OD2e-7	18.88%	20.20	0.234%
123	242ND2e-8	19.68%	20.41	0.020%	294	242OD2e-8	18.84%	20.07	0.031%
124	242ND5e-6	4.68%	23.97	1.963%	295	242OD5e-6	13.64%	23.91	2.815%
125	242ND5e-7	24.20%	21.05	0.333%	296	242OD5e-7	21.28%	20.47	0.504%
126	242ND5e-8	19.06%	20.13	0.046%	297	242OD5e-8	13.46%	20.43	0.070%
127	321ND1e-5	2.68%	36.48	1.871%	298	321OD1e-5	1.84%	38.94	2.701%
128	321ND1e-6	1.44%	34.00	0.205%	299	321OD1e-6	1.36%	34.62	0.406%
129	321ND1e-7	1.28%	33.78	0.020%	300	321OD1e-7	1.24%	33.50	0.050%
130	321ND2e-6	1.52%	34.57	0.381%	301	321OD2e-6	1.68%	35.19	0.763%
131	321ND2e-7	1.28%	33.70	0.042%	302	321OD2e-7	1.28%	33.79	0.101%
132	321ND2e-8	1.25%	33.52	0.004%	303	321OD2e-8	1.33%	33.54	0.011%
133	321ND5e-6	1.44%	35.23	0.887%	304	321OD5e-6	1.60%	36.91	1.575%
134	321ND5e-7	1.56%	33.82	0.110%	305	321OD5e-7	1.28%	34.07	0.225%
135	321ND5e-8	1.26%	33.40	0.012%	306	321OD5e-8	1.46%	33.68	0.027%
136	322ND1e-5	1.68%	31.76	0.879%	307	322OD1e-5	1.72%	31.78	1.127%
137	322ND1e-6	1.52%	30.66	0.100%	308	322OD1e-6	1.04%	30.54	0.114%
138	322ND1e-7	1.20%	30.40	0.009%	309	322OD1e-7	1.12%	30.38	0.018%
139	322ND2e-6	1.28%	30.73	0.195%	310	322OD2e-6	1.20%	30.73	0.263%
140	322ND2e-7	1.48%	30.46	0.021%	311	322OD2e-7	1.40%	30.35	0.034%
141	322ND2e-8	1.21%	30.33	0.002%	312	322OD2e-8	1.25%	30.33	0.005%
142	322ND5e-6	1.36%	31.21	0.426%	313	322OD5e-6	1.48%	31.12	0.587%
143	322ND5e-7	1.20%	30.53	0.047%	314	322OD5e-7	1.20%	30.46	0.073%
144	322ND5e-8	1.14%	30.37	0.004%	315	322OD5e-8	1.50%	30.34	0.011%
145	421ND1e-5	2.04%	35.45	0.589%	316	421OD1e-5	2.84%	36.38	0.914%
146	421ND1e-6	2.64%	34.68	0.120%	317	421OD1e-6	2.28%	34.91	0.130%

Table 51 Output parameters of the (ND) and (OD) models (Cont.)

#	Model	ε_{peak}	ϕ_{max}	I_{Mom}	#	Model	ε_{peak}	ϕ_{max}	I_{Mom}
147	421ND1e-7	2.36%	34.45	0.011%	318	421OD1e-7	2.16%	34.63	0.016%
148	421ND2e-6	2.44%	34.82	0.171%	319	421OD2e-6	2.28%	34.98	0.242%
149	421ND2e-7	2.20%	34.63	0.039%	320	421OD2e-7	2.12%	34.70	0.028%
150	421ND2e-8	2.21%	34.42	0.002%	321	421OD2e-8	2.21%	34.50	0.004%
151	421ND5e-6	2.12%	35.13	0.319%	322	421OD5e-6	2.28%	35.63	0.460%
152	421ND5e-7	2.28%	34.70	0.062%	323	421OD5e-7	2.40%	34.88	0.071%
153	421ND5e-8	2.42%	34.58	0.004%	324	421OD5e-8	2.22%	34.63	0.008%
154	422ND1e-5	2.16%	31.21	0.335%	325	422OD1e-5	2.12%	31.18	0.429%
155	422ND1e-6	2.28%	30.91	0.043%	326	422OD1e-6	2.24%	30.94	0.083%
156	422ND1e-7	2.16%	30.89	0.004%	327	422OD1e-7	2.24%	30.93	0.013%
157	422ND2e-6	2.32%	30.97	0.083%	328	422OD2e-6	2.16%	30.94	0.130%
158	422ND2e-7	2.20%	30.90	0.009%	329	422OD2e-7	2.28%	30.97	0.024%
159	422ND2e-8	2.33%	30.90	0.001%	330	422OD2e-8	2.21%	30.90	0.005%
160	422ND5e-6	2.24%	31.10	0.186%	331	422OD5e-6	2.32%	31.04	0.252%
161	422ND5e-7	2.16%	30.92	0.022%	332	422OD5e-7	2.16%	30.89	0.047%
162	422ND5e-8	2.26%	30.91	0.002%	333	422OD5e-8	2.30%	30.90	0.009%
163	TTTND1e-5	1.40%	35.89	2.831%	334	TTTOD1e-5	1.80%	38.28	4.186%
164	TTTND1e-6	1.52%	31.51	0.375%	335	TTTOD1e-6	1.16%	32.21	0.806%
165	TTTND1e-7	1.00%	30.93	0.071%	336	TTTOD1e-7	1.44%	31.35	0.107%
166	TTTND2e-6	1.24%	32.45	0.653%	337	TTTOD2e-6	1.40%	33.23	1.469%
167	TTTND2e-7	1.32%	31.10	0.073%	338	TTTOD2e-7	1.36%	31.35	0.204%
168	TTTND2e-8	1.17%	30.75	0.009%	339	TTTOD2e-8	1.25%	30.71	0.033%
169	TTTND5e-6	1.36%	34.06	1.467%	340	TTTOD5e-6	1.40%	35.64	2.676%
170	TTTND5e-7	1.44%	31.15	0.211%	341	TTTOD5e-7	1.44%	31.43	0.476%
171	TTTND5e-8	1.98%	30.83	0.035%	342	TTTOD5e-8	1.18%	30.88	0.054%

REFERENCES

Abbireddy, C., & Clayton, C. R. I. (2010). Varying initial void ratios for DEM simulations. Géotechnique, 60(6), 497-502.

Agnolin, I., & Roux, J. N. (2008). On the elastic moduli of three-dimensional assemblies of spheres: Characterization and modeling of fluctuations in the particle displacement and rotation. International Journal of Solids and Structures, 45(3), 1101-1123.

Alarcon-Guzman, A., Leonards, G. A., & Chameau, J. L. (1988). Undrained monotonic and cyclic strength of sands. Journal of Geotechnical Engineering, 114(10), 1089-1109.

Bagi, K. (2005). An algorithm to generate random dense arrangements for discrete element simulations of granular assemblies. Granular Matter, 7(1), 31-43.

Barreto, D., C. O'Sullivan, & L. Zdravkovic (2008) Specimen generation approaches for DEM simulations. In S. Burns, P. Mayne, & J. Santamarina (Eds.), International symposium on deformation characteristics of a geomaterials, 4, Atlanta, GA, 22-24 September, 2008. IOS Press.

Belytschko, T. (1983). An overview of semidiscretization and time integration procedures. Computational Methods for Transient Analysis (A 84-29160 12-64). Amsterdam, North-Holland, 1-65.

Belytschko, T., W. Liu, & B. Moran (2000). Nonlinear Finite Elements for Continua and Structures. Wiley.

Cavarretta, I., M. Coop, & C. O'Sullivan (2010). The Influence of particle characteristics on the behaviour of coarse grained soils. Geotechnique 60(5), 413-424.

Cheung, G. (2000). Micromechanics of sand production in oil wells. Ph.D. thesis, Imperial College London.

Cho, G. C., Dodds, J., & Santamarina, J. C. (2006). Particle shape effects on packing density, stiffness, and strength: Natural and crushed sands. Journal of Geotechnical and Geoenvironmental Engineering, 132(5), 591-602.

Cleary, P. (2000). DEM simulation of industrial particle flows: case studies of dragline excavators, mixing in tumblers and centrifugal mills. Powder Technology 109(1-2), 83-104.

Cowper, G. R., Symonds, P. S., United States., & Brown University. (1957). Strain-hardening and strain-rate effects in the impact loading of cantilever beams. Providence, R.I: Division of Applied Mathematics, Brown University.

Cundall, P. (1971). A computer model for simulating progressive large-scale movements in blocky rock systems. In Proc. Symp. Int'l Soc. Rock Mech., Nancy II, Art. 8.

Cundall, P. (1987). Distinct element models of rock and soil structure. In E. Brown (Ed.), Analytical and Computational Methods in Engineering Rock Mechanics. Allen and Unwin.

Cundall, P. (1988). Computer simulations of dense sphere assemblies. Micromechanics of granular materials, 4, 113-123.

Cundall, P. & O. Strack (1978). The distinct element method as a tool for research in granular media, Part I, Report to NSF.

Cundall, P. & O. Strack (1979). A discrete numerical model for granular assemblies. Geotechnique 29(1), 47-65.

da Cruz, F., Emam, S., Prochnow, M., Roux, J. N., & Chevoir, F. (2005). Rheophysics of dense granular materials: Discrete simulation of plane shear flows. Physical Review E, 72(2), 021309.

Desmond, K. W., & Weeks, E. R. (2009). Random close packing of disks and spheres in confined geometries. Physical Review E, 80(5), 051305.

Donzé, F. V., & Bernasconi, P. (2004). Simulation of the blasting patterns in shaft sinking using a discrete element method. Electronic Journal of Geotechnical Engineering, 9, 1-44.

Dutt, M., Hancock, B., Bentham, C., & Elliott, J. (2005). An implementation of granular dynamics for simulating frictional elastic particles based on the DL_POLY code. Computer physics communications, 166(1), 26-44.

Dyer, K. R. (1970). Grain size parameters for sandy-gravels. Journal of Sedimentary Research, 40(2).

Frangin, E., Rousseau, J., Marin, P., & Daudeville, L. (2007). Some aspects of combined finite/discrete element method. Discrete Element Group for Hazard Mitigation Annual Report, 3.

Gong, G., Thornton, C., & Chan, A. H. (2011). DEM Simulations of Undrained Triaxial Behavior of Granular Material. Journal of Engineering Mechanics,138(6), 560-566.

Hanley, K., Huang, X., O'Sullivan, C., & Kwok, C. Y. (2013). Challenges of simulating undrained tests using the constant volume method in DEM. In AIP Conference Proceedings. American Institute of Physics.

Huang, X., Hanley, K. J., O'Sullivan, C., & Kwok, C. Y. (2014). Exploring the influence of interparticle friction on critical state behaviour using DEM.International Journal for Numerical and Analytical Methods in Geomechanics,38(12), 1276-1297.

Ishihara, K., Tatsuoka, F., & Yasuda S. (1975), Undrained deformation and liquefaction of sand under cyclic stresses, Soils and Foundations, 15, 29–44.

Itasca (2004). PFC2D 3.10 Particle Flow Code in Two Dimensions, Theory and Background volume (Third ed.). Minneapolis, Minnesota.

Itasca Consulting Group, 2007. PFC3D Version 4.0 User Manual. Itasca Consulting Group, MN, USA.

Jerier, J. F., Imbault, D., Donze, F. V., & Doremus, P. (2009). A geometric algorithm based on tetrahedral meshes to generate a dense polydisperse sphere packing. Granular Matter, 11(1), 43-52.

Jiang, M. J., Konrad, J. M., & Leroueil, S. (2003). An efficient technique for generating homogeneous specimens for DEM studies. Computers and geotechnics, 30(7), 579-597.

Kong, C. M., & Lannutti, J. J. (2000). Effect of agglomerate size distribution on loose packing fraction. Journal of the American Ceramic Society, 83(9), 2183-2188.

Kuhn, M. (2006). Oval and ovalplot: Programs for analyzing dense particle assemblies with the discrete element method: http://faculty.up.edu/kuhn/oval/doc/oval_0618.pdf

Kuwano, O., Ando, R., & Hatano, T. (2013, June). Granular friction in a wide range of shear rates. In POWDERS AND GRAINS 2013: Proceedings of the 7th International Conference on Micromechanics of Granular Media (Vol. 1542, No. 1, pp. 32-37). AIP Publishing.

Li, Y., Y. Xu, & C. Thornton (2005). A comparison of discrete element simulations and experiments for sand piles composed of spherical particles. Powder Technology 160, 219-228.

Lin, X & Ng, T.-T. (1995) "Contact Detection Algorithms for Three-Dimensional Ellipsoids in Discrete Element Method", International Journal for Numerical and Analytical Methods in Geomechanics, 19(9), 653-659.

Lin, X., & Ng, T.-T. (1997). A three-dimensional element model using arrays of ellipsoids. Geotechnique, 47(2), 319–329.

Malone, K. F., & Xu, B. H. (2008). Determination of contact parameters for discrete element method simulations of granular systems. Particuology, 6(6), 521-528.

Marketos, G., & Bolton, M. D. (2010). Flat boundaries and their effect on sand testing. International journal for numerical and analytical methods in geomechanics, 34(8), 821-837.

Milburn, R. J., Naylor, M. A., Smith, A. J., Leaper, M. C., Good, K., Swift, M. R., & King, P. J. (2005). Faraday tilting of water-immersed granular beds. Physical Review E, 71(1), 011308.

Modenese, C., Utili, S., & Houlsby, G. T. (2012). A numerical investigation of quasi-static conditions for granular media.

Munjiza, A. (2004). The combined finite-discrete element method. John Wiley.

Munjiza, A., Owen, D. R. J., & Crook, A. J. L. (1998). An M (M− 1K) m proportional damping in explicit integration of dynamic structural systems. International journal for numerical methods in engineering, 41(7), 1277-1296.

Newmark, N. M. (1959). A method of computation for structural dynamics. ASCE (Vol. 85, No. 3, pp. 67-94).

Ng, T.-T. (2004). Behavior of Ellipsoids of Two Sizes. Journal of Geotechnical and Geoenvironmental Engineering, 130, 10, 1077-1083.

Ng, T. T. (2005). Behavior of gravity deposited granular material under different stress paths. Canadian geotechnical journal, 42(6), 1644-1655.

Ng, T.-T. (2006). Input parameters of discrete element methods. ASCE Journal of Engineering Mechanics 132(7), 723-729.

Ng, T.-T. & Dobry, R. (1994) "Numerical Simulations of Monotonic and Cyclic Loading of Granular Soil", Journal of Geotechnical Engineering, ASCE, 120(2), 388-403.

Ng, T. T., Zhou, W., Ma, G., & Chang, X. L. (2014). Damping and particle mass in DEM simulations under gravity. Journal of Engineering Mechanics,141(6), 04014167.

O'Sullivan, C. (2002). The application of discrete element method to finite deformation problems. Ph.D. thesis, University of Berkeley.

O'Sullivan, C. (2011). Particulate Discrete Element Modelling: A Geomechanics Perspective. London: Spon/Taylor & Francis. Print.

O'Sullivan, C. & G. Bray (2002). Relating the response of the idealized analogue particles and real sands. In Numerical Modeling in Micromechanics via Particle Methods, pp. 157-164. A. A. Balkema.

O'Sullivan, C. & J. D. Bray (2004). Selecting a suitable time-step for discrete element simulations that use the central-difference time integration approach. Engineering Computations 21(2/3/4), 278-303.

O'Sullivan, C., L. Cui, & S. O'Neil (2008). Discrete element analysis of the response of granular materials during cyclic loading. Soils and Foundations 48, 511-530.

Padbidri, J. M., & Mesarovic, S. D. (2011). Acceleration of DEM algorithm for quasistatic processes. International Journal for Numerical Methods in Engineering, 86(7), 816-828.

Plassiard, J. P., Belheine, N., & Donzé, F. V. (2009). A spherical discrete element model: calibration procedure and incremental response. Granular Matter, 11(5), 293-306.

Potyondy, D. O. & P. A. Cundall (2004). A bonded-particle model for rock. International Journal of Rock Mechanics and Mining Sciences 41(8),1329-1364.

Perez, J. L., Kwok, C. Y., Huang, X., & Hanley, K. J. (2016). Assessing the quasi-static conditions for shearing in granular media within the critical state soil mechanics framework. Soils and Foundations, 56(1), 152-159.

Sheng, Y., C. Lawrence, B. Briscoe, & C. Thornton (2004). Numerical studies of uniaxial powder compaction process by 3D DEM. Engineering Computations 21(2/3/4), 304-317.

Shiu, W. J., Donzé, F. V., & Magnier, S. A. (2005). Numerical study of rockfalls on covered galleries by the discrete element method. Discrete Element Group for Risk Mitigation, 67.

Sibille, L., Nicot, F., Donzé, F. V., & Darve, F. (2007). Material instability in granular assemblies from fundamentally different models. International journal for numerical and analytical methods in geomechanics, 31(3), 457-481.

Siiriä, S., & Yliruusi, J. (2007). Particle packing simulations based on Newtonian mechanics. Powder technology, 174(3), 82-92.

Šmilauer, V. & B. Chareyre (2010). Yade DEM Formulation in Yade Documentation (V. Šmilauer, ed.), The Yade Project, 1st ed.

Stroeven, P., & Stroeven, M. (1999). Assessment of packing characteristics by computer simulation. Cement and concrete research, 29(8), 1201-1206.

Thomas, J. W. (2013). Dispersion and Dissipation. In Numerical partial differential equations: finite difference methods (Vol. 22). Springer Science & Business Media.

Thornton, C. (2000). Numerical simulation of deviatoric shear deformation of granular media. Geotechnique 50(1), 43-53.

Thornton C. & S. Antony (2000). Quasi-static shear deformation of a soft particle system. Powder Technology 109, 179-191.

Thornton, C. & Z. Ning (1998). A theoretical model for the stick/bounce behaviour of adhesive, elastic-plastic spheres. Powder Technology 99, 154-162.

Thornton, C., & Sun, G. (1993). Axisymmetric compression of 3D polydisperse systems of spheres. Powders and grains, 93, 129-134.

Tu, X., & Andrade, J. E. (2008). Criteria for static equilibrium in particulate mechanics computations. International journal for numerical methods in engineering, 75(13), 1581-1606.

Verdugo, R., & Ishihara, K. (1996). The steady state of sandy soils. Soils and Foundations, 36(2), 81-91.

Wang, C. Y., Wang, C. F., & Sheng, J. (1999). A packing generation scheme for the granular assemblies with 3D ellipsoidal particles. International Journal for Numerical and Analytical Methods in Geomechanics, 23(8), 815-828. M.

Yoshimine, M., Ishihara, K., & Vargas, W. (1998). Effects of principal stress direction and intermediate principal stress on undrained shear behavior of sand, Soils and Foundations, 38 (3) (1998), pp. 179‑188.

Zhou, W., Ma, X., Ng, T. T., Ma, G., & Li, S. L. (2016). Numerical and experimental verification of a damping model used in DEM. Granular Matter,18(1), 1-12.